Density Matrix Modelling of Terahertz Frequency Quantum Cascade Lasers: Steady State Analysis and Maxwell-Bloch Dynamics

Aleksandar Demić
University of Leeds
School of Electronic and Electrical Engineering

Submitted in accordance with the requirements for the degree of
Doctor of Philosophy
31st December 2019

The candidate confirms that the work submitted is his own, except where work which has formed part of jointly authored publications has been included. The contribution of the candidate and the other authors to this work has been explicitly indicated below. The candidate confirms that appropriate credit has been given within the thesis where reference has been made to the work of others.

Chapters 3, 4, 6, 7, 8 are original author's work in which some experimental results were obtained externally via either direct correspondence with experimental teams or available online material. Chapter 1 and 2 are literature review and contain little contribution by the author, Chapter 5 is a product of collaboration with a group at University of Nottingham.

Chapter 3 and Chapter 6 contain detail model description that have appeared in two publications:

> A. Demić, A. Grier, Z. Ikonić, A. Valavanis, C. A. Evans, R. Mohandas, L. Li, E.H. Linfield, A. G. Davies, and D. Indjin, Infinite-Period *Density-Matrix Model for Terahertz-Frequency Quantum Cascade Lasers*, IEEE Transactions on Terahertz Science and Technology 7, 4 (2017).
>
> A. Demić, Z. Ikonić R. W. Kelsall, D. Indjin, *Density matrix superoperator for periodic quantum systems and its application to quantum cascade laserstructures*, AIP Advances 9, 9 (2019).

Five figures in Chapter 4 have been adapted from versions appearing in IEEE publication above.

Figure in section 4.4.2 has been adapted from conference poster session:

> A. Demić, Z. Ikonić, R. W. Kelsall, D. Indjin, *Thermal modelling of QCLs via density matrix approach*, Poster session, International Quantum Cascade Laser School and Workshop IQCLSW18, Cassis, France, 2018

Chapter 5 has been constructed by theoretical contribution of the author in a joint collaboration with University of Nottingham that has been published in:

A. Dunn, C. Poyser, P. Dean, A. Demić, A. Valavanis, D. Indjin, M. Salih, I. Kundu, L. Li, A. Akimov, A. G. Davies, E. Linfield, J. Cunningham and A. Kent, *High-Speed Modulation of a Terahertz Quantum Cascade Laser by Coherent Acoustic Phonon Pulses*, Nature Communications, 2020 (accepted for publication).

Two figures in Chapter 5 have been adapted from the ones appearing in the publication.

The best you can do for the future is to give 100% of yourself today.

Acknowledgements

It is my great pleasure to express a deep sense of gratitude to my supervisors Dragan Indjin, Zoran Ikonić, and Robert Kelsall who have supported my research and have always been able to provide critical discussion and clarifications on challenging theoretical aspects of this project. Zoran's comments and vast knowledge on nearly every aspect of semiconductor physics have been invaluable to my project throughout the years, and Dragan's commitment to project progress, publication assistance and enthusiasm have greatly assisted me in completing this work.

I would like to express my gratitude to my colleagues, friends and family who have supported me throughout the course of this work.

I am grateful to Alex Valavanis who provided great deal of clarifications on the numerical implementation of qclsim code at the beginning of my work and also interesting discussions and ideas over the years. My special gratitude goes to my childhood friend Vladimir Nešić who provided me with great literature and advice on C++ programming which allowed me to efficiently restructure the code and implement numerous upgrades to the model.

I would also like to acknowledge previous researchers in this group who contributed on the scattering rate calculation code development along Alex: Jonathan Cooper, Craig Evans, Nikola Prodanović, Vladimir Jovanović and Andrew Grier. Special thanks go to Andrew who clarified the numerical implementation of the density matrix code developed by Dr Viet Dinh and himself.

I appreciate and give thanks to the Leeds International Research Scholarship (LIRS) for the support through a doctoral training grant award and Advanced Research Computing (ARC) team for providing me access to supercomputer cluster ARC2.

I would also like to thank many excellent collaborators: Jelena Radovanović and Nikola Vuković at University of Belgrade and Gary Agnew, Xiaoqiong Qi and Aleks Rakić at the University of Queensland. It

has been a privilege to work together and visit each of these groups during my research. I would like to express my gratitude to Dr Aniela Dunn and Prof. John Cunningham at University of Leeds and Prof. Anthony Kent at University of Nottingham for a very fruitful collaborative work on high speed modulation of QCL devices.

My thanks also go to Dr Massoud Ghalaii with whom I shared office for four years along numerous scientific discussions, and to colleagues from the group with whom I spent a lot of time in developing teaching experience at University of Leeds.

Aleksandar Demić, December 2019

Abstract

Terahertz frequency quantum cascade lasers (QCLs) are state of the art structures that exploit multiple quantum well (MQW) system to generate emission by radiative transition between very narrow spaced energy levels ($\sim$ 12 meV) through resonant tunnelling quantum mechanical process. The complexity of MQW prevents use of *ab initio* models, and only models that exploit the periodicity of the structure may be applied.

Terahertz frequency devices can have 3 - 12 (and more) states per MQW period, thus there is an interest for a general model that is not dependent on number of states per module. Additionally, the resonant tunnelling process experiences significant issues with typically used semi-classical rate equation (RE) models, by generating discontinuities due to the lack of coherent quantum mechanical transport within these models. The quantum mechanical models such as Non-Equilibrium Green Function (NEGF) and Density Matrix (DM) approaches therefore, need to be applied. NEGF models provide detail analysis of quantum effects, however they typically exhibit very high numerical cost which limits modelling QCLs with large number of states per module. On the other hand, DM approaches have low numerical complexity which allows more versatility of the model applications.

This thesis will focus on DM approach that is independent on number of states per module. Both NEGF and DM have been avoided in wide spread use also due to their complicated mathematical formulation. One of the main contributions of this work is a detail algebraic simplification of DM model, where its entire construction can be laid out by a single algebraic expression which also allows straightforward numerical implementation, similar to RE models.

The low numerical cost of DM approach allows further expansion of the model by coupling the transport model to Maxwell wave equation (creating Maxwell-Bloch (MB) model) and investigating dynamic processes and properties of emitted radiation. This thesis will present the first (to the best of author's knowledge) dynamic Maxwell-Bloch model for terahertz frequency QCLs, that is independent on number of states per period. In addition to this, MB model will be extended to allow reinjection of optical radiation to the laser cavity which will formulate general model for optical feedback intereferometry that would be capable of studying the self–mixing (SM) effect.

Overall, steady–state and dynamics analysis of terahertz frequency QCLs will be discussed through several applications that model experimental current-voltage-power characteristics, acoustic phonon modulation, Maxwell-Bloch dynamics and self-mixing interferometry dynamics. This thesis will also discuss the potential applications of DM model in design of terahertz frequency QCLs, where Chapter 8 will present a novel structure proposal that provides high temperature performance, comparable to the current record designs.

Abbreviations

ACP	**AC**oustic **P**honon
ADS	**A**lloy **D**isorder **S**cattering
ARC2	**A**dvanced **R**esearch **C**omputing **2**
BTC	**B**ound–**T**o–**C**ontinuum
CW	**C**ontinuous–**W**ave
DFT	**D**ensity **F**unctional **T**heory
DM	**D**ensity **M**atrix
EE	**E**lectron–**E**lectron
FIR	**F**ar–**I**nfra**R**ed
IFR	**I**nter**F**ace **R**oughness
LK	**L**ang **K**obayashi
ILL	**I**njection Lasing **L**evel
IMP scattering	**I**onised i**MP**urity scattering
LLL	**L**ower **L**asing **L**evel
LO–phonon	**L**ongitudinal **O**ptical–phonon
MB	**M**axwell **B**loch
MBE	**M**olecular **B**eam **E**pitaxy
MIR	**M**id–**I**nfra**R**ed
MM waveguide	**M**etal–**M**etal waveguide
NDR	**N**egative **D**ifferential **R**esistance
NEGF	**N**on–**E**quilibrium–**G**reen–**F**unction
NRWA	**N**on Rotating **W**ave **A**pproximation
ODE	**O**rdinary **D**ifferential **E**quation
QCL	**Q**uantum **C**ascade **L**aser
RE	**R**ate **E**quation
RWA	**R**otating **W**ave **A**pproximation
SM	**S**elf–**M**ixing
SP waveguide	**S**ingle **P**lasmon waveguide
TDP	**T**ime **D**ependent **P**erturbation
THz	**T**erahertz
ULL	**U**pper Lasing **L**evel

Contents

List of Figures

List of Tables

List of publications [1]

1. A. Demić, V. Milanović, J. Radovanović, *Bound states in the continuum generated by supersymmetric quantum mechanics and phase rigidity of the corresponding wavefunctions*, Phys. Lett. A **379**, 2707-2714 (2015).
2. A. Demić, V. Milanović, J. Radovanović, M. Musić, *WKB method for potentials unbounded from below*, Mod. Phys. Lett. B **30**, 1650003 (2016).
3. A. Demić, J. Radovanović, V. Milanović, *Analysis of the influence of external magnetic field on transition matrix elements in quantum well and quantum cascade laser structures*, Superlattices and Microstructures **96**, 134-149 (2016).
4. A. Demić, A. Grier, Z. Ikonić, A. Valavanis, C. A. Evans, R. Mohandas, L. Li, E.H. Linfield, A. G. Davies, and D. Indjin, *Infinite-Period Density-Matrix Model for Terahertz-Frequency Quantum Cascade Lasers*, IEEE Transactions on Terahertz Science and Technology **7**, 4 (2017).
5. A. Demić, Z. Ikonić, R. W. Kelsall, D. Indjin, *Density matrix superoperator for periodic quantum systems and its application to quantum cascade laser structures*, AIP Advances **9**, 9 (2019).
6. A. Rakić, Y.Lim, T. Taimre, G. Agnew, X. Qi, K. Bertling, S. Han, S. Wilson, I. Kundu, A. Grier, Z. Ikonić, A. Valavanis, A. Demić, J. Keeley, L. Li, E. Linfield, A. Davies, P.Harrison, B. Ferguson, G. Walker, T. Prow, D. Indjin, H. Soyer, *Optical feedback effects on terahertz quantum cascade lasers: modelling and applications*, Proc. SPIE **10030**, Infrared, Millimeter-Wave, and Terahertz Technologies IV, 1003016 (2016)
7. A. Dunn, C. Poyser, P. Dean, A. Demić, A. Valavanis, D. Indjin, M. Salih, I. Kundu, L. Li, A. Akimov, A. G. Davies, E. Linfield, J. Cunningham and A. Kent, *High-Speed Modulation of a Terahertz Quantum Cascade Laser by*

---

[1] Publications 4–8 are a relevant for work presented in this thesis, publication 7 is accepted, publication 8 is under review

Coherent Acoustic Phonon Pulses, Nature Communications, 2020 (accepted for publication).

8. X. Qi, G. Angew, T. Taimre, S. Han, Y. L. Lim, K. Bertling, A. Demić, P. Dean, D. Indjin and A. Rakić, *Laser feedback interferometry in multi-mode terahertz quantum cascade lasers*, Optics Express, 2020 (under review).

List of conference presentations [1]

1. A. Demić, V. Milanović, J. Radovanović, *Influence of nonparabolicity and external magnetic field on dipole matrix elements in quantum cascade laser structure*, **Poster session**, International Quantum Cascade Laser School and Workshop IQCLSW16, Cambridge, UK, 2016.

2. A. Demić, *Terahertz-frequency quantum cascade lasers and coherent modelling of transport via density-matrix method*, **Invited talk**, IEEE Invited seminar, School ITEE, University of Queensland, Brisbane, Australia.

3. A. Demić, A. Grier, Z. Ikonić, A. Valavanis, R. Mohandas, L. Li, E.H. Linfield, A. G. Davies, and D. Indjin, *Density Matrix Model for bound to continuum terahertz quantum cascade lasers*, **Contributed talk**, IOP International Workshop on Computational Nanotechnology IWCN17, Windermere, Lake District, 2017.

4. A. Demić, A. Grier, Z. Ikonić, A. Valavanis, R. Mohandas, L. Li, E.H. Linfield, A. G. Davies, and D. Indjin, *Density Matrix Superoperator for Terahertz Quantum Cascade Lasers*, **Contributed talk**, International School and Conference on Photonics Photonica2017, Belgrade, Serbia, 2017.

5. A. Demić, Z. Ikonić, R. W. Kelsall, D. Indjin, *Thermal modelling of QCLs via density matrix approach*, **Poster session**, International Quantum Cascade Laser School and Workshop IQCLSW18, Cassis, France, 2018.

---

[1] Converences 2–6 are a relevant for work presented in this thesis

6. A. Demić, Z. Ikonić and D. Indjin, *Ultrafast Dynamics of Quantum Cascade Laser: Modelling and Optical Properties*, **Poster session**, International School and Conference on Photonics Photonica2019, Belgrade, Serbia, 2019.

Chapter 1

Introduction

1.1 Semiconductor lasers

Laser (Light Amplification by Stimulated Emission of Radiation) represents a concept of a device that emits coherent electromagnetic radiation. The principle of laser operation lies in the sustainability of the stimulated emission. Typically, all lasers operate on the quantum mechanic principles and generally require: i) a laser medium that contains two or multi-level system (including carriers in semiconductors) ii) a pumping process that sustains population inversion between at least two quantum mechanical energy levels so that transitions generate the desired electromagnetic radiation and iii) an optical feedback element that directs the radiation to be amplified either through a single or multiple pass across the medium [1]. A typical laser structure is presented in Fig. 1.1.

Note that population inversion is not achieved exclusively through the presence of the energy levels. A good example is a free electron laser [2] that uses highly accelerated electrons that are focused over a periodic set of magnets. The magnetic field periodically curves the electrons' trajectory, and in each "bend" of the trajectory, a photon is emitted due to the change of the electron's velocity. So far, these structures represent the most powerful and most tunable lasers and they are able to emit radiation between X-Ray and microwave part of the electromagnetic spectrum. However, major flaw of free electron lasers is a need for a particle accelerator, and a variety of other media is used to cover the spectrum, most notably gas, chemical dyes, solid-state and semiconductor lasers [3].

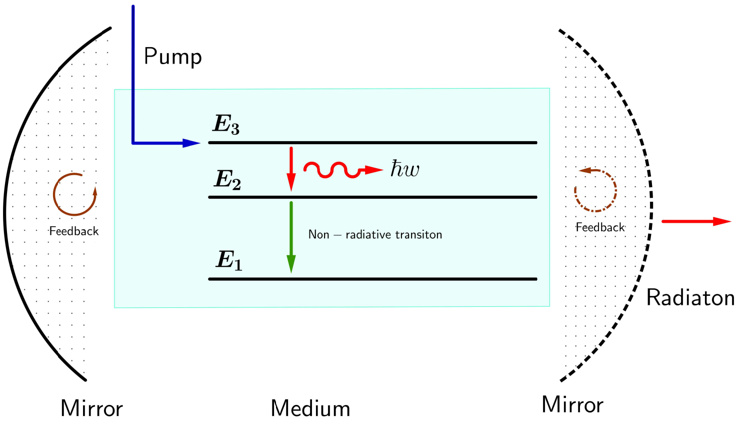

Figure 1.1: The principle of typical laser operation. The medium is pumped into higher states, and radiative transition generates emission of photons at a frequency determined by the energy level separation. The amplification process is periodically repeated by using a feedback element, in this case a Fabry-Pérot resonator that consists of one non transparent and one semi-transparent mirror.

Semiconductor lasers were first demonstrated in 1962 in GaAs PN junction [4]. As crystalline structures, semiconductors exhibit periodicity in their atomic potential that results in formation of energy bands that the carriers may occupy. In every semiconductor, two bands are of interest: the valence band (E_V) which is nearly fully occupied by electrons and the conduction band (E_C) which is nearly empty. These bands are separated by energy energy gap E_G. In principle, lasing transition in diode lasers occurs between E_C and E_V bands and emission frequency is determined by the size of the energy gap.

Theoretically, semiconductors are able to cover any desired frequency, as long as the material with the appropriate direct energy gap is available, and a variety of binary, ternary and quaternary semiconductor materials [5] may be employed. At first, it may seem impossible to achieve semiconductor lasers in far-infrared portion of the electromagnetic spectrum, because a structure with such low band gap ($\sim$ 10 meV) would not represent a semiconductor, but rather a metal.

Throughout the development of the diode lasers [6], various quantum mechanical effects have been employed in order to improve their operation, namely imposing the constraints on the carrier transport by the use of hetero-junctions which create quantum wells and barriers [7]. The introduction of the heterojunctions, allowed engineering of the band-structure potential and the study of the state of the art multiple quantum well theoretical proposals presented in [8, 9, 10] that offered a novel lasing concept in semiconductors, which was able to surpass the band gap limit on the desired emitting frequency.

1.2 Quantum Cascade Laser

The pioneering proposal in [10] presented a potential lasing semiconductor structure that employs multiple quantum wells in the valence or the conduction band. The periodicity of the quantum well superlattice would induce the formation of energy subbands within the valence or conduction band, in a similar fashion as the atomic potential in the crystalline lattice of the semiconductor forms the energy bands. The population inversion may be sustained through the application of external bias and the tunnelling process between the wells. This cascading structure is presented in Fig. 1.2b) and the principle of its operation is fundamentally different from that in the conventional diode lasers. Quantum Cascade Laser (QCL) is a unipolar device as it uses only electron transport in the conduction band and its cascading structure promises generation of significantly larger number of photons because in diode lasers, one electron can only create one photon after the recombination process with a hole, while in the QCLs one electron may create as many photons as there are periods in the cascade, if the tunnelling efficiency is high.

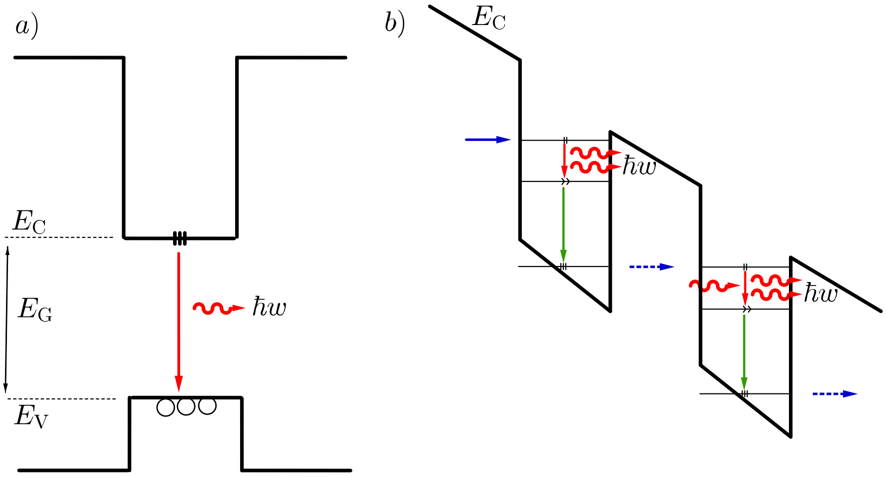

Figure 1.2: a) Inter–band transition in the diode laser, the emitting frequency is determined by the size of the energy gap and the recombination of electrons and holes. b) Intra–band (inter–subband) transition in the quantum cascade laser. The lasing transition occurs between the energy subbands within the conduction band. The population inversion is maintained through the application of the external bias and the tunnelling effect.

The first QCL was demonstrated in 1994 by [11] in $Al_{0.48}In_{0.52}As$/ $Ga_{0.47}In_{0.53}As$ structure, that lased at 4.2 μm giving promising advantages over diode lasers in terms of the threshold current and mode linewidth, but more importantly, the possibility of designing sources in mid-infrared (MIR) and far-infrared (FIR). A variety of material systems (InP/InGaAs, GaAs/AlGaAs,InAs/ AlSb ...) and designs [12, 13] have been employed to generate QCLs at room temperature [14, 15] and with high power performance [16, 17] emitting frequencies from 3 μm [18] to 16 μm [19]. The QCLs have found numerous applications across the MIR spectrum in chemical sensing [20, 21], free-space communications [22], medical diagnostics [23], industrial process monitoring [24], plasma spectroscopy [25], gas spectroscopy [26], etc.

1.3 Terahertz Quantum Cascade Laser

The Terahertz (THz) (or FIR) region is located between the microwave and the mid-infrared region and the required energy level separation is $1.2 - 30$ meV as depicted in Fig. 1.3. This frequency range had been nearly inaccessible due to the meagre availability of the possible sources, such as p-Ge laser [27], THz parametric oscillator [28] and free electron laser [29].

$$\boldsymbol{E_{\mathrm{meV}} = 4.14 \cdot \nu_{\mathrm{THz}} = 1239.84 \cdot \lambda_{\mu\mathrm{m}}^{-1}}$$
$$\boldsymbol{\nu_{\mathrm{THz}} = 299.78 \cdot \lambda_{\mu\mathrm{m}^{-1}}}$$

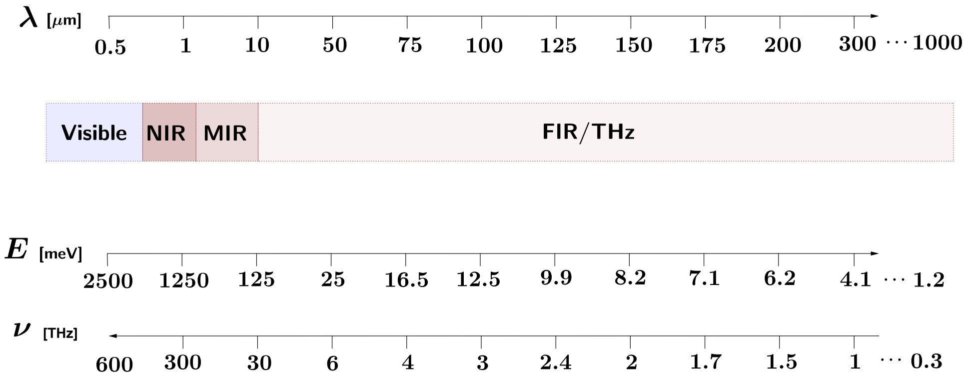

Figure 1.3: a) Electromagnetic spectrum across wavelength λ, photon energy E and frequency ν, scaled in μm, meV and THz respectively

The principle presented in Fig. 1.2b) allows the construction of light sources with very narrow energy separation and the first THz QCL was demonstrated in 2002 [30] in GaAs at 4.4 THz, that lased up to 50K. Since then, a variety of structures and designs have been presented [31, 32] that delivered sources from 1.2 THz [33, 34] to 5.4 THz [35], and enabled lasing up to 210K [36] in pulsed operation, without the assistance of external magnetic field.

The temperature limitation of the THz QCLs comes from the difficulty of maintaining the low $\sim$ 10 meV energy separation at higher temperatures and the lack of the supporting technology for alternative material systems other than GaAs [37]. The upper frequency limit is determined by the material properties, namely the existence of highly absorbing Reststrahlen band in GaAs/AlAs above 6 THz [38, 39], while the lower frequency limit is attributed to the fact that the required energy separation for radiation below 1 THz is lower than 4.1 meV and designing a structure that can prevent absorption, even at the cryogenic temperatures, is very challenging. Some of the performances have been improved by using external magnetic field [40] where lasing up to 225 K was reported, however the only available room temperature THz QCL sources employ frequency difference non-linear effects through the use of the MIR QCLs [41, 42]. These structures up to now generate very low optical power, due to the very low efficiency of the non–linear processes.

1.4 THz QCL designs

The band-structure engineering for the THz QCLs is more challenging than for the MIR QCLs, mostly due to the low energy difference between lasing levels requirement. The principle described in Fig. 1.2b) is not feasible with a repetition of a single quantum well, but rather with a periodic repetition of a multiple quantum well stack, where both selective injection into upper lasing level and efficient extraction from the lower lasing level is maintained with reasonable dynamics working range. The period of any QCL structure needs to ensure that the population inversion is maintained and this is achieved through the design of the active region which contains lasing states and the injector/collector region that efficiently transports the carriers between the active regions by resonant tunnelling effect.

- The active region needs to generate the desired emission through the radiative transition between an upper lasing level (ULL) and a lower lasing level (LLL). Quantum-mechanically, each energy state is described by the corresponding wavefunction, whose square moduli represent the state occupation probability. If two states have highly overlapping wavefunctions, there is a high probability of their interaction. For the ULL → LLL transition only radiative interaction is of interest, and fully overlapped ULL and LLL states (vertical transition) are not generally desired, since the absorption probability for interaction between LLL and ULL is also higher, along with potential non-radiative processes that may occur when subbands are full [43], especially at higher temperature [44]. On the other hand, material gain is proportional to the wavefunction overlap through the square of the dipole matrix element, and wavefunction misalignment (diagonal transition) between ULL and LLL is not desired. A good QCL design needs to find a compromise between these two effects.

- The injector region needs to be efficiently coupled with the active region so that it maintains the population inversion through two effects: i) collection/extraction of the carriers from LLL and ii) injection of those carriers into the ULL of the next period. Employment of an additional injection lasing level (ILL) is therefore required. Note that in any quantum mechanical system, electron would always tend to the lower potential energy, and the ILL is usually the ground state of the QCL period, usually separated from the LLL by LO-phonon energy (36 meV in GaAs) for efficient extraction of carriers from LLL. However in order for the transition LLL → ILL to be optimal, a cluster of intermediate states may be employed. ILL also needs to be strongly coupled (nearly aligned) with the ULL of the next period. The use of additional intermediate states provides more efficient depopulation of LLL leading to the high power operation of the QCL, however it limits the temperature operation of the device, since parasitic absorption is more likely to occur, and another compromise needs to be made.

For the THz QCLs, this has led to three major designs [31, 45]: Resonant-phonon (LO-phonon) structure, Bound-to-continuum (BTC) structure and Hybrid structure.

1.4.1 LO-phonon design

The LO-phonon design [46, 44, 47] comprises only a small number of quantum wells, usually two in the active region and one or two in the injector region. This design, therefore, has only several energy states as depicted in Fig. 1.4. The key feature of this design is its temperature performance. The depopulation of the LLL is optimised through the use of LO-phonon scattering mechanism. The LO-phonon energy in GaAs is 36 meV, and that value corresponds to the energy difference between LLL and ILL.

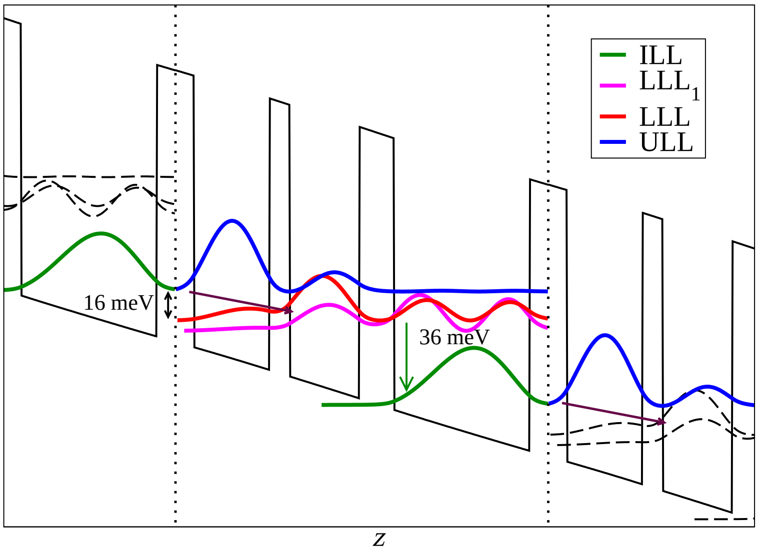

Figure 1.4: LO-phonon design of the high temperature performance structure [47] that is lasing in the pulsed operation up to 200K. The lasing transition is diagonal, the depopulation of LLL is obtained through an intermediate level labelled as LLL$_1$ which scatters to the ILL through the LO-phonon process. ILL is then resonantly coupled with the ULL of the adjacent period (One QCL period is denoted by dotted vertical lines).

The LO-phonon scattering mechanism is dominant in any QCL structure, and it is also essential to prevent the depopulation of the ULL [31] as well. This is achieved through the addition of intermediate state between LLL and ILL (labelled as LLL$_1$ in Fig. 1.4). This state is strongly coupled with the LLL, and at the same time its wavefunction is located in the same well as the ILL. This has two major advantages: i) LLL is depopulated efficiently to the intermediate state from the adjacent well and ii) intermediate state undergoes the LO-phonon transition to the ILL, without having any significant overlap with the ULL.

Another approach to suppress parasitic leakage is to employ higher barriers as was done in the record highest temperature QCL [36] that lases up to 210K. The barrier height is controlled by molar fraction of Al, x, which is added to GaAs, creating Al$_x$Ga$_{1-x}$As alloy. The value of $x = 0.15$ is most common for nearly all realised THz QCLs. The reason for this, is that with low barriers (around 125 meV), the design does not suffer significantly due to experimental tolerance during the growth. Another issue with high barrier THz QCL is the necessity for higher doping, since electrons are more confined than in low barrier material. For these reasons, the record temperature [36] device operates with very high current density. However, breaching the previous record of 200K [47] has allowed thermoelectric cooling systems to be used instead of liquid Helium, which enables broader industry applications of THz technology.

The advantages of LO-phonon design are:

- Short period length which significantly reduces fabrication and growth issues
- Temperature robustness in pulsed operation at higher frequencies, due to the low number of energy states

The drawbacks:

- Very high threshold current that also results in high voltage operation
- Very bad temperature performance in continuous-wave (CW) operation due to the previous drawback (heating of the device).
- Low coupling strength between ILL and ULL
- Non optimal temperature performance in pulsed operation at lower frequencies due to the difficulty of maintaining the population inversion, mostly due to the previous drawback.
- Non optimal optical power performance due to the diagonal lasing transition and relatively low injection efficiency

Several variations of LO-phonon design have been realised. A scattering assisted QCL design [48] essentially represents inverted LO-phonon structure. Instead of extracting LLL by LO-phonon transition, ULL is being pumped by this process, while LLL is being extracted through resonant tunnelling. For that reason, the first well in the design needs to be narrow in order to “lift” the first state ∼36 meV above ULL and the injection barrier needs to be thin in order to efficiently depopulate LLL. This design did not provide significant benefits when compared to the other ones [49] mainly due to parasitic states that were not suppressed by the design itself. Recently, this issue has been addressed by proposing designs with higher AlGaAs barriers [50] (Al molar fraction $x = 0.2 - 0.3$). This design has several significant disadvantages, such as very high operating voltage, very high current density at the threshold, bad temperature performance with $\mathrm{Al_{0.15}Ga_{0.85}As}$ barriers and fabrication issues with $x > 0.15$ barriers. The latter disadvantage is a consequence of slight variation of x during the growth. Additionally, designs with high barriers require higher doping which increases the threshold current (the record structure lases only at threshold current as high as 10 A).

Another variation of LO-phonon design is a scattering assisted device that has two consecutive LO-phonon transitions ensuring that both ULL and LLL are being pumped/extracted by this mechanism. This structure has generated the highest temperature performance at low frequencies [51]. The main issue, however is a very high bias (voltage) needed to align the states by $\approx 36 + 8 + 36$ meV per period. Chapter 8 of the thesis will present similar design scheme to [51] which does not need very high operating bias operation and represents a novel design that has not been investigated in literature so far. Calculation and optimisation technique presented in Chapter 8 has yielded several active region designs that promise temperature performance above that of the present record holding structure.

1.4.2 BTC design

The BTC design [33] is composed of a large number of quantum wells, mimicking chirped superlattice structures designed for MIR QCLs. The presence of multiple quantum wells results in the formation of quasi-continuous mini-bands rather than clearly outlined set of bound states as in LO-phonon structures. These mini-bands contain a dense set of bounds states between LLL and ILL, while ULL remains bound – isolate in energy spectrum in optically active part of the structure (which is the reason for the design's name).

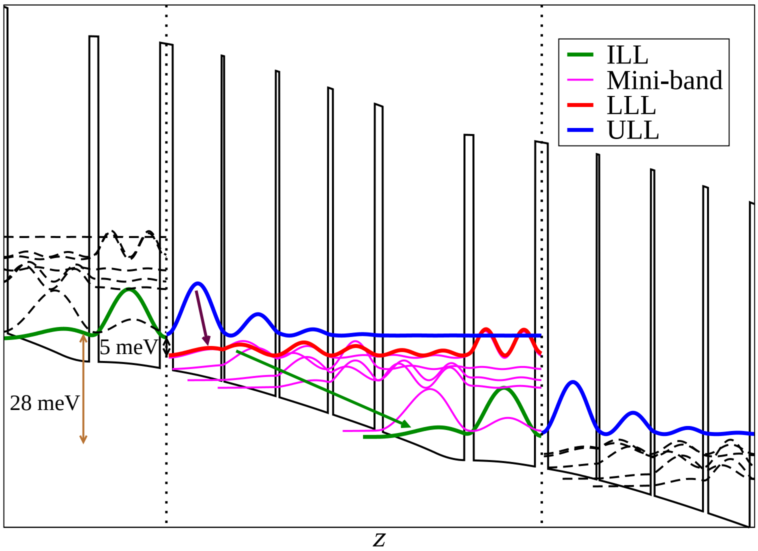

Figure 1.5: The BTC design of the low frequency record structure [33] (without the assistance of the magnetic field) that is lasing at 1.2 THz. One QCL period is denoted by vertical dotted lines. The lasing transition is mostly vertical. The LLL is relaxed to the ILL with the diagonal transitions within the mini-band (denoted by the green arrow). The ILL and some of the lower mini-band states then couple with the ULL from the adjacent period. The ULL - ILL energy difference within the same module must be kept below LO-phonon energy (36 meV).

The main aim of the BTC structure is in optimising the LLL depopulation and the injection to the adjacent period ULL by connecting the LLL and ILL with a cluster of narrow states. As the electrons always tend to the lower energy the relaxation within the mini-band is very likely to occur, however absorbing processes are highly probable as well, which is the reason why the number of quantum wells needs to be high, in order to ensure that the wavefunctions of each state within the mini-band are spatially shifted mimicking the diagonal transition in the traditional sense as shown in Fig. 1.5. Note that the lasing transition is mainly vertical, which results in higher material gain. The important specification of this design is that the energy difference between the ULL and ILL (within the same period) must be lower than LO-phonon energy in order to avoid the depopulation of the ULL by direct electron – LO–phonon scattering. Since the LO-phonon scattering process is not dominant at low temperatures, this design is very suitable for CW operation, however the large number of closely separated states disables high-temperature applications. The advantages of the BTC design are:

- Low current threshold which enables CW operation.
- Very good performance at low frequency
- Very good power performance at low temperatures
- High injection and extraction efficiency, the injection to the adjacent period is highly coupled which tolerates the fabrication and growth variations.

The drawbacks:

- Bad performance with the temperature increase due to the large number of closely spaced energy levels
- High period length that affects the growth

1.4.3 Hybrid design

The Hybrid design [52] represents the combination of the former two. This design takes the advantage of high temperature performance of the LO-phonon structures and high extraction efficiency (and high power) of the BTC structures. In the simplest manner, this structure can be explained as bound-to-continuum-to-bound meaning that the ULL is bound, the LLL is formed as a narrow mini-band, and the ILL is separated from the LLL by the LO-phonon energy.

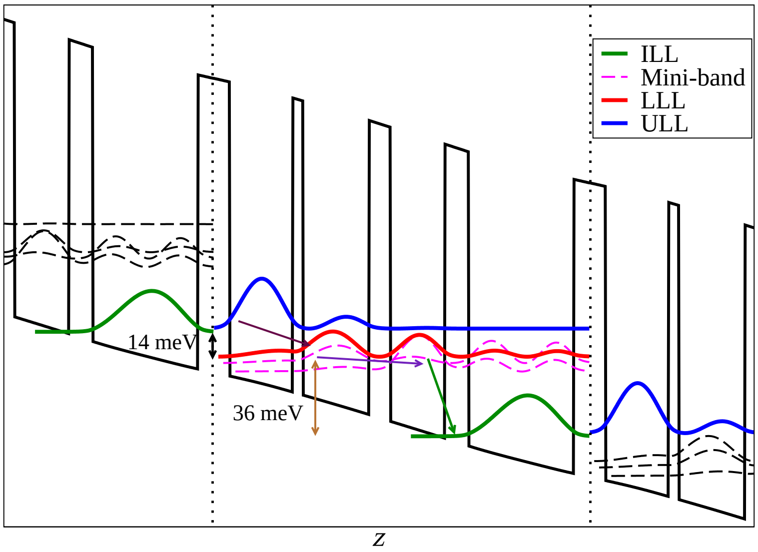

Figure 1.6: The Hybrid design of the record highest power structure [53]. Vertical dotted lines denote one period of the structure. The lasing transition is diagonal, while LLL is the top of the mini-band. The mini-band relaxation is very fast and mostly consists of direct transitions, but the transition from the top to the bottom of the mini-band is overall diagonal (as depicted by the purple arrow). The structure is designed in a such way that the middle state of the mini-band is separated from the ILL by the LO phonon energy, and this transition is vertical, ensuring very efficient extraction.

.

The mini-band that forms below the LLL helps in its depopulation, and this is further enhanced by incorporating the LO-phonon transition in the ILL. This design solves the main issues from the previous two: i) The efficient mini-band extraction compensates for the low coupling strength between ILL and ULL and the current threshold is lower than in the LO-phonon structures which enables CW operation, ii) the operating temperature is higher than in the BTC structures due to the LO-phonon extraction stage, iii) The period length is shorter than in the BTC structures, which allows stacking of high number of periods ($\sim$150) in order to obtain high optical power. As the LO-phonon process is dominant at higher temperatures, this design displays very broad optical power dynamic range and currently holds the records for the highest power [53], the highest frequency [35] and the highest temperature CW [54] THz QCL. The advantages of the Hybrid design are:

- Very high optical power performance, due to the period length and efficient injection and extraction.
- Very good performance at high frequency
- Very broad dynamic range
- Moderate current threshold which enables CW operation

The drawbacks:

- Moderate temperature performance in pulsed operation due to the miniband
- Moderate current threshold value
- High period length that affects the growth

1.5 Growth, Fabrication and Waveguides for THz QCL

1.5.1 Growth and Fabrication

The nanotechnology has been immeasurably boosted by the invention of Scanning Tunnelling Microscopy (STM) [55] and Molecular Beam Epitaxy (MBE) [56]. The latter method allowed physical deposition of very thin epitaxial atomic layers of material and this started the realisation of structures in nanoscale. MBE is today the well established technology, especially for wide spread material systems such as Si and GaAs. The main advantage of MBE is the slow deposition rate (less than 1000 nm per hour) that requires high vacuum in order to reduce impurities in the layers.

THz QCLs require high precision of growth, and the main issue in the fabrication is the reproducibility despite the high calibration [57, 58]. In general, QCL designs with longer periods and higher number of layers display greater variation, however the Hybrid and BTC design have more efficient pumping of ULL than the LO-phonon design and the performance of the device is not significantly impacted. The temperature performance should be better with the larger chip size, however that also may cause growth defects.

The details of full fabrication and growth processes are beyond the scope of this thesis. Generally, they involve a multitude of highly sensitive steps that apart from MBE growth, involve several photolithography, etching, annealing, deposition and cleaving techniques along with the state-of-the-art calibration and process monitoring [59].

MBE needs to be calibrated for the specific material system. Apart from GaAs, THz QCLs have been realised in InGaAs with InAlAs, GaAsSb, AlInGaAs barriers [37, 60], but none of them match the performance of GaAs devices. Semiconductors with lower effective mass are preferable due to the potential for the larger material gain, however the LO-phonon energy needs to be significantly higher as well. Currently, the only room temperature semiconductor THz QCLs are realised through non-linear frequency difference effect that uses combination of MIR QCLs [41].

High interest is drawn by nitride structures due to the very large LO-phonon energy ($\sim$90 meV) and quantum dot QCLs due to the additional restrictions of the transport, however the growth technology is extremely challenging. Nitride structures display built in polarisation, creating saw-like band potential profile due to material strain, and realising a single quantum well has been very challenging [61, 62]. On the top of that GaN has quite large electron effective mass that may reduce the laser gain. Theoretically, the low effective mass semiconductors introduce higher non-parabolicity, which increases the transition line broadening.

1.5.2 Waveguides

Every laser requires a feedback element that directs the generated light to be amplified through single or multiple passes through the medium. The main issue with THz radiation is that the free carrier absorption is very high [31] and unique waveguide designs have been developed that use plasmonic effect [63] in metals or highly doped semiconductors. The characterisation of waveguides in Fabri-Pérot setup is determined by the mirror loss α_m and the waveguide loss α_w.

The mirror loss depends on the cavity length L_c and reflectivity of the left R_L and the right R_R mirror (which are usually equal) as $\alpha_\mathrm{m} = -L_\mathrm{c}^{-1}\ln(\sqrt{R_\mathrm{L}R_\mathrm{M}})$ and for $R_\mathrm{L} = R_\mathrm{R} = (n+1)^2/(n-1)^2$ the logarithm value varies in range $[-0.6, -0.46]$, as most III-V semiconductors have the refractive index n between 3 and 3.8. For GaAs superlattice [64] the value $n \approx 3.25$ $(= \sqrt{\epsilon_\infty})$ can be taken and the mirror loss is roughly $\alpha_\mathrm{m}[\mathrm{cm}^{-1}] = 5.5\ L_\mathrm{c}^{-1}$ [mm] which indicates the lower losses for longer cavities.

The waveguide loss is dominant and requires detailed consideration of the dielectric properties of the material [45, 65]. The primary mechanism is the free carrier absorption $\alpha_\mathrm{fc} \propto N_\mathrm{D}\lambda^2\mu_\mathrm{e}^{-1}(T)$ where N_D is the doping density, and μ_e is electron mobility that depends on temperature and doping density. It is clear that the operating wavelength strongly influences the free carrier loss.

The laser starts working once the confined light in the waveguide overcomes the total loss:

$$\Gamma g_\mathrm{th} = \alpha_\mathrm{m} + \alpha_\mathrm{w} \tag{1.1}$$

where Γ represents the mode confinement factor which is defined as the fraction of light confined in the active region. Throughout this thesis we will use the model developed in this group in [45] that uses one-dimensional transfer matrix method to determine the dielectric function and total loss $(\alpha_\mathrm{m} + \alpha_\mathrm{w})$ in the waveguide which is also capable of determining the modal overlap Γ.

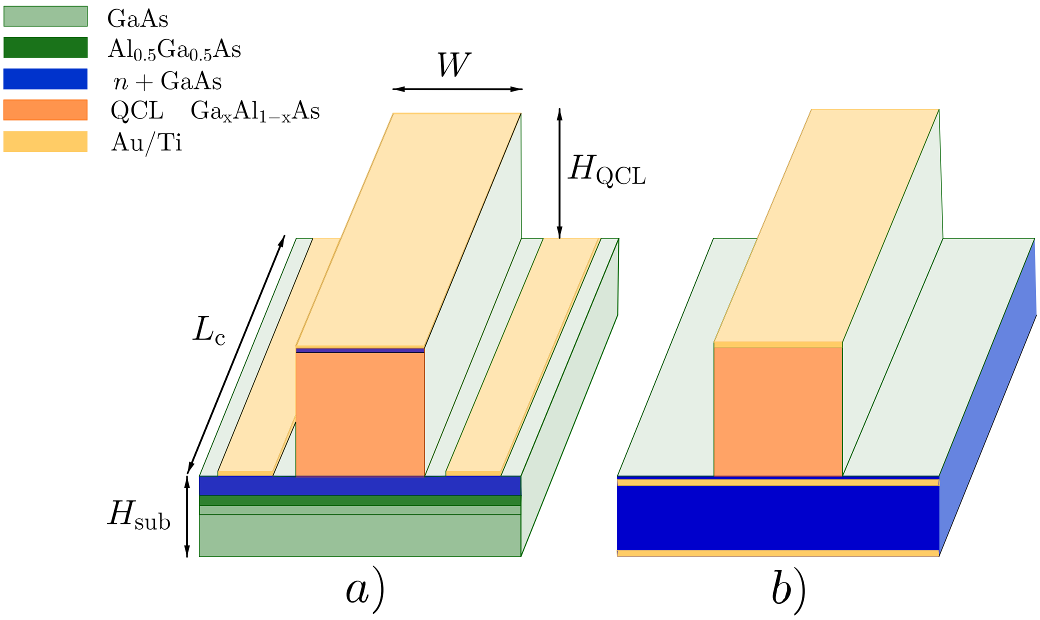

Figure 1.7: a) SP waveguide b) MM waveguide. The scale has been adjusted for better view, note that the usual dimensions are $H_{sub} \approx 200 - 300$ μm, $L_c \approx 1 - 4$ mm, $W \approx 100 - 250$ μm, $H_{QCL} = 9 - 15$ μm.

Two types of waveguides have been developed for THz QCLs: semi-insulating single-plasmon (SP) and metal-metal (MM) waveguide [31] that are presented in Fig. 1.7.

For the SP waveguide, the active region is "sandwiched" between the two highly doped thin layers, and this ridge is grown on a semi-insulating GaAs and finished off by the top metal contact. Such configuration forms surface plasmon modes throughout the doped region, the top metal contact prevents the dissipation of light, however the bottom contact allows the light to propagate through the substrate. This results in a relatively small modal overlap ($\Gamma \approx 0.1 - 0.5$), however the free-carrier loss is minimised because the overlap with the doped layers is small.

The MM-waveguide uses metal contacts instead of the highly doped layers. This allows very high confinement of light in the active region ($\Gamma \approx 1$), however the free-carrier loss is considerably higher than in the SP waveguides. The additional benefit of the MM-waveguide is the higher mirror reflectivity ($R \approx 0.5 - 0.9$)

that results in the lower mirror loss, and overall the MM-waveguides have lower modal loss (total loss divided by Γ) than the SP-waveguides.

The advantages of the SP waveguides are very good beam profile properties and very high power, while the main disadvantage is the higher current threshold (due to the higher loss) and the higher thermal dissipation which mainly limits CW operation. The advantages of the MM-waveguides are in low thermal dissipation and low current threshold, while the power output and beam quality are non-optimal.

Note that the thermal dissipation highly affects the active region of QCL, and this will be discussed in detail in chapter 4.

1.6 Modelling approaches

The modelling of laser structures can usually be split into a coupled system of the gain medium model and the waveguide model equations.

The gain medium modelling requires the investigation of the quantum transport and the thermal effects in the medium. The thermal effects are represented by the heat equation, while the quantum transport effects are described by the Schrödinger equation. In solid state devices, the general approach would account for the many-body crystalline structure through the density functional theory (DFT) [66, 67] and the carrier transport through the Schrödinger-Poisson approach by usually employing the Non-Equilibrium-Green-Function (NEGF) method [68, 69, 70, 71]. The more common approaches would avoid many-body modelling with DFT by adopting the one-electron approximation and focus only on Schrödinger-Poisson equation by employing simpler methods than NEGF.

The waveguide modelling requires solving the Maxwell's wave equation. Depending on the type of the resonator, various dynamical properties, multimode behaviour and non-linear effects may be investigated. The outline of the modelling approaches for THz QCLs is briefly presented in table 1.1.

Gain medium modelling				
Transport models				**Thermal model**
3-level RE	N-level RE	DM	NEGF	Heat equation
• Simple • Intuitive • Analytic expressions • Low computational cost • No coherent transport • Too few levels	• Simple • Applicable for any N • Low computational cost • No coherent transport	• Coherent transport • Applicable for any N • Moderate computational cost • Cumbersome mathematics • Incomplete transport consideration • Debatable input parameters	• General • Detail transport analysis • Cumbersome mathematics • Very high computational cost	• Linear model possible • Breaks periodicity • Fitting approach • Debatable material parameters

Waveguide modelling		
Travelling wave method	**Fourier method**	
	Slow-envelope approximation	Multi-mode
• Spatial effects • Dispersion effects • Partial differential equation • High computational cost	• Simple • Low computational cost • No spatial effects	• Higher computational cost • Mode coupling parameters

Table 1.1: Overview of some properties of modelling approaches

1.6.1 Transport modelling in QCLs

The detailed theoretical background for the Schrödinger-Poisson equation and the transport mechanisms will be presented in Chapter 2. For a crystalline semiconductor structure, the solution yields energy levels E_i and their corresponding wavefunctions ψ_i. This allows extraction of the energy level population n_i and the transition (scattering) times τ_{ij} between the levels i and j. The scattering mechanisms represent a perturbation effect and simpler methods treat them by perturbation theory, while the more extensive methods such as the density matrix (DM) [72] and the NEGF employ complex many-body interaction. Historically however, the rate equation (RE) method that uses perturbed transport has been a dominant model for laser description ranging from a 3-level to N-level consideration. The main drawback of RE is that it represents a semi-classical model and cannot fully account for the resonant tunnelling effect in QCLs and quantum models such as the density matrix [73, 61, 74] and NEGF [69, 75] approach need to be employed.

3-level and rate equation model

The 3-level model can be applied to nearly any laser structure [1]. The rate equations have an intuitive formulation and depict flow of carriers across each level. The model assumes the existence of carrier pump that generates the population inversion. For resonant tunnelling structures such as QCL, injection can be allowed into the lower level as well, through the introduction of the injection efficiency η, as depicted in Fig. 1.8 (assuming injection to level 1 is very small/neglected).

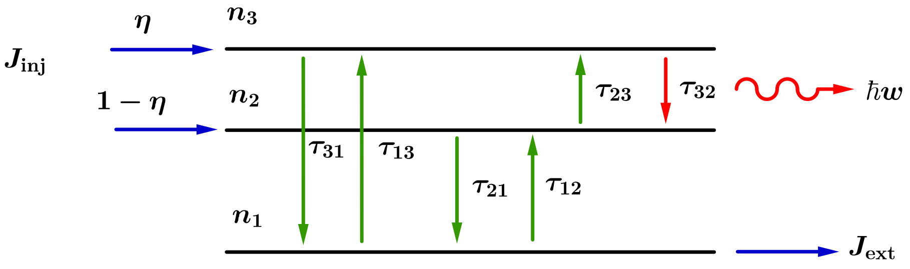

Figure 1.8: 3 - level transport

Each level is characterised by its population n_i and all interactions between the levels are characterised through the scattering times τ_{ij}. Additionally, we can define a value $\tau_i^{-1} = \sum_j \tau_{ij}^{-1}$ that describes all transitions from level i to all other levels. This value represents the level lifetime and it is commonly used for the laser characterisation. The rate equations for a 3-level system are:

$$\begin{aligned} \frac{dn_3}{dt} &= \eta\frac{J_{\text{inj}}}{e} - \frac{n_3}{\tau_3} + \frac{n_2}{\tau_{23}} + \frac{n_1}{\tau_{13}} \\ \frac{dn_2}{dt} &= (1-\eta)\frac{J_{inj}}{e} + \frac{n_3}{\tau_{32}} - \frac{n_2}{\tau_2} + \frac{n_1}{\tau_{12}} \\ \frac{dn_1}{dt} &= -\frac{J_{\text{ext}}}{e} + \frac{n_3}{\tau_{31}} + \frac{n_2}{\tau_{21}} - \frac{n_1}{\tau_1} \end{aligned} \tag{1.2}$$

or in matrix form:

$$\begin{aligned} \frac{d}{dt}\begin{pmatrix} n_3 \\ n_2 \\ n_1 \end{pmatrix} &= \begin{pmatrix} -\frac{1}{\tau_3} & \frac{1}{\tau_{23}} & \frac{1}{\tau_{13}} \\ \frac{1}{\tau_{32}} & -\frac{1}{\tau_2} & \frac{1}{\tau_{12}} \\ \frac{1}{\tau_{31}} & \frac{1}{\tau_{21}} & -\frac{1}{\tau_1} \end{pmatrix}\begin{pmatrix} n_3 \\ n_2 \\ n_1 \end{pmatrix} + \begin{pmatrix} \eta J_{\text{inj}} \\ (1-\eta)J_{\text{inj}} \\ -J_{\text{ext}} \end{pmatrix} \\ \frac{dn}{dt} &= Wn + J_\eta \end{aligned} \tag{1.3}$$

where W is usually referred to as the rate matrix. In steady state, the derivatives tend to zero and $J_{\mathrm{inj}} = J_{\mathrm{ext}}$, the solution of Eq. (1.3) is $n = -W^{-1}J_{\eta}$. The model can be intuitively extended to any number of levels, and pumping effect can be generalised by addition of individual level pumping efficiencies, although it is more common to employ $\eta = 1$.

For a QCL structure, we can neglect absorption at low temperatures, this will simplify Eq. (1.3) significantly and by setting $\tau_{12}^{-1}, \tau_{13}^{-1}, \tau_{1}^{-1}, \tau_{23}^{-1}$ to zero the system yields analytical solution:

$$\begin{aligned} n_3 &= \eta\tau_3\frac{J}{e} \\ n_2 &= \tau_2\left(1-\eta(1-\frac{\tau_3}{\tau_{32}})\right)\frac{J}{e} \end{aligned} \tag{1.4}$$

The optical gain [45] G_{32} is usually fitted to the Lorentzian function, and it is proportional to the population inversion $\Delta n_{32} = n_3 - n_2$:

$$\begin{aligned} G_{32} &= \frac{4\pi e}{\epsilon_0 n}\frac{z_{32}^2}{2\gamma_{32}L_{\mathrm{P}}\lambda}\left(\eta\tau_3 - \tau_2\left(1-\eta(1-\frac{\tau_3}{\tau_{32}})\right)\right)J \\ G_{32} &\overset{\eta=1}{=} \frac{4\pi e}{\epsilon_0 n}\frac{z_{32}^2}{2\gamma_{32}L_{\mathrm{P}}\lambda}\tau_3\left(1-\frac{\tau_2}{\tau_{32}}\right)J \end{aligned} \tag{1.5}$$

where z_{32} is the dipole matrix element between the ULL (level 3) and LLL (level 2), $2\gamma_{32}$ is the full width at half-maximum (FWHM) of the Lorentzian function, L_{P} is QCL period length and $\lambda = hcE_{32}^{-1}$ is the lasing wavelength determined by the energy separation between the ULL and LLL. The modal gain represents $G_{\mathrm{M}} = G_{32}J^{-1}$ and for the structure to lase it is required to reach the threshold g_{th} given by Eq. (1.1).

It is clear from Eq. (1.5) that modal gain benefits from the high injection efficiency, very short LLL lifetime (τ_2) and high ULL τ_3 lifetime, shorter QCL period, shorter wavelength and larger dipole matrix element z_{32}, although there is a trade off since τ_{32} is inversely proportional to z_{32}.

This model on its own gives a good background for the laser characterisation, in terms of its simple parameters, and it is applicable to a variety of MIR and LO-phonon design THz QCLs. In the literature, the term $\tau_2\tau_{32}^{-1}$ may be used as target for minimisation optimisation techniques. The more common term of interest is refereed to as oscillator strength $f_{ij} = \frac{2m_0}{\hbar^2}(E_i - E_j)z_{ij}^2$ (where i is usually ULL, and

j LLL) and many optimisation techniques may focus strictly on it, as it has been for the former temperature record THz QCL [47]. Oscillator strength benefits from larger energy separation and dipole element, meaning that it favours the structures with direct radiative transition and higher emitting frequency. These properties, however do not ensure the best performance at higher temperatures, if structure design has multiple parasitic channels that could be suppressed by larger barriers (which reduces f_{32}, but increases $\tau_2\tau_{32}^{-1}$).

The inherent drawback of RE is its inability of modelling quantum effects such as the coherent tunnelling. The 3-level setup does not show how the carriers are injected in the subsequent period of QCL and even in the N-level RE model, the alignment of the resonant states would cause the singularities in the model results since the transition time would be estimated as an instant effect [76, 74].

Density matrix model

The density matrix model represents a quantum approach that uses a wavefunction basis to form a statistical ensemble of all possible interactions in the system. This is particularly useful in systems where mixed states are of interest. The time-dependent Schrödinger equation describes the time evolution of pure state $|\psi(t)\rangle$ represented by its Hamiltonian $\hat{H}$, while the density matrix introduces an operator $\hat{\rho} = \left|\hat{\psi(t)}\right\rangle \left\langle\hat{\psi(t)}\right|$ which, when substituted into the Schrödinger equation (instead of $|\psi(t)\rangle$), describes evolution of the ensemble of wavefunctions that correspond to the chosen basis. The new equation is called Liouville equation:

$$\frac{d\hat{\rho}}{dt} = -\frac{i}{\hbar}[\hat{H}, \hat{\rho}] \tag{1.6}$$

and its derivation can be found in many quantum mechanics books [77]. If the wavefunction basis consists of pure states, Eq. (1.6) would provide information on evolution of mixed states through its off-diagonal elements $\hat{\rho_{ij}} = \left|\hat{\psi_i}\right\rangle \left\langle\hat{\psi_j}\right|$. It is also common to add perturbation theory scattering rates, similarly as in Eq. (1.3) by adding dissipator term $D = -(\frac{\rho}{\tau})_{\text{relax}}$ to Eq. (1.6). This term would account for processes that are not included in the Hamiltonian, but cause decoherence of the system.

In application to QCLs, the difference between RE and DM is in the different Hamiltonians. RE solves the Schrödinger-Poisson equation for the two-period Hamiltonian of the system, while DM solves it only in one period in a tight-binding approximation by putting infinitely thick barriers on either side of the period. The solution of the tight-binding problem is then used as the basis for Eq. (1.6) and the tight-binding Hamiltonian is extended to include finite dephasing time through the barrier as well as Rabi oscillations at the frequency $\Delta_{ij'}/\hbar$, where $\Delta_{ij'}$ is the anticrossing energy between states i and j' where j' is the state from the adjacent period which is aligned with state i due to the external bias.

It can be shown that equations that correspond to the diagonal of the matrix system in Eq. (1.6) (with the dissipator) are actually the rate equations. In [74] we showed that model output of the DM approach contains the output from RE model. DM can be viewed as generalisation of RE approach, and it is possible to add correction terms to RE model [76, 78] to account for the quantum effects.

Vast literature is available [79, 80, 81] for DM implementation in a 3-level scheme, however in this thesis the main focus will be on modelling bound-to-continuum and Hybrid THz QCL structures that employ large number of energy levels per period. Chapter 3 will focus in detail on DM model that was first presented in [82] and then generalised for arbitrary number of states per period in our group, in [73, 61]. One of the main contributions of this thesis is in the detailed mathematical description of this model [83] and its adjustment for the dynamical modelling that was partly published in [83] which will be discussed in chapter 7.

1.6.2 Thermal modelling of THz QCLs

QCLs represent highly complex structures. The active region consists of ~ 100 periods and each period comprises at least six layers (for the three-well LO-phonon structures) of quantum barriers and wells. Implementing *ab initio* approaches like DFT is virtually impossible, along with the accounting of the quantum behaviour of all the periods. For that reason nearly all QCL models [76] exploit the periodicity of the structure for the transport modelling techniques. This however imposes that the effect of the external bias is uniform, which is not generally correct. It is likely that different periods have different bias conditions [68, 84, 85] due to the nature of the sample and the dynamics of the current flow between the contacts. This can be circumvented by treating the constant electric bias as an effective value, however THz QCLs are highly influenced by thermal effects as well.

Thermal distribution of the carriers strongly influences the Schrödinger-Poisson equation, and due to the cooling setup of QCLs it is likely that different periods have different temperatures, and this would not only cause the shifts in the bias, but also the changes in the current transport and the optical characteristics of different periods.

QCLs usually operate in continuous-wave or pulsed operation and thermal effects are particularly critical for CW, where the device is heated due to the electrical losses in the circuit. The cooling setup of QCL puts the operating (cold finger or heat sink) temperature on the substrate bottom contact (Fig. 1.7) and it is expected that the temperature would rise towards the top contact, due to the electrical power dissipation in the active region. Note that the process is anisotropic, however the critical effect occurs in the lateral direction, since the thickness of QCL stack is much smaller than its width and length. Fourier law of conduction (the heat equation) in one dimension is:

$$\rho_{\mathrm{m}} c_{\mathrm{p}} \frac{\partial T}{\partial t} = \frac{\partial}{\partial z}\left(k_z \frac{\partial T}{\partial z}\right) + \frac{P_{\mathrm{e}}}{V_{\mathrm{V}}} \tag{1.7}$$

where ρ_{m} is the material density, c_{p} is the specific heat capacity, k_z is thermal conductivity in lateral direction, P_{e} is the electrical power and V_{V} is the volume of the active region. In steady state, this equation only requires the information on thermal conductivity which is spatially dependent due to the heterostucture layers in the active region. It is possible to use Abele's interpolation scheme [86] to determine k_z in the barriers, however it is debatable whether the bulk values can be used, since the phonon modes would be different. It is more reliable to model the active region as a homogeneous material with a smaller conductivity than in the bulk. It has been estimated that for the GaAs superlattice, $k_z \approx 9.6T^{-0.14}$ Wm^{-1}K^{-1} [87]. The heat generation is present only in the ridge of the device, specified by dimensions $L_{\mathrm{C}} \times W \times H_{\mathrm{QCL}}$ as presented in Fig. 1.7.

For illustration, we can assume that k_z and P_e are constant. In the segment $[0, H_{\mathrm{QCL}}]$ we can assume boundary conditions $\frac{\partial T}{\partial z}|_{z=0} = 0$ and $T|_{z=H_{\mathrm{QCL}}} = T_{\mathrm{sub}}$, and analytical solution is $T = T_{\mathrm{sub}} + \frac{P_{\mathrm{e}}}{2k_z V_{\mathrm{V}}}\left(\frac{H_{\mathrm{QCL}}^2 - z^2}{2}\right)$. This is a parabolic dependence and we can introduce an effective active region temperature, by integrating additionally over the $[0, H_{\mathrm{QCL}}]$ segment, this yields $T = T_{\mathrm{sub}} + \frac{H_{\mathrm{QCL}} P_{\mathrm{e}}}{3k_z W L_{\mathrm{c}}}$ (note that we used $V_{\mathrm{V}} = H_{\mathrm{QCL}} L_{\mathrm{c}} W$). Although this derivation is ambiguous, steady state solution of the heat equation in the form:

$$T = T_{\mathrm{H}} + R_{\mathrm{TH}} P_{\mathrm{e}} \tag{1.8}$$

where R_{TH} is a thermal constant, has been the usual model for thermal effects in QCLs [45]. Interestingly, the analytically derived thermal resistance would be equal to $R_{\mathrm{TH}} = \frac{H_{\mathrm{QCL}}}{3k_z W L_{\mathrm{c}}}$ and this does give intuitive confirmation that QCLs with wide ridge, long cavity and shorter active region display better thermal performance. However, electrical power is the product of current and voltage, which when re-scaled to the current density and electrical field $P_{\mathrm{e}} = IV = JKWL_{\mathrm{c}}H_{\mathrm{QCL}}$ cancel the dimension terms in R_{TH} and only suggests that the height of QCL ridge H_{QCL} has the main effect on heating. Experimentally however, devices with larger WL_{c} do heat less, however due to the fabrication process, probability of defects is higher, and size optimisation needs to be performed (note that larger L_{c} also reduces cavity loss).

Note that Eq. (1.8) has been phenomenologically derived from the experimental observations. The derivation we performed assumed constant electrical power, constant thermal conductivity and most importantly, we averaged the analytical solution in the active region. Note also that Eq. (1.8) has a free term of the heat sink temperature T_{H}, while our derivation took into account that substrate temperature would be different. The main issue with Eq. (1.8) is that R_{TH} is not a constant, but rather a fitting parameter [45] which will unfortunately be different for the different heat sink temperatures. This will make modelling of the temperature dependence of the threshold current very challenging.

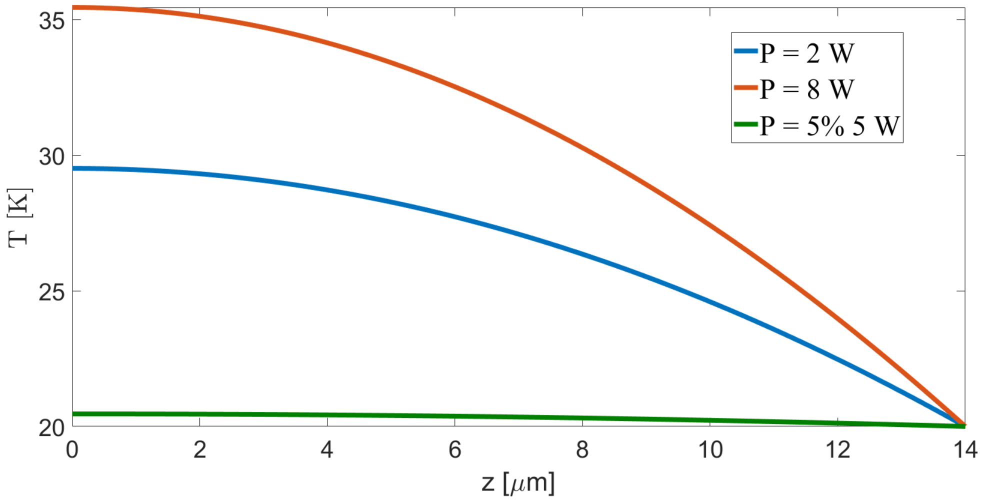

Figure 1.9: Numerical solution of the steady state heat equation, using $k_z = 9.6T^{-0.14}$ Wm^{-1}K^{-1} [87] for a ridge of 200 × 3000 × 14 μm size. The top of the substrate temperature is set to 20 K, and solution was plotted only across the 14 μm thick active region for three constant power values. The green line corresponds to the pulsed operation of QCL with 5% duty cycle, while blue and red correspond to the CW operation.

The numerical solution in steady state of Eq. (1.7) is presented in Fig. 1.9 and it is clear that different periods would have different temperatures in CW operation. The simulation used $k_z = 9.6T^{-0.14}$ Wm^{-1}K^{-1} [87] and assumed constant power, which is mostly true at low temperatures in QCLs. Note that this simulation assumed that the top of the substrate is at heat sink temperature, which is also an approximation, Eq. (1.7) needs to be solved across the substrate as shown in [86]. The electrical power can be represented as $P_\mathrm{e} = \sigma_\mathrm{d} IV$ where σ_d is the duty cycle (100% for CW, 2-15% for pulsed operation), I is the electrical current and V the voltage.

The thermal model in Eq. (1.8) has almost negligible effect in pulsed operation, however due to the dynamics of the process, the appropriate equation is Eq. (1.7) and the specific heat capacity c_p is dependent on temperature.

Chapter 4 will present in detail the steady state modelling of QCL structures in CW and pulsed operation that accounts for thermal effects, where pulsed modelling of QCLs shows to be more reliable.

1.6.3 Maxwell wave equation

In general, Maxwell's wave equation for a homogeneous, isotropic medium, without the external magnetic field is [1]:

$$\nabla^2\mathbf{E} - \frac{1}{v_{\mathrm{g}}^2}\frac{\partial^2\mathbf{E}}{\partial t^2} - \frac{\sigma}{\epsilon_0 c^2}\frac{\partial\mathbf{E}}{\partial t} = \frac{1}{\epsilon_0 c^2}\frac{\partial^2\mathbf{P}}{\partial t^2} \tag{1.9}$$

where $\mathbf{E}(\mathbf{r},t)$ is the optical electric field, $\mathbf{P}(\mathbf{r},t)$ is the medium polarisation, $v_{\mathrm{g}} = cn^{-1}$ is the group velocity, σ is the conductivity that accounts for the ohmic losses in the cavity [1] [1] and n is the refractive index. Note that it applies $\sigma = \epsilon_0 n c g_{\mathrm{th}}$ when combined with Fabri-Perót resonator in Eq. (1.1).

Equation (1.9) is rarely being solved in this form. The common approximations are travelling wave method and Fourier method.

Travelling wave method

The travelling wave method (TW) assumes that the electrical field propagates as a combination of the forward f^+ and the backward f^- wave $E(z,t) = \frac{1}{2}\, f^+(z,t)$ $e^{i(kz-\omega t)} + \frac{1}{2}f^-(z,t)e^{-i(kz+\omega t)} + c.c$ where k and ω are the corresponding wave number and the frequency, respectively, and $\omega = kv_{\mathrm{g}}$. We additionally assume, that the polarisation will follow the symmetry of the electrical field and have similar form: $P(z,t) = P^+(z,t)e^{i(kz-\omega t)} + P^-(z,t)e^{-i(kz-\omega t)} + c.c.$ When this is plugged into Eq. (1.9) under slow-varying envelope approximation, we have:

$$\frac{1}{v_{\mathrm{g}}}\frac{\partial f^\pm}{\partial t} \pm \frac{\partial f^\pm}{\partial z} + \frac{\sigma}{n\epsilon_0 c}f^\pm = i\frac{\omega}{n\epsilon_0 c}P^\pm \tag{1.10}$$

More detailed derivation of Eq. 1.10 can be found in the Appendix A. This equation can be combined with the transport models which can yield information on the polarisation. The density matrix model, for instance, can provide the polarisation directly, and material gain is directly proportional to the polarisation $g \approx -\frac{\omega}{n\epsilon_0 c}\frac{\mathrm{Im}\{P\}}{\mathrm{Re}\{E\}}$.

The application of Eq. (1.10) to QCLs can be found in [88], however, these equations are of interest when modelling spatial properties of the optical field and effects that employ coupled cavities or frequency combs. Solving Eq. (1.10) is a

---

[1] In some literature this term is added separately

challenging task as it requires detailed consideration of numerical stability issues and the computational cost is higher than for the commonly employed Fourier method.

Fourier method

The Fourier method is the most commonly employed approximation for the wave equation. The electric field is presented as a collection of orthogonal normal modes $\mathbf{u_n}(\mathbf{r})$ that are modulated by the time dependent envelopes $E_n(t)$, $\mathbf{E}(\mathbf{r},t) = \sum_n \mathbf{u_n}(\mathbf{r})E_n(t)$. The orthogonal modes satisfy the Laplace equations $(\nabla^2 + k_n^2)\mathbf{u_n}(\mathbf{r}) = 0$ and when this is substituted in Eq. (1.9), we obtain:

$$\frac{\partial^2 E_n}{\partial t^2} + \frac{\sigma}{\epsilon_0 n^2}\frac{\partial E_n}{\partial t} + \omega_n^2 E_n = -\frac{1}{\epsilon_0 n^2}\frac{\partial^2 P_n}{\partial t^2} \tag{1.11}$$

where ω_n are the resonance frequencies of the cavity. $\mathbf{u_n}(\mathbf{r})$ and ω_n are the eigenvectors and eigenvalues of the empty cavity (without polarisation) [1]. This formulation of the wave equation may be used for multimode modelling of laser structure [1]. For a single mode structure, the usual approach is to introduce a slow varying envelope $E(t)$ and seek the response to a cosine excitation at carrier frequency ω as $E_n = E(t)(e^{i\omega t} + e^{-i\omega t})$, with $P_n = P(t)(e^{i\omega t} + e^{-i\omega t})$ Eq. (1.11) becomes:

$$\frac{\partial E}{\partial t} = -\left(\frac{\sigma}{2\epsilon_0 n^2} + i(\omega - \omega_n)\right)E - i\frac{\omega}{2\epsilon_0 n^2}P \tag{1.12}$$

In single mode lasers, the lasing frequency is at resonance with the cavity mode $\omega_n = \omega$, and this further simplifies Eq. (1.12). Eq. (1.12) is the most widely used Maxwell equation for laser modelling, and it is often presented without prior derivation. Detailed derivation of Eqs. (1.10,1.11) is given in the Appendix A.

Note that the polarisation $\mathbf{P}$ is expanded in the same orthogonal basis $\mathbf{u_n}(\mathbf{r})$, because $\mathbf{P}$ is usually produced coherently through the electric field, however if there is some coupling between the modes, or the presence of non-linear effects, a separate equation similar to Eq. (1.9) can be formulated for $P_n(t)$ [1].

Dynamic laser modelling will be presented in Chapter 6. It can be shown that the real part of Eq. (1.12) has a term $(loss - gain)E$ which describes the fundamental principle of the laser operation, in the sense that the generated optical electric field will tend to equalise the modal gain and modal loss in the steady state.

1.7 Self-mixing interferometry

The fact that FIR spectrum has been almost inaccessible for research before the development of THz QCLs shows their significance and possible applications [32, 89, 90]. In this thesis, one of the focuses will be on modelling of the self-mixing (SM) interferometry applications.

The self-mixing interferometry represents an interferometry effect in the laser due to the external homodyne optical feedback. This effect has been demonstrated for multiple laser types [91] and its principle relies on the reinjection of the laser light into the cavity. Normally, the reflected radiation is detrimental to the laser performance, however if the small portion of the laser's own radiated light is reinjected into the cavity by using the third, external mirror, the effect can be experimentally measured. More importantly, the measured signal (terminal voltage) can be used to extract the information on the properties of the external mirror/target. This presents a unique possibility of using the laser as a light source and a detector at the same time [92].

The range of detectors for THz radiation are nearly as limited as the range of sources [32], and along with the already expensive QCL cooling system, using the SM effect represents an ideal solution. The SM in THz QCLs is further boosted by their superior characteristics in terms of the fast gain recovery and the lack of the relaxation oscillations. Group in Leeds is currently a leading research institution in self–mixing interferometry THz QCL applications with multiple pioneering achievements [93, 94, 95, 96, 97] along with the collaborative group in University of Queensland, Australia [98, 99, 100, 101].

The modelling of SM effect relies on adding a feedback term to the slow-varying envelope wave equation Eq. (1.12) written for diode laser and this is commonly referred as the Lang-Kobayashi (LK) model [102]. The modified wave equation is:

$$\frac{\partial E}{\partial t} = \left(i(\omega_n - \omega) + \frac{1}{2}\left(\Gamma G - \frac{1}{\tau_{\mathrm{p}}}\right)\right) E + \tilde{\kappa} E(t - \tau_{\mathrm{ext}}) e^{-i\omega\tau_{\mathrm{ext}}} \tag{1.13}$$

where ΓG represents modal gain rate, τ_{p} photon lifetime in the cavity, τ_{ext} external cavity round-trip time and $\tilde{\kappa}$ feedback coupling rate. This equation with a complex variable can be converted into two equations corresponding to the real and the imaginary part or the amplitude and the phase equation, or the amplitude squared (proportional to optical power) and the phase equation [91].

Note that LK model has been developed phenomenologically for the diode lasers, and the derivation of Eq. (1.13) from Eq. (1.12) requires introduction of gain factor G (unit s^{-1}) that is coupled to the population inversion [7].

This requires the modelling of QCLs for SM effect to revert to an effective two-level model [103, 104] common for diode lasers. As discussed earlier, RE models are not fully applicable to THz QCLs, furthermore the number of states in QCL period is much larger than two and coherent transport model needs to be applied. The DM model for diode laser has been coupled to Eq. (1.13) before the introduction of LK model [105] and theory that extends the Maxwell equation to account for feedback beyond phenomenological consideration, has been developed [1].

Note that Eq. (1.13) still describes the fundamental property that the feedback would modify the electric field in the cavity, and this may effectively be modelled as a reduction of the loss, which represents the effective mirror model [7] and was applied to QCLs in [106].

The main issue in the derivation of Eq. (1.13) is that it uses the diode laser parameters such as the gain factor G which is usually obtained through the linearisation of the material gain profile. Additionally, the information on the medium polarisation is lost. The modelling techniques for THz QCLs, described earlier, all yield material gain, and the optical feedback needs to be introduced in Eq. (1.13) instead, as suggested in [1]. Chapter 6 presents the dynamic modelling of THz QCL, while Chapter 7 gives a detailed study of the SM effect, coupled with the DM model that is independent on the number of states considered.

1.8 Thesis outline

This thesis presents the numerical modelling of THz QCLs by the DM model and focuses on the modelling of the dynamic effects with feedback, specifically the self-mixing effect. Chapter 2 presents the theoretical background for the scattering mechanisms employed for the transport description in QCL along with the RE model that has been developed in previous work within this group.

Chapter 3 relies on DM model developed in 2012 [73] and 2015 [61], however methodology used in this chapter is a novel and original work, that resulted in publications [74, 83]. This chapter offers full mathematical explanation behind the DM model and presents the DM system in a compact algebraic form.

Chapter 4 explains the technical application of the steady-state QCL modelling and applies the DM model to several exemplar QCL structures. The considered structures correspond to the designs described in Introduction 1.4 to display the broad versatility of the model. Comparison of the DM and RE models from Chapter 2 is also given. This model has been used in several successful collaborations with groups in University of Queensland, Australia, University of Nottingham, United Kingdom and University of Belgrade, Serbia.

Chapter 5 focuses on acoustic modulation of THz QCLs. This chapter is a product of joint research with University of Nottingham. A publication by Dr. Aniela Dunn is most recently accepted in Nature Communications [107], and the theoretical work of this publication was performed by the author of this thesis and will be presented in this chapter. This modulation scheme is based on sending an acoustic wave that creates a strain deformation potential which perturbs the QCL structure, allowing state of the art modulation technique.

Chapter 6 extends the DM model presented in Chapter 3 for the dynamic applications. To our knowledge, this work represents the first Maxwell-Bloch model for QCL structure that is independent on the number of states in one QCL module. Content of this work has resulted in the publication [83] which also displayed the simplest algebraic formulation of the DM model that was also described in Chapter 3. The dynamic model has been applied to several structures and some known concepts of QCL dynamics have been discussed.

Chapter 7 modifies the Maxwell wave equation from Chapter 6 by adding the self-mixing feedback term. This allows modelling of SM interferometry techniques except the frequency sweep which requires alterations of the model that are not numerically feasible in reasonable time (coupling the dynamic heat equation to account for heating effects).

Chapter 8 discusses QCL designs and proposes novel and original structures for improved temperature performance, by employing the model presented in Chapter 4.

Chapter 9 presents the concluding remarks, potential applications of the model in the current form and the future challenges and the drawbacks of the model.

Chapter 2

Schrödinger-Poisson equation and transport mechanisms

The carrier transport in nanostructures is heavily dependent on quantum mechanical effects, and this chapter will illustrate the calculation of the electronic structure under the envelope function approximation which will determine the output characteristics of the QCL. The Schrödinger–Poisson equation will be presented along with the discussion of the numerical procedure for determining the quantised energy levels and their wavefunctions. We will also discuss the scattering mechanisms that describe the interaction of carriers with the alloy disorder, the impurities within the material, the interface of the heterostructure, the acoustic and optical vibrations of the lattice and the other carriers. The models in this chapter do not present author's original work and rely on the derivations available in the literature and the numerical code that was developed by previous research in this group [1]. However, the author did restructure the original code for the numerical optimisation, that has significantly speeded up the simulation of one QCL structure, from ~ 2 hours to ~ 5 minutes, which allowed the author to upgrade the model for the dynamical study and the SM effect, which will be discussed in the following chapters.

---

[1] Dr Vladimir Jovanović, Dr Alex Valavanis, Dr Jonathan Cooper, Dr Craig Evans, Dr Nenad Prodanović, Dr Andrew Grier and their supervisors' works

2.1 Schrödinger equation

The Schrödinger equation that would yield energy levels in QCL, similar to the ones in Fig. 1.1 is derived through several approximations. The electronic structure of the bulk semiconductor material involves the many-body interaction between the atoms in a periodic lattice. We are mainly interested in properties of electrons that are able to flow through the structure, and therefore create the electrical current. To obviate the need for the many-body considerations, the periodicity of the lattice is exploited through the introduction of the envelope function approximation [108] and the one-electron approximation [109].

The one-electron approximation assumes that the quantum mechanical properties can be determined by considering the properties of a single electron, therefore neglecting any interaction with other electrons. This does not mean that the electrons do not have any influence in the system, but rather that eigenvalues and eigenfunctions of the single electron Hamiltonian are not significantly influenced by the interaction part of the Hamiltonian. The perturbation techniques can still be used to account for this negligence. This is a standard technique which avoids the many-body consideration, both in the atomic and the electronic structure of the material.

An electron in the semiconductor lattice "sees" the Hamiltonian consisting of the kinetic operator $\hat{T}$, the atomic potential $\hat{U}_\mathrm{a}$ and the conduction band potential $\hat{U}$. The potentials have only spatial dependence, and time-independent Schrödinger equation may be used. The envelope function approximation essentially decouples the effects of $\hat{U}_\mathrm{a}$ and $\hat{U}$ by assuming that the solution has a form of the product of the individual potential's solutions. The derivation, however is not straightforward, and it employs several approximations, most notably, that we are seeking the solution around the bottom of the conduction band – the Gamma Γ_c point. This is a good approximation in GaAs which is a direct band gap semiconductor, but inter-valley scattering may be of high importance in materials with low effective mass, like GaSb [110] or indirect semiconductors like Si [111]. The slow varying envelope approximation can be found in [108] and it is explained in the Appendix B.

The Schrödinger equation under the envelope function approximation in the semiconductor with a direct band gap is:

$$\left(-\frac{\hbar^2}{2}\nabla\frac{1}{m(\mathbf{r})}\nabla+U(\mathbf{r})\right)\psi_{3D}=\left(E-E_{C,0}\right)\psi_{3D} \tag{2.1}$$

where $E_{\mathrm{C},0}$ is the energy at the bottom of the conduction band (Gamma point), the kinetic operator was written in $\nabla\frac{1}{m(\mathbf{r})}\nabla$ form to account for the spatial dependence of the effective mass, due to the heterostructure layers, and ψ_{3D} is the envelope wavefunction that modulates the wavefunction that corresponds to the atomic potential (Appendix B). Depending on the level of the spatial freedom of the structure, or in other words, whether we are dealing with the quantum wells (1D restriction), quantum wires (2D restriction) or quantum dots (3D restriction), Eq. (2.1) takes different forms, resembling the Fourier method of separation of variables.

For a quantum well system, we assume that the motion of the electron in plane is free $U_x=U_y=0, U_z=V(z)$ and that the wavefunction can be written as a product of a plane wave in the plane $\mathbf{r}_{\|}=\{x,y\}$ and z–dependent envelope function $\psi(z)$ in the direction of the layer growth, $\psi_{\mathrm{3D}}=A^{-\frac{1}{2}}\psi(z)e^{i\mathbf{k}\mathbf{r}_{\|}}$ where A is the normalisation constant equal to the layer surface, and $\mathbf{k}=(k_x,k_y)$ is the wavevector in plane. The effective mass and the potential only vary in the z direction and we can take $E_{\mathrm{C},0}=0$ for simplicity (since we can shift energy coordinate system to our own preference). The Schrödinger equation for the quantum well system obtained by the bandstructure potential $V(z)$ is:

$$\left(-\frac{\hbar^2}{2}\frac{d}{dz}\frac{1}{m(z)}\frac{d}{dz}+V(z)\right)\psi=\left(E+\frac{\hbar^2k^2}{2m}\right)\psi \tag{2.2}$$

The dispersion relation of energy in form $E_{\mathrm{s}}(k)=E+\frac{\hbar k^2}{2m}$ is commonly referred to as a subband energy and it physically shows that 1D alternation of wells and barriers caused by the heterostructure layers in QCL gives discrete energy levels E, but allows a continuous dispersion in k plane. Equation Eq. (2.2) needs to be solved for a continuous set of k values, which is not numerically feasible.

The common approach is to find the value of the subband energy minima E by setting k to zero. The influence of k can then be treated as a correction to the potential V, through the perturbation theory and the effect may be incorporated into the effective mass. Additionally, the approximation from which the Eq. (2.2) has been derived, in particular focusing only around the Γ_c point of Brillouin zone, is not viable for higher energies and the dispersion relation may have additional terms (powers of k) causing the non-parabolic subband dispersion.

The most commonly used approximation uses the two-band Kane model which introduces the correction in the form $m^*(z,E) = m(z,0)\left(1 + \alpha_\mathrm{k}(E - V)\right)$. Parameter α_k is inversely proportional to the band gap energy. The non-parabolicity effects affect the subband minima energy values, especially when the higher states are of interest. In GaAs–based QCLs, this approximation is adequate, since the band gap is large ($\sim$ 1.42 eV), and states are relatively low. Additional corrections can be made directly to the energy dispersion relation by using the multi-band (usually 6,14 or 26 – band) **kp** model, however these corrections are negligible in GaAs QCLs, even with the application of the magnetic field [112].

If we substitute the mass $m(z)$ by an effective value $m^*(z,E)$ and focus on the subband minima energy by setting k to zero, equation (2.2) can be turned into the eigenvalue problem $H\psi = E\psi$ through the finite difference approach [108, 113]. However the introduction of the energy dependent effective mass, turns Eq. (2.2) into a non-linear eigenvalue problem, which can be solved by searching for an energy E_i that provides zero eigenvalue of $\left(H(E_i) - E_i I\right)\psi_i = \lambda_i \psi_i$ equation.

2.2 Poisson equation

In order to achieve the flow of electrons, the semiconductor material needs to be doped. This is a common technique in diode lasers, although in QCLs the manipulation of the carrier flow is different. The QCL is unipolar device and needs only electrons as carriers, thus donor doping is needed. The dopants represent ionised impurities in the semiconductor crystal lattice that provide free electrons. Both of these carriers induce their own contribution to the electric field whose potential ϕ may be treated through the Poisson equation:

$$\frac{d^2\phi}{dz^2} = -\frac{e}{\epsilon_0 n^2}\left(N_\mathrm{d}^+(z) - \rho_\mathrm{c}(z)\right) \tag{2.3}$$

where $N_{\mathrm{d}}^{+}(z)$ is the distribution of the ionised donors and $\rho_{\mathrm{c}}(z)$ is the spatial distribution of the electrons. If all donors are ionised, their distribution equals to the concentration of the donor doping level N_{D} which is a justifiable approximation at higher temperatures. At lower temperatures, the distribution is given through the standard doped semiconductor theory as $N_{\mathrm{d}}^{+}(z) = N_{\mathrm{D}}\left(1 - \left(1 + \frac{1}{2}e^{\frac{E_{\mathrm{D}}(z)-E_{\mathrm{F}}}{k_{\mathrm{B}}T}}\right)^{-1}\right)$ where E_{D} and E_{F} are the donor energy level and Fermi level, respectively.

The electron distribution is spread throughout several subbands that arise from the Schrödinger equation. The QCL is a non-equilibrium device and each subband i has Fermi-Dirac distribution of electrons with its own quasi-Fermi level E_{QFi} (and electron temperature) which is linked to the subband population as:

$$n_i = \frac{m_{\mathrm{d}} k_B T_i}{\pi \hbar^2}\left(\frac{E_{\mathrm{QFi}}}{k_{\mathrm{B}} T_i} + \ln(1 + e^{\frac{E_{\mathrm{QFi}}}{k_{\mathrm{B}} T_i}})\right) \tag{2.4}$$

The subband populations can be obtained through the transport model (RE, DM, NEGF ...) and require solving the Schrödinger equation. The spatial distribution of the electrons in subband i is given through the product of the population n_i and its probability given by $|\psi_i(z)^2|$, thus the total electron distribution is determined as a sum over all the subbands:

$$\rho_{\mathrm{c}}(z) = \sum_i n_i |\psi_i(z)|^2 \tag{2.5}$$

To solve Eq. (2.3), information on $\rho_{\mathrm{c}}(z)$ is needed through the solution of Eq. (2.2), however the potential in Eq. (2.2) needs to be corrected by the solution of Eq. (2.3) which is commonly referred to as the Hartree potential, which results in a system of coupled differential equations.

This system can be solved through an iterative procedure that uses an initial guess for $n(z)$ and solves Eqs. (2.2,2.3) separately, and then repeating the procedure, until convergence. The system of Eqs. (2.2,2.3) is commonly referred as Schrödinger-Poisson equation, and iterative approach as self-consistent approach.

The numerical discretisation of Schrödinger-Poisson equation may be treated through the finite-difference method that yields tridiagonal eigenvalue problems, that have direct solution by the Gaussian elimination (Thomas algorithm [114]), if the matrix is diagonally dominant. This is presented in Appendix C.

2.3 Fermi golden rule

The perturbation theory for the Schrödinger equation has been the most common technique for treating various effects that are not included in the Hamiltonian, with a requirement that the perturbation Hamiltonian has much smaller magnitude (in terms of its elements in the matrix form) than the Hamiltonian of the unperturbed system.

If the perturbation is only spatially dependent, the framework expands the wavefunction and the energy to include correction terms that depend on the perturbation Hamiltonian simply through its matrix elements (the diagonal elements, for instance, are the first correction to the energy) [112].

The time–independent Schrödinger equation is applicable only to the spatially dependent Hamiltonians. The derivation strongly depends on this, as it essentially applies the Fourier variable separation approach by assuming that the wavefunction can be written as a product of only time dependent and only spatially dependent function. When this is plugged into the general Schrödinger equation, the separation approach results in a usual sum of the only time and only space-dependent terms, and the only solution is if they individually equal to a constant. For the time dependent part of the equation, this constant turns out to be the energy, and the time dependent part of the total wavefunction has a form $e^{-\frac{iEt}{\hbar}}$ while the spatial part needs to be determined by solving the time-independent Schrödinger equation. Clearly, as soon as the Hamiltonian becomes time-dependent, the Fourier separation is no longer possible, and the physical "meaning" of the energy is lost.

The time–dependent perturbation theory requires that the perturbation Hamiltonian $H'(t)$ does not affect energies of the system obtained by the unperturbed Hamiltonian. This formalism provides corrections to the wavefunction of the unperturbed system. This may be used to obtain the transition probabilities caused by $H'(t)$. The first and the second correction term of the wavefunction ψ_f, due to the interaction with the wavefunction ψ_i for $f \neq i$ have the form:

$$\begin{aligned}
\psi_f^{(1)} &= -\frac{i}{\hbar}\int_{t_0}^{t} H'_{fi}(t')e^{i\omega_{fi}t}dt' \\
\psi_f^{(2)} &= -\frac{1}{\hbar^2}\sum_m \int_{t_0}^{t}\int_{t_0}^{t'} H'_{fm}(t')H'_{mi}(t'')e^{i\omega_{fm}t'+i\omega_{mi}t''}dt''dt'
\end{aligned} \tag{2.6}$$

where $\omega_{fi} = \hbar^{-1}(E_f - E_i)$ is a frequency proportional to the energy separation. The first correction, resembles the Fourier transform of the perturbation Hamiltonian. To obtain the physical interpretation, the modulus squared of the wavefunction gives the probability of transition $P_{i\to f} = |\psi_f|^2 = |\delta_{fi} + \psi_f^{(1)} + \psi_f^{(2)}|^2$.

Approach in Eq. (2.6) may be used to treat a variety of the time dependent perturbations such as the effect of the propagation of an acoustic wave through the QCL stack which will be discussed in Chapter 5.

If we assume that the first correction term in Eq. (2.6) is dominant, and that the perturbation is harmonic in the form $H' = V'(\mathbf{r})e^{-i\omega t}\theta(t)$ where $\theta(t)$ is a step function, we obtain:

$$\psi_f^{(1)} = -\frac{i}{\hbar}V'_{fi}\frac{\sin\left(\frac{\omega_{fi}-\omega}{2}t\right)}{\frac{\omega_{fi}-\omega}{2}}e^{\frac{\omega_{fi}-\omega}{2}t} \tag{2.7}$$

The probability of the transition $i \to f$ is given as $P_{i\to f} = |\psi_f^{(1)}|^2$. If we define the transition rate as $W_{i\to f} = \lim_{t\to\infty}\frac{P_{i\to f}}{t}$ and use the limit properties of the *sinc* function, we obtain the Fermi golden rule:

$$W_{if} = \frac{2\pi}{\hbar^2}|V'_{fi}|^2\delta(\omega_{fi} - \omega) \tag{2.8}$$

The delta function depends on the energy difference between the states f and i, and since in our case this dependence has parabolic dispersion relation with k as shown in Eq. (2.2), the scattering may occur for any value of k. This extends the principle presented in 1.1 and introduces the interaction between the parabolic energy subbands.

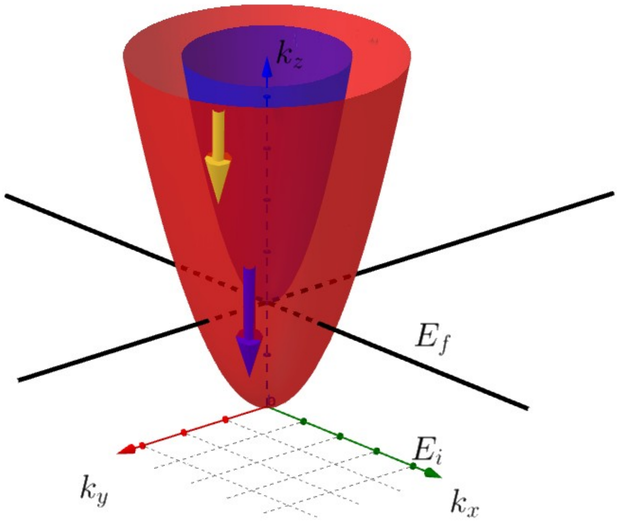

Figure 2.1: Energy subbands of two states following the parabolic dispersion relation with k. Transition that satisfy the delta function selection may occur within the subband (the yellow line) or between two different subbands (the purple line).

These subbands are continuous in k space, and the transport may be envisioned as the interaction between the parabolas depicted in Fig. 2.1 where Fermi golden rule serves as a selection rule which restricts k_f and k_i so that they satisfy the delta function selection principle. The interactions also need to satisfy the energy conservation law, thus the kinetic-balance model needs to be introduced, which will add an additional iterative procedure to the Schrödinger-Poisson equation, resulting in a self-self-consistent method.

The static perturbation potentials in form $H' = V(\mathbf{r})\theta(t)$ are actually more common than the harmonic ones, and we may set ω to zero in Eq. (2.8) to obtain the static perturbation Fermi golden rule (or alternatively solve Eq. (2.6), which will clearly reduce to the Fourier transform of a step function):

$$\begin{aligned} W_{if}(k_i) &= \frac{2\pi m^*}{\hbar^3|k_\alpha}||V'_{fi}|^2\delta(|k_f| \pm |k_\alpha|)\theta(k_f^2) \\ k_\alpha &= \sqrt{k_i^2 - \frac{2m^*E_{fi}}{\hbar^2}} \end{aligned} \tag{2.9}$$

where the step function $\theta(k_f^2)$ was added to ensure that the final state lies in the final subband [111].

This derivation substituted the parabolic subband dependence, assumed the identical effective mass in i and f subbands and used the properties of the delta function. However, we are interested in the averaged scattering rate that occurs between the subband i and all the other subbands. Nominally, this requires us to sum Eq. (2.9) for different values of k_f. Since this is a continuous variable, the sum can be switched to the integration and we can additionally improve the expression by implementing the Pauli selection rule which states that scattering cannot occur, if the state is already occupied. The reduced W'_{if} and the averaged $\bar{W_{if}}$ scattering rates are:

$$\begin{aligned}
W'_{if}(k_i) &= \frac{Am^*}{2\pi\hbar^3}\Theta((k_{\alpha^2})(1 - f_{\mathrm{FD}}(E_{\mathrm{s}f}, T_{\mathrm{e}})) \int |V'_{fi}|^2 d\phi \\
\bar{W_{if}} &= \frac{\int_0^\infty f_{\mathrm{FD}}(E_{\mathrm{si}}, T_e) W'_{if} k_i dk_i}{\pi n_i} \\
f_{\mathrm{FD}}(E_{\mathrm{s}}, T_{\mathrm{e}}) &= \left(e^{\frac{1}{k_{\mathrm{B}} T_{\mathrm{e}}}\left(E + \frac{\hbar^2 k^2}{2m^*} - E_{\mathrm{F}}\right)} + 1 \right)^{-1}
\end{aligned} \tag{2.10}$$

where A is the surface area and ϕ is the angle (both arise from the transformation of a sum into an integral when polar coordinate system is used), k_{B} is the Boltzmann constant, E_{F} is the Fermi level, T_{e} is the electron temperature, n_i is the population of the subband i and E_{si} and $E_{\mathrm{s}f}$ are the parabolic subband energies of the states i and f, respectively. The Fermi-Dirac $f_{\mathrm{FD}}(E_{\mathrm{s}}, T_{\mathrm{e}})$ distribution gives the occupancy probabilities of subband E_{s}. Note that the delta function selected $k_f = k_\alpha$ above, the detail derivation can be found in [111]. The integration of $\bar{W_{if}}$ is usually applied over the finite boundaries, as it can be approximated that 99% of the subband population lies below 4.6 $k_{\mathrm{B}} T_{\mathrm{e}}$. Note that the Fermi energy E_{F} cannot be defined in a non-equilibrium system as a QCL. Instead, each subband has its own quasi-Fermi level and the electron temperature, which complicates Eq. (2.10) further, however the simplification can be provided through the kinetic balance model.

The wavefunction basis for the determination of V_{fi} matrix elements are not the envelope wavefunctions obtained by Eq. (2.2), but rather the full wavefunction $\psi_{\mathrm{3D}} = A^{-\frac{1}{2}}\psi(z)e^{i\mathbf{k}\mathbf{r}_\parallel}$ and for the most scattering effects V_{fi} would not depend on the transversal wavevector which will cancel 2π, and the spatial integration of V_{fi} would also cancel the normalisation parameter A.

We may separately treat several elastic and non-elastic perturbation effects with Eq. (2.8) to describe the intersubband scattering transition processes in QCLs (and plethora of quantum well systems). The obtained rates are additive, and transport may be modelled through the rate equation or the density matrix model. The scattering rates obtained by Eq. (2.8) are semi-classical and incoherent, however the DM model may account for the quantum effects, and even extend the Fermi golden rule [72]. The main drawback of Eq. (2.8) is that this is a perturbation approach, and non-equilibrium-Green-function model treats the scattering Hamiltonians in a different manner, giving more precise values [76, 68], but more demanding computational implementations.

2.4 Alloy disorder scattering

The heterostructure with any semiconductor materials theoretically breaks the crystal lattice structure of the bulk material. For that reason, materials need to be well matched, so that the heterostructure remains stable. This results in pairs of the adequate materials that can be combined to form a quantum well heterostructure, and some may even allow mismatch of the lattice constants, that leads to strain. The GaAs in QCLs is commonly used for the quantum well material and it is well matched with the AlAs which is used for the quantum barrier material. The formation of the barriers is achieved by doping the GaAs with a fraction of Al that creates $\mathrm{Al}_x\mathrm{Ga}_{1-x}\mathrm{As}$ where x represents the barrier alloy content. The lattice constant of GaAs is the same as that of AlGaAs for any x fraction, however the band gap is direct up to $x = 0.45$ which is a crucial property for the laser operation.

The atoms of the heterostructure do not form the perfect periodic crystal potential as in the bulk material. The stochastic presence of the Al atoms represents an impurity in the lattice that causes the scattering. It is not feasible to treat this effect on atomic scale with Schrödinger equation, however this effect may be treated as a perturbation.

The alloy disorder scattering (ADS) formulates a virtual GaAl atom with potential $V_{\mathrm{GaAl}} = x(z)V_{\mathrm{Ga}}(\mathbf{r}_\parallel) + (1 - x(z)V_{\mathrm{Al}}(\mathbf{r}_\parallel))$. The virtual crystal lattice potential is then formed through the summation across the crystal. The perturbation potential is the difference between the actual and the virtual crystal lattice potential. This difference is small and can be approximated to $V_{\text{diff}} \approx \frac{a^3}{8} V_{ad}\delta(\mathbf{r}_{\|}))$ where a is the lattice constant of the well material (GaAs) and V_{ad} is a constant alloy scattering potential [115] which can be taken as the offset between the barrier and the well material. V_{diff} is the perturbation on the atomic scale, and its matrix elements need to include the full wavefunction, including both the Bloch and the envelope function. The mean square value for V_{fi} elements [111] is:

$$|V_{fi}'^{\text{ADS}}|^2 = \frac{a^3 V_{\text{ad}}^2}{8A} \int |\psi_f|^2 |\psi_i|^2 x(z)\,(1 - x(z))\,dz \tag{2.11}$$

This needs to be plugged in Eq. (2.10), and the reduced scattering rate due to the alloy disorder is given as:

$$W_{if}'(k_i) = \frac{m^* a^3}{8\hbar^3} \Theta(k_\alpha^2)(1 - f_{\text{FD}}(E_{\text{sf}}, T_{\text{e}})) V_{\text{ad}}^2 \int |\psi_f|^2 |\psi_i|^2 x(z)\,(1 - x(z))\,dz \tag{2.12}$$

The term $|V_{fi}'^{\text{ADS}}|$ is constant with the wavevector which simplifies the calculation of the average scattering rate in Eq. (2.12). Additionally, the spatial dependence of the alloy fraction alternates as wells and barriers alternate. In the wells $x = 0$ and the integration can be performed only across the barriers, and since $x = const$ in every barrier (in most QCL designs), the ADS scattering is only a consequence of the wavefunction overlaps in usually relatively thin barriers.

2.5 Ionised impurity scattering

The doping in semiconductors introduces new atoms in the bulk semiconductor lattice, thus creating a defect or impurity in it. In order to create electron charge, the dopant atoms need to release an electron upon incorporation in the lattice. This leaves the dopant atom positively charged and Coulomb interaction may occur with the free electrons. The ionised impurity (IMP) scattering therefore employs a perturbation Hamiltonian in Coulomb form:

$$V'^{\text{IMP}} = \frac{e^2}{4\pi\epsilon_0 n^2 |\mathbf{r} - \mathbf{r_0}|} \tag{2.13}$$

where $\mathbf{r_0}$ is a spatial coordinate of the impurity.

The confinement of wells and barriers in QCLs only occurs in one spatial direction (z) and calculation of the matrix elements of this perturbation can be further simplified. The full wavefunction has a form $\psi_{\mathrm{3Di}} = A^{-\frac{1}{2}} e^{i\mathbf{k_i r}} \psi_i$ and the square matrix elements of V'^{IMP} can be simplified to the form:

$$\begin{aligned}\left|V'^{\mathrm{IMP}}_{fi}\right|^2 &= \left(\frac{e^2}{2\epsilon_0 n^2 q}\right)^2 J_{fi}\\ J_{fi} &= \int l_0 |I_{fi}|^2 dz_0\\ I_{fi} &= \int \psi_f^* e^{-q|z-z_0|}\psi_i dz\end{aligned} \tag{2.14}$$

where $\mathbf{q} = \mathbf{k_f} - \mathbf{k_i}$ represents scattering wavevector. A single impurity perturbation is given only through the $|I_{fi}|^2$, the introduction of J_{fi} is performed in order to account for all impurities throughout the volume. This is done by integration of the impurities $|I_{fi}|^2$ on a thin slice $l_0(z_0)dz_0$ across z_0. The detailed derivation can be found in [111].

When we substitute Eq. (2.14) in Eq. (2.10), we obtain the reduced scattering rate due to ionised impurities as:

$$W'_{if}(k_i) = \frac{m^* e^4}{4\pi\hbar^3\epsilon_0^2 n^4}\Theta((k_\alpha^2)(1 - f_{\mathrm{FD}}(E_{\mathrm{s}f}, T_{\mathrm{e}}))\int_0^\pi \frac{J_{fi}}{(q_\alpha + q_{\mathrm{TF}})^2} d\phi \tag{2.15}$$

where $q_{\mathrm{TF}} = \frac{me^2}{2\pi\epsilon_0 n^2\hbar^2}$ is the Thomas-Fermi inverse scattering length introduced to correct the model for the screening effect. The presence of multiple electrons over a single positive ion, weakens the Coulombic interaction of the ion and remote electrons. This correction to the scattering wavevector q needs to be added into I_{fi} and J_{fi} as well (and due to the selectivity of the delta function, needs to equal to q_α).

Since matrix elements I_{fi} depend on modulus $|z - z_0|$, simplification in form:

$$\begin{aligned}I_{fi} &= e^{-q_\alpha z_0} C_{fi}^- + e^{q_\alpha z_0} C_{fi}^+\\ C_{fi}^- &= \int_{-\infty}^{z_0} \psi_f^* e^{q_\alpha z}\psi_i dz\\ C_{fi}^+ &= \int_{z_0}^{\infty} \psi_f^* e^{-q_\alpha z}\psi_i dz\end{aligned} \tag{2.16}$$

can be exploited for the numerical optimisation by tabulating the exponential terms and avoiding their multiple calculation.

IMP scattering is highly sensitive to the wavefunction overlap, and doping may be employed in areas of the QCL stack where scattering is desirable, however the active region in QCLs where optical transition takes place is not doped due to the detrimental effect on the optical linewidth [61, 76].

2.6 Interface roughness scattering

The confinement of the electron transport in the QCLs is obtained by alternation of quantum wells and barriers in one direction, z. In most representations, the conduction band potential, is presented only in one dimension, since the Schrödinger in Eq. (2.2) assumed that an electron is free in other two dimensions. An actual 3D spatial form of the conduction band potential represents “sheets” of wells and barriers as presented in Fig. 2.2. The THz QCL device usually employs ≈ 100 periods whose total height is around 12 μm, while the ridge width is $10 - 20$ times larger, and cavity length is $100 - 200$ times larger. The interfaces between wells and barriers across this area are not perfectly flat as the material composition fluctuates, effectively producing interface roughness. Also note that the potential drop between the wells and the barriers is not perfectly steep as in most heterostructure models.

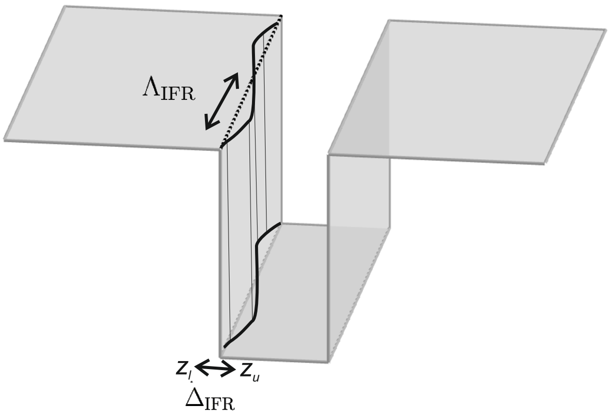

Figure 2.2: The interface roughness of the quantum well and the barrier junction that cause perturbation to the conduction band potential and cause scattering.

The formation of imperfections across QCL is random and the appropriate model assumes their Gaussian distribution such that Gaussian Fourier transform $\Delta_z(\mathbf{r})$ with the root mean square (r.m.s) height Δ_{IFR} and the correlation length Λ_{IFR} has average property $<\Delta_z(\mathbf{r})\Delta_z(\mathbf{r_0})>=\Delta^2_{\mathrm{IFR}}e^{-\frac{|\mathbf{r}-\mathbf{r_0}|}{\Lambda^2_{\mathrm{IFR}}}}$. The perturbation potential around an interface I is:

$$V_I'^{\mathrm{IFR}}=-\Delta_z(\mathbf{r})\frac{dV}{dz}\mathrm{rect}\left(\frac{z-z_{\mathrm{I}}}{z_{\mathrm{u}}-z_{\mathrm{l}}}\right) \tag{2.17}$$

where the conduction band potential deviation occurs over a rectangle that deviates from the nominal position z_{I} towards the lower and the upper bound z_{l} and z_{u}, respectively. Similarly as in IMP scattering derivation, the Bloch wavefunction would serve towards the inverse Fourier transform of the in-plane dependence of the perturbation potential, which leads to final form of the matrix elements [111]:

$$\begin{aligned} |V_{Ifi}'^{\mathrm{IFR}}|^2 &= \frac{|F_{Ifi}\Delta_{\mathrm{IFR}}\Lambda_{\mathrm{IFR}}|^2\pi}{A}e^{-\frac{q^2\Lambda^2_{\mathrm{IFR}}}{4}} \\ F_{Ifi} &= \int_{z^I_{\mathrm{l}}}^{z^I_{\mathrm{u}}}\psi_f^*\frac{dV}{dz}\psi_i dz \end{aligned} \tag{2.18}$$

where $\mathbf{q}=\mathbf{k_f}-\mathbf{k_i}$ is the scattering wavevector.

The reduced scattering rate (Eq. (2.10)) across interface I is given as:

$$W'_{Iif}(k_i) = \frac{m|F_{Ifi}|^2\Delta_{\mathrm{IFR}}^2\Lambda_{\mathrm{IFR}}^2}{\hbar^3}\Theta(k_\alpha^2)(1 - f_{\mathrm{FD}}(E_{\mathrm{s}f}, T_{\mathrm{e}}))\int_0^\pi e^{-\frac{q_\alpha^2\Lambda_{\mathrm{IFR}}}{4}}d\phi \tag{2.19}$$

The integral in Eq. (2.19) can be solved by using the identity $\int_0^\pi e^{a\cdot cos\phi}d\phi = \pi I_0(a)$ where I_0 is the regular modified cylindrical Bessel function of the zeroth order. To obtain the overall scattering rate across all interfaces, we may perform direct summation (since there is no correlation):

$$\begin{aligned} W'_{if}(k_i) &= \frac{\pi m\Delta_{\mathrm{IFR}}^2\Lambda_{\mathrm{IFR}}^2}{\hbar^3}\beta(k_i)\sum_I |F_{Ifi}|^2 \\ \beta(k_i) &= e^{-\frac{(k_i^2+k_\alpha^2)\Lambda_{\mathrm{IFR}}^2}{4}} I_0\left(\frac{k_i k_\alpha\Lambda_{\mathrm{IFR}}^2}{2}\right)\Theta(k_\alpha^2)(1 - f_{\mathrm{FD}}(E_{\mathrm{s}f}, T_{\mathrm{e}})) \end{aligned} \tag{2.20}$$

The matrix elements F_{Ifi} in Eq. (2.18) represent a general form where the interface between a well and a barrier has some transition spatial dependence. In case where the heterojunction is modelled by a step change in the conduction band potential, the derivative becomes the delta function and $F_{Ifi} \approx V_{\mathrm{Ib}}\psi_f^*(z_i)\psi_i(z_i)$ where V_{Ib} is the barrier height. The interface roughness scattering mechanism mainly depends on the wavefunction overlap at the interfaces, and on the barrier height. This mechanism is more significant in structures with higher barriers and more interfaces.

Note that the correlation length and the correlation height are not known in advance. For that reason, this mechanism serves as a fitting tool in simulations. The dependence of the current density and material gain of QCL is mostly linear with Δ_{IFR} and Λ_{IFR} with the higher sensitivity on Δ_{IFR} [74]. Chapter 4 will present the application of the model to several QCL structures, where Λ_{IFR} will be varied between $20 - 120$ Å and Δ_{IFR} between $0.1 - 3$ Å. Note that IFR scattering may sometimes be employed to compensate for the commonly neglected mechanisms such as electron-electron scattering or yet unknown mechanisms.

2.7 LO-phonon scattering

The previously mentioned scattering mechanisms were all elastic, hence there was no loss of energy in the process. The optical (LO) scattering is a non-elastic mechanism in which the electron would partly lose its energy, transferring it to the crystal or gain the energy from it. The interaction with the crystal lattice is modelled by the introduction of an imaginary particle – phonon, with which the electrons may interact. The lattice is modelled as a harmonic oscillator where the phonons vibrate causing a periodic perturbation of the strain which perturbs the overall conduction band potential. The harmonic oscillator is modelled by the usual second quantization formalism [108]:

$$\begin{aligned} \frac{\hat{p_q}^2}{2m} + \frac{m\omega_q^2\hat{u_q}^2}{2} &= \hbar\omega_q(\hat{a_q}^\dagger\hat{a_q} + \frac{1}{2}) \\ \hat{a_q} &= \sqrt{\frac{m\omega_q}{2\hbar}}\hat{u_q} + i\sqrt{\frac{1}{2\hbar m\omega_q}}\hat{p_q} \\ \hat{u_q} &= \sqrt{\frac{\hbar}{2m\omega_q}}(\hat{a_q} + \hat{a_q}^\dagger) \end{aligned} \tag{2.21}$$

where $\mathbf{q}$ is the phonon wavevector, $\hat{u_q}$ and $\hat{p_q}$ are the Hermitian displacement and momentum operators, respectively, that correspond to the phonon frequency ω_q. The overall displacement vector is obtained as a sum of all u_q for all possible polarisation modes j:

$$\mathbf{u}(\mathbf{r}) = N_{\text{cell}}^{-\frac{1}{2}} \sum_q \sum_j \sqrt{\frac{\hbar}{2m\omega_q}} \mathbf{e}_{\mathbf{q},j}(\hat{a_q} + \hat{a_q}^\dagger)e^{i\mathbf{qr}} \tag{2.22}$$

where N_{cell} is the number of crystal unit cells and $\mathbf{e}_{\mathbf{q},j}$ is the unity polarisation vector. The polarisation is directly proportional to the displacement through the dielectric constant. The Hamiltonian of the interaction (known as Fröhlich interaction) is a spatial derivative of the polarisation, and it reads [108, 86, 111]:

$$\begin{aligned} V'^{\text{ph}} &= \sum_q \frac{C}{q}(\hat{a_q}e^{i\mathbf{qr}} + \hat{a_q}^\dagger e^{-i\mathbf{qr}}) \\ C &= -i\sqrt{\frac{2\pi e^2\hbar\omega_{\text{LO}}^2}{V_{\text{c}}}\left(\frac{1}{\epsilon(\infty)} - \frac{1}{\epsilon(0)}\right)} \end{aligned} \tag{2.23}$$

where ω_{LO} is the longitudinal phonon frequency, $\epsilon(\infty)$ is the dielectric constant at ω_{LO} and V_{c} is the volume of the crystal. This interaction employs wavevector $\mathbf{q}$ in all three spatial dimensions. For the determination of the matrix elements of V'^{ph}, $\psi_{3\text{D}}$ needs to be used and after the lengthy derivation, the reduced scattering rates, in accordance with Eq. (2.12) are:

$$\begin{aligned}
W'_{if} &= \frac{\Upsilon}{2}(1-f_{\text{FD}}(E_{\text{s}f},T_{\text{e}}))\Theta(k_i^2-\frac{2m^*\Delta_E}{\hbar^2})\int\frac{\pi|G_{fi}(q_z)|^2}{\sqrt{q_z^4+2q_z^2(2k_i^2-\frac{2m^*\Delta_E}{\hbar^2})+(\frac{2m^*\Delta_E}{\hbar^2})^2}}dk_z\\
G_{fi} &= \int\psi_f^*e^{-iq_zz}\psi_i dz\\
\Upsilon &= \frac{2m^*e^2\omega_{\text{LO}}}{h^2}P'\\
P' &= \left(\frac{1}{\epsilon(\infty)}-\frac{1}{\epsilon(0)}\right)\left(N_0+\frac{1}{2}\mp\frac{1}{2}\right)\\
N_0 &= \left(e^{\frac{\hbar\omega_{\text{LO}}}{k_{\text{B}}T}}-1\right)^{-1}
\end{aligned}\tag{2.24}$$

where the factor $\Delta_E = E_f - E_i \pm \hbar\omega_{\text{LO}}$ is taken with $-\hbar\omega_{\text{LO}}$ for the phonon absorption and with $+\hbar\omega_{\text{LO}}$ for the phonon emission. The number of phonons N_0 is described by the temperature dependent Bose-Einstein distribution. Additionally, similarly to the IMP scattering, the lattice vibrations would be affected locally by the electron presence, thus screening of the electrons needs to be included through the screening length Λ_{s} that alters the z-component of the phonon wavevector $q_z^2 \to q_z^2(1+\frac{\Lambda_{\text{s}}^2}{q_z^2})^2$. The usual approaches are Park and Debye methods [86]:

$$\begin{aligned}
\Lambda_{\text{s}}^{\text{Debye}} &= \sqrt{\frac{\epsilon k_{\text{B}}T}{e^2N_{\text{D}}}}\\
\Lambda_{\text{s}}^{\text{Park}} &= \frac{e^2}{\pi\hbar^2\epsilon(0)}\sum_i\frac{\sqrt{2m^*E_i}\,m^*f^{\text{FD}}(E_i)}{\pi\hbar}
\end{aligned}\tag{2.25}$$

The LO-phonon scattering mechanism is a crucial process for operation of the THz QCLs. The LO-phonon energy $\hbar\omega_{\text{LO}}$ in GaAs is ~36 meV and this presents one of the main limitations for the THz operation of the GaAs THz QCL structures at higher temperatures. The scattering rates in Eq. (2.24) strongly depend on the level separation and their population through the Δ_E term, and have additional temperature dependence through Bose-Einstein phonon distribution and the screening length.

2.8 Acoustic phonon scattering

The acoustic phonon (ACP) scattering process is closely related to the LO phonon process, and the main difference is in the consideration of the different dispersion relation branch. The phonon dispersion relation has two branches, the upper (optical branch) and the lower (acoustic branch). In the upper branch, two atoms vibrate with the opposite phase, while in the lower branch, they oscillate with the same phase (at long wavelength). The interaction Hamiltonian for the acoustic phonon scattering may be taken as in Eq. (2.23) where the main difference would be in different form of the coupling constant C. For the LO-phonon process C is derived by considering polarisation and finding its derivative, for the acoustic phonon process we may take that the phonon frequency is proportional to the speed of sound $\omega_q = qv_\mathrm{s}$ and this would make parameter C proportional to q which would cancel in Eq. (2.23). However, rather than altering the C in Eq. (2.23) it is more efficient to take advantage of the fact that atoms oscillate in phase, with the same amplitude U_0, this means that average potential energy is $\rho_\mathrm{m} V_\mathrm{c} U_0^2 \omega_q^2/2$ (where ρ_m is material density) and equating this to the quantized phonon energy gives the amplitude U_0 [111, 86]. All atoms oscillate in phase as $u(z) = U_0 e^{i(q_z z - \omega_q t)}$ and by using linear relation between energy and strain $V' = D_\mathrm{ac} V_\mathrm{strain} = D_\mathrm{ac} \frac{\partial u}{\partial z}$, where D_ac is the deformation potential, we obtain the interaction energy in form:

$$V'^{\mathrm{ac}} = D_\mathrm{ac} \sqrt{V_\mathrm{c} \frac{2\hbar}{\rho \omega_q}} e^{iq_z z - i\omega_q t} \tag{2.26}$$

The lengthy derivation (which can be found in [86]), brings Eq. (2.12) to:

$$
\begin{aligned}
W'_{if} &= \frac{D_{\mathrm{ac}}^2 m^*}{\rho_{\mathrm{m}} v_{\mathrm{s}} h^2}(1 - f_{\mathrm{FD}}(E_{\mathrm{s}f}, T_{\mathrm{e}}))\left(N_0 + \frac{1}{2} \mp \frac{1}{2}\right) \\
&\times \int_0^{\infty}\int_0^{2\pi} |G_f i(q_z)|^2 \frac{\alpha_1\sqrt{\alpha_1^2 + q_z^2}\,\Theta(\alpha_1) + \alpha_2\sqrt{\alpha_2^2 + q_z^2}\,\Theta(\alpha_2)}{\alpha_1 - \alpha_2} d\phi dq_z \qquad (2.27) \\
\alpha_{1,2} &= -k_i cos\phi \pm \sqrt{k_i^2 cos^2\phi - \frac{2m^*(E_f - E_i)}{\hbar^2}}
\end{aligned}
$$

The acoustic phonon process is elastic and slower than LO-phonon scattering. Typically, its effect is negligible for THz QCLs compared to electron–LO–phonon scattering, and its numerical implementation in simulations in Chapter 4 will often be taken with lower precision than the other scattering processes.

2.9 Electron Electron scattering

The electron-electron (EE) scattering accounts for the many-body interactions between the electrons in the energy subbands. The interaction Hamiltonian is identical to the IMP scattering process in Eq. (2.13), however the main difference is that $\mathbf{r_0}$ represents a coordinate of another electron. The difficulty of this process is that both electrons are described by their own wavefunctions, and in order to account for the interaction, four electrons need to be considered and there are sixteen possible scattering processes, half intersubband, half intrasubband. Although the interaction Hamiltonian is relatively simple, the Fermi golden rule in Eq. (2.8) needs to consider the transition from a two-level state $|i, j\rangle$ to $|f, g\rangle$ which leads to a quadrupole integral for the matrix element $V'^{\mathrm{ee}}_{f,g,i,j}$. The main challenge is that the delta function would need to satisfy the four energy conservation conditions, rather than the two as in the other scattering mechanisms.

The detailed derivation is outside of scope of this thesis, and can be found in [86, 111]. The scattering rate for $|i, j\rangle \rightarrow |f, g\rangle$ transition is:

$$\begin{aligned}
W_{i,j,f,g}; &= \frac{m^* e^4}{8h^3\epsilon_0^2 n^2} \int \int_0^{2\pi} \int_0^{2\pi} \frac{|A_{f,g,i,j}|^2}{q_{xy}^2} P_j(\mathbf{k_j}) d\theta d\alpha k_j dk_j \\
A_{f,g,i,j} &= \int \int \psi_f^*(z')\psi_g^*(z') e^{-q_{xy}|z-z'|}\psi_i(z)\psi_j(z) dz' dz \\
4q_{xy}^2 &= 2k_{ij}^2 + \delta k_0^2 - 2k_{ij}\sqrt{k_{ij}^2 + \delta k_0^2}\, cos\theta \\
k_{ij} &= k_i^2 + k_j^2 - 2k_i k_j cos\alpha
\end{aligned} \tag{2.28}$$

where $P_j(\mathbf{k_j}) = f_{\mathrm{FD}}(E_{\mathrm{s}j}, T)$ is the Fermi–Dirac distribution function.

The screening of the electrons needs to be added to account for the reduction of the scattering rate. This can be done by altering the dielectric constant in form $\epsilon_0 n^2 \to \epsilon_0 n^2 \epsilon_{\mathrm{sc}}$ where the screening is given as [116]:

$$\begin{aligned}
\epsilon_{\mathrm{sc}} &= 1 + \frac{e^2}{2\epsilon_0 n^2 q_{xy}} \Pi_{ii}(q_{xy}, T) A_{i,i,i,i} \\
\Pi_{ii} &= \int_0^{\infty} \frac{\Pi_{ii}(q_{xy}, T=0)}{4k_{\mathrm{B}} T cosh^2\left(\frac{E_{\mathrm{F}} - E}{2k_{\mathrm{B}}T}\right)} \\
\Pi_{ii}(q_{xy}, T=0) &= \frac{m^*}{\pi\hbar^2}\left(1 - \Theta(q_{xy} - 2\sqrt{2\pi N_i})\sqrt{1 - \frac{8\pi N_i}{q_{xy}^2}}\right)
\end{aligned} \tag{2.29}$$

The EE scattering is computationally very expensive, as for N states, it has N^4 numerical burden, while all other process have N^2 complexity. The numerical implementation can take advantage of relation $A_{i,j,f,g} = \int \psi_f^* \psi_i I_{jg}(q,z) dz$ where $I_{jg}(q,z)$ is identical to the matrix elements from the IMP scattering process in Eq. (2.16). Apart from the numerical cost, the difficulty of the EE process is its physical interpretation and validity. The derivation assumed classical Hamiltonian where quantum effect of the many-body interaction of the two state system can be presented by a product of the single state wavefunctions with no correlation. The choice of the screening depends on the temperature and state population and it can significantly affect the results. Some numerical load can be reduced by neglecting intersubband interaction of largely separated states, however this may cause significant changes in the final results [76]. It can be estimated that the intersubband EE interaction thermalises the subbands similarly as the other elastic process (not significantly), while intrasubband EE interaction has more significant effect. Since IFR mechanism is used for the model fitting, the simulations in

Chapter 4 neglect the EE interaction and assume that any EE contribution may be compensated by the IFR process. The validity of this approximation will also be examined in Chapter 4.

2.10 Kinetic balance equation

The mentioned scattering mechanisms all employ the Hamiltonians with classical interpretation. The quantum nature of the transport is only accounted through the Fermi-Golden rule and therefore any model that consists of such scattering rates is considered as semi-classical. The Fermi-Golden rule dictated the energy selection principle through the delta function that is purely the consequence of the quantum-mechanical nature of the energy levels, however all scattering mechanisms have a collision interpretation in the classical sense, and therefore energy conservation law equation is needed. The distribution of the electrons in each subband is considered to be Fermi-Dirac, however laser is a non-equilibrium device driven by the application of the external bias. This can be modelled by assigning Fermi-Dirac distribution to each subband individually, with its own electron temperature and a quasi-Fermi level.

The kinetic energy distribution can be modelled in similar framework as the RE model. Each subband may gain or lose the kinetic energy and this may be described by an electron temperature. If the scattering occurs between the subbands $i \to f$, the subband f is heated and gains the kinetic energy, while the subband i loses it. Additionally if the scattering process is inelastic, the gain/loss of kinetic energy is further changed. The difference between the kinetic energy of the subband f, E_k^f and the kinetic energy of the subband i, E_k^i is:

$$\begin{aligned} \Delta E_k &= E_k^f - E_k^i = E_i - E_f + \delta E \\ \delta E &= \begin{cases} \pm E_{\mathrm{LO}}, & \text{for phonon absorption/emission process} \\ 0, & \text{for elastic scattering process} \end{cases} \end{aligned} \tag{2.30}$$

Each subband i has population of n_i and average scattering rate $\bar{W_{if}}$ for a variety of the scattering mechanisms. The transfer of the kinetic energy between the subbands i and f can be described by introducing the kinetic energy rates

w_{if}^{+} and w_{if}^{-} that represent the rate at which the kinetic energy of the subband f is increasing and the rate at which the kinetic energy of the subband i is decreasing. These rates are introduced through the normalisation over the Fermi-Dirac distribution:

$$\begin{aligned} w_{if}^{+} &= \frac{\int E_k^f \bar{W}_{if} f_{\mathrm{FD}}(E_{\mathrm{QF}}^i, T_i)(1 - f_{\mathrm{FD}}(E_{\mathrm{QF}}^f, T_f) dE_k^i}{\int f_{\mathrm{FD}}(E_{\mathrm{QF}}^i, T_i) dE_k^i} \\ w_{if}^{-} &= \frac{\int E_k^i \bar{W}_{if} f_{\mathrm{FD}}(E_{\mathrm{QF}}^i, T_i)(1 - f_{\mathrm{FD}}(E_{\mathrm{QF}}^f, T_f) dE_k^i}{\int f_{\mathrm{FD}}(E_{\mathrm{QF}}^i, T_i) dE_k^i} \end{aligned} \tag{2.31}$$

where E_{QF}^i is the quasi-Fermi level of the subband i. By using Eq. (2.30) it leads to $w_{if}^{+} = \Delta E_k \bar{W}_{if} + w_{if}^{-}$. Note that for the intrasubband scattering process, it means $w_{ii}^{+} = w_{ii}^{-}$ which is particularly relevant for the electron-electron mechanism [108]. The kinetic energy transfer equation is defined as a net process:

$$\frac{d\epsilon_k}{dt} = \sum_i n_i w_{if}^{+} - n_f w_{fi}^{-} \tag{2.32}$$

At steady state Eq. (2.32) equals to zero and if we assume the nearest neighbor approximation where we only consider scattering interactions between two periods, we would obtain a system of $2N$ non-linear equations that yield N electron temperatures and N subband concentrations, where N is the number of the subbands per one QCL period. The main issue with this system is with the Fermi-Dirac distribution. The averaging of the reduced scattering rates in Eq. (2.10) and the kinetic energy rates in Eq. (2.31) both require quasi-Fermi levels and the subband temperatures T_i which makes Eq. (2.32) numerically and mathematically challenging to solve since this equation needs to be coupled with the Schrödinger-Poisson equation. The common approximation that simplifies the calculation assumes equithermal subbands – all subbands have an electron temperature T_{e} that satisfies Eq. (2.32) [117]. This approximation does not physically support the laser operation principle since the paradigm requires the maintenance of the population inversion between ULL and LLL meaning that LLL (and ILL) receives more kinetic energy than other levels. However, equithermal approximation may be interpreted as an effective temperature approximation similarly as the electric field domain formation is circumvented by assuming a constant bias over the entire QCL stack. The simplification of Eq. (2.32 [108, 118] results in kinetic balance equation [86, 119]:

$$\sum_{\text{processes}} \sum_{f} \sum_{i} n_i \bar{W_{if}}^{\text{process}} \Delta E_k^{\text{process}} = 0 \tag{2.33}$$

where "processes" represents all elastic and non-elastic scattering processes that are considered, note that ΔE_k depends on this as well, in accordance with Eq. (2.30).

2.11 Self-self-consistent algorithm

The equithermal subband approximation removed the necessity for the kinetic energy rates in Eq. (2.31) and quasi-Fermi levels. However Eq. (2.33) still needs to be solved self-consistently with the self-consistent approach for the Schrödinger-Poisson equation [119, 43]. The kinetic balance equation (2.33) is a numerical minimisation problem which can be solved by numerous approaches such as Brent algorithm [120]. The Schrödinger–Poisson equation is numerically solved as a coupled system of the discretised nonlinear eigenvalue and linear matrix problem (Appendix C) in an iterative procedure. The solution yields the subband energies and the wavefunctions, which are then plugged again into the transport model (i.e. the Density Matrix) for fine-tuning of the output parameters: current density J, material gain g and optical power L. The transport model can be further coupled with the Maxwell equations for the determination of the dynamic properties of the optical power. The algorithm schematic is presented in Fig. 2.3.

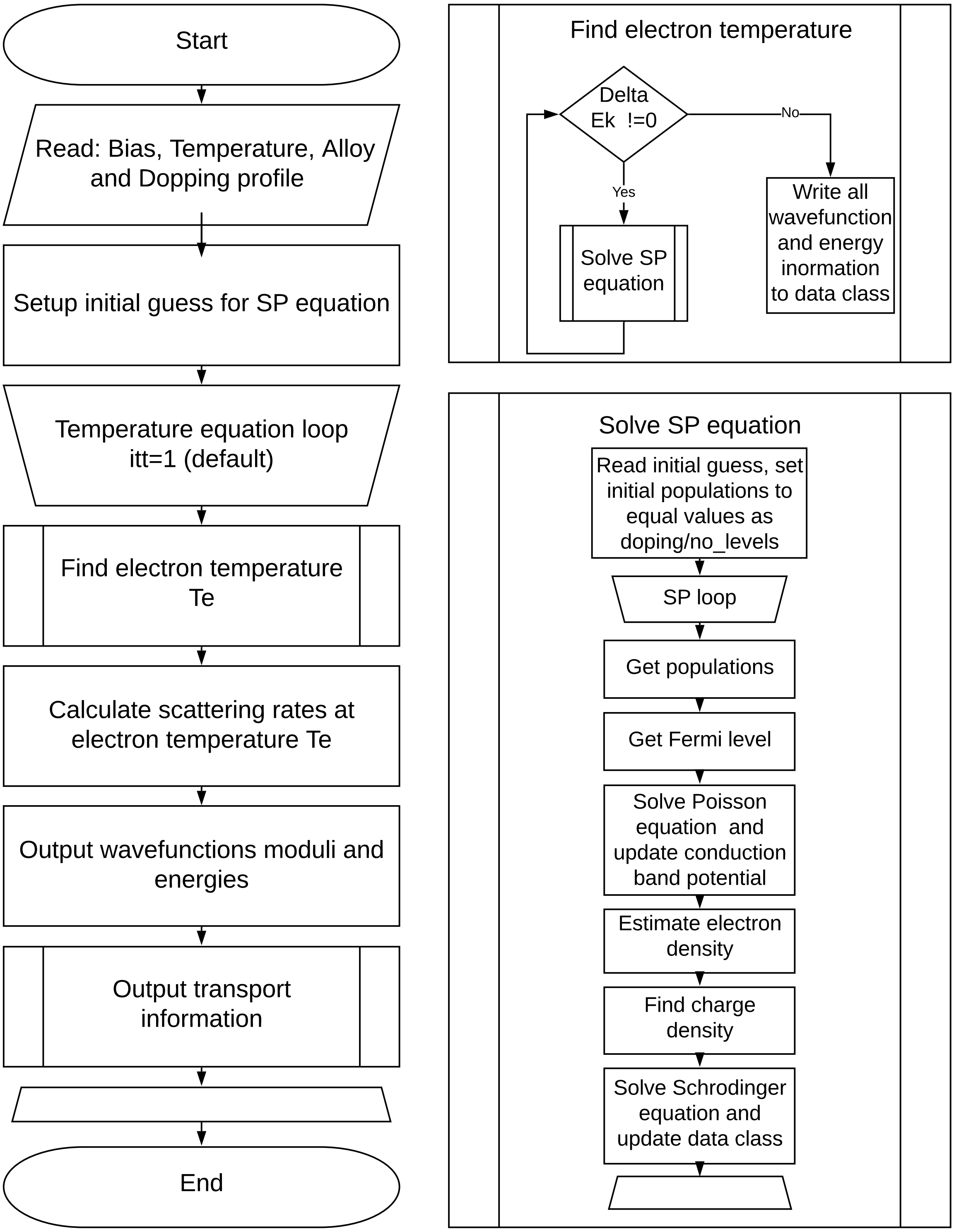

Figure 2.3: Simplified flowchart of the simulation code. The algorithm consists of two nested self-consistent approaches that are solving the Schrödinger–Poisson equation and Kinetic balance equation. Note that Schrödinger–Poisson equation is implemented via for loop, allowing user specification for number of iterations which (with some care) may reduce the simulation time.

The initial structure of the numerical implementation in Leeds group employed independent codes that were solving different parts of the algorithm. This implementation was needed due to the historic reasons and limitation of the RAM memory at the time of the development. For a single external bias point K_i the simulation time was around 2 hours and sweeping the bias for generation of an adequate $I - V$ graph yielded the overall simulation time of several days. Since the model can be fitted to the experiment by variation of the interface roughness parameters, modelling one QCL structure required extensive total simulation time. However, some approximations, such as a guess for the electron temperature (which avoids kinetic balance equation) could be used to speed up the process.

The author of this thesis took advantage of the supercomputer facilities (ARC2) at University of Leeds and developed a numerical script which runs independent simulations for different biases K_i on different processors, which (if the processors are immediately available) reduced the code operation to the time required for a simulation of the single bias point. Furthermore, the author restructured the code into a set of C++ classes instead of independent codes. This circumvented excessive reading/writing of the temporary data. The author also unified all scattering mechanisms (except EE) into a single class in order to avoid multiple invoking of identical loops. This optimisation work reduced the single external bias K_i operating time from $\sim$ 2 hours to $\sim$ 5–10 minutes which allowed the author to add optical power calculation into the model, along with the study of the dynamic effects given by the Maxwell equation.

Figure 2.3 reflects the exact implementation of the simulation script, however the processes are broken into $\sim$ 20 C++ classes. The structure of the code keeps all external input in a single class (QCLOptions) where user can select multitude of options (choice of transport model, manual input of electron temperature or waveguide loss, IFR parameters, number of simulation points (number of states per modules, number of time points for dynamics model, number of Schrödinger–Poisson iterations, number of thermal equation iterations etc.)). The output of the code is split into two classes. Class QCLInput is continuously updated during self-self consistent algorithm and contains full subband and conduction band potential information, while transport models (DM and RE) separately output information on transport characteristics (current density, material gain, optical power, frequency dependence of material gain, time dependencies within the dynamics model etc.). In addition to C++ codes, few simulations scripts have been constructed in order to sweep input parameters on ARC2 and ease user interaction with the code.

The steady–state simulation results are presented in Chapter 4, while dynamics modelling and the simulation results are given in Chapters 6 and 7.

Chapter 3

Density Matrix Model

The semi-classical models such as Rate Equation approach consider transitions of electrons between discrete energy levels while neglecting coherence effects and quantum mechanical dephasing. The density matrix model is capable of solving the shortcomings of RE model and can be viewed as its generalisation. Nominally, the computational cost of the DM model is squared in comparison with the RE model. Furthermore, the DM model has more complex formulation and requires advanced mathematical understanding. The algebra needed for the DM theory is presented in Appendix D and it is recommended to review it prior to this Chapter. The model is based on the former research at University of Leeds [1], however the entire mathematical formulation and the numerical implementation represents author's original work that resulted in few publications [74, 83]. This chapter will present the DM theory for QCL structures in detail and discuss the periodic boundary conditions, the nearest neighbour approximation, the dipole approximation, the non-rotating-wave approximation (NRWA) and the output properties which can be directly written as extensions of the RE model expressions. The mathematical formulation allows efficient numerical implementation and also offers a direct possibility of coupling the DM model with the Maxwell equation for the study of the dynamic properties of QCLs discussed in Chapter 7.

---

[1] Dr Andrew Grier, Dr Viet Dinh

3.1 Liouville Equation

The density matrix formalism was first introduced by J. Von Neumann [121, 122] and its applications span throughout a variety of fields in Quantum Mechanics [77, 79]. As discussed in section 1.6.1, the density matrix operator is constructed as $\hat{\rho} = \left|\psi\hat{(t)}\right\rangle \left\langle\psi\hat{(t)}\right|$. The normalisation condition of the Schrödinger equation is $\sum_i \left|\hat{\psi_i}\right\rangle \left\langle\hat{\psi_i}^*\right| = 1$ and if the wavefunction basis is expanded in coefficient form $\psi_i = C_i\phi_i$ where ϕ_i is a basis function, the density matrix represents all combinations of C_i coefficients in form $\rho_{ij} = C_i C_j^*$. The sum of the main diagonal elements of the density matrix therefore represents the probability normalisation condition, and the entire matrix can be viewed as a probability measure. Since the wavefunction holds information on all properties of the quantum system, the density matrix formalism may be viewed as a statistical phase-space probability measure of the distribution of wavefunctions and any property that may be derived through them. The simpler point of view, interprets the density matrix formalism as evolution of a statistical ensemble. The Schrödinger equation describes behaviour of a single quantum system, while the density matrix formalism describes statistical behaviour of the ensemble of such quantum system. This provides an opportunity of describing coherent effects and mixed quantum states.

The evolution of the density matrix can be simply derived by finding the derivative of $\hat{\rho} = \left|\psi\hat{(t)}\right\rangle \left\langle\psi\hat{(t)}\right|$ and using the time-dependent Schrödinger equation $i\hbar\frac{\partial\psi}{\partial t} = \mathcal{H}\psi$. The resulting equation is the Liouville equation:

$$i\hbar\frac{d\hat{\rho}}{dt} = [\hat{\mathcal{H}}, \hat{\rho}] + i\hbar\hat{\mathcal{D}} \tag{3.1}$$

where $\hat{\mathcal{H}}$ is the Hamiltonian, and $\hat{\mathcal{D}}$ is the dissipator which is additionally included. The main requirement for a physical solution is that ρ must be a positive semi-definite matrix. This is ensured if the dissipator is written in Lindblad form [123, 124, 125, 126]. Physically, the dissipator represents all processes that are not included in the Hamiltonian, such as various perturbation effects. Clearly, all transport mechanisms discussed in Chapter 2 can be treated as perturbative effects via Fermi golden rule and the dissipator would have a form $\hat{\mathcal{D}} = -\frac{\hat{\rho}}{\tau}$. The Fermi golden rule satisfies the Lindblad formulation, however the scattering mechanisms discussed in Chapter 2 would still add semi-classical treatment of transport. The dissipator can be further altered to add dephasing effects and such DM model can be viewed as a generalisation of the RE approach. Note that alternative formulations of the dissipator are possible [72] and may offer improved insight of the quantum properties of the system.

3.2 The nearest neighbour and the infinite periods approximation

The early DM models for the study of the QCLs [81, 127, 82, 47] considered several states (ULL, LLL, and ILL) which is justified for modelling of MIR [88] and THz LO-phonon structures. Note that even for a three level consideration, DM approaches may result in large number of equations ≈ 27 where analytical solution is not feasible. The later approaches [61, 73, 74, 128, 129, 130, 131, 132] developed DM models that were applicable for the arbitrary number of states per period. This thesis will focus on the model developed in Leeds group [73, 61, 74] that essentially generalises the earlier technique in [82].

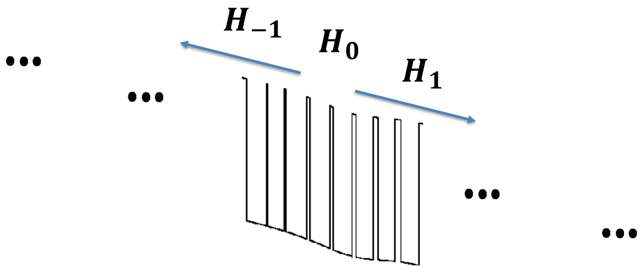

Figure 3.1: The nearest neighbour approximation. One QCL period is depicted by its Hamiltonian H_0 and it interacts with its neighbours through the interaction Hamiltonians $H_{\pm1}$

.

Similarly to the semiconductor crystal theory, we will exploit the periodicity of QCL structure by setting the number of periods Q to the infinity. Furthermore, we will apply the tight-binding nearest neighbour approximation that assumes that one QCL period only interacts with its nearest neighbours. The resulting Hamiltonian can be written as a tridiagonal matrix:

$$\mathcal{H} = \begin{pmatrix} H_0 & H_1 & 0 & \cdots & \cdots & \cdots & 0 \\ H_{-1} & \ddots & \ddots & \ddots & \cdots & \cdots & \vdots \\ 0 & \ddots & H_0 & H_1 & 0 & \cdots & \vdots \\ \vdots & \ddots & H_{-1} & H_0 & H_1 & \ddots & \vdots \\ \vdots & \vdots & 0 & H_{-1} & H_0 & \ddots & 0 \\ \vdots & \vdots & \vdots & \ddots & \ddots & \ddots & H_1 \\ 0 & \cdots & \cdots & \cdots & 0 & H_{-1} & H_0 \end{pmatrix} + eKL_{\mathrm{P}} \begin{pmatrix} \frac{Q}{2} & 0 & \cdots & \cdots & \cdots & \cdots & 0 \\ 0 & \ddots & \ddots & \cdots & \cdots & \cdots & \vdots \\ \vdots & \ddots & 1 & \ddots & \cdots & \cdots & \vdots \\ \vdots & \vdots & \ddots & 0 & \ddots & \cdots & \vdots \\ \vdots & \vdots & \vdots & \ddots & -1 & \ddots & \vdots \\ \vdots & \vdots & \vdots & \vdots & \ddots & \ddots & 0 \\ 0 & \cdots & \cdots & \cdots & \cdots & 0 & -\frac{Q}{2} \end{pmatrix} \tag{3.2}$$

where L_{P} is the length of one QCL period. We are focusing on one QCL period, surrounded by $\frac{Q}{2}$ neighbours on either side. The central period Hamiltonian is given by H_0, while the interaction with its left and right neighbour is given by H_{-1} and H_1 respectively. The second term in Eq. (3.2) is added to account for the application of the external electric field K. We assume that the neighbours to the right of H_0 have lower potential (hence the $-$ sign within the matrix) as depicted in Fig. 3.1. Note that this is not correct orientation for the actual QCL operation – application of bias tilts the potential from right to left, however, this can be rectified by reversing the order of QCL layers in the simulation. The Hamiltonian $\mathcal{H}$ must be Hermitian and it applies $H_0 = H_0^\dagger$ and $H_1 = H_{-1}^\dagger$.

QCL is a resonant tunnelling device, thus interaction between the periods needs to take that into account. As the external electric field K is varied, periods of QCL tilt bringing ILL and ULL into resonance. However, as K is varied, the energy of two discrete levels may not fully align in quantum well system. Instead, they reach the minimal energy separation – the anti-crossing energy at K_{A} value of the electric field. For any field $K > K_{\mathrm{A}}$ the levels would swap their energy position (anti-cross) and transport would resume normally. At $K = K_{\mathrm{A}}$ the resonant effects take place. If ILL from one period is (nearly) aligned with ULL from the adjacent period, the device would yield maximum optical power as the transport would be the most efficient. The resonance between two states causes the population of electrons to be in phase coherence, and the wave packet would oscillate at Rabi frequency, damped by the dephasing processes [81]. Multiple resonances may occur for the same value of K causing multiple coherent effects that may not be modelled by RE approach.

The tight-binding scheme requires solving the Schrödinger–Poisson equation on one QCL period where conduction band potential is “flattened” at its endpoints. For that reason, the period of QCL must start from the injection barrier. The resulting wavefunctions form an orthonormal basis for the density matrix formalism, and we may assume that all periods have identical wavefunctions translated by the corresponding period distance from the central period.

The simplest approximation for the period interaction Hamiltonian is to adopt the standard resonant tunnelling approach [133] across the injection barrier where the interaction between a state from the upper period i_1 and a state from the central period j_0 is

$$H_{1_{i_1 j_0}} = \sqrt{\langle i_1 | \, V - V_{\mathrm{TB}_0} \, | j_0 \rangle \, \langle i_1 | \, V - V_{\mathrm{TB}_1} \, | j_0 \rangle} \tag{3.3}$$

V is the conduction band potential of the infinite structure consisting of Q QCL periods. V_{TB_0} and V_{TB_1} are the tight binding conduction band potentials that correspond to the central period and the period left to it, respectively. The tight binding potential V_{TB_0} is equivalent to the potential of one period where all the other periods are replaced by the potential's endpoints (the standard tight-binding scheme). Note that $V_{\mathrm{TB}_1}(z) = V_{\mathrm{TB}_0}(z + L_\mathrm{P}) + eKL_\mathrm{P}$ due to the structure periodicity. Since the wavefunctions have the spatial offset of one period, the value of $\langle i_1 | \, V - V_{\mathrm{TB}_{0,1}} \, | j_0 \rangle$ depends mostly on how much the wavefunctions “leak” through the injection barrier. This approximation is debatable, because the original approach [133] was considering the resonance between two quantum wells, rather than two multiple quantum well periods. We will keep this formalism due to its simplicity, and the fact that model provides good match with the experimental results (which are presented in the next Chapter), with a note that more general approach could be applied as in [72].

The wavefunction basis is taken in the tight-binding fashion on one period and for that reason, the density matrix will follow the tridiagonal form of the Hamiltonian in Eq. (3.2):

$$\rho = \begin{pmatrix} \rho_0 & \rho_1 & 0 & \cdots & \cdots & \cdots & 0 \\ \rho_{-1} & \ddots & \ddots & \ddots & \cdots & \cdots & \vdots \\ 0 & \ddots & \rho_0 & \rho_1 & 0 & \cdots & \vdots \\ \vdots & \ddots & \rho_{-1} & \rho_0 & \rho_1 & \ddots & \vdots \\ \vdots & \vdots & 0 & \rho_{-1} & \rho_0 & \ddots & 0 \\ \vdots & \vdots & \vdots & \ddots & \ddots & \ddots & \rho_1 \\ 0 & \cdots & \cdots & \cdots & 0 & \rho_{-1} & \rho_0 \end{pmatrix} \tag{3.4}$$

Note that the external electric field breaks the symmetry of the Hamiltonian in Eq. (3.2) on the main diagonal, however we still assume that its effect is small, and that the wavefunction basis may be spatially translated to adjacent periods. This approximation will have significant effects on the derivation of the output parameters.

The commutator in Eq. (3.1) employs a product of two tridiagonal matrices, which results in pentadiagonal matrix yielding five equations. We only have three unknown density matrix partitions, and the system seems to be overdetermined. However, equations of interest are the ones which correspond to the central three diagonals. The additional two equations $[H_1, \rho_1] = [H_{-1}, \rho_{-1}] = 0$ are the consequence of the duplication of information in the system. This commonly occurs in the nearest neighbour approximation. Nominally, we should assume that the density matrix is full for avoiding this issue. However, since the interaction with the second period is highly unlikely due to the spatial separation of the wavefunctions in QCL structure, we may take the density matrix as in Eq. (3.4). We are forcing the system to interact with its nearest neighbour, and the additional equations are a residue of interaction between the first and the second neighbour, which duplicates the information of the system.

The equations of interest are:

$$\begin{aligned}
i\hbar\frac{d\rho_1}{dt} &= [H_0,\rho_1] + [H_1,\rho_0] + eKL_\mathrm{P}\rho_1 - i\hbar\frac{\rho_1}{\tau_\mathrm{D}} \\
i\hbar\frac{d\rho_0}{dt} &= [H_{-1},\rho_1] + [H_0,\rho_0] + [H_1,\rho_{-1}] - i\hbar\frac{\rho_0}{\tau_{\mathrm{D}_0}} - i\hbar\frac{\rho_0}{\tau} \\
i\hbar\frac{d\rho_{-1}}{dt} &= [H_{-1},\rho_0] + [H_0,\rho_{-1}] - eKL_\mathrm{P}\rho_{-1} - i\hbar\frac{\rho_{-1}}{\tau_\mathrm{D}}
\end{aligned} \tag{3.5}$$

where the dissipator assumed that inter-period relaxation is purely coherent and given by a dephasing tensor τ_D, while central period involves coherent interaction and incoherent interaction given by a tensor τ where all scattering interactions are considered via Fermi-golden rule.

The system in Eq. (3.5) is nonlinear and it comprise $3N^2$ equations written in matrix form. The solution of such system is not trivial, and it requires linear transformation of Eq. (3.5). Formally, the Liouville equation (3.1) can be linearised in form $i\hbar\rho_\mathrm{lin} = \mathcal{L}\rho_\mathrm{lin}$ where $\mathcal{L}$ is commonly referred as the Liouvillian superoperator. However, with the nearest period approximation, we obtained the system in Eq. (3.5) which needs to be linearised by a different superoperator. In the following sections, we will discuss its derivation in detail. Note that our formalism can be expanded to the higher neighbour approximation [83] and we may additionally introduce the interaction with the device contacts, by altering the form of the Hamiltonian [134] and using the properties of banded matrices [135].

3.3 Commutator linearisation

A mathematical expression $AXB = C$ where, A, B, C and X are square matrices of the same size, can be written in linear form as $(A \otimes B^T)X' = C'$ where X' and C' are vectorised forms of the original matrices X and C unpacked row-wise and $\otimes$ is Kronecker tensor product [136]. More details can be found in Appendix D.

The commutator $[A, X]$ therefore linearises as $(A \otimes I - I \otimes A^T)X'$ where I is an identity matrix of the same size as A. The commutator part of Eq. (3.1) often introduces operator $\hat{\mathcal{L}} = \hat{\mathcal{H}} \otimes I - I \otimes \hat{\mathcal{H}}^T$ which with the corresponding linearisation of the dissipator in Eq. (3.1) forms the Liouvillian superoperator.

In the case of the periodic structure, we cannot formulate the linearisation of Eq. (3.1) in this form, since the Hamiltonian in Eq. (3.2) is infinite banded matrix with high level of symmetry. Instead, we need to linearise each commutator in Eq. (3.5) individually. If we neglect dissipator terms in Eq. (3.5), we have a system:

$$\begin{aligned}
i\hbar\frac{d\rho'_1}{dt} &= (H_0\otimes I - I\otimes H_0^T)\rho'_1 + (H_1\otimes I - I\otimes H_1^T)\rho'_0 + eKL_\mathrm{P}(I\otimes I)\rho'_1\\
i\hbar\frac{d\rho'_0}{dt} &= (H_{-1}\otimes I - I\otimes H_{-1}^T)\rho'_1 + (H_0\otimes I - I\otimes H_0^T)\rho'_0 + (H_1\otimes I - I\otimes H_1^T)\rho'_{-1}\\
i\hbar\frac{d\rho'_{-1}}{dt} &= (H_{-1}\otimes I - I\otimes H_{-1}^T)\rho'_0 + (H_0\otimes I - I\otimes H_0^T)\rho'_{-1} - eKL_\mathrm{P}(I\otimes I)\rho'_{-1}
\end{aligned} \tag{3.6}$$

If wavefunction basis on one period has N states, each equation in Eq. (3.6) consists of N^2 equations. We can group the vectorised forms $\rho'' = \rho'_1, \rho'_0, \rho'_{-1}$ into a single vector of $3N^2$ size. If we separate the Kronecker product terms in Eq. (3.6) into groups that perform the operation from the left and from the right, we may write:

$$\begin{aligned}
i\hbar\frac{d}{dt}\begin{pmatrix}\rho'_1\\ \rho'_0\\ \rho'_{-1}\end{pmatrix} = &\left[\begin{pmatrix}H_0 & H_1 & 0\\ H_{-1} & H_0 & H_1\\ 0 & H_{-1} & H_0\end{pmatrix}\boxtimes\begin{pmatrix}I & I & I\\ I & I & I\\ I & I & I\end{pmatrix}\right]\begin{pmatrix}\rho'_1\\ \rho'_0\\ \rho'_{-1}\end{pmatrix}\\
&-\left[\begin{pmatrix}I & I & I\\ I & I & I\\ I & I & I\end{pmatrix}\boxtimes\begin{pmatrix}H_0^T & H_1^T & 0\\ H_{-1}^T & H_0^T & H_1^T\\ 0 & H_{-1}^T & H_0^T\end{pmatrix}\right]\begin{pmatrix}\rho'_1\\ \rho'_0\\ \rho'_{-1}\end{pmatrix}\\
&+eKL_\mathrm{P}\left[\begin{pmatrix}I & 0 & 0\\ 0 & 0 & 0\\ 0 & 0 & -I\end{pmatrix}\boxtimes\begin{pmatrix}I & I & I\\ I & I & I\\ I & I & I\end{pmatrix}\right]\begin{pmatrix}\rho'_1\\ \rho'_0\\ \rho'_{-1}\end{pmatrix}
\end{aligned} \tag{3.7}$$

where $\boxtimes$ represents Khatri-Rao product [137, 138, 139]. Khatri-Rao product is defined as a "dot" product of partitioned matrices, where the "dot" is the Kronecker tensor product. Different definitions exist in the literature [140] and we will focus on that in [141, 142], which requires matrices to be partitioned in identical manner as presented in Appendix D. This type of product is particularly useful for describing systems of equations involving Kronecker tensor products.

Each zero in Eq. (3.7) is $N \times N$ zero matrix. Note that the last term in Eq. (3.7) is a consequence of a constant term $\pm eKL_\mathrm{P}$ multiplying the vectorised forms of the density matrix blocks, and the Kronecker tensor product of two identity matrices simply creates identity matrix of a larger size, in our case $I \otimes I = I_{N^2}$, $I \otimes 0 = 0_{N^2}$. If we introduce:

$$H = \begin{pmatrix} H_0 & H_1 & 0 \\ H_{-1} & H_0 & H_1 \\ 0 & H_{-1} & H_0 \end{pmatrix}, \Upsilon \ = eKL_\mathrm{P} \begin{pmatrix} I & 0 & 0 \\ 0 & 0 & 0 \\ 0 & 0 & -I \end{pmatrix}, I_\mathrm{U} = \begin{pmatrix} I & I & I \\ I & I & I \\ I & I & I \end{pmatrix}$$
$$\rho'' = \begin{pmatrix} \rho'_1 \\ \rho'_0 \\ \rho'_{-1} \end{pmatrix} \tag{3.8}$$

the commutator part of Eq. (3.6) linearises as:

$$i\hbar\frac{d\rho''}{dt} = \left(H \boxtimes I_\mathrm{U} - I_\mathrm{U} \boxtimes H^{.T} + \Upsilon \boxtimes I_U\right)\rho'' \tag{3.9}$$

Note that the second term in Eq. (3.9) uses "dot" transpose $.T$ operation on the Hamiltonian H which only transposes the blocks individually, as in the second term on right hand side of Eq. (3.7). This operation is not identical to the transpose of H, because the reduced Hamiltonian that we introduced in (3.8) is Hermitian and it applies $H_0 = H_0^\dagger$ and $H_1 = H_{-1}^\dagger$.

3.4 Dissipator linearisation

The dissipator in Eq. (3.5) is introduced by tensors τ_D and τ which represent coherent dephasing and incoherent scattering in the QCL. This formulation allows scattering only within the central period, while dephasing is allowed between the periods as well. This is fundamentally different from the RE approach which neglects the dephasing effect, but allows inter period scattering.

In this DM model, the scattering only occurs within the central period described by the density matrix block ρ_0 and, as in RE approach, incoherent effects only affect the subband populations [79] (which are given by the diagonal elements of ρ_0):

$$\left(\frac{\rho_0}{\tau}\right)_{ii} = -\frac{\rho_{0_{ii}}}{\tau_i} + \sum_{j\neq i} \frac{\rho_{0_{jj}}}{\tau_{ji}} \tag{3.10}$$

where $\tau_i^{-1} = \sum_j \tau_{ij}^{-1}$ are state lifetimes.

The dephasing can be interpreted from dipole example [1]. If a wavefunction is approximated as a mixture of two states that have single-state wavefunctions $\psi_i = a_i(t)e^{-iE_it/\hbar}\psi_i(\boldsymbol{r})$ and $\psi_j = a_j(t)e^{-iE_jt/\hbar}\psi_j(\boldsymbol{r})$, the probability will have three terms: i) individual occupancies $|a_i(t)\psi_i(\boldsymbol{r})|^2$ ii) and $|a_j(t)\psi_j(\boldsymbol{r})|^2$ iii) and sinusoidal component at frequency equal to the energy spacing between states i and j. The latter term resembles the dipole oscillation in the classical mechanics, and directly corresponds to the off-diagonal elements in the density matrix. This term decays as $a_i(t)a_j(t)\psi_i(\boldsymbol{r})\psi_j(\boldsymbol{r})$, and this decay is proportional to the decay of $|a_i(t)a_j(t)|$, however these terms describe level occupancy and they can have a phase $a_i(t) = |a_i(t)|e^{i\phi_i}$ which creates additional term $e^{i(\phi_j-\phi_i)}$. This phase can be randomised by the dephasing processes that do not change occupancies (amplitudes of a_i, a_j) which is referred to as the pure dephasing. The dephasing affects every off-diagonal element in the density matrix, regardless of the block it is located in, and the most common approach introduces it as:

$$\begin{aligned} \frac{\rho_{0,\pm1_{ij}}}{\tau_{ij}} &= -\frac{\rho_{0,\pm1_{ij}}}{\tau_{||_{ij}}}, \quad \rho_0 : i \neq j \\ \frac{1}{\tau_{||_{ij}}} &= \frac{1}{2\tau_i^*} + \frac{1}{2\tau_i^*} + \frac{1}{\tau_{ii}^*} + \frac{1}{\tau_{jj}^*} - \frac{2}{\sqrt{\tau_{ii}^{\mathrm{IFR}}\tau_{jj}^{\mathrm{IFR}}}} \end{aligned} \tag{3.11}$$

where scattering rates and lifetimes with an asterisk $*$ exclude interface roughness mechanism. IFR effect on coherence is added differently [61] through rates with IFR notation. Note that the coherent dephasing does not occur in the central period for $i = j$. The dephasing time $\tau_{||_{ij'}}$ between state i from the central period and state j' from the adjacent period is identical to $\tau_{||_{ij}}$ where j is a state from the central period, because the wavefunctions in the adjacent period are spatially translated and expression in Eq. (3.11) is invariant.

The direct implementation of Eqs. (3.10,3.11) results in matrices that consist of unknown terms, however we are mainly interested in following the linear vectorisation of the density matrix blocks from the previous section, and decoupling the tensor form. Unfortunately, a direct algebraic transformation similar to the

Kronecker or the Khatri-Rao product is not possible, and linearisation needs to be performed through mathematical induction.

Let us construct three tensor matrices:

$$\frac{1}{\tau}=\begin{pmatrix} -\tau_1^{-1} & \tau_{12}^{-1} & \cdots & \tau_{1N}^{-1} \\ \tau_{21}^{-1} & \tau_2^{-1} & \ddots & \tau_{2N}^{-1} \\ \vdots & \vdots & \vdots & \vdots \\ \tau_{N1}^{-1} & \tau_{N2}^{-1} & \cdots & \tau_N^{-1} \end{pmatrix}, \quad \frac{1}{\tau_{\mathrm{D}}}=\begin{pmatrix} \tau_{||11}^{-1} & \tau_{||12}^{-1} & \cdots & \tau_{||1N}^{-1} \\ \tau_{||21}^{-1} & \tau_{||22}^{-1} & \ddots & \tau_{||2N}^{-1} \\ \vdots & \vdots & \vdots & \vdots \\ \tau_{||N1}^{-1} & \tau_{||N2}^{-1} & \cdots & \tau_{||NN}^{-1} \end{pmatrix}$$
$$\frac{1}{\tau_{\mathrm{D}_0}}=\begin{pmatrix} 0 & \tau_{||12}^{-1} & \cdots & \tau_{||1N}^{-1} \\ \tau_{||21}^{-1} & 0 & \ddots & \tau_{||2N}^{-1} \\ \vdots & \vdots & \vdots & \vdots \\ \tau_{||N1}^{-1} & \tau_{||N2}^{-1} & \cdots & 0 \end{pmatrix} \tag{3.12}$$

It implies that $\frac{1}{\tau_{\mathrm{D}_0}}=\frac{1}{\tau_{\mathrm{D}}}-\mathrm{diag}(\frac{1}{\tau_{\mathrm{D}}})$.

Let us apply Eqs. (3.10,3.11) for $N=2$ and focus on dissipator terms in Eq. (3.5) for block ρ_0 and ρ_1 (ρ_{-1} has identical form) :

$$\begin{aligned} i\hbar\frac{d\rho_1}{dt} &= -i\hbar\begin{pmatrix} \frac{\rho_{1_{11}}}{\tau_{||11}} & \frac{\rho_{1_{12}}}{\tau_{||12}} \\ \frac{\rho_{1_{21}}}{\tau_{||21}} & \frac{\rho_{1_{22}}}{\tau_{||22}} \end{pmatrix} \\ i\hbar\frac{d\rho_0}{dt} &= -i\hbar\begin{pmatrix} \frac{\rho_{0_{22}}}{\tau_{||21}} & 0 \\ 0 & \frac{\rho_{0_{11}}}{\tau_{||12}} \end{pmatrix} - i\hbar\begin{pmatrix} -\frac{\rho_{0_{11}}}{\tau_1} & \frac{\rho_{0_{12}}}{\tau_{||12}} \\ \frac{\rho_{0_{21}}}{\tau_{||21}} & -\frac{\rho_{0_{22}}}{\tau_2} \end{pmatrix} \end{aligned} \tag{3.13}$$

When ρ_0 and ρ_1 are vectorised row-wise, Eq. (3.13) transforms to:

$$\begin{aligned} i\hbar\frac{d\rho_1'}{dt} &= -i\hbar\begin{pmatrix} \frac{1}{\tau_{||11}} & 0 & 0 & 0 \\ 0 & \frac{1}{\tau_{||12}} & 0 & 0 \\ 0 & 0 & \frac{1}{\tau_{||21}} & 0 \\ 0 & 0 & 0 & \frac{1}{\tau_{||22}} \end{pmatrix}\begin{pmatrix} \rho_{1_{11}} \\ \rho_{1_{12}} \\ \rho_{1_{21}} \\ \rho_{1_{22}} \end{pmatrix} = -i\hbar D_1'\rho_1' \\ i\hbar\frac{d\rho_0'}{dt} &= -i\hbar\begin{pmatrix} -\frac{1}{\tau_1} & 0 & 0 & \frac{1}{\tau_{21}} \\ 0 & 0 & 0 & 0 \\ 0 & 0 & 0 & 0 \\ \frac{1}{\tau_{12}} & 0 & 0 & -\frac{1}{\tau_2} \end{pmatrix}\begin{pmatrix} \rho_{0_{11}} \\ \rho_{0_{12}} \\ \rho_{0_{21}} \\ \rho_{0_{22}} \end{pmatrix} - i\hbar\begin{pmatrix} 0 & 0 & 0 & 0 \\ 0 & \frac{1}{\tau_{||12}} & 0 & 0 \\ 0 & 0 & \frac{1}{\tau_{||21}} & 0 \\ 0 & 0 & 0 & 0 \end{pmatrix}\begin{pmatrix} \rho_{0_{11}} \\ \rho_{0_{12}} \\ \rho_{0_{21}} \\ \rho_{0_{22}} \end{pmatrix} = -i\hbar D_0'\rho_0' \end{aligned} \tag{3.14}$$

By performing mathematical induction for $N = 3$ and $N = N + 1$ and repeating the derivation of Eq. (3.14) the dephasing terms in Eq. (3.5) linearise by placing elements of $\frac{1}{\tau_{\mathrm{D}}}$ and $\frac{1}{\tau_{\mathrm{D}_0}}$ from Eq. (3.12) row-wise, on a main diagonal of a $N^2 \times N^2$ matrix.

The incoherent scattering given by $\frac{1}{\tau}$ in Eq. (3.12) needs to undergo more complicated transformation that is not directly apparent from $N = 2$ case in Eq. (3.14). If we decompose $\frac{1}{\tau}$ into a sum of N^2 matrices T_{ij} that only have one element $\frac{1}{\tau_{ij}}$ in the ij-th position while all other elements are set to zero, the corresponding linearisation matrix would be a transpose of a block $N \times N$ matrix with T_{ij} blocks as its elements:

$$
\begin{aligned}
\frac{1}{\tau} &= \begin{pmatrix} -\tau_1^{-1} & \tau_{12}^{-1} & \cdots & \tau_{1N}^{-1} \\ \tau_{21}^{-1} & -\tau_2^{-1} & \ddots & \tau_{2N}^{-1} \\ \vdots & \vdots & \vdots & \vdots \\ \tau_{N1}^{-1} & \tau_{N2}^{-1} & \cdots & -\tau_N^{-1} \end{pmatrix} = \\
&\begin{pmatrix} -\tau_1^{-1} & 0 & \cdots & 0 \\ 0 & 0 & \ddots & 0 \\ \vdots & \vdots & \vdots & \vdots \\ 0 & 0 & \cdots & 0 \end{pmatrix} + \begin{pmatrix} 0 & \tau_{12}^{-1} & \cdots & 0 \\ 0 & 0 & \ddots & 0 \\ \vdots & \vdots & \vdots & \vdots \\ 0 & 0 & \cdots & 0 \end{pmatrix} + \cdots + \begin{pmatrix} 0 & 0 & \cdots & 0 \\ 0 & 0 & \ddots & 0 \\ \vdots & \vdots & \vdots & \vdots \\ 0 & 0 & \cdots & -\tau_N^{-1} \end{pmatrix} \\
&= T_{11} + T_{12} + \cdots + T_{NN} \\
\left(\frac{1}{\tau}\right)_{\mathrm{lin}} &= \begin{pmatrix} T_{11} & T_{12} & \cdots & T_{1N} \\ T_{21} & T_{22} & \ddots & T_{2N} \\ \vdots & \vdots & \vdots & \vdots \\ T_{N1} & T_{N2} & \cdots & T_{NN} \end{pmatrix}^T
\end{aligned}
\tag{3.15}
$$

Note that both expansions have straightforward numerical implementation. In C++, both expansions run two nested loops $i, j = 0 \cdots N - 1$ and construct $N^2 \times N^2$ linear forms of τ_{D} and τ as $\left(\frac{1}{\tau_{\mathrm{D}}}\right)_{\mathrm{lin}} (iN + j, iN + j) = \frac{1}{\tau_{||_{ij}}}$ and if $i \neq j$, $\left(\frac{1}{\tau}\right)_{\mathrm{lin}} (iN + i, jN + j) = \frac{1}{\tau_{ji}}$, all other elements are zero. The dissipator terms in Eq. (3.5) therefore linearise as:

$$
\begin{gathered}
i\hbar\frac{d\rho''}{dt} = -i\hbar\begin{pmatrix} D'_1 & 0 & 0 \\ 0 & D'_0 & 0 \\ 0 & 0 & D'_{-1} \end{pmatrix}\rho'' = -i\hbar D''\rho'' \\
D'_1 = D'_{-1} = \left(\frac{1}{\tau_{\mathrm{D}}}\right)_{\mathrm{lin}}, \quad D'_0 = \left(\frac{1}{\tau_{\mathrm{D}_0}}\right)_{\mathrm{lin}} + \left(\frac{1}{\tau}\right)_{\mathrm{lin}}
\end{gathered}
\tag{3.16}
$$

The linearised dissipator terms in Eq. (3.16) are $N^2 \times N^2$ matrices (zero matrices as well) and need to be added to Eq. (3.9) after Khatri-Rao product is performed. The superoperator for periodic system $\mathcal{L}_{\mathrm{QCL}}$ is:

$$
\begin{aligned}
\frac{d\rho''}{dt} &= \mathcal{L}_{\mathrm{QCL}}\ \rho'' \\
\mathcal{L}_{\mathrm{QCL}} &= -\frac{i}{\hbar}\left(H \boxtimes I_{\mathrm{U}} - I_{\mathrm{U}} \boxtimes H^{\cdot T} + \Upsilon \boxtimes I_U - i\hbar D''\right)
\end{aligned}
\tag{3.17}
$$

3.5 Dipole approximation

The DM formalism is directly linked to the optical properties of the quantum system which is represented by its Hamiltonian. In QCL structure, we assume that the optical interaction occurs only within the period and thus only H_0 partition of the Hamiltonian in Eq. (3.2) is affected.

The common approach is to model quantum level system as a dipole antenna that resonates at a specific level transition energy. For that reason we formulate the Hamiltonian of the central period as a sum of the tight-binding Hamiltonian $\hat{V_{\mathrm{TB}}}$ and the dipole interaction energy $\hat{V_{\mathrm{d}}} = -\boldsymbol{\mu}\boldsymbol{E}$,where $\boldsymbol{\mu} = -e\boldsymbol{r}$ is the electric dipole moment operator [79] and $\boldsymbol{E}(\mathbf{r}, t)$ is the optical electric field. The matrix form of the central period Hamiltonian could then be written as $H_0 = H_{\mathrm{DC}} + H_{\mathrm{AC}}$ where H_{DC} is a diagonal matrix consisting only of the tight–binding energies on the main diagonal and $H_{\mathrm{AC}} = -eZE(z, t)$ where Z is the dipole matrix consisting of the expectation values of the position operator $Z_{ij} = \langle i|\,\hat{z}\,|j\rangle$. Note that in the QCL we assume that transport in (x, y) plane is free, and QCL layers are grown in z direction.

The optical electrical field needs to be modelled by Maxwell equation Eq. (1.9). Additionally, the polarisation in Eq. (1.9) can be obtained by DM formalism through the expectation value of the polarisation operator $\hat{P} = -eN_{\mathrm{D}}\hat{z}$

where N_{D} is spatial concentration of carriers (or the doping level). In DM approach expectation value of any operator $\hat{O}$ can be found as $\langle O \rangle = \mathrm{Tr}(\hat{\rho}\hat{O})$, thus polarisation is calculated as $P = -eN_{\mathrm{D}}\mathrm{Tr}(\rho Z)$. For this reason, Eq. (1.9) is coupled to the Liouville equation (3.5) creating a complicated set of differential equations. Note that any approximation for the Maxwell wave equation discussed in section 1.6.3 affects the Liouville equation and its linearisaiton.

3.6 Non-rotating wave approximation

In section 1.6.3 and Appendix A we discussed travelling wave and Fourier approaches that simplify the Maxwell equation. Both approaches have been successfully applied to QCLs [88, 74] along with the multi frequency optical field components that allow the study of non–linear effects [129]. In this work we will focus on Fourier approach under the slow-envelope approximation given by Eq. (1.12).

A very common approximation formulates optical interactions between the levels by assuming the optical electrical field as $E_{\mathrm{RWA}} = E_0 e^{\pm i\omega t}$ where sign is taken depending on the relative level position. Such model represents a rotating wave approximation (RWA) and it requires a careful consideration of which elements of H_{AC} Hamiltonian partition have $+$ or $-$ exponential term. RWA is only feasible for systems with several states, and its generalisaiton to N state system is challenging. The biggest advantage of RWA is that it does not extend the Lioville equation significantly, however it does not simplify the numerical and mathematical implementation.

The generalisation of RWA models the optical field as a cosine wave at the resonant frequency ω, $E_{\mathrm{NRWA}} = E(t)(e^{i\omega t} + e^{-i\omega t})$ and this represents the non-rotating-wave-approximation (NRWA). The central period Hamiltonian block has a form $H_0 = H_{\mathrm{DC}} + H_{\mathrm{AC}}^{+} e^{i\omega t} + H_{\mathrm{AC}}^{-} e^{-i\omega t}$ where $H_{\mathrm{AC}}^{\pm} = -eZE(t)$. This represents a time dependent driving term to the Liouville equation (3.5) and we need to assume that each density matrix block ρ_k, $k = 0, 1, -1$ will have three components $\rho_k = \rho_k^{\mathrm{DC}} + \rho_k^{+} e^{i\omega t} + \rho_k^{-} e^{i\omega t}$. When this is substituted in Eq. (3.5), the system size increases three times, consisting of $9N^2$ equations:

$$\begin{aligned}
i\hbar\frac{d\rho_1^-}{dt} &= [H_{\mathrm{DC}},\rho_1^-] + [H_{\mathrm{AC}}^-,\rho_1^{\mathrm{DC}}] + [H_1,\rho_0^-] + eKL_{\mathrm{P}}\rho_1^- - i\hbar\frac{\rho_1^-}{\tau_{\mathrm{D}}} - \hbar\omega\rho_1^- \\
i\hbar\frac{d\rho_1^{\mathrm{DC}}}{dt} &= [H_{\mathrm{DC}},\rho_1^{\mathrm{DC}}] + [H_1,\rho_0^{\mathrm{DC}}] + [H_{\mathrm{AC}}^+,\rho_1^-] + [H_{\mathrm{AC}}^-,\rho_1^+] + eKL_{\mathrm{P}}\rho_1^{\mathrm{DC}} - i\hbar\frac{\rho_1^{\mathrm{DC}}}{\tau_{\mathrm{D}}} \\
i\hbar\frac{d\rho_1^+}{dt} &= [H_{\mathrm{DC}},\rho_1^+] + [H_{\mathrm{AC}}^+,\rho_1^{\mathrm{DC}}] + [H_1,\rho_0^+] + eKL_{\mathrm{P}}\rho_1^+ - i\hbar\frac{\rho_1^+}{\tau_{\mathrm{D}}} + \hbar\omega\rho_1^+ \\
i\hbar\frac{d\rho_0^-}{dt} &= [H_{-1},\rho_1^-] + [H_{\mathrm{AC}}^-,\rho_0^{\mathrm{DC}}] + [H_{\mathrm{DC}},\rho_0^-] + [H_1,\rho_{-1}^-] - i\hbar\frac{\rho_0^-}{\tau_{\mathrm{D}_0}} - i\hbar\frac{\rho_0^-}{\tau} - \hbar\omega\rho_0^+ \\
i\hbar\frac{d\rho_0^{\mathrm{DC}}}{dt} &= [H_{-1},\rho_1^{\mathrm{DC}}] + [H_{\mathrm{DC}},\rho_0^{\mathrm{DC}}] + [H_{\mathrm{AC}}^+,\rho_0^-] + [H_{\mathrm{AC}}^-,\rho_0^+] + [H_1,\rho_{-1}^{\mathrm{DC}}] - i\hbar\frac{\rho_0^{\mathrm{DC}}}{\tau_{D_0}} - i\hbar\frac{\rho_0^{\mathrm{DC}}}{\tau} \\
i\hbar\frac{d\rho_0^+}{dt} &= [H_{-1},\rho_1^+] + [H_{\mathrm{DC}},\rho_0^+] + [H_{\mathrm{AC}}^+,\rho_0^{\mathrm{DC}}] + [H_1,\rho_{-1}^+] - i\hbar\frac{\rho_0^+}{\tau_{\mathrm{D}_0}} - i\hbar\frac{\rho_0^+}{\tau} + \hbar\omega\rho_0^+ \\
i\hbar\frac{d\rho_{-1}^-}{dt} &= [H_{-1},\rho_0^-] + [H_{\mathrm{DC}},\rho_{-1}^-] + [H_{\mathrm{AC}}^-,\rho_{-1}^{\mathrm{DC}}] - eKL_{\mathrm{P}}\rho_{-1}^- - i\hbar\frac{\rho_{-1}^-}{\tau_{\mathrm{D}}} - \hbar\omega\rho_{-1}^- \\
i\hbar\frac{d\rho_{-1}^{\mathrm{DC}}}{dt} &= [H_{-1},\rho_0^{\mathrm{DC}}] + [H_{\mathrm{DC}},\rho_{-1}^{\mathrm{DC}}] + [H_{\mathrm{AC}}^+,\rho_{-1}^-] + [H_{\mathrm{AC}}^-,\rho_{-1}^+] - eKL_{\mathrm{P}}\rho_{-1}^- - i\hbar\frac{\rho_{-1}^-}{\tau_{\mathrm{D}}} \\
i\hbar\frac{d\rho_{-1}^+}{dt} &= [H_{-1},\rho_0^+] + [H_{\mathrm{DC}},\rho_{-1}^+] + [H_{\mathrm{AC}}^+,\rho_{-1}^{\mathrm{DC}}] - eKL_{\mathrm{P}}\rho_{-1}^+ - i\hbar\frac{\rho_{-1}^+}{\tau_{\mathrm{D}}} + \hbar\omega\rho_{-1}^+
\end{aligned} \tag{3.18}$$

The system in Eq. (3.18) is non–linear and needs to undergo similar linearisation steps discussed in sections 3.3 and 3.4 in order to formulate a linear superoperator suitable for numerical implementation. However, this system has high level of symmetry and we may construct similar form of the superoperator to the one in Eq. (3.17). Let us assume general NRWA form of H_j and ρ_k partitions as $H_j = H_j^{\mathrm{DC}} + H_j^+ e^{i\omega t} + H_j^- e^{-i\omega t}$ and $\rho_k = \rho_k^{\mathrm{DC}} + \rho_k^+ e^{i\omega t} + \rho_k^- e^{i\omega t}$, the commutator $[H_j,\rho_k]$ splits into three equations:

$$\begin{aligned}
e^{-i\omega t}: &\quad [H_j^{\mathrm{DC}},\rho_k^-] + [H_j^-,\rho_k^{\mathrm{DC}}] \\
e^{0}: &\quad [H_j^-,\rho_k^+] + [H_j^{\mathrm{DC}},\rho_k^{\mathrm{DC}}] + [H_j^+,\rho_k^-] \\
e^{i\omega t}: &\quad [H_j^+,\rho_k^{\mathrm{DC}}] + [H_j^{\mathrm{DC}},\rho_k^+]
\end{aligned} \tag{3.19}$$

If we repeat commutator linearisation as in Eq. (3.7), Eq. (3.19) can be written as:

$$\left(\begin{pmatrix} H_j^{\mathrm{DC}} & H_j^{-} & 0 \\ H_j^{+} & H_j^{\mathrm{DC}} & H_j^{-} \\ 0 & H_j^{+} & H_j^{\mathrm{DC}} \end{pmatrix} \boxtimes I_{\mathrm{U}} - I_{\mathrm{U}} \boxtimes \begin{pmatrix} H_j^{\mathrm{DC}^T} & H_j^{-^T} & 0 \\ H_j^{+^T} & H_j^{\mathrm{DC}^T} & H_j^{-^T} \\ 0 & H_j^{+^T} & H_j^{\mathrm{DC}^T} \end{pmatrix}\right) \begin{pmatrix} \rho_k^{-'} \\ \rho_k^{\mathrm{DC}'} \\ \rho_k^{+'} \end{pmatrix} \tag{3.20}$$

where terms with the apostrophe represent the vectorised forms of the corresponding matrices.

Transformation in Eq. (3.20) needs to be applied to every commutator in Eq. (3.5), however if we introduce a NRWA expansion rule as:

$$H_j^{\mathrm{NRWA}} \rightarrow \begin{pmatrix} H_j^{\mathrm{DC}} & H_j^{-} & 0 \\ H_j^{+} & H_j^{\mathrm{DC}} & H_j^{-} \\ 0 & H_j^{+} & H_j^{\mathrm{DC}} \end{pmatrix}, \qquad \rho_k^{\mathrm{NRWA}'} \rightarrow \begin{pmatrix} \rho_k^{-'} \\ \rho_k^{\mathrm{DC}'} \\ \rho_k^{+'} \end{pmatrix} \tag{3.21}$$

and apply it to each Hamiltonian and constant block in Eq. (3.8) (note that H_{-1}, H_1 and I (within Υ) do not have $\pm$ terms), and expand I_{U} into 9×9 partitioned matrix system filled by $N \times N$ identity matrices I, the system in Eq. (3.19) linearises as [83]:

$$\begin{aligned} \frac{d\rho^{\mathrm{NRWA}''}}{dt} &= \mathcal{L}_{\mathrm{QCL}}^{\mathrm{NRWA}} \rho^{\mathrm{NRWA}''} \\ \mathcal{L}_{\mathrm{QCL}}^{\mathrm{NRWA}} &= -\frac{i}{\hbar}\Big(H^{\mathrm{NRWA}} \boxtimes I_{\mathrm{U}}^{\mathrm{NRWA}} - I_{\mathrm{U}}^{\mathrm{NRWA}} \boxtimes H^{\mathrm{NRWA}\cdot T} \\ &\qquad + \Upsilon^{\mathrm{NRWA}} \boxtimes I_{\mathrm{U}}^{\mathrm{NRWA}} - i\hbar D''^{\mathrm{NRWA}} + \hbar\omega\Omega^{\mathrm{NRWA}}\Big) \end{aligned} \tag{3.22}$$

where

- H^{NRWA} is a 9×9 partitioned Hamiltonian obtained by applying Eq. (3.21) on each block of the Hamiltonian in Eq. (3.8), each partition (including zeros) in H^{NRWA} is $N \times N$ matrix.

- The external electric field term $\Upsilon^{\mathrm{NRWA}''}$ can technically be constructed by applying the rule in Eq. (3.21) on Υ in Eq. (3.8) by treating the identity matrices as DC terms. However, instead of this $\Upsilon^{\mathrm{NRWA}''}$ can be directly implemented as a 9×9 partitioned matrix, where blocks on the main diagonal are $I, I, I, 0, 0, 0, -I, -I, -I$ and each partition has $N \times N$ size and all other blocks are zero matrices.

- $I_{\mathrm{U}}^{\mathrm{NRWA}}$ is a 9×9 partitioned matrix filled with identity matrices of $N \times N$ size. For the Khatri-Rao product in (3.22), this matrix only needs to have partitions at positions in which H^{NRWA} has non-zero partitions, however $I_{\mathrm{U}}^{\mathrm{NRWA}}$ has a direct algebraic formulation as: $I_{\mathrm{U}}^{\mathrm{NRWA}} = U_{9\times9} \otimes I_{N\times N}$, where $U_{9\times9}$ is a 9×9 unit matrix (matrix filled with unit values).

- $\rho^{\mathrm{NRWA}''}$ is a column vector of $9N^2$ size, whose elements correspond to the stacked vectorised forms of $\rho_1^{-'}, \rho_1^{\mathrm{DC}'}, \rho_1^{+'}, \rho_0^{-'}, \rho_0^{\mathrm{DC}'}, \rho_0^{+'}, \rho_{-1}^{-'}, \rho_{-1}^{\mathrm{DC}'}, \rho_{-1}^{+'}$ in that respective order.

- The dissipator $D^{\mathrm{NRWA}''}$ can technically be constructed by applying the rule in Eq. (3.21) to blocks of D' in Eq. (3.16), with notion that those blocks do not have $\pm$ terms, and have $N^2 \times N^2$ size. In simpler sense, $D^{\mathrm{NRWA}''}$ is 9×9 block diagonal matrix, where 9 blocks on the main diagonal are $D'_1, D'_1, D_1, D'_0, D'_0, D_0, D'_1, D'_1, D'_1$ and each has $N^2 \times N^2$ size.

- Frequency terms in NRWA are the consequence of the time derivative of the density matrix in the Liouville equation and this is illustrated by Ω^{NRWA}. These terms originally had exponentials $e^{\pm i\omega t}$, when we take the derivative of $\frac{d\left(\rho_k^{\pm} e^{\pm\omega t}\right)}{dt} = e^{\pm i\omega t}\left(\frac{d\rho_k^{\pm}}{dt} \pm i\omega\rho_k^{\pm}\right)$, the factor $i\hbar$ from the left hand side of Eq. (3.18) turns $\pm\omega$ term to $\mp\hbar\omega$ which changes the sign again when moved to the right hand side of Eq. (3.18). In Eq. (3.18) frequency terms occur only in odd equations and alternate as $-\hbar\omega, 0, \hbar\omega \cdots$. Since this is a constant multiplying the entire block $\rho_k^{0,\pm}$, the linear form would be $N^2 \times N^2$ identity matrix. For that reason Ω^{NRWA} is a diagonal 9×9 partitioned matrix, where elements on the main diagonal are $I_{N^2}, 0_{N^2}, -I_{N^2}, I_{N^2}, 0_{N^2}, -I_{N^2}, I_{N^2}, 0_{N^2}, -I_{N^2}$. Algebraically, this can also be constructed as $\Omega^{NRWA} = (I_{3\times3} \otimes G_{3\times3}) \otimes I_{N^2\times N^2}$ where G is a matrix with entries $1, 0, -1$ on the main diagonal.

It is important to note that the Liouvillian $\mathcal{L}_{\mathrm{QCL}}^{\mathrm{NRWA}}$ is a partitioned pentadiagonal 9×9 matrix where each partition has $N^2 \times N^2$ size [74, 83], however five diagonals are only the consequence of the Khatri–Rao product between H^{NRWA} and $I_{\mathrm{U}}^{\mathrm{NRWA}}$, all other terms in Eq. (3.22) only affect the main block diagonal of the system. For that reason it is not numerically advisable to construct these terms separately into several $9N^2 \times 9N^2$ matrices, but rather directly add them once the Khatri-Rao product is performed.

3.7 Steady state solution and normalisation

The normalisation condition for the density matrix is that its trace needs to have the unit value since the diagonal elements physically represent the probability. This affects the basis chosen for DM, and since we focused on one QCL period, this condition needs to be satisfied only by DC block of the central period partition of the density matrix. We can substitute one of the equations corresponding to a diagonal elements of $\rho_0^{\mathrm{DC}'}$ block and steady state solution would simply be given as:

$$\begin{aligned} \sum_i \rho_{0_{ii}}^{\mathrm{DC}} &= 1 \\ \frac{d\rho^{\mathrm{NRWA}''}}{dt} &= \mathcal{L}_{\mathrm{QCL}}^{\mathrm{NRWA}} \rho^{\mathrm{NRWA}''} + B \\ \rho^{\mathrm{NRWA}''}(t \to \infty) &= -\left(\mathcal{L}_{\mathrm{QCL}}^{\mathrm{NRWA}}\right)^{-1} B \end{aligned} \tag{3.23}$$

where B is a column vector of $9N^2$ size whose elements are zeros, except at the position where normalisation condition is implemented. In numerical procedure that we implemented, we chose to substitute an equation targeting N–th population (N–th element of the main diagonal of $\rho_0^{\mathrm{DC}'}$) which lies in $(5N^2 - 1)$–th line of the system.

The alternative approach is to reduce the system by one equation by substituting $\rho_{0_{NN}}^{\mathrm{DC}} = 1 - \sum_{i \neq N} \rho_{0_{ii}}^{\mathrm{DC}}$ in the entire system, however former approach is substantially simpler.

The steady state analysis of various QCL structures is presented in the next chapter. Equation (3.23) consists of $9N^2$ equations that are complex. For steady state analysis, inversion of such Liouvillian is straightforward and we did not use its sparse properties or a potential possibility of block-Gaussian elimination. For the dynamic analysis, system in Eq. (3.23) is not numerically feasible and we need to take advantage of Hermitian symmetry of the density matrix and Hamiltonian in order to split the system into a set of real equations and this will be discussed in Chapter 6.

The approach we presented in this Chapter can be further generalised for a variety of the tight–binding models (i.e. graphene [143]) and detailed summary was published by the author in [83].

3.8 Current density, material gain and optical power

The macroscopic properties of QCL structure can be obtained by finding the expectation values of the current density and the polarisation operators:

$$\begin{aligned} \hat{J} &= \frac{i}{\hbar} e N_{\mathrm{D}} [\hat{\mathcal{H}}, \hat{z}] \\ \hat{P} &= -e N_{\mathrm{D}} \hat{z} \end{aligned} \tag{3.24}$$

The expectation values need to be calculated by using the overall density matrix in Eq. (3.4). We reduced the initial infinite system to three equations in Eq. (3.5) and formulated the reduced Hamiltonian H in Eq. (3.8) for linearisation purposes, however it is incorrect to apply reduced expressions for finding the expectation values. This was discussed in detail in author's publication in [74]. When we seek product of two partitioned matrices, partitions at corners act similarly as initial conditions in finite difference models and add incorrect contributions to the overall result. Expectation values in DM formalism are obtained as a trace of the product of the density matrix and the operator (in matrix form). Since we have infinite matrices of size $Q \times Q$, $Q \to \infty$, the expectation value of operator $\hat{O}$ may be determined by finding the limit $\langle \hat{O} \rangle = \lim_{Q\to\infty} \frac{1}{Q} \mathrm{Tr}\left(\hat{\rho}\hat{O}\right)$. The current density is therefore calculated as [74]:

$$\begin{aligned} J &= \frac{i}{\hbar} e N_{\mathrm{D}} \mathrm{Tr}\left(\rho_0[H_0, Z] + \rho_{-1}[H_1, Z] + \rho_1[H_{-1}, Z] + L_{\mathrm{P}}\left(H_1\rho_{-1} - \rho_1 H_{-1}\right)\right) \\ &= -\frac{i}{\hbar} e N_{\mathrm{D}} \mathrm{Tr}\left[Z\left([H_0, \rho_0] + [H_1, \rho_{-1}] + [H_{-1}, \rho_1]\right) - L_{\mathrm{P}}\left(H_1\rho_{-1} - \rho_1 H_{-1}\right)\right] \\ &= e N_{\mathrm{D}} \mathrm{Tr}\left(Z\left(\frac{d\rho_0}{dt} + \frac{\rho_0}{\tau} + \frac{\rho_0}{\tau_{D_0}}\right)\right) + \frac{i}{\hbar} e N_{\mathrm{D}} L_{\mathrm{P}} \mathrm{Tr}\left(H_1\rho_{-1} - \rho_1 H_{-1}\right) \end{aligned} \tag{3.25}$$

The expressions in Eq. (3.25) are obtained by using the rotating properties of trace operation. Interestingly, the current density is proportional to the trace of the central equation in Eq. (3.5) and additional term $L_{\mathrm{P}}\left(H_1\rho_{-1} - \rho_1 H_{-1}\right)$ which is a consequence of the application of the external electric field. Note that this term applies the periodic boundary condition.

The expectation value of the polarisation is simpler, and it reads:

$$P = -e N_{\mathrm{D}} \mathrm{Tr}\left(Z\rho_0\right) \tag{3.26}$$

The NRWA approximation causes J and P to have three components, however measurable properties are the DC term of the current density and the response to the optical field which is determined by $+$ or $-$ term of the polarisation ($P^+ = P^-$):

$$\begin{aligned} J_{\mathrm{DC}} = &-\frac{i}{\hbar} e N_{\mathrm{D}} \mathrm{Tr}\Big[Z\Big([H_{-1}, \rho_1^{\mathrm{DC}}] + [H_{\mathrm{DC}}, \rho_0^{\mathrm{DC}}] + [H_{\mathrm{AC}}^+, \rho_0^-] + [H_{\mathrm{AC}}^-, \rho_0^+] + [H_1, \rho_{-1}^{\mathrm{DC}}]\Big) \\ &- L_{\mathrm{P}}\Big(H_1\rho_{-1}^{\mathrm{DC}} - \rho_1^{\mathrm{DC}} H_{-1}\Big)\Big] \\ P^+ = &-e N_{\mathrm{D}} \mathrm{Tr}\Big(Z\rho_0^+\Big) \end{aligned} \tag{3.27}$$

Note that the polarisation P^+ needs to be inserted in Maxwell equation, thus creating a system of coupled equations since H_{AC} is proportional to the optical field.

Material gain can be obtained from the polarisation, assuming that QCL is isotropic linear medium whose polarisation has a form $P^+ = \epsilon_0 \chi E$. Imaginary part of the susceptibility χ represents the material gain:

$$g = \frac{\omega}{cn\epsilon_0}\frac{\mathrm{Im}\{P^+\}}{\mathrm{Re}\{E\}} = -\frac{\omega}{cn\epsilon_0}eN_{\mathrm{D}}\frac{\mathrm{Im}\left\{\mathrm{Tr}\left(Z\rho_0^+\right)\right\}}{\mathrm{Re}\{E\}} \tag{3.28}$$

The optical field intensity can be obtained as:

$$S = \frac{cn\epsilon_0}{2}|E|^2 \tag{3.29}$$

The experimental properties are usually measured as the optical power L, the current I and the voltage V and are commonly presented on a single graph referred to as $L-I-V$ characteristic of QCL. These values are obtained by scaling the optical intensity and the current density by emitting surface WL_{c}, and the external electric field by the active region thickness H_{QCL} and also account for the resistance of the contacts, respectively.

$$\begin{aligned} L &= SWL_{\mathrm{c}} \\ I &= J_{\mathrm{DC}}WL_{\mathrm{c}} \\ V &= KH_{\mathrm{QCL}} + IR_{\mathrm{c}} \end{aligned} \tag{3.30}$$

The contact resistance R_{c} is added to describe the effects of QCL contacts on the structure [61] and its values are small $\sim 0-3\ \Omega$, however necessary if a precise fitting of the model to the experiment is needed.

The optical intensity requires the information on the optical electric field E given by Maxwell equation, however in steady–state, any laser needs to clamp its gain to the loss, and real part of Maxwell equation in Eq. (1.12) can be written as $(loss - gain)E = 0$ by using the expression in Eq. (3.28). The material gain will be largest when the optical field is small, and as the optical field is increasing, the gain will saturate [1]. For that reason, instead of solving Eq. (1.12), we can vary E until the value of the material gain saturates to the value of loss by employing a minimisation algorithm. The obtained value for the optical power would be a steady–state result. If dynamic behaviour is of interest, solving Eq. (1.12) (and coupling it to DM model) is necessary.

3.9 Connection to the RE approach

In simplest terms, the rate equation approach only focuses on equations that lie on the main diagonal of Liouville equation. Current density in RE approach is calculated as [111]:

$$J_{\mathrm{DC}}^{\mathrm{RE}} = \frac{e}{L_{\mathrm{P}}} \left(\sum_{i} \sum_{j \neq i} n_i \left(\frac{Z_{ii} - Z_{jj}}{\tau_{ij}^{*}} \right) \right) \tag{3.31}$$

If we take the steady state value of DC component of the third equation in Eq. (3.25), and write the sum form of trace operation of term $\frac{\rho_0}{\tau}$ by using Eq. (3.10), we can write an expression for current density in DM model as [74]:

$$J_{\mathrm{DC}}^{\mathrm{DM}} = \frac{e}{L_{\mathrm{P}}} \left(\sum_{i} \sum_{j \neq i} n_i \left(\frac{Z_{ii} - Z_{jj}}{\tau_{ij}} \right) \right) + \frac{e n_{\mathrm{S}}}{L_{\mathrm{P}}} \mathrm{Tr} \left(\frac{Z \rho_0^{\mathrm{DC}}}{\tau_{D_0}} + L_{\mathrm{P}} (H_1 \rho_{-1} - \rho_1 H_{-1}) \right) \tag{3.32}$$

where we applied $n_i = N_{\mathrm{S}}\, \rho_{ii}$ where N_{S} is sheet doping density, and $N_{\mathrm{S}} = N_{\mathrm{D}} L_{\mathrm{P}}$.

The first term in Eq. (3.32) is nearly identical to the expression for RE current density in Eq. (3.31), however the major difference is that in Eq. (3.31) inter–period scattering is considered as well (hence τ_{ij}^{*} notation) and wavefunction basis was extended on two periods while the wavefunction basis for DM is obtained by solving the Schrödinger–Poisson equation on one QCL period.

Equations (3.31, 3.32) still illustrate close connection of these two models, which is partly the consequence of the dissipator form that we chose for our formulation in Eq. (3.10).

Chapter 4

Steady-State-Modelling of THz QCLs

The density matrix model discussed in the previous chapter provides efficient numerical approach for modelling THz QCLs. The $L-I-V$ characteristic of QCL is dependent on the design, temperature, and type of QCL operation (pulsed or CW). The steady-state modelling combines DM approach, self-self consistent Schrödinger-Poisson equation, thermal equation and medium loss model. This chapter will discuss the fitting procedure to the experimental results for various THz QCL structures, along with the challenges and the limitations of the overall model. Chapter will also provide comparison with RE approach, discussion on the significance of the electron-electron scattering and the possibility of exploiting the model for optimisation of high temperature performance THz QCL designs.

4.1 Fitting challenges

The experimental characterisation of QCL is provided by a temperature dependent $L-I-V$ characteristic and emission frequency dependence, usually measured both in pulsed and CW operation. Fitting the theoretical model to all experimental graphs with single set of fitting parameters is not feasible, mainly due to the large number of approximations within various models involved in the procedure and some fluctuations in the measurement itself. The latter issue is more apparent in pulsed operation where laser is driven by periodic current pulses, while the voltage and the optical power are being measured. The measurement records periodic set of voltage and optical power values that correspond to each current pulse. A single point on the pulsed $L-I-V$ characteristic however represents an averaged value of the pulsed measurement points obtained by a lock-in amplifier, therefore adding a slight tolerance in the result. The theoretical model is highly sensitive, which is further critical due to the scaling of the output parameters with the device dimensions in Eq. (3.30) (also note that we assume linear distribution of the electric bias across the active region and homogeneous distribution of the current density across the emitting cross section).

The input of the DM model is the electric bias, while in the experimental setup, the device is driven by the current. Furthermore, the voltage is obtained by Eq. (3.30) which assumes uniform distribution of the electric field across the active region, which may not be fully correct. Additionally, nearly every QCL device gives a multimode lasing spectrum, however the theoretical approach we are presenting will solely focus on the frequency that provides the highest material gain, although it is possible to account for other modes.

The most debatable model is the thermal equation discussed in 1.6.2 often taken under the linear approximation in Eq. (1.8), which is critical for CW operation. The reliability of the model is therefore low for CW operation, mainly due to the fact that different periods of the QCL active region exhibit different temperatures as depicted in Fig. 1.9, thus the periodic infinite-period approach for transport is not fully applicable without relatively rough approximation.

Initial THz QCL RE models were mainly focusing on modelling the current around the threshold or the peak optical power at particular heat sink temperature, however RE models required detail processing of the simulation data due to the non physical results. The DM model does not have such issues, and higher fitting precision to the experiment is feasible. The approach is independent on the number of states per period, and it can, in principle, be applied to any design. The steady state model consists of:

- Transport model
- Waveguide model

- Thermal model

All three models are coupled, and each has a corresponding fitting parameter. The most important fitting parameters are within the transport model. The interface roughness scattering mechanism, discussed in 2.6 uses Gaussian - like distribution to describe somewhat random imperfections of the QCL layers. These parameters directly affect the current and represent the key fitting tool. The waveguide model uses a one-dimensional transfer matrix method that determines the dielectric function of the medium [45] discussed in 1.5.2. However, medium is three-dimensional and Drude model of thin heterostructure layers is debatable. The loss is dependent on temperature, however the threshold gain in some simulations may require manual setting instead of using this model, especially for devices that use metal-metal waveguides. The thermal model under the linear approximation has shown discrepancy even within the experimental measurement, and its validity will be particularly discussed.

The following sections will discuss IFR fitting parameters by fitting several exemplary structures at single heat sink temperature, significance of EE scattering, comparison with RE approach and fitting the temperature dependence of the threshold current.

4.2 Interface roughness scattering parameters

The average imperfections of heterojunction interfaces between QCL layers as depicted in section 2.6 and Fig. 2.2 are described by Gaussian distribution characterised through the IFR correlation length Λ_{IFR} and r.m.s. height Δ_{IFR}. The QCL structure consists of hundreds of interfaces and these parameters are not known in advance and may vary from structure to structure even for the identical layer design. Reproducibility of QCL growth and fabrication is a known issue and in modelling approaches IFR parameters are often employed as fitting tools.

The model is independent on the number of states per QCL module and therefore on the QCL design type. For that reason, the fitting procedure will be demonstrated on a highly complex design, such as BTC QCL. The layer structure [74] (based on earlier work in [144]) is presented in Fig. 4.1

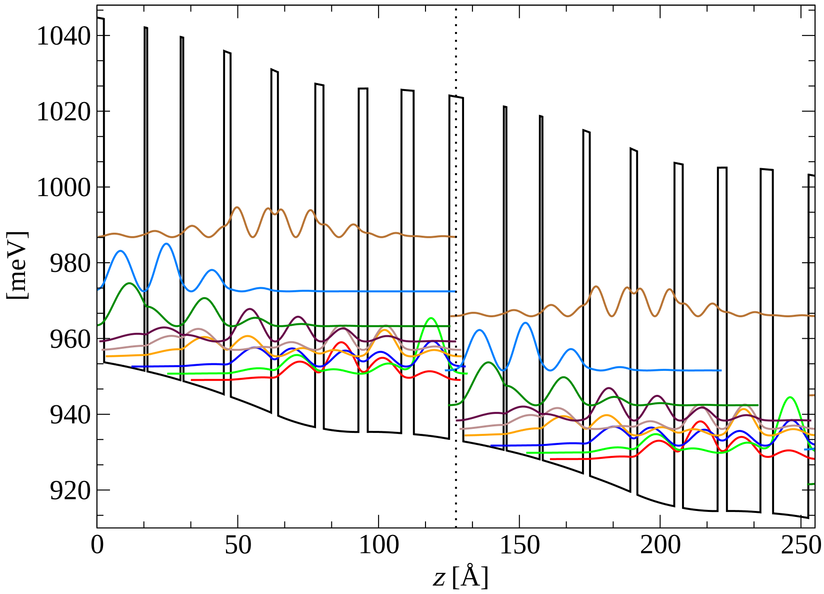

Figure 4.1: Layer thicknesses for the analysed BTC QCL design, starting with the injection barrier (until dotted horizontal line), are **5.0**/14.4/**1.0**/11.8 /**1.0**/14.4/**2.4**/14.4/**2.4***13.2*/**3.0**/*12.4*/**3.2**/12.0/**4.4**/12.6 nm, $\mathrm{Al}_{0.1}\mathrm{Ga}_{0.9}$ As barriers are shown in bold and wells doped to $1.3 \cdot 10^{16}$ cm^{-3} are underlined. Two periods are shown, along with the corresponding wavefunctions moduli squared.

The effects of IFR parameters at bias $K = 1.8\,\frac{\mathrm{kV}}{\mathrm{cm}}$ on the material gain, current density and optical power are presented in Fig. 4.2

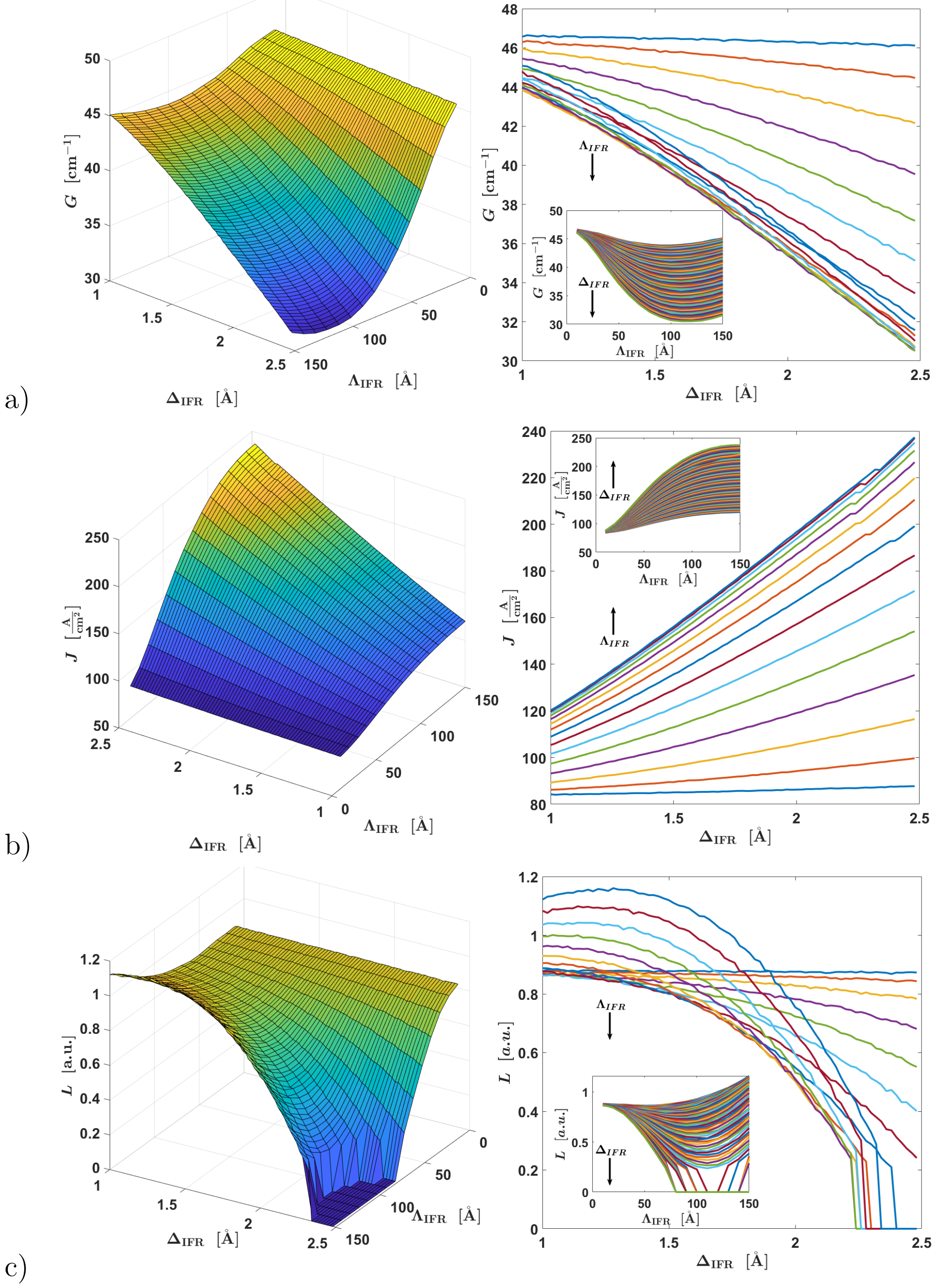

Figure 4.2: a) Material gain, b) Current density and c) Optical power dependence on IFR parameters Λ_{IFR} and Δ_{IFR} at $K = 1.8\ \frac{\mathrm{kV}}{\mathrm{cm}}$ at heat sink temperature of 20 K. Figures on the left hand side present the dependence on both parameters, while figures on the right hand side are one dimensional projections of the dependence on the left hand side (effect of Δ_{IFR} is plotted first, while Λ_{IFR} is being varied, and insets show vice versa).

The interface roughness parameters always increase the current density and decrease the material gain and therefore the optical power. The r.m.s. height Δ_{IFR} has a stronger effect than the correlation length, and for a fixed Λ_{IFR}, Δ_{IFR} will have linear effect on the current density and the material gain, while in contrast, the effect is usually linear only in the range $\Lambda_{\mathrm{IFR}} \approx\ 20 - 80$ Å as it can be observed in Fig. 4.2. This observation is consistent in all designs simulated so far and for that reason, these parameters are usually swept in range $\Lambda_{\mathrm{IFR}} \approx\ 20 - 100$ Å and $\Delta_{\mathrm{IFR}} \approx 0.1 - 3$ Å.

4.2.1 $L - I - V$ fitting at fixed temperature in pulsed operation

The fitting procedure at fixed temperature in pulsed operation is performed in several steps:

- Determining the material modal threshold gain by either using a waveguide loss model from [45] for surface plasmon waveguides or using an estimated value of $g_{\mathrm{th}} = 18 - 20\ \mathrm{cm}^{-1}$ for double metal waveguides. In rare cases, manual alterations of the values provided by model in [87] are needed, which is justifiable by the fact that this model performs one dimensional analysis and neglects effects in the perpendicular plane. For BTC structure in Fig. 4.1, waveguide loss at $T = 20$ K, determined by [87] is $g_{\mathrm{th}} = 33.56\ \mathrm{cm}^{-1}$.

- Determining a point of the highest interest on experimental $L - I - V$ characteristic. This is usually lasing threshold or the peak of the optical power dependence on current. The latter point can be found by sweeping bias for typical values of $\Delta_{\mathrm{IFR}} = 1$ Å and $\Lambda_{\mathrm{IFR}} = 80$ Å in order to detect at which bias the maximum optical power occurs, if possible. Some QCL designs “turn off” due to the high electrical heating or the high current during the experimental measurement and $I - L$ dependence does not have a maximum. However, resonant bias is usually known by the design itself.

- Performing a two dimensional sweep of Δ_{IFR} and Λ_{IFR} at fixed bias with two aims: a) to match the current density at the chosen bias (usually the one that corresponds to the peak of optical power) and b) to match the current density at the threshold at the same time. Alternatively, if resonant bias is not known, fixing i.e. $\Lambda_{\mathrm{IFR}} = 80$ Å and sweeping Δ_{IFR} and the bias can be performed in order to match the experimental $I - L$ as much as possible.

- Determining the contact resistance which fits the experimental $I - V$ dependence. Typical values are $0.1 - 3$ Ω and finding this parameter is trivial.

The initial sweep of bias, indicated that BTC structure in Fig. 4.1 resonates at $K = 2\ \frac{\mathrm{kV}}{\mathrm{cm}}$. At 20 K, the threshold current density is 139 $\frac{\mathrm{A}}{\mathrm{cm}^2}$ while at the peak of the optical power, the current density is 182 $\frac{\mathrm{A}}{\mathrm{cm}^2}$. In order to match these two values, IFR parameters were varied as presented in Fig. 4.3.

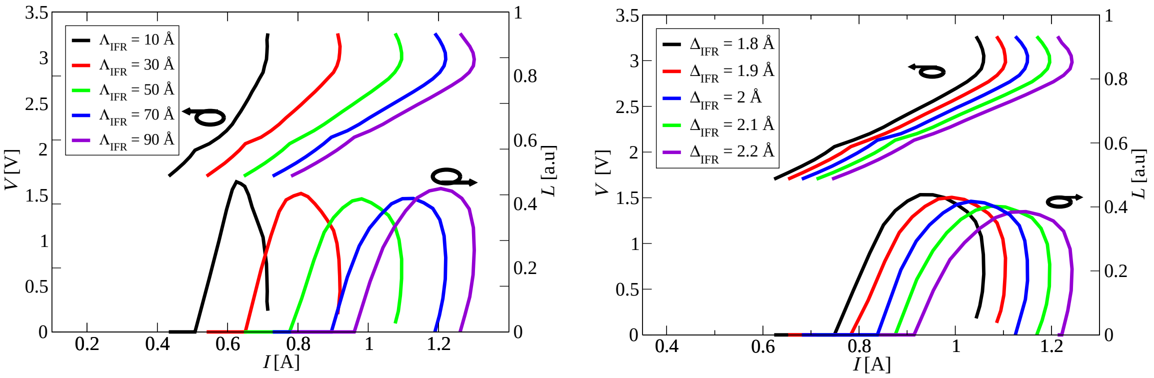

a) b)

Figure 4.3: $L - I - V$ fitting of BTC device at 20 K by varying a) IFR correlation length Λ_{IFR} for fixed $\Delta_{\mathrm{IFR}} = 2.03$ Å b) IFR r.m.s. height for fixed $\Lambda_{\mathrm{IFR}} = 80$ Å. Contact resistance for $I - V$ dependencies was not included.

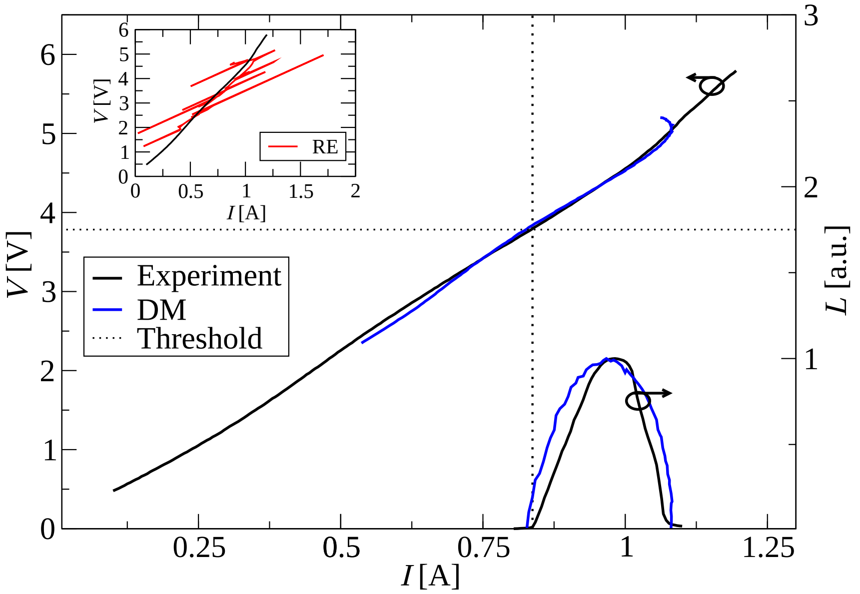

Figure 4.4: $L-I-V$ characteristic of the BTC device at 20 K in pulsed operation. Contact resistance is 2.15 Ω. Both DM model fit (blue) and RE model fit (inset - red) were fitted to experimental threshold at $(I_\mathrm{t}, V_\mathrm{t}) = (0.83\,\mathrm{A}, 3.78\,\mathrm{V})$. Experimental $I-L$ data is presented along DM $I-L$ data and normalised in arbitrary units.

.

Simulations performed in Fig. 4.3 again show that varying Λ_IFR outside the linear range (i.e 10 Å) causes changes in shape of $L-I-V$ indicating a potential non-physical value, while varying Δ_IFR has a consistent linear effect. The values Λ_{IFR} = 80 Å, Δ_IFR = 2.03 Å provide a perfect fit of the optical power dependence, and adding a contact resistance of 2.15 Ω provides a perfect fit of experimental measurement at 20 K as presented in Fig. 4.4.

Note that the optical power is presented in arbitrary units. The reason for this is that the actual optical power generated by QCL is not known. The experimental measurement is dependent on the efficiency of detector (usually a bolometer) which is in range of 15 – 30%. Additionally, the detector measures optical power originating from all modes, while the simulation performs the calculation of the dominant optical mode. For these reasons, the fitting procedure is focused on fitting the dynamic range and not the amplitude of $I-L$ dependence.

4.2.2 Comparison of Density Matrix and Rate equation model

The inset in Fig. 4.4 shows RE model fit to the experimental $I-V$ dependence. This has not been obtained by procedure discussed in 4.2.1, due to the lack of photon number equation (which would yield optical power dependence) in the implementation of RE model developed previously in the group. This RE model can only provide current density fitting to the experiment shown in Fig. 4.5.

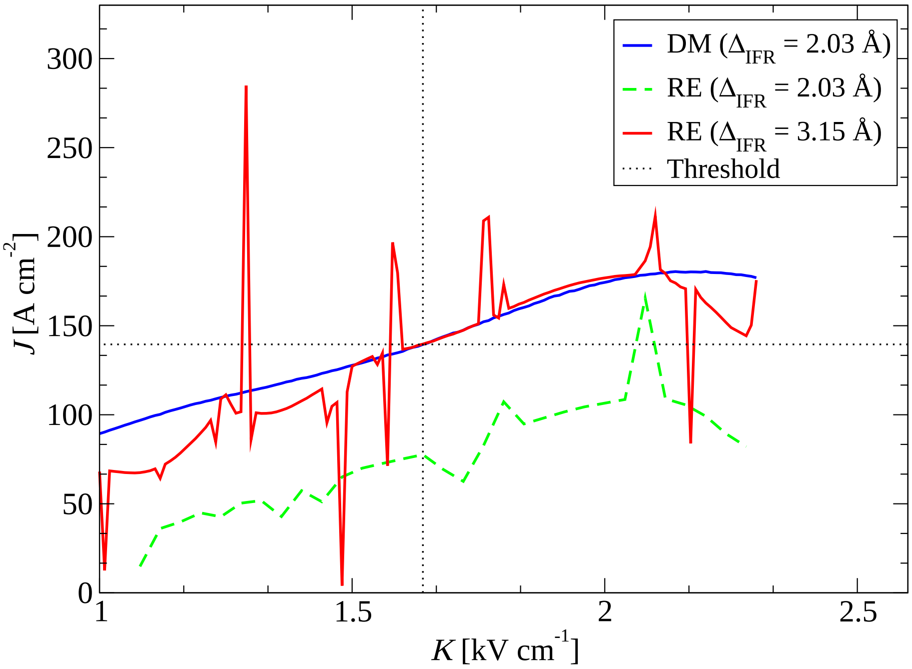

Figure 4.5: Current density versus electric field from RE (red) and DM model (blue). Results were fitted to threshold point at $(K_t, J_t) = (1.64\ \text{kV/cm}, 139.5\ \text{A cm}^{-2})$. RE model requires $\Delta'_{\text{IFR}} = 3.15$ Å for threshold fit, while DM needs $\Delta_{\text{IFR}} = 2.03$ Å. Results for $\Delta'_{\text{IFR}} = 2.03$ Å for RE model are also displayed (dashed green).

The RE simulation has been initially performed with the identical IFR parameters as those used in Fig. 4.4, however the results yielded much lower current density (and a higher material gain) than the DM simulation, as depicted in Fig. 4.5 by the dashed green line. A match between the two models can be obtained by using $\Delta_{\text{IFR}} = 3.15$ Å. Note that both DM and RE models predict the lasing frequency correctly, as shown in Fig. 4.6

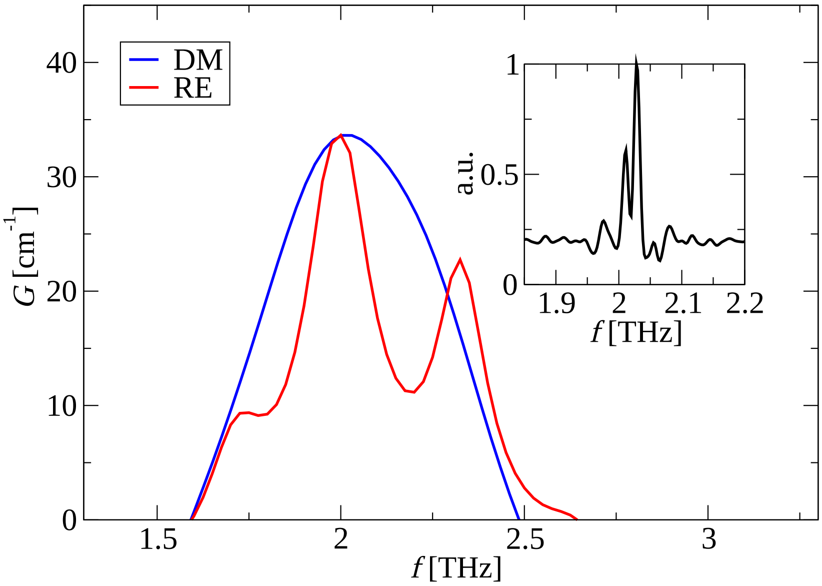

Figure 4.6: Gain versus frequency from RE (red) and DM model (blue). Results were fitted to losses of 33.56 cm^{-1} at threshold point $(K_{\mathrm{t}}, J_{\mathrm{t}}) = (1.64\,\mathrm{kV\,cm^{-1}}, 139.5\,\mathrm{A\,cm^{-2}})$ at 20 K. Inset shows experimental spectral measurement at 20K at threshold bias.

This difference between fitting parameters occurred due to differences between RE and DM models. RE and DM models do not use the same wavefunctions as basis for the transport model and intermodule transport is modelled differently, although the current density does link two models as shown in (3.32) in section 3.9. RE model uses extended wavefunctions by solving Schrödinger-Poisson equation on two QCL periods, while DM uses the basis on one period under tight-binding approximation. The occurrence of non physical spikes in RE output is a known issue, occurring due to the lack of coherent effects in the RE model setup. During the tunnelling through the injection barrier, two states at resonance are split by the anti-crossing energy (<1 meV) where wave packet oscillated through the barrier at Rabi frequency [81]. DM model directly implements this coherent effect as discussed in Eq. (3.3) while RE model assumes that these nearly aligned states perform identical transport as any two other states under consideration, which forms a discontinuity in scattering rate. In simpler terms, RE model assumes instantaneous transport through the injection barrier, while DM model provides finite coherent time needed for carriers to tunnel through.

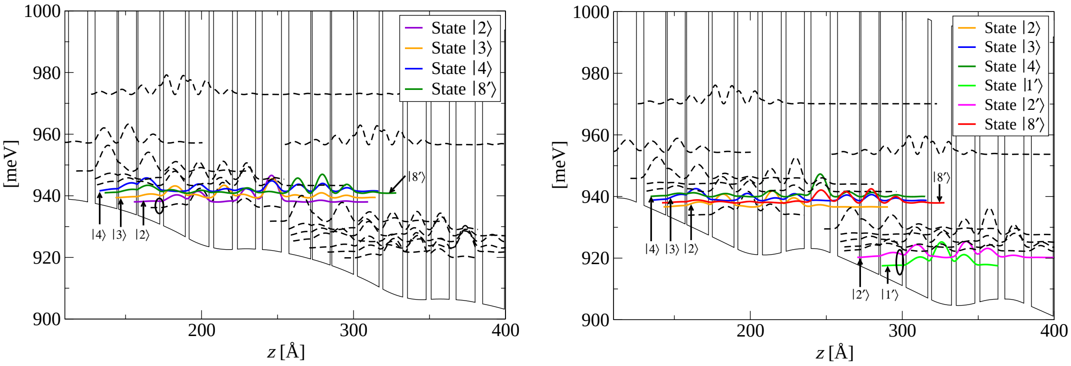

a) b)

Figure 4.7: Band diagram and the corresponding wavefunctions at a) $K = 1.28\,\mathrm{kV\,cm^{-1}}$ (non-spike point) and b) $K = 1.29\,\mathrm{kV\,cm^{-1}}$ (spike point). States of interest are labeled as $|i\rangle$ if they belong in the left period and $|i'\rangle$ if they belong in the adjacent period to the right. Circles indicate the change of the second state in the spike point.

In order to closely examine what happens around a spike, we will focus around the point $K = 1.3\,\frac{\mathrm{kV}}{\mathrm{cm}}$ in Fig. 4.5. In Fig. 4.7 we present band diagram and the corresponding wavefunctions moduli at a non-spike point $K = 1.28\,\frac{\mathrm{kV}}{\mathrm{cm}}$ and at the spike point $K = 1.29\,\frac{\mathrm{kV}}{\mathrm{cm}}$. In the left figure, we can see that the fourth state from the left period $|4\rangle$ is nearly aligned with the 8th state $|8'\rangle$ from the adjacent period at $K = 1.28\,\frac{\mathrm{kV}}{\mathrm{cm}}$. At $K = 1.29\,\frac{\mathrm{kV}}{\mathrm{cm}}$ (on the second figure) position of the states has changed. State $|8'\rangle$ is now nearly aligned with the state $|2\rangle$ however compared to the situation at $K = 1.28\,\frac{\mathrm{kV}}{\mathrm{cm}}$ it seems that the state $|2\rangle$ does not exist at $K = 1.29\,\frac{\mathrm{kV}}{\mathrm{cm}}$ (indicated by circles).

Effectively, state $|8'\rangle$ from the second period before resonance became state $|4\rangle$ in the first period after resonance, this then caused the shift of states when two figures are compared ($|8'\rangle_a \rightarrow |4\rangle_b$, $|4\rangle_a \rightarrow |3\rangle_b$ and $|3\rangle_a \rightarrow |2\rangle_b$, changes are purposely colored the same in Fig. 4.7a,b). This observation occurs at every spike present in Fig. 4.5 and it depicts that RE model predicts non physical high currents due to instantaneous non-local transport for spatially separated resonances, which has detrimental effects in the electron transport. Note that depending on the resolution of electric field points in the simulation, more spikes would occur due to a higher probability of producing state alignment (it is also possible to have multiple anticrossings at one bias point).

The DM model does not suffer from such a behaviour and it is required for QCL study. However DM model is applied under tight binding approximation at the period ends. The layer structure needs to be provided from the injection barrier (as in Fig. 4.1) otherwise localisation of the states within the module would be affected differently. RE model can still provide useful information during the design of novel structures because it would be able to display extended wavefunction and the effect of the injection barrier by not forcing the wavefunctions to attenuate rapidly as in DM model.

4.3 Electron-Electron scattering

Electron-electron scattering is often neglected due to its numerical complexity and the ambiguity of the model itself. As discussed in 2.9 this mechanism is a Columbic interaction involving four electrons. The many-body effect and generation of a two–electron wavefunction from single–electron ones is a rough approximation and the entire model is further distorted by neglecting non-parabolicity of the subbands and adding phenomenological screening effect.

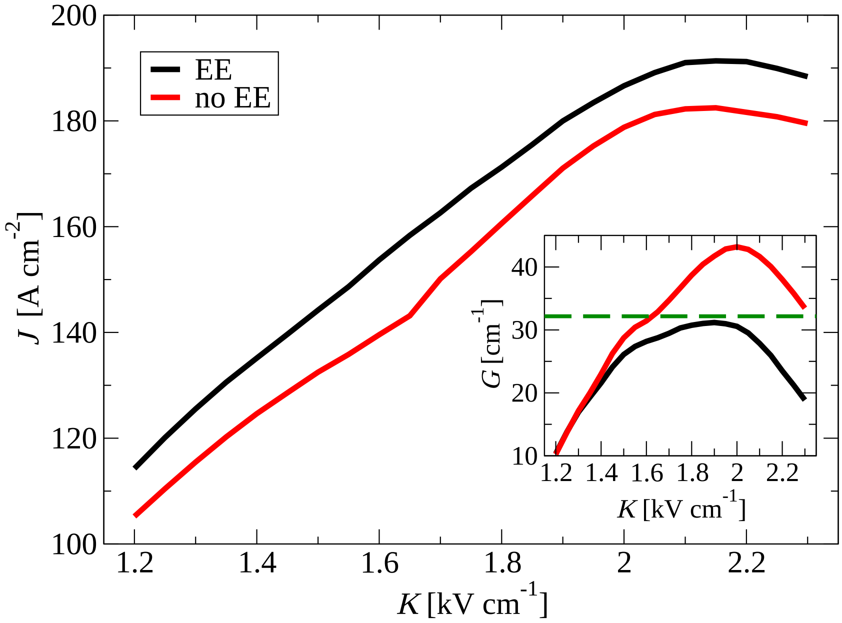

Figure 4.8: Current density versus applied bias with inclusion of EE (black line) and without EE (red line) scattering. Inset shows the material gain. Dashed green line depicts the threshold.

The main justification for neglecting EE mechanism is very wide fitting range of IFR mechanism shown in Fig. 4.2. In most cases, EE scattering has more detrimental effect on the material gain, rather than on the current density, as shown in Fig. 4.8. Fitting the data to the experiment with the inclusion of EE mechanism would need different IFR parameters ($\Delta_{\mathrm{IFR}} = 1.5$ Å, $\Lambda_{\mathrm{IFR}} = 100$ Å) and the simulation time would be greatly extended.

In author's publication in [74] the fitting procedure discussed in the previous sections did provide good results at 20 K in pulsed operation and EE scattering was not considered. On the other hand, some QCL designs, like [145] cannot be well matched with the experiment even when fitting $L - I - V$ at a single temperature in pulsed operation, which will be further discussed in the next section.

4.4 Temperature dependence

Thermal performance of QCL is mainly limited by thermalisation of subbands at high temperatures, especially due to LO-phonon scattering process. The BTC QCLs cannot achieve high temperature performance due to the narrow cluster of states which undergo multiple absorption transitions that degrade the population inversion. LO-phonon assisted designs can improve the temperature performance, which led to the pulsed operation up to 210 K [36].

The electrical heating in pulsed operation should not be the main limiting factor and it is often neglected in modelling. This means that fitting parameters obtained for one temperature should be applicable for the entire $L-I-V$ characterisation in pulsed operation for all heat sink temperatures. However, several issues arise with fitting the temperature dependence of the current:

- Sensitivity of the model and stiffness of conversion of the current density to current. Slight variation of the model output (the current density) is expected from the model, however, to obtain the current, this value needs to be multiplied by a surface of QCL cross-section (usually 150 μm$\times$2000 μm). This creates bigger variation while fitting the results.

- Modal loss (threshold gain) is dependent both on the current and frequency. The one-dimensional model [65] that is used introduces the additional variation of the model output values. Note that the transport model is highly sensitive on the value of the threshold gain which can also be observed in the inset in Fig. 4.8.

- The electron temperature discussed in 2.10 has the main effect on the temperature dependence of the transport model. The issue with the approach given in Eq. (2.33) is that the self-self-consistent algorithm seeks unique electron temperature of all the subbands involved in the transport model. Physically, this is not fully correct, since the QCL is non-equilibrium device where lasing subbands may have different electron temperatures [146, 147, 148, 37, 149] and this may be more apparent in LO-phonon structures rather than BTC design [149]. The temperature obtained by

Eq. (2.33) satisfies the energy conservation law, however transport characteristics would represent an average result. Additionally, the EE scattering mechanism does not affect the electron temperature mainly because it is very challenging (and debatable) to model the kinetic energy balance similar to Eq. (2.30) for a four electron process.

- IFR scattering parameters are most commonly employed as a fitting tool. The fitting approach discussed in 4.2.1 only seeks a pair of IFR parameters value that match a single point (or two) of interest, however it is clear from Fig. (4.2) that multiple pairs may exist, and that the fitting approach may need to be altered in order to find IFR parameters able to match the full experimental $L-I-V$ output.
- Electrical heating of the device is also present in the pulsed operation. Although this effect is very small, introducing a rough approximation to the lattice temperature $\approx R_{\mathrm{TH}} d_c I V$ (R_{TH} - heating resistance, d_c - duty cycle) may provide better results due to high sensitivity of the model.
- The transport model uses electric bias as an input and displays very high sensitivity to its variation. The numerical implementation of the overall model is already parallelising the simulations for different bias values, and reducing the bias step is not numerically feasible. For this reason it is often challenging to fit the model at the threshold current, even at single heat sink temperature. Additionally, the optical power is calculated through minimisation algorithm that exploits the gain saturation effect, however this approach assumes that the optical electric field is purely real in order to avoid a two-dimensional minimisation implementation. The dynamical model considers both real and imaginary part of the optical electric field and may provide a better result and display the transient around the threshold. This will be further discussed in the Chapter 7.

4.4.1 Pulsed operation

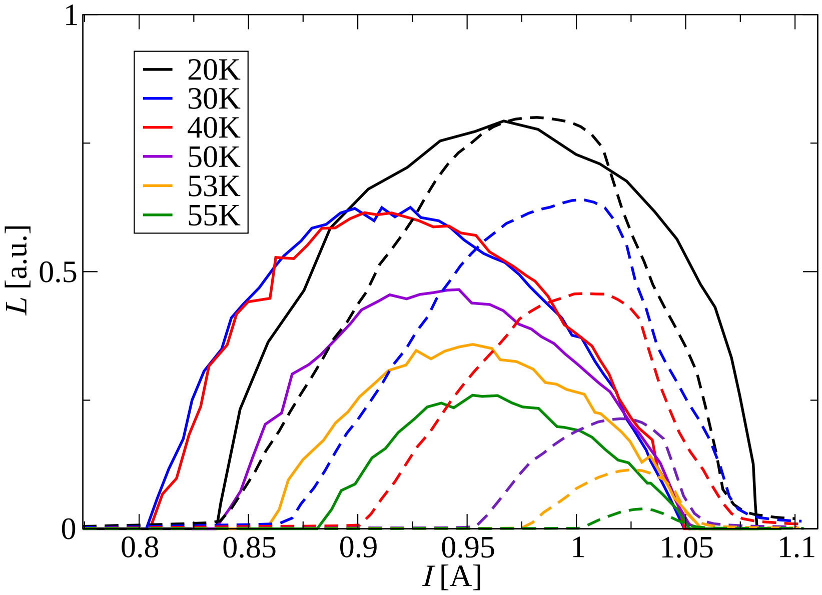

Figure 4.9: $I - L$ characteristics for different heat sink temperatures. Full lines represent simulation results, while dashed lines represent the experimental measurements. Scaling was performed so that the peak ratio is consistent in both results. Dependence of cavity loss on temperature in accordance with [45, 87] has been included.

Figure 4.9 shows somewhat poor agreement with the experimental measurements (apart from the fitted $I - L$ dependence at 20K) when the temperature is varied [74]. The main issues in Fig. 4.9 are that the threshold current dependence shows unexpected behaviour (reduction with the increase of temperature), the dynamic ranges at higher temperatures are greatly overestimated and the optical power decrease with the temperature is underestimated. To rectify these issues, we will focus on value of current $I = 1.01$ A and address some of the previously discussed potential reasons for non ideal result. Several techniques may be applied to the model for potential improvement. It was noticed that the threshold gain is reduced with the temperature increase in model [45, 87]. Since the model is highly sensitive to this value, one approach is to use fixed value of the threshold gain that was used to obtain the initial fit at 20 K. Additionally, some electrical heating is present at pulsed operation, and adding an increase of the temperature by $R_{\mathrm{TH}} d_{\mathrm{c}} I V$ may provide improvement.

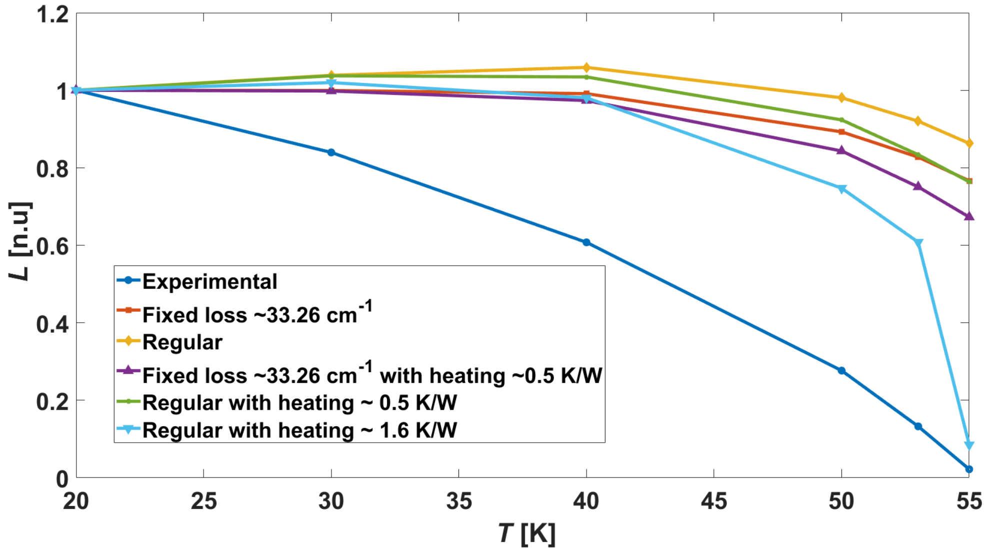

Figure 4.10: Optical power dependence on temperature shown as relative ratio to the value at 20 K at current $I = 1.01$ A. Only 6 temperatures were used in the experiment, thus full lines only serve for illustration, markers show the correct behaviour.

Figure 4.10 displays that using a fixed value of loss provides some improvement, however, as estimated in [74] the electrical heating has a more significant effect. The improved $I - L$ temperature dependence that corresponds to heating of ~ 2 K/W is presented in Fig. 4.11.

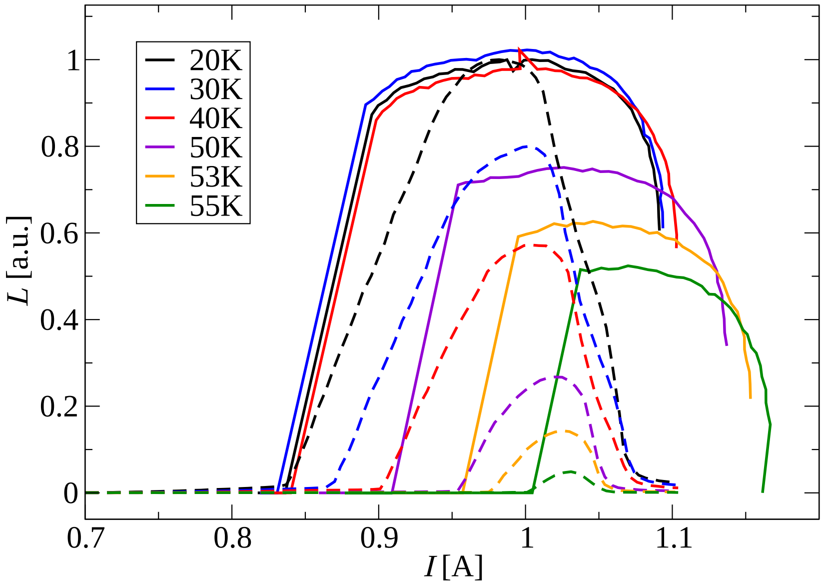

Figure 4.11: $I - L$ characteristics for different heat sink temperatures with added electrical heating $R_{\mathrm{TH}} d_{\mathrm{c}} IV = 1.6$ [K/W] $\times\, IV$. Full lines represent simulations result, while dashed lines represent the experimental measurements. Scaling was performed so that the peak ratio is consistent in both results (amplitude of each curve has been divided by peak value of $I - L$ dependence at 20K).

The added electrical heating in Fig. 4.11 has provided only slight improvement in comparison to the results in Fig. 4.9. Although seemingly the threshold current is well matched at 20 K and 55 K, the transient around the threshold current is too steep and its discussion is not fully valid. The main improvement is in relative ratio of the optical power amplitudes presented in Fig. 4.10, however results for 20,30, and 40 K are very similar, which is not correct. Additionally the dynamic range is still greatly overestimated at higher temperatures.

To analyse the reason for such behaviour, we shall focus on temperature dependence of the model output at single bias point rather than interpolating the results as in Fig. 4.10.

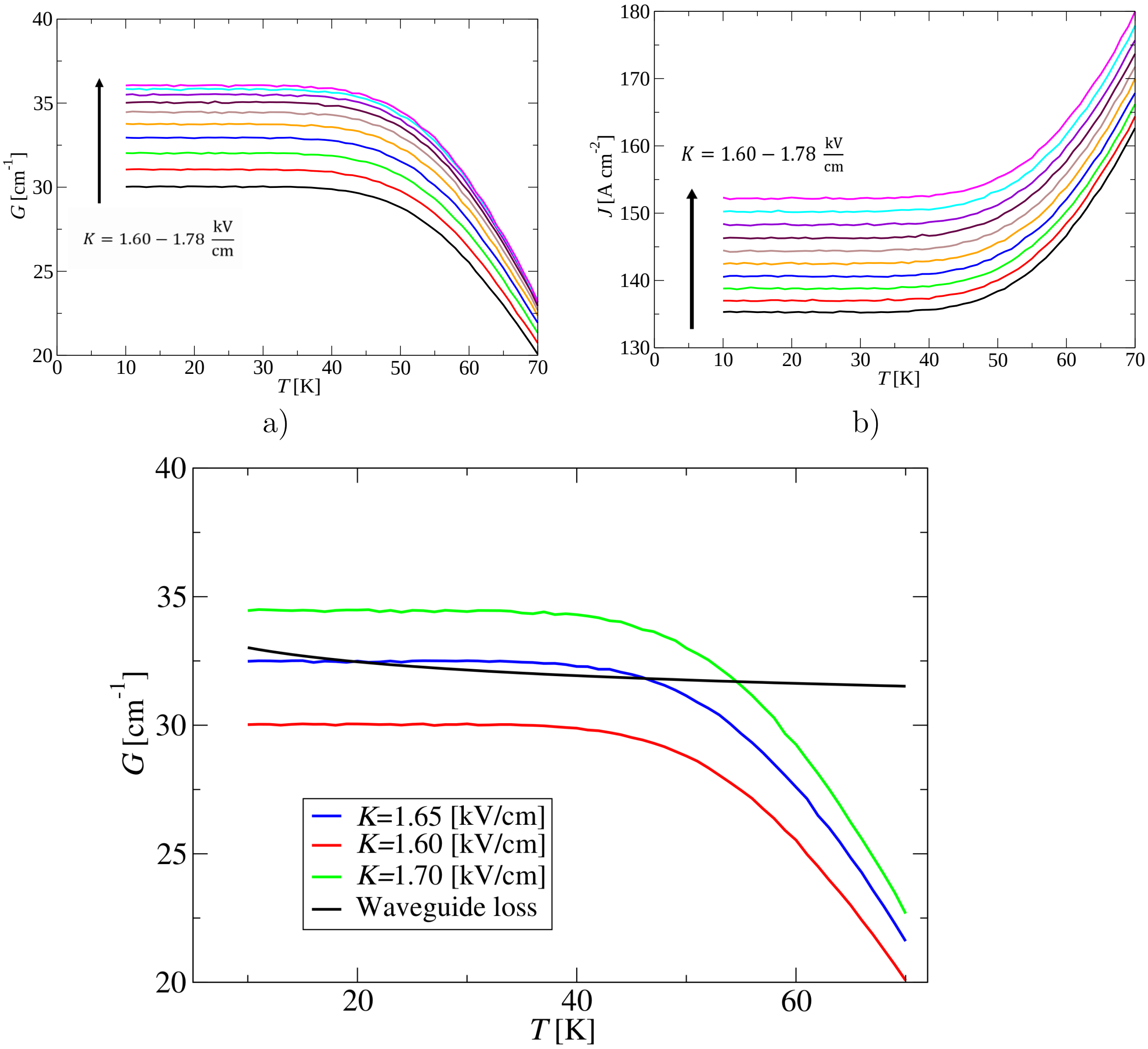

a) b)

c)

Figure 4.12: a) Material gain and b) current density dependence on temperature for multiple value of electric bias. c) Material gain dependence on temperature for electric bias points around the threshold. Black solid line represents the threshold gain determined by the model in [45, 87]

Figure 4.12 displays the expected converse effect between the current density and material gain with the variation of temperature. The dependencies are constant for wide range of temperatures. This causes very similar $I-L$ dependencies in the temperature range 10 - 40 K. The main reason why the threshold current was dropping with the increase of temperature in Fig. 4.9 is the slight drop of the threshold gain in Fig. 4.12c) with temperature (which also illustrates the model's high sensitivity). The temperature behaviour in Fig. 4.12 is mainly determined by the scattering mechanisms included in the transport model, mainly the LO-phonon process. Note that all these processes have been averaged over Fermi-Dirac distribution (as in Eq. 2.10) at single electron temperature as discussed in 2.10. Although such approach significantly simplifies the model and improves its performance, this simplification disables the overall model to correctly predict the experimental temperature behaviour.

4.4.2 CW operation

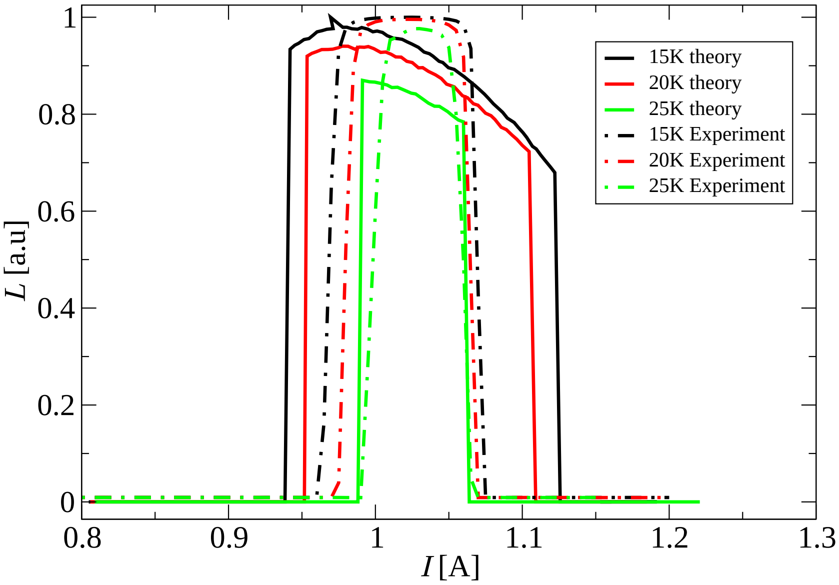

Figure 4.13: $I-L$ characteristics for different heat sink temperatures in CW operation. Full lines represent simulation results, while dashed lines represent the experimental measurements. Scaling was performed so that the peak ratio is consistent in both results.

Figure 4.13 shows the fitting results for CW operation. Fitting was performed to match the experimental dynamic range at 25 K. The novel fitting parameter that was introduced was the thermal constant $R_{\text{TH}} = 9.6\ K/W$. The only difference to the result in Fig. 4.9 was adding increase of the operating temperature in the form $T = T_{\text{cf}} + R_{\text{TH}}IV$, where T_{cf} is the cold finger temperature. Similarly as in Fig. 4.9 and 4.11 there is a considerable difference between the theoretical and experimental results for different cold finger temperatures (apart the one that the model was fitted to). The model is more sensitive and harder to fit when electrical heating is considered, as the electrical power of the device varies in a wide range while bias is being swept. The main issue is that the contact resistance which increases the voltage also affects the fitting procedure, making this a two dimensional fitting challenge. Overall, the observations are consistent with the previous discussion that the model is not fully able match the temperature behaviour with the linear electric heating approximation. Possible improvement of the temperature fitting procedure, is to allow different R_{TH} values at different cold finger temperatures, as modelled in [87, 86], however note that the disparity in temperature dependence of QCL output characteristics occurs due to multitude of approximation involved in the model. Additionally, the overall model for CW operation is highly approximative, as it is experimentally (and physically) known that QCL periods are not exposed to the same operating conditions [150].

4.5 Temperature optimisation

Interestingly, this model is capable of predicting the maximum operating temperature of QCL device. The behaviour similar to Fig. 4.12 has been observed within multiple THz QCL designs even without the IFR parameter fitting. Knowing that the threshold gain for most surface plasmon waveguides is $40 - 60$ cm^{-1} and for most metal-metal waveguides $20 - 30$ cm^{-1}, it is possible to predict the maximum operation temperature of the device. This enables using this model for design optimisation. Simulations of several exemplary structures are presented in Fig. 4.14.

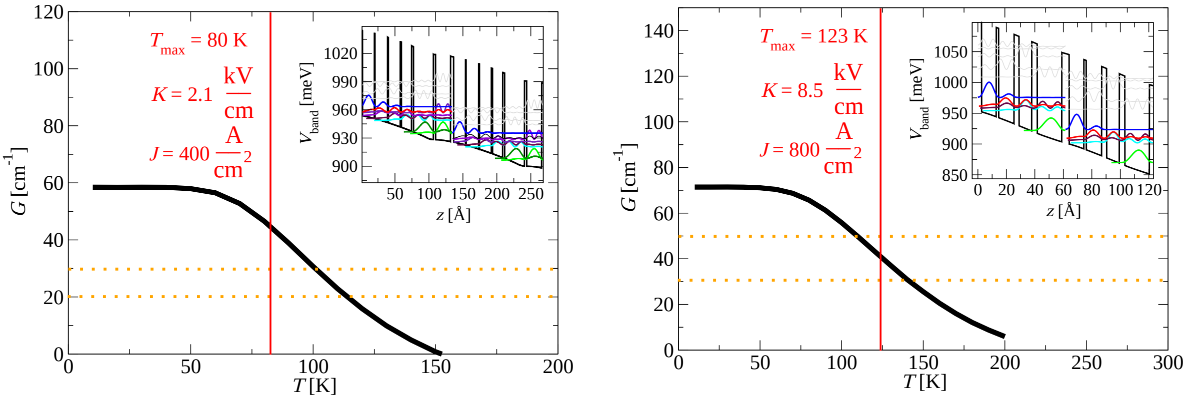

a) 1.2 THz BTC QCL [33]

b) 3.4 THz Hybrid QCL [53]

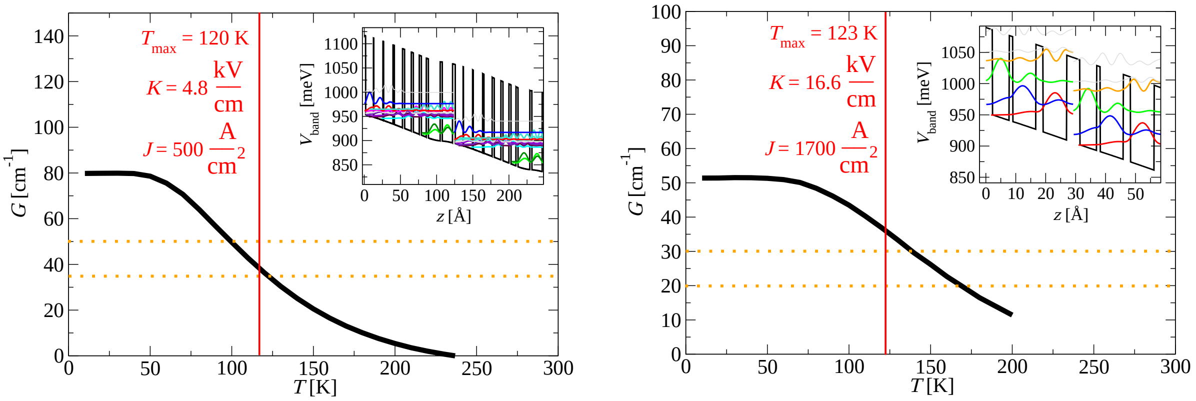

c) 3.5 THz Hybrid QCL [151]

d) 3.3 THz scattering assisted QCL [49]

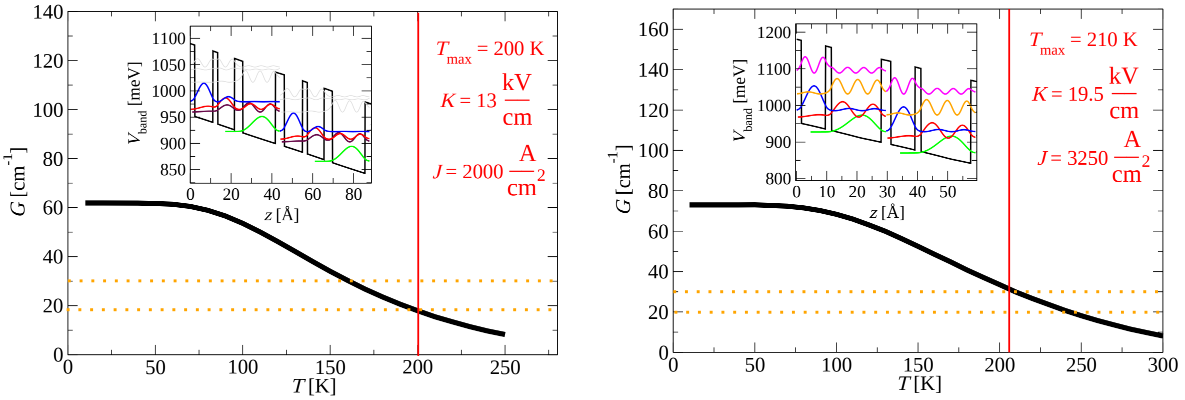

e) 3 THz LO-phonon QCL [47]

f) 3.9 THz LO-phonon QCL [36]

Figure 4.14: Material gain dependence on temperature for several QCL designs at their respective resonant bias. a) The lowest frequency THz QCL [33], b) The highest power THz QCL (> 1 W, fabricated in Leeds) [53], c) Hybrid THz QCL [151] (it displays very wide dynamic range, suitable for self-mixing interferometry applications), d) Scattering - assisted QCL (designed and fabricated in Leeds) [49],

Figure 4.14: e) Former high operating temperature record THz QCL (200 K) [47], f) The highest temperature THz QCL (210 K) [36]. The vertical red line displays experimental cut-off temperature, while orange lines roughly display the region of expected modal loss. Structures a), d), e) and f) were fabricated with metal-metal waveguide, structures b) and c) used surface-plasmon waveguide. Insets show the layer sequence with wavefunction moduli.

The 1.2 THz structure seemingly does not match with the model prediction in Fig. 4.14. However, the threshold gain in [33] was estimated around 20 cm^{-1} which is highly unlikely for such low frequency. The waveguide loss study in [152] indicates that the value should be around $40-50$ cm^{-1} in this frequency range making the prediction in Fig. 4.14 very good.

For QCLs that operate around 3.5 THz, the modal loss in metal-metal waveguide is usually around 20 cm^{-1}, and some results in Fig. 4.14 do overestimate the cut-off temperature. However, when electrical heating is taken into account, even though only pulsed operation is being considered, the model predicts the cut off temperature remarkably well, given the fact that no IFR scattering parameters were varied to fit any of the results in Fig. 4.14. Simulations were performed with $\Delta_{\mathrm{IFR}} = 1$ Å, $\Lambda_{\mathrm{IFR}} = 80$ Å and EE scattering was not considered. To account for the electrical heating, it is convenient to express electrical power by scaling the units as:

$$P_{\mathrm{e}} = J\ [\frac{\mathrm{kA}}{\mathrm{cm}^2}] \times K\ [\frac{\mathrm{kV}}{\mathrm{cm}}] \times V_{\mathrm{QCL}}\ [\mu\mathrm{m}^2\ \mathrm{m}] = H_{\mathrm{F}} \times V_{\mathrm{QCL}}\ [\mu\mathrm{m}^2\ \mathrm{m}] \tag{4.1}$$

The heating factor H_{F} in Eq. (4.1) determined simply by the product of the current density and electric bias in such units can provide a rough estimate for the electrical heating effect in pulsed operation. The heating factors that correspond to the designs in Fig. 4.14 at the cut-off temperatures are: a) 0.84, b) 6.8, c) 2.4, d) 28.22, e) 26 and f) 63.375 $[\frac{\mathrm{kA}\times\mathrm{kV}}{\mathrm{cm}^3}]$. If the common fabrication dimensions are used as $15 \times 200 \times 0.002$ $[\mu\mathrm{m}^2 \times \mathrm{m}] \approx 6$ $[\mu\mathrm{m}^2 \times \mathrm{m}]$ and assuming a 2% duty cycle and thermal constant $R_{\mathrm{TH}} = 7$ K/W, the linear electric heating approximation in form $R_{\mathrm{TH}} d_{\mathrm{c}} P_{\mathrm{e}}$ for these designs would be $0.84 \times H_{\mathrm{F}}[K]$. This clearly shifts the model predictions nearly ideally at 20 cm^{-1} loss limit in Fig. 4.14 for designs d) - f) (apart for the design in subfigure e) because this operating temperature was achieved by very large dimensions of the structure in [47] which results in the lower thermal constant). Note that these values were taken arbitrarily, and studying each of the designs individually would show that the model predicts the cut off temperature remarkably well. However, for any optimisation purposes, a 10-20% tolerance is expected. The rule of thumb is to expect heating proportional to $0.5 - 0.9 \times H_\mathrm{F}$ (or directly as $1 \times H_\mathrm{F}$ which overestimates the effect, however would pose as a very strict optimisation condition).

A novel THz QCL design for the high temperature operation will be discussed in Chapter 8 where the temperature performance estimation presented here will be exploited in determining the layer sequences that generate the desired structure.

Chapter 5

Acoustic phonon pulse modulation of THz QCL

High speed modulation of laser sources is essential for a variety of applications. This chapter will discuss a novel state-of-the-art modulation scheme that employs electron-phonon interaction and perturbs the QCL operation by a propagating deformation potential wave induced by an acoustic wave. Most of modulation schemes for QCLs are electronic and are limited by parasitic device impedance enabling modulation up to 35 GHz. Theoretically, QCLs do not exhibit relaxation oscillations and may be modulated over 100 GHz. This modulation scheme shows potential for such high speed performance and was studied in a collaboration with an experimental group at University of Nottingham. The chapter focuses on theoretical modelling of this effect developed by the author and then used as theoretical support to explain experimental results in a recent joint publication (accepted) [107] with experimental teams in Leeds and Nottingham University.

5.1 Acoustic phonon effect in semiconductor superlattice

The acoustic phonon generation in semiconductor superlattice was first demonstrated in pump-probe experiment in [153]. The similarity between light and sound propagation equations [154] has generated applications of using a superlattice as a reflective mirror for phonons. Acoustic phonons in semiconductor structures describe mechanical atomic vibrations that are in phase. The theory presented in section 2.8 describes acoustic phonon vibrations for bulk semiconductors, which is not fully accurate for superlattice structures, however would be acceptable for carrier transport. It is possible to additionally perturb these atomic vibrations (and therefore the material strain) by additionally heating the device by an external laser pump [155]. This perturbs the deformation potential that is a consequence of acoustic phonons.

A simple way of generating acoustic phonon wave is by heating a thin metallic film bonded to a semiconductor material. Detailed explanation can be found in [156, 157, 158]. The metallic film irradiated by a femtosecond laser pulse absorbs the energy E_f which causes the temperature rise [159, 160]:

$$\Delta T(z) = -\frac{1-R_\mathrm{f}}{c_\mathrm{f} A z'} E_\mathrm{f} \cdot \exp\left(-\frac{z}{z'}\right) \tag{5.1}$$

where R_f is the reflection coefficient of the film, c_f is the specific heat capacity (per unit volume), z is the film growth direction, z' is the absorption depth of the film and A is area of the irradiated spot on the film. This temperature change causes linearly proportional isotropic stress [161] which initiates longitudinal acoustic waves within the film. After multiple reflections of this wave, strain signal that leaves the film has bipolar nature. Note that generated strain signal is not directly proportional to the energy transferred by the laser to the film due to electron diffusion effects, which broadens the profile of the bipolar acoustic signal [162, 161].

The detailed parametric formula for the strain signal can be found in [161]. In this thesis, this signal will be modelled as Gaussian derivative function in time and space. The propagation of this strain signal throughout a superlattice causes acoustic phonon vibrations that modulate sequential tunnelling between wells and barriers. Nominally, this causes domain formation as the signal propagates, however it can be modelled by an effective electric field model [163] by performing pulsed irradiation of the metallic film.

A detailed theoretical and experimental review of pump-probe technique for acoustic phonon generation in GaAs/AlGaAs superlattice can be found in [161].

5.2 Acoustic phonon modulation effect in THz QCL

A QCL structure is optically active superlattice and acoustic phonon effect may serve as a very fast optical modulation scheme. The voltage modulating properties of this effect have been previously demonstrated in resonant tunnelling diode [164, 165] and weekly coupled superlattice structures [161]. The joint research with Nottingham University has demonstrated this effect for the first time in THz QCL structures [107].

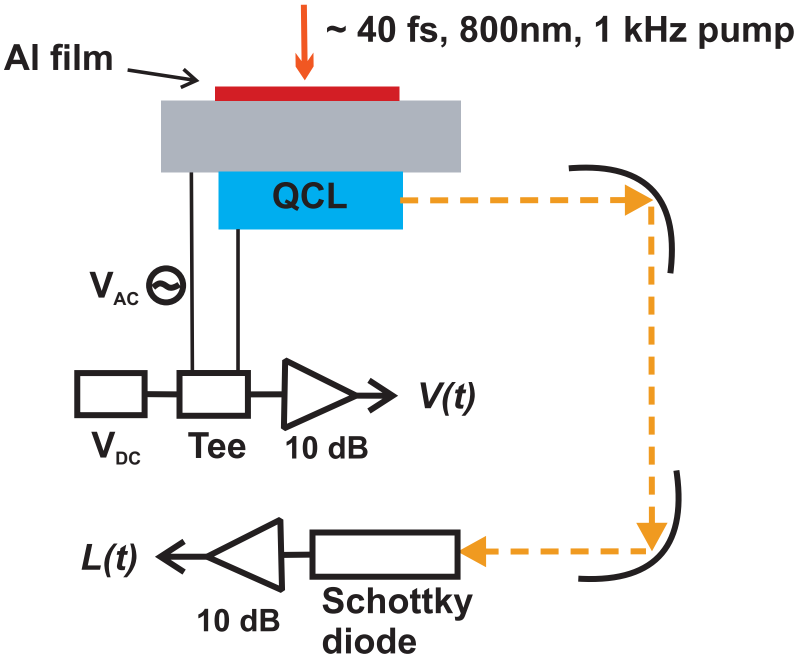

Figure 5.1: Experiment setup. Ridge of QCL device (blue) is grown on GaAs substrate (gray) mounted on cold finger at temperature (not shown) of 10K. The bottom of substrate is covered by thin Al transducer film that is pumped by external 800 nm femtosecond pulses. QCL device is operating in pulsed operation and driven by 5% duty cycle voltage source, connected to bias tee. Voltage difference and optical power are measured by two 10 dB lock in amplifiers.

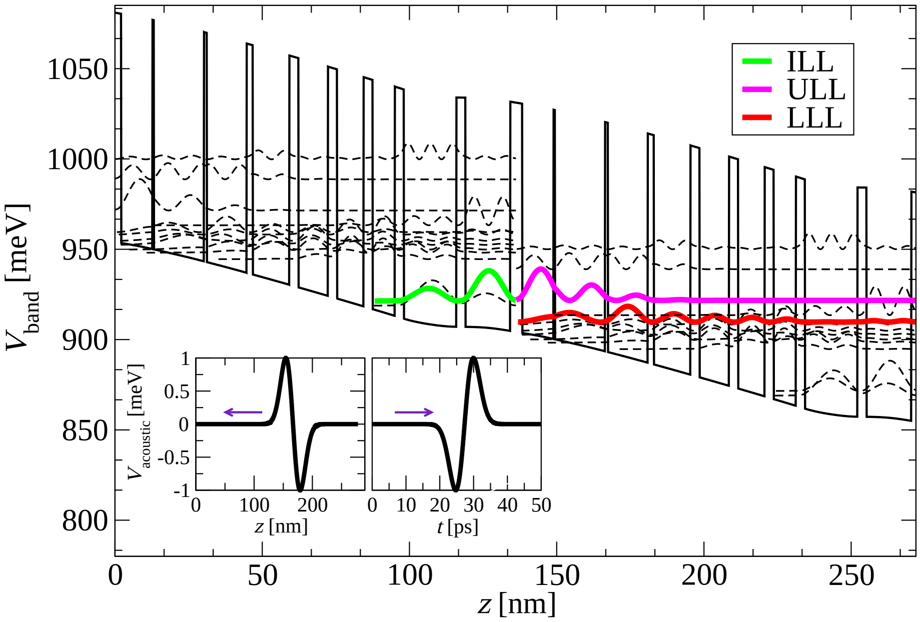

Figure 5.2: Layer thicknesses for the analysed hybrid QCL design, starting with the injection barrier, are **4.1**/10.6/**0.5**/17.0/**1.0**/13.5/**2.1**/12.4/**3.1**/10.0/**3.1**/9.0/**3.1**/75/**3.1**/*17.8*/**3.1**/15.2 nm, $\mathrm{Al_{0.14}Ga_{0.86}As}$ barriers are shown in bold and the well doped to $3.2 \cdot 10^{16}$ cm^{-3} is underlined. Two periods are shown at the resonance bias $K = 3.63\ \frac{\mathrm{kV}}{\mathrm{cm}}$ along with the corresponding wavefunctions moduli squared. Insets show spatial and temporal form of approximated strain wave that is propagating throughout all periods of QCL structure.

The experimental setup presented in Fig. 5.1 uses a 2.7 THz QCL based on hybrid design [145] whose layer structure is shown in Fig. 5.2. The QCL active region consists of 88 periods grown on semi-insulating GaAs substrate, processed into surface-plasmon waveguide of 150 μm width and 2 mm cavity length. The substrate was additionally cleaved for the thermal dissipation effect to take place, and a thin (100 nm) Al acoustic transducer film was deposited at the back of the substrate. In order to generate acoustic pulses, the experiment needed to be conducted at low temperature (15 K) due to acoustic transparency of the material. A femtosecond Ti:Sapphire laser was run under pulsed operation, generating 40 fs pulses aimed at the transducer film. Note that the bottom of the substrate in Fig. 5.1 is at cold finger, however a small aperture was made, to allow irradiation by the femtosecond pump. The QCL device was also driven in pulsed operation with 50 μm voltage pulses with synchronised repetition rate as the femtosecond pump. Measurement of voltage change were procured by a microwave (14 GHz bandwidth) bias tee and 10 dB lock in amplifier, while optical power was measured by Schottky diode and the amplifier. The experimental measurement at three voltage points of interest[1] is presented in Fig. (5.3).

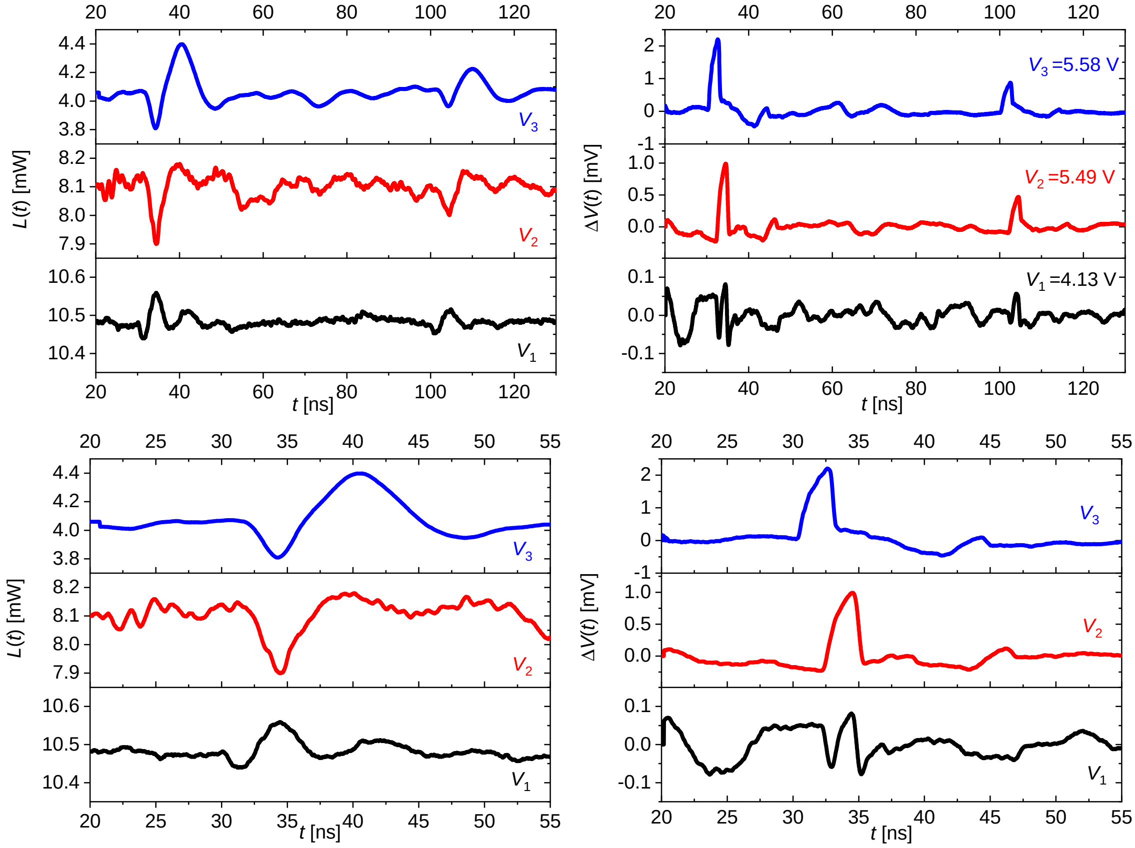

a) Measured optical power

b) Measured voltage difference

Figure 5.3: Experimental results for measured optical power and voltage difference. Figures at the bottom are are expanded around the first echo of the acoustic signal from the figures at the top. Voltage V_1 corresponds to the voltage point on the rising part of optical power dependence, while V_2, V_3 ($V_3 > V_2$) correspond to the falling part.

Figure (5.3) shows the time dependence of the observed signal. In both the

---

[1] Courtesy of Dr. Aniela Dunn (Univerity of Leeds) and Prof. Anthony Kent (University of Nottingham)

voltage and the optical power measurement, two echoes can be noticed on a timescale needed for the acoustic pulse to propagate through the structure. The first response occurs 32 ns after the pump excitation, which corresponds to the time needed for the acoustic pulse to travel through the substrate at 4800 ms^{-1} speed of longitudinal sound propagation. The subsequent echoes are observed every 70 ns (only the second echo is shown in Fig. 5.3) due to multiple reflections of the acoustic wave across the entire structure. Several observations can be made from Fig. (5.3):

1. Time needed for the acoustic pulse to travel through the entire stack of QCL is ~6 ns and time for the signal to reach the top contact is ~38 ns. The signal, however only shows the response during the propagation of the signal in one direction ("forward") and the second response is observable at ~70 ns. This indicates that the acoustic signal only affected the transport when propagating towards the top contact.
2. Voltage difference measurement always resulted in an increase of voltage, regardless which portion of $L-I-V$ dependence was modulated.
3. Optical power measurement has bipolar nature and it switches polarity depending on whether modulation is done on the rising (at voltage V_1) or falling portion (at voltage V_2, V_3) of $L-I-V$ dependence.
4. At the peak of the $L-I-V$ dependence the response could not be distinguished from the noise (not shown in Fig. 5.3).

The lack of signal at the peak of the optical power dependence on current and signal polarity behaviour of the measurement can, in principle, be explained through standard electric modulation approach. Assuming that the acoustic wave perturbs the voltage as bipolar dependence, the mostly linear $I-V$ dependence of QCL device would mostly replicate the modulation signal. Since $I-L$ dependence changes its linearity after the peak, the measured signal would change polarity and there would be no signal at the peak (due to its "flatness"). Additionally, the response would be stronger at voltage point that is located on sharper slope of $L-I-V$ dependence. It is possible to employ this modulation approach and provide a quantification of the effect, as it was done in the theoretical section in [107], showing sound agreement with the measurement data. For an in-depth understanding of this effect in THz QCL, a model that describes quantum mechanical nature of QCL needs to be applied. All the observations above can be qualitatively explained through the time dependent perturbation theory, while a quantitative model would be very challenging.

The observed modulation depth $\Delta L/L$ is around 6%. The voltage and optical power signal observation were limited by parasitic impedance (rise time of $\sim$ 800 ps) and Schottkey detector response. Theoretically, the transient time of this mechanism is determined by signal propagation through QCL structure, thus higher modulation frequency would be attainable with thinner QCL active regions or generating the acoustic wave on several selected QCL periods. It could be also feasible to employ the acoustic perturbation on all QCL periods by setting an acoustic standing wave (i.e by putting acoustic Bragg mirrors) on the device, which would generate a stronger modulation depth. The main challenge in realising higher speed is the $\approx$ 32 ns needed for the strain signal to propagate through the substrate and reach the active region of the QCL structure. This limit may be averted by sending a train of narrow spaced strain pulses. A narrow spaced train of strain pulses may deteriorate due to interference or may behave as one collective heating signal that does not alternate. The QCL dynamics is on picosecond scale and it is also unknown how would a perturbation on similar timescale affect the overall behaviour and more experimentation is needed.

5.3 Time dependent perturbation theory

The propagating acoustic wave effect may be viewed as additional perturbation to the deformation potential D_{ac} in section 2.8, however its effect conversely has more significance on transport than ACP scattering mechanism itself. Modelling this effect in THz QCL is very challenging. It is estimated that bipolar strain has an amplitude of 0.1 - 1 meV and temporal width of 15 - 20 ps as presented in the inset in Fig. 5.2. The amplitude of the signal is much smaller than the subband energy making this signal suitable for perturbation theory, however the timescale is similar to subband lifetime, and propagation of the signal affects periods sequentially. The latter issue prevents feasible quantization of this effect, because the periodical foundation of QCL modelling would be broken and formation of the electric bias domains is a certainty.

The general time dependent perturbation theory (TDP) presented in Chapter 2.3 may therefore be used to explain only qualitatively the consequences of the acoustic signal propagation. The TDP theory provides interaction probabilities by determining wavefunction interaction corrections in Eq. (2.6). These expressions resemble Fourier transformation, however their values would be largest when energies are aligned ($\omega_{fi} = 0$). This means that the second correction in Eq. (2.6) must be included as well. This property of TDP theory implies that the acoustic effect will mainly affect energy subbands with narrow spacing and that the effect would be the strongest between the states involved in resonant tunnelling, depicted as ILL and ULL in Fig. (5.2).

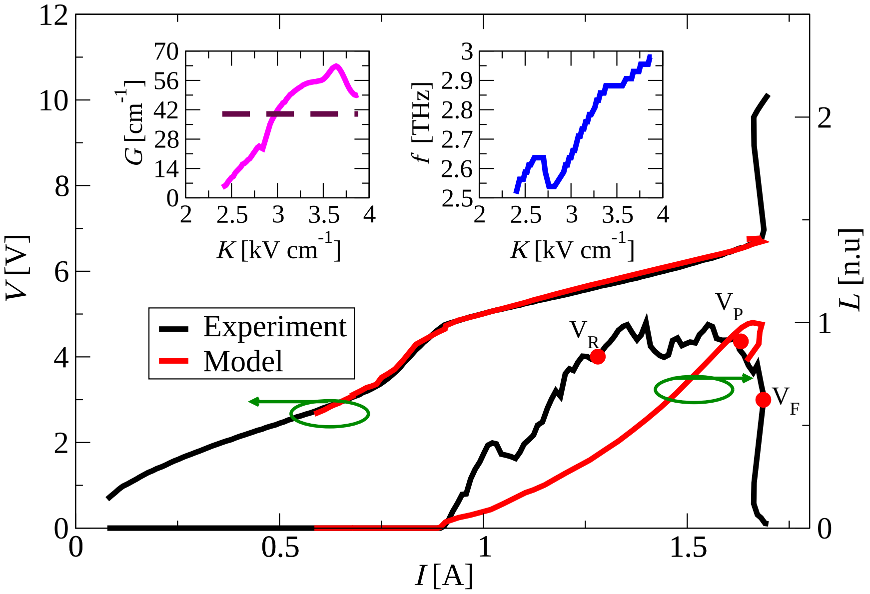

Figure 5.4: $L - I - V$ characteristic of hybrid device in Fig. 5.2 at 20 K in pulsed operation. Contact resistance is 1.5 Ω. The IFR parameters are $\Lambda_{\mathrm{IFR}} = 80$ Å, $\Delta_{\mathrm{IFR}} = 0.95$ Å, EE scattering mechanism was considered as well. Insets show material gain (left) and frequency (right) dependence on applied external bias. Note that both insets focus on the mode with the highest material gain, and other modes are being ignored in the calculation.

The fitting procedure discussed in Chapter 4 cannot be performed to provide the perfect $L-I-V$ agreement, due to the noisy measurement data around the peak of the optical power dependence caused most likely by multi-mode behaviour of the device and mode hopping effect. For that reason, the fitting procedure was aimed at the negative differential resistance (NDR) occurrence. When QCL is displaying NDR, the voltage starts to rapidly increase, the current is dropping and radiation from QCL is sharply decreasing. For that reason, the numerical result in Fig. 5.4 for optical power is not shown after the NDR occurrence as the model is overestimating the effect as it can be seen by the sharp curving of the model's $L-I-V$ results in the figure. Additionally, note that the theoretical model predicts steady increase of the optical power with the current, while the experimental $I-L$ dependence is bell shaped. This is the consequence of limiting the model only to one waveguide mode, meaning that only the frequency that has the highest material gain is considered. For that reason, the optical power is shown in normalised units, and $I-L$ modelling is focused on fitting the dynamic range.

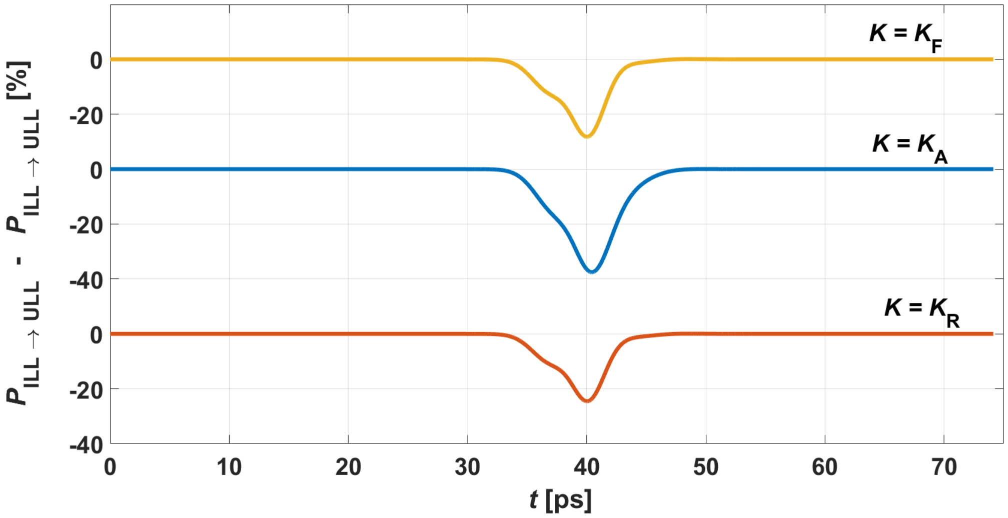

Figure 5.5: Net probability between tunneling states due to the transit of the acoustic wave, calculated using a time-dependent perturbation model for biases after subband alignment ($K_\mathrm{F} = 3.63$ kVcm^{-1}), at alignment ($K_\mathrm{F} = 3.53$ kVcm^{-1}) and before alignment ($K_\mathrm{R} = 3.36$ kVcm^{-1}). The timescale of the simulation is set so that the pulse can propagate over two adjacent periods.

The TDP approach was performed at three bias points of interest, $K_{\mathrm{R}} < K_{\mathrm{P}}$, K_{P} and $K_{\mathrm{F}} > K_{\mathrm{P}}$ that correspond to the voltage values before the peak, at the peak, and after the peak of the optical power dependence, respectively.

At each of these bias points, self-self-consistent Schrödinger-Poisson equation has been solved providing the wavefunction basis for the application of the TDP theory. The perturbation Hamiltonian was modelled as Gaussian derivative function:

$$\frac{X}{\sqrt{2\pi}\,\sigma_{\mathrm{a}}^{2}} \exp\left(-\frac{X^{2}}{2\sigma_{\mathrm{a}}^{2}}\right) \tag{5.2}$$

where $X = ct - kz$, $\sigma_{\mathrm{a}} = 13$ nm, $c = 4780$ ms^{-1}, $k = 1.012$ m^{-1}. The Gaussian dependence is afterwards normalised to the approximated amplitude of the signal of 1 meV.

The simulations in Fig. 5.5 were performed when signal propagates towards the top contact of QCL as indicated in Fig. 5.2. Since TDP provides interaction probability, the first approximation effect would be to seek the net charge that would undergo the tunnelling effect. It is a good approximation to assume equal population of ILL and ULL subbands and present the net TDP effect directly. The main simulation observation was that regardless of the operating bias, the net probability of transport between ILL and ULL is always negative. This indicates higher interaction probability for electrons to scatter back at the ILL, or in other words, the acoustic wave lowers the tunnelling efficiency as it propagates through QCL periods. Since a constant current must flow through QCL, the effect in Fig. 5.5 will cause an increase of QCL resistivity, and therefore always result in voltage increase which was observed in the experiment as well.

In terms of optical power, Fig. 5.5 can also explain the polarity change in the experiment. At the peak of optical power, subbands ILL and ULL are fully aligned up to energy difference equal to the anticrossing energy ($\sim$0.3 meV). Before the resonant tunnelling alignment, the subband energy $E_{\mathrm{ILL}} < E_{\mathrm{ULL}}$ and converse effect occurs after the subband alignment (as these state anti-cross). An increase of voltage on the rising edge of $I-L$ dependence (at bias K_{R}) would therefore bring the tunnelling states effectively closer together which would increase the optical power, while an increase of voltage on the falling edge of $I-L$ dependence (at bias $K = K_{\mathrm{F}}$) would have the opposite effect.

The simulation however indicates that the strongest effect would occur at bias K_{P} that corresponds to the peak of $I - L$, however experimentally, this resulted in non observable measurement. TDP theory predicts that an increase of voltage at this point should result in a signal with similar polarity as on the falling edge of $I - L$, however, note that this QCL structure has very "flat" and noisy $I-L$ dependence at the peak (Fig. 5.4), and the lack of signal is clear from electronic point of view. From quantum mechanical point of view, the "flatness" of this structure is one of the main arguments of hybrid design QCLs which have very wide dynamical range. In Fig. 5.2 it can be seen that state $|2\rangle$ is ILL. However, ground state forms a mini-band with ILL, and injection to ULL in the next period is being additionally done by the ground state as well, resulting in broader dynamic range and broader peak power range. The fluctuation of optical power most likely occurs due to change of ILL from $|2\rangle$ to $|1\rangle$. Naturally, any additional perturbation in this range would not result in distinct observable result.

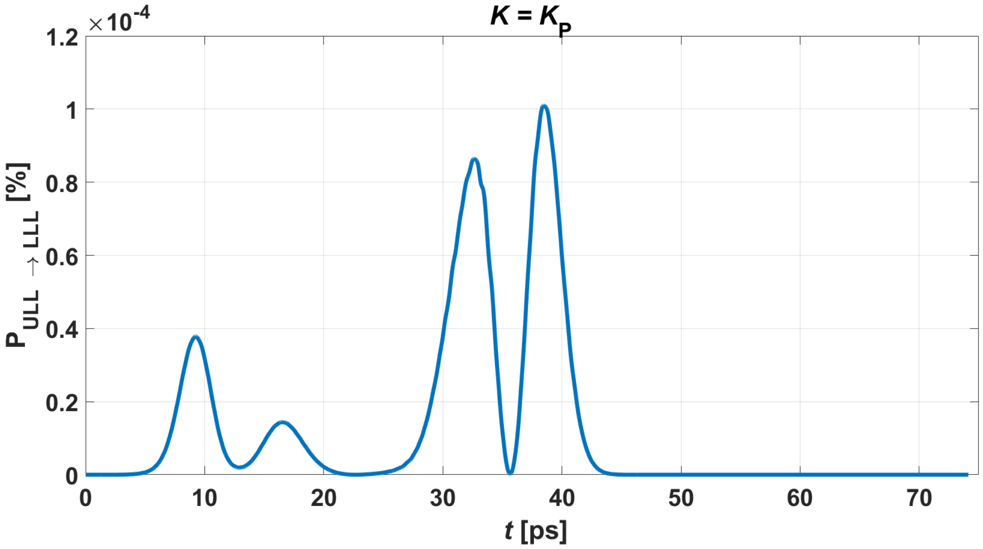

Figure 5.6: $L-I-V$ characteristic of hybrid device in Fig. 5.2 at 15 K in pulsed operation. Contact resistance is 1.5 Ω. The IFR parameters are $\Lambda_{\mathrm{IFR}} = 80$ Å, $\Delta_{\mathrm{IFR}} = 0.95$ Å, EE scattering mechanism was considered.

This modulation approach also affects the QCL radiative transport. However, TDP only provides significant effect when two narrowly spaced energy subbands are considered. In Fig. 5.6 interaction probability between the lasing states is presented. Note that here the converse probability is not significant, as the population of the LLL is much lower than ULL when laser is working. The very weak effect in Fig. 5.6 was expected as energy spacing is $\approx$ 12 meV, while the perturbation had 1 meV amplitude.

From the modelling point of view, the acoustic wave effect does have a very low amplitude and TDP theory could be extended to yield another scattering mechanism, however its effect would not be noticeable because more dominant transport mechanism occur on more significant energy scale (i.e. LO-phonon mechanism at $\sim$36 meV). The main challenge with modelling is that the signal is travelling both in time and space, on a timescale similar to state lifetimes. The Fermi-golden rule with TDP approach would unjustly assume that this perturbation is affecting every QCL period at the same time. A more appropriate approach would be using Landau-Zener theory [166, 167] in order to address the complicated nature of acoustic wave.

From the theoretical approach used in this chapter it can be concluded that this effect may yield a higher modulation depth with QCLs with narrow injection barriers, such as bound-to-continuum or scattering assisted devices. In general, since this effect is omitting the tunnelling, and design with highly sensitive subband alignment (as LO-phonon or BTC QCLs) would yield better observable effect at the peak of $I - L$ dependence. In terms of transport effect and potential frequency modulation, designs with narrowly spaced energies should yield better desired performance.

NB: The TDP model in this section was main contribution of the author in joint research and publication with Dr. Anila Dunn and Prof. Antony Kent (University of Nottingham). EE mechanism was not implemented within the transport model at the time of the collaboration. Thus, the values of few selected bias points of interests differ from the ones in the publication, where fitting procedure was performed without EE scattering mechanism.

Chapter 6

Density Matrix Model Dynamics

The dynamical properties of QCL require solving a coupled system of differential equations in complex coordinate space consisting of DM model, Maxwell wave equation and thermal equation. Numerically, DM model has the highest cost, and requires solving $9N^2$ equations in complex coordinate space. However, the density matrix itself is Hermitian and a significant reduction of equations is possible. This chapter will transform the system reviewed in Chapter 3 to obtain $10N^2$ differential equations in real coordinate space and couple them to the Maxwell equation under the slow envelope approximation. The dynamic model will then be applied to an exemplary QCL structure offering key insight into QCL dynamics along with the possibility of extending the model for optical feedback applications.

6.1 Reduced superoperator for DM model

The superoperator derived in Eq. (3.22) originates from the initial set of equations (3.5). Density matrix is a Hermitian operator, and when this is applied to the initial partitioned density matrix in Eq. (3.4) it follows that $\rho_0 = \rho_0^\dagger$ and $\rho_1 = \rho_{-1}^\dagger$. It also follows that the first and the third equation in Eq. (3.5) are complex conjugates of each other, however both are needed in solving because the second equation couples them.

The system expands three times when NRWA approximation is applied yielding $9N^2$ equations given in Eq. (3.18). Note that NRWA implies that the density matrix partition is $\rho_k = \rho_k^{\mathrm{DC}} + \rho_k^{+} e^{i\omega t} + \rho_k^{-} e^{i\omega t}, k = 0, \pm 1$ and from Hermiticity, the following equalities apply:

$$\begin{aligned} \rho_0^{+} &= (\rho_0^{-})^{\dagger}, & \rho_1^{+} &= (\rho_{-1}^{-})^{\dagger}, & \rho_1^{-} &= (\rho_{-1}^{+})^{\dagger} \\ \rho_0^{\mathrm{DC}} &= (\rho_0^{\mathrm{DC}})^{\dagger}, & \rho_1^{\mathrm{DC}} &= (\rho_1^{\mathrm{DC}})^{\dagger}, & \rho_{-1}^{\mathrm{DC}} &= (\rho_{-1}^{\mathrm{DC}})^{\dagger} \end{aligned} \tag{6.1}$$

Due to the Hermiticity, the third equation in (3.5) does not need to be solved, and in NRWA system in Eq. (3.18), the last three equations (and any of equations involving $\rho_0^{\pm}$) can be discarded due to identities in Eq. (6.1), yielding a reduced system of $5N^2$ equations:

$$\begin{aligned} i\hbar\frac{d\rho_1^{+}}{dt} &= [H_{\mathrm{DC}}, \rho_1^{+}] + [H_{\mathrm{AC}}^{+}, \rho_1^{\mathrm{DC}}] + [H_1, \rho_0^{+}] + eKL_{\mathrm{P}}\rho_1^{+} - i\hbar\frac{\rho_1^{+}}{\tau_{\mathrm{D}}} + \hbar\omega\rho_1^{+} \\ i\hbar\frac{d\rho_1^{\mathrm{DC}}}{dt} &= [H_{\mathrm{DC}}, \rho_1^{\mathrm{DC}}] + [H_1, \rho_0^{\mathrm{DC}}] + [H_{\mathrm{AC}}^{+}, \rho_1^{-}] + [H_{\mathrm{AC}}^{-}, \rho_1^{+}] + eKL_{\mathrm{P}}\rho_1^{\mathrm{DC}} - i\hbar\frac{\rho_1^{\mathrm{DC}}}{\tau_{\mathrm{D}}} \\ i\hbar\frac{d\rho_1^{-}}{dt} &= [H_{\mathrm{DC}}, \rho_1^{-}] + [H_{\mathrm{AC}}^{-}, \rho_1^{\mathrm{DC}}] + [H_1, (\rho_0^{+})^{\dagger}] + eKL_{\mathrm{P}}\rho_1^{-} - i\hbar\frac{\rho_1^{-}}{\tau_{\mathrm{D}}} - \hbar\omega\rho_1^{-} \\ i\hbar\frac{d\rho_0^{+}}{dt} &= [H_{-1}, \rho_1^{+}] + [H_{\mathrm{DC}}, \rho_0^{+}] + [H_{\mathrm{AC}}^{+}, \rho_0^{\mathrm{DC}}] + [H_1, (\rho_1^{-})^{\dagger}] - i\hbar\frac{\rho_0^{+}}{\tau_{\mathrm{D_0}}} - i\hbar\frac{\rho_0^{+}}{\tau} + \hbar\omega\rho_0^{+} \\ i\hbar\frac{d\rho_0^{\mathrm{DC}}}{dt} &= [H_{-1}, \rho_1^{\mathrm{DC}}] + [H_{\mathrm{DC}}, \rho_0^{\mathrm{DC}}] + [H_{\mathrm{AC}}^{+}, (\rho_0^{+})^{\dagger}] + [H_{\mathrm{AC}}^{-}, \rho_0^{+}] + [H_1, (\rho_1^{\mathrm{DC}})^{\dagger}] \\ &\quad - i\hbar\frac{\rho_0^{\mathrm{DC}}}{\tau_{\mathrm{D_0}}} - i\hbar\frac{\rho_0^{\mathrm{DC}}}{\tau} \end{aligned} \tag{6.2}$$

The terms in red colour in Eq. (6.2) are the consequence of Eq. (6.1). These terms have special commutator linearisation that is discussed in Appendix D. Technically, this system can be used instead of Eq. (3.18) for the steady state solution (and even semi-analytical result may be derived by block Gaussian elimination), however the superoperator would not have straightforward symmetric expansion that was discussed in Chapter 3. Numerically, inverting $9N^2$ and $5N^2$ superoperator in Eq. (3.23) has similar CPU time cost on modern processors (note that usually $N \sim 3 - 12$) which is why the numerical implementation and the system construction was explained as in Chapter 3. For the dynamical properties, we must take the reduced form. If we construct the following:

$$
\begin{aligned}
H_{\mathrm{red}} &= \begin{pmatrix} H_{\mathrm{DC}} & H_{\mathrm{AC}}^{+} & 0 & H_1 & 0 \\ H_{\mathrm{AC}}^{-} & H_{\mathrm{DC}} & H_{\mathrm{AC}}^{+} & 0 & H_1 \\ 0 & H_{\mathrm{AC}}^{-} & H_{\mathrm{DC}} & 0 & 0 \\ H_{-1} & 0 & 0 & H_{\mathrm{DC}} & H_{\mathrm{AC}}^{+} \\ 0 & H_{-1} & 0 & H_{\mathrm{AC}}^{-} & H_{\mathrm{DC}} \end{pmatrix}_{5N\times 5N} \\
I_{\mathrm{U_{red}}} &= \begin{pmatrix} I & I & I & I & I \\ I & I & I & I & I \\ I & I & I & I & I \\ I & I & I & I & I \\ I & I & I & I & I \end{pmatrix}_{5N\times 5N} \\
\Upsilon_{\mathrm{red}} &= eKL_{\mathrm{P}} \begin{pmatrix} eKL_{\mathrm{P}}I_{N^2} & 0 & 0 & 0 & 0 \\ 0 & eKL_{\mathrm{P}}I_{N^2} & 0 & 0 & 0 \\ 0 & 0 & eKL_{\mathrm{P}}I_{N^2} & M_1 & 0 \\ 0 & 0 & M_1 & 0 & 0 \\ 0 & M_1 & 0 & M_{\mathrm{AC}}^{+} & 0 \end{pmatrix}_{5N^2\times 5N^2} \\
D''_{\mathrm{red}} &= \begin{pmatrix} D'_1 & 0 & 0 & 0 & 0 \\ 0 & D'_1 & 0 & 0 & 0 \\ 0 & 0 & D'_1 & 0 & 0 \\ 0 & 0 & 0 & D'_0 & 0 \\ 0 & 0 & 0 & 0 & D'_0 \end{pmatrix}_{5N^2\times 5N^2} \\
\Omega_{\mathrm{red}''} &= \begin{pmatrix} I_{N^2} & 0 & 0 & 0 & 0 \\ 0 & 0 & 0 & 0 & 0 \\ 0 & 0 & -I_{N^2} & 0 & 0 \\ 0 & 0 & 0 & I_{N^2} & 0 \\ 0 & 0 & 0 & 0 & 0 \end{pmatrix}_{5N^2\times 5N^2} \\
\rho_{\mathrm{red}} &= \begin{pmatrix} \rho_1^{+'} \\ \rho_1^{DC'} \\ \rho_1^{-'} \\ \rho_0^{+'} \\ \rho_0^{DC'} \end{pmatrix}_{5N^2\times 1}
\end{aligned}
\tag{6.3}
$$

where I is $N \times N$ identity matrix, I_{N^2} is $N^2 \times N^2$ identity matrix. Zero blocks in

H_{red} are $N\times N$ in size, while all other zero blocks are $N^2\times N^2$ in size. M_1 and M_{AC}^{+} are special sub-Liovillian superoperators that correspond to linearisation of commutator consisting of H_1 and H_{AC}^{+}, respectively, that also correspond to the terms in red colour in Eq. (6.2). Formally, the issue with these terms is that they target the conjugate transpose of the unknown, while requesting row-wise vectorisation of the original (non-transposed) density matrix block. While the commutator $[A, X]$ has direct linearisation through Kronecker product as $A\otimes I - I\otimes A^T$, the commutator $[A, X^T]$ which requires same vectorisation as linear form of $[A, X]$ does not have linearisation determined by a particular operation in algebra literature. The derivation therefore needs to be done by mathematical induction as presented in detail in appendix D.3. Algebraically, we can construct linear form of $[A, X^T]$ as $(I_{\text{R}}\boxtimes A_{\text{R}} - (I_{\text{R}}\boxtimes A_{\text{R}})^T)$ where A_{R} is partitioned one-column matrix where each column is a row of the the original matrix A, and I_{R} is a column partitioned matrix (with N partitions) where each partition is identity matrix I of $N\times N$ size. We can introduce $M_{\text{r1}} = I_{\text{R}}\boxtimes H_1, M_{\text{ac1}} = I_{\text{R}}\boxtimes H_{\text{AC}}$ and define $M_1 = M_{\text{r1}} - M_{\text{r1}}^T, M_{\text{AC}} = M_{\text{ac1}} - M_{\text{ac1}}^T$, however the numerical implementation of M_{r1} and M_{ac1} does not need to follow its definition, since the numerical code in C++ is straightforward, with two nested loops $i, j = 1, \cdots N$, $M_{\text{r1}}(iN+j, span(jN, (j+1)N-1)) = A.row(i)$ (span operation and .row operation are part of armadillo algebra library that was used, span focuses on particular set of columns within $iN+j$ row and this code replicates i–th row of matrix A obtained by .row function).

The reduced superoperator for linearising the system in Eq. (6.2) is:

$$\begin{aligned} \frac{d\rho''_{\text{red}}}{dt} &= \mathcal{L}_{\text{red}}\rho''_{\text{red}} \\ \mathcal{L}_{\text{red}} &= -\frac{i}{\hbar}\left(H_{\text{red}}\boxtimes I_{\text{U}_{\text{red}}} - I_{\text{U}_{\text{red}}}\boxtimes H_{\text{red}}^{T} + \Upsilon_{\text{red}} - i\hbar D''_{\text{red}} + \hbar\omega\Omega''_{\text{red}}\right) \end{aligned} \tag{6.4}$$

The Khatri–Rao product needs to be performed before adding other terms. These additional terms in Eq. (6.3) are sparse, and mostly have elements only on the main block diagonal, thus a formal construction as in Eq. (6.3) is not necessary, and manual addition (to the specific blocks after the Khatri–Rao product) may be performed instead.

6.2 Superoperator of DM model in real plane

The system in Eq. (6.3) and its linear form in Eq. (6.4) is written in complex plane, however many C++ libraries (as GSL [168]) need a system of real equations. Splitting the real and imaginary parts in Eq. (6.3) would result in a system of $10N^2$ real equations. Fortunately, an expansion rule similar to Eq. (3.21) is possible. Consider a commutator $-i[H_k, \rho_k]$, where both are complex $H_k = H_{k_\mathrm{R}} + iH_{k_\mathrm{I}}$ and $\rho_k = \rho_{k_\mathrm{R}} + i\rho_{k_\mathrm{I}}$. The commutator results in two equations:

$$\begin{aligned} \mathrm{Im}: &\quad [H_{k_\mathrm{I}}, \rho_{k_\mathrm{I}}] - [H_{k_\mathrm{R}}, \rho_{k_\mathrm{R}}] \\ \mathrm{Re}: &\quad [H_{k_\mathrm{I}}, \rho_{k_\mathrm{R}}] + [H_{k_\mathrm{R}}, \rho_{k_\mathrm{I}}] \end{aligned} \tag{6.5}$$

Linear form of Eq. (6.5) is:

$$\left(\begin{pmatrix} H_{k_\mathrm{I}} & -H_{k_\mathrm{R}} \\ H_{k_\mathrm{R}} & H_{k_\mathrm{I}} \end{pmatrix} \boxtimes \begin{pmatrix} I & I \\ I & I \end{pmatrix} - \begin{pmatrix} I & I \\ I & I \end{pmatrix} \boxtimes \begin{pmatrix} H^T_{k_\mathrm{I}} & H^T_{k_\mathrm{R}} \\ -H^T_{k_\mathrm{R}} & H^T_{k_\mathrm{I}} \end{pmatrix} \right) \begin{pmatrix} \rho_{k_\mathrm{I}} \\ \rho_{k_\mathrm{R}} \end{pmatrix} \tag{6.6}$$

This is similar to the rotation matrix for any complex number, however we are interested in formulation multiplied by imaginary unity, since most terms have this form in Eq. (6.4), thus we define a complex rotation expansion rule as:

$$H_k^{\mathrm{rot}} \to \begin{pmatrix} H_{k_\mathrm{I}} & -H_{k_\mathrm{R}} \\ H_{k_\mathrm{R}} & H_{k_\mathrm{I}} \end{pmatrix} \tag{6.7}$$

Additionally, terms in red colour in Eq. (6.2) target complex conjugate of the density matrix partitions, this has the same effect as multiplying the second equation in Eq. (6.5) by -1 and the expansion rule for the linearised form of $[H_k, \rho_k^T] = M_k \rho_k'$ would be:

$$M_k^{\mathrm{rot}} \to \begin{pmatrix} M_{k_\mathrm{I}} & -M_{k_\mathrm{R}} \\ -M_{k_\mathrm{R}} & -M_{k_\mathrm{I}} \end{pmatrix} \tag{6.8}$$

The expanded superoperator of real equations can be written as:

$$\begin{aligned} \frac{d\rho_{\mathrm{red}}^{\mathrm{rot}''}}{dt} &= \mathcal{L}_{\mathrm{red}}^{\mathrm{rot}} \rho_{\mathrm{red}}^{\mathrm{rot}''} \\ \mathcal{L}_{\mathrm{red}}^{\mathrm{rot}} &= \frac{1}{\hbar} \left(H_{\mathrm{red}}^{\mathrm{rot}} \boxtimes I_{\mathrm{U_{red}}}^{\mathrm{rot}} - I_{\mathrm{U_{red}}}^{\mathrm{rot}} \boxtimes H_{\mathrm{red}}^{rot \cdot T} + \Upsilon_{\mathrm{red}}^{\mathrm{rot}} + \hbar D_{\mathrm{red}}'' + \hbar\omega \Omega_{\mathrm{red}}^{\mathrm{rot}''} \right) \end{aligned} \tag{6.9}$$

where:

- $H_{\mathrm{red}}^{\mathrm{rot}}$ is a $10N \times 10N$ partitioned matrix, obtained from the one in Eq. (6.3) by applying expansion rule in Eq. (6.7). Note that only H_{AC} block has an imaginary part, and that real basis of wavefunctions was used to obtain blocks $H_{\pm 1}$.

- $I_{\mathrm{U_{red}}}^{\mathrm{rot}}$ is $10N \times 10N$ partitioned matrix, where each partition is identity matrix I. It can be algebraically formed as $U_{10\times 10} \otimes I_{N\times N}$.

- $\Upsilon_{\mathrm{red}}^{\mathrm{rot}}$ is $10N^2 \times 10N^2$ partitioned matrix obtained from the one in Eq. (6.3) by applying the rule Eq. (6.7) to terms $eKL_{\mathrm{P}}I_{N^2\times N^2}$, treating them as purely real, and rule (6.8) to terms M_1 and M_{AC}.

- D''_{red} is a $10N \times 10N$ partitioned matrix, obtained by applying rule Eq. (6.7) by treating this matrix as purely imaginary, because this term contained additional imaginary unity in Eq. (6.4) (this also causes the sign change in front of this term). In simpler terms, D''_{red} is block diagonal matrix with elements $D'_1, D'_1, D'_1, D'_1, D'_1, D'_1, D'_0, D'_0, D'_0, D'_0$ on the main diagonal.

- $\Omega_{\mathrm{red}}^{\mathrm{rot}\prime\prime}$ is a $10N \times 10N$ partitioned matrix obtained from the one in Eq. (6.3 by applying the rule in Eq. (6.7) on each I_{N^2} element, treating it as purely real.

- $\rho_{\mathrm{red}}^{\mathrm{rot}\prime\prime}$ is $10N^2$ column vector consisting of stacked vectorised elements

  $$\rho_{1\mathrm{I}}^{+\prime}, \rho_{1\mathrm{R}}^{+\prime}, \rho_{1\mathrm{I}}^{\mathrm{DC}\prime}, \rho_{1\mathrm{R}}^{\mathrm{DC}\prime}, \rho_{1\mathrm{I}}^{-\prime}, \rho_{1\mathrm{R}}^{-\prime}, \rho_{0\mathrm{I}}^{+\prime}, \rho_{0\mathrm{R}}^{+\prime}, \rho_{0\mathrm{I}}^{\mathrm{DC}\prime}, \rho_{0\mathrm{R}}^{\mathrm{DC}\prime}$$

  in that order.

6.3 Normalisation of the superoperator

The normalisation condition is given in Eq. (3.23). For the steady state solution we can replace one of the equations $\rho_{0_{ii}}^{\mathrm{DC}}$ given by the superoperator in Eq. (6.4) and obtain a simple linear system as in Eq. (3.23). For the dynamical solution, it is much better to implement the normalisation condition by discarding the equation targeting $\rho_{0_{NN}}^{\mathrm{DC}}$ (we chose the last state), and substituting it by $\rho_{0_{NN}}^{\mathrm{DC}} = \sum_{i\neq N} 1 - \rho_{0_{ii}}^{\mathrm{DC}}$, the resulting system of equations can then be written as:

$$\frac{d\rho_{\mathrm{dyn}}}{dt} = \mathcal{L}_{\mathrm{dyn}}\rho_{\mathrm{dyn}} + B_N \tag{6.10}$$

where $\mathcal{L}_{\mathrm{dyn}}$ is obtained from $\mathcal{L}^{\mathrm{rot}}_{\mathrm{red}}$ by applying the normalisation condition, ρ_{dyn} lacks the real and imaginary part of $\rho^{\mathrm{DC}}_{0_{NN}}$, otherwise it is identical to $\rho^{\mathrm{rot}''}_{\mathrm{red}}$ from Eq. (6.9). The $\mathcal{L}_{\mathrm{dyn}}$ matrix is similar to $\mathcal{L}^{\mathrm{rot}}_{\mathrm{red}}$ and it differs in the lack of rows and columns (imaginary and real part) that correspond to the $\rho^{\mathrm{DC}}_{0_{NN}}$ element in the original system ($(5N^2-1)$–th row and column) and each column targeting $\rho^{\mathrm{DC}}_{0_{ii}}, i \neq N$ is altered by subtracting the columns targeting imaginary and real part of $\rho^{\mathrm{DC}}_{0_{NN}}$ from the original system. The $\mathcal{L}_{\mathrm{dyn}}$ matrix therefore has $(10N^2 - 2 \times 10N^2 - 2)$ size. B_N is $10N^2 - 2$ column vector that is actually a column from the original superoperator that targeted the real part $\rho^{\mathrm{DC}}_{0_{NN}}$ while the two rows were omitted since the equations targeting real and imaginary part of $\rho^{\mathrm{DC}}_{0_{NN}}$ are deleted. The detailed explanation on how $\mathcal{L}_{\mathrm{dyn}}$ and B_N are generated from the initial system is given in Appendix D.4.

6.4 Maxwell – Bloch equations

The formal solution of linear system in Eq. (6.10) can simply be determined through eigenvectors and eigenvalues of $\mathcal{L}_{\mathrm{dyn}}$, however this is only possible if the optical electric field is considered constant. The superoperator depends on the optical electric field through H_{AC} partition of the reduced Hamiltonian in Eq. (6.3). The optical electric field is given by Maxwell equation, and if we adopt Fourier approach under slow-envelope approximation in Eq. (1.12), the real E_{R} and imaginary part E_{I} of this equation may be written as:

$$\begin{aligned}\frac{\partial E_{\mathrm{R}}}{\partial t} &= -\frac{\sigma}{2\epsilon_0 n^2}E_{\mathrm{R}} + (\omega-\omega_n)E_{\mathrm{I}} + \frac{\omega}{2\epsilon_0 n^2}\,\mathrm{Im}\{P\}\\ \frac{\partial E_{\mathrm{I}}}{\partial t} &= -(\omega-\omega_n)E_{\mathrm{R}} - \frac{\omega}{2\epsilon_0 n^2}\,\mathrm{Re}\{P\}\end{aligned} \tag{6.11}$$

If we apply the expressions for the polarisation in Eq. (3.27), material gain in Eq. (3.28), and that the conductivity is linked to the modal loss as $\sigma = \epsilon_0 n c g_{\mathrm{th}}$, where modal threshold gain is given by Eq. (1.1), as $g_{\mathrm{th}} = (\alpha_{\mathrm{m}} + \alpha_{\mathrm{w}})\Gamma^{-1}$, we can write Eq. (1.12) as:

$$
\begin{aligned}
\frac{\partial E_{\mathrm{R}}}{\partial t} &= \frac{c}{2n}\left(g-g_{\mathrm{th}}\right)E_{\mathrm{R}}+(\omega-\omega_n)E_{\mathrm{I}} \\
\frac{\partial E_{\mathrm{I}}}{\partial t} &= -\frac{c}{2n}g_{\mathrm{th}}E_{\mathrm{I}}-(\omega-\omega_n)E_{\mathrm{R}}+\frac{eN_{\mathrm{D}}\omega}{2\epsilon_0 n^2}\,\mathrm{Re}\Big\{Tr(Z\rho_0^{+})\Big\}
\end{aligned}
\tag{6.12}
$$

We can also assume that the resonant frequency would be exactly equal to the Fabry–Perot́ mode $\omega = \omega_n$ which simplifies Eq. (6.12) further. The real part of Eq. (6.12) illustrates the key mechanism of damping the optical gain to modal loss.

The system of equations given by Eq. (6.10) and Eq. (6.12) is non-linear system of ordinary differential equations (ODE) commonly referred in literature as Maxwell–Bloch (MB) equations [169]. The MB equations are usually written for several states only, however the formulation developed by the author of this thesis in Eqs. (6.10,6.12) is general and independent on the number of states considered. The mathematical formulation in Eq. (6.10) and Eq. (6.12) with the relative mathematical simplicity of Eq. (6.9), allows a better insight into the DM approach and a straightforward numerical implementation. The system comprises $10N^2$ equations and may be solved by numerous packages available in C++ GSL library [168].

The important note should be made on the choice of the initial conditions for the density matrix elements and optical electric field. The natural choice is to assume that optical electric field is low (i.e. $E_{\mathrm{R}} = E_{\mathrm{I}} = 1$ Vm^{-1}) and the density matrix initial condition may be set to the steady solution for such value of the optical electric field. Physically, however this is not fully correct. The optical field is generated in the cavity by numerous transitions in the medium, regardless if the device is lasing or not. This represents spontaneous emission, and some moderate values for E may be chosen as well.

The material gain is calculated by dividing the imaginary part of the polarisation by the real part of the optical electric field, and therefore, if initial condition for E_{R} is not properly set and a change of sign occurs, the material gain would display non–physical discontinuity. This may be ignored as it would not affect the steady state value, however it may be rectified by changing the initial condition once its sign is known at the steady state solution.

6.5 QCL Dynamics

The system of Eqs. (6.10,6.12) may be numerically implemented in relatively straightforward manner. Since this is an ODE system of the first order, numerous solvers exist across multiple mathematical libraries. The implementation for this work has used a GSL library within C++ [1] and exploited Runge-Kutta Cash-Karp algorithm suitable for stiff problems [168].

This algorithm requires very small simulation time–step (100 fs). For this reason its needed CPU–time is expectedly higher in comparison to the steady state model discussed in Chapter 4. For a twelve states QCL, steady–state model needs approximately 20 minutes for simulation at a single bias point, while dynamic model requires approximately a couple of hours. Note, however, that the steady–state model does not consider the imaginary part of the optical electric field, doing so would require a two dimensional minimisation algorithm which would significantly increase the simulation time. The steady state solution of the dynamic model does provide different values for optical power and the current density and its use is advised if high precision of data is required from the model.

---

[1] Note that GSL library is also supported in C, however all GSL algorithms require functions in specific format as $f(x, parameters)$ where *parameters* is a pointer of void type. Usual methodology is to formulate a structure of all parameters, however C++ allows very convenient approach, where all parameters can be put in a class, and GSL function can be declared as static function within the class. This allows sending class pointer **this** to the GSL function as *parameters* pointer and allows usage of all parameters and class methods to the GSL function. Given that the formulation of the system in Eq. 6.10 requires cumbersome algebra methods, use of GSL functions in this way is highly recommended.

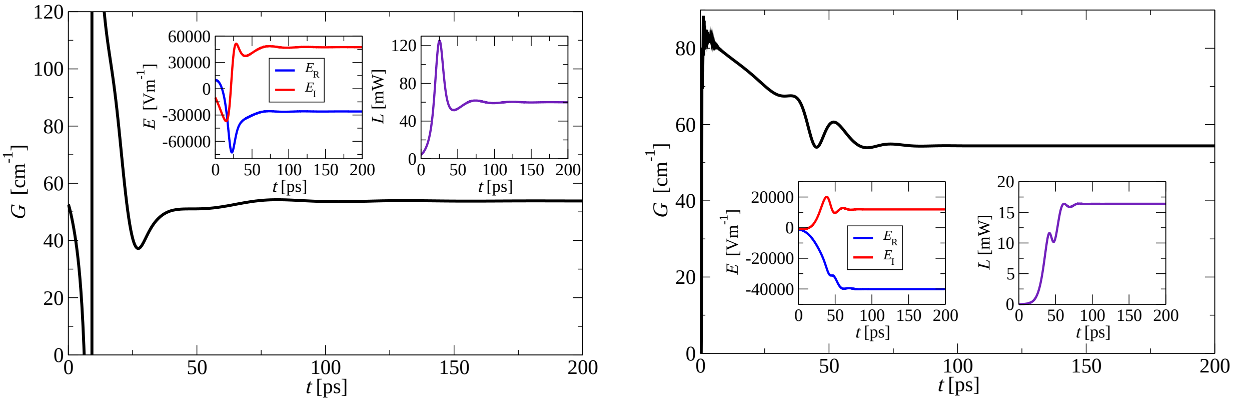

a) 3.4 THz high power QCL [53]

b) 3.4 THz Hybrid QCL [151]

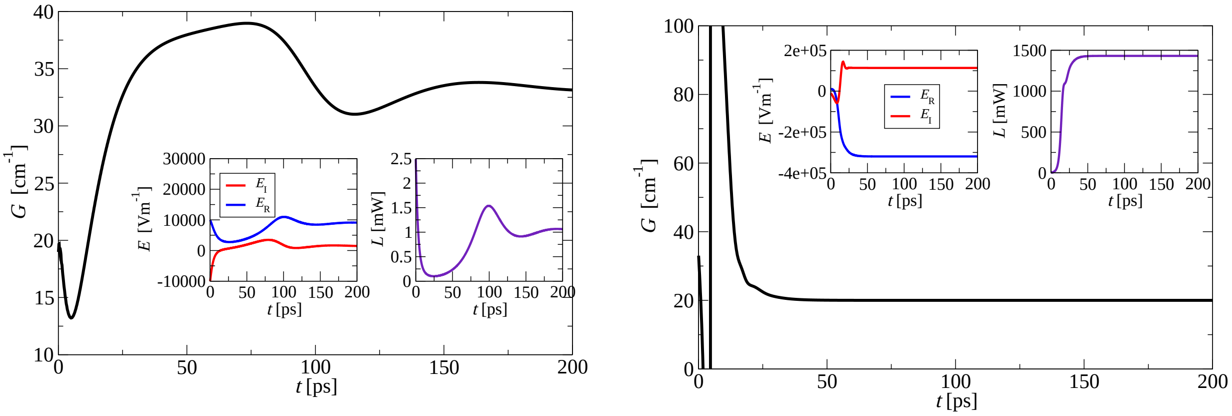

c) 2 THz BTC QCL [74]

d) 3.9 THz LO-phonon QCL [36]

Figure 6.1: Material gain dependence on time for several QCL designs at their respective resonant bias at 20 K. a) The highest power THz QCL (> 1 W, fabricated in Leeds)[53] at $K = 8.8\ \frac{\mathrm{kV}}{\mathrm{cm}}$, b) Hybrid THz QCL[151] at $K = 4.7\ \frac{\mathrm{kV}}{\mathrm{cm}}$, c) BTC QCL (designed and fabricated in Leeds) [112, 144] at $K = 1.95\ \frac{\mathrm{kV}}{\mathrm{cm}}$, f) The highest temperature THz QCL (210 K) [36] at $K = 19\ \frac{\mathrm{kV}}{\mathrm{cm}}$. Inset on the left side presents the time dependence of optical electrical field (real (blue) and imaginary (red) part), and the inset on the right side displays the time dependence of optical power. Structures a) and b) and c) were fabricated with surface plasmon waveguide, while structures d) has metal-metal waveguide.

Figure 6.1 presents some of the key features of THz QCL laser dynamics. The round trip time of lasing cavity of length L_c is $2nL_\mathrm{c}/c \approx 22\ L_\mathrm{c}$ [ps mm^{-1}]. The usual cavity lengths are $1 - 3$ mm, meaning that the round trip time is on the scale of $\approx 22 - 66$ ps. In all examples in Fig. 6.1 it can be noted that the transient effect occurs on timescale that is typically faster than the round trip time. This also means that due to the short ULL lifetime ($\sim$12 ps) QCL devices would not display any relaxation oscillations [170], which occur with other types of lasers. The fast gain recovery time of THz QCLs has been experimentally observed [171, 172, 173] and this is highly important property for modulation applications.

The initial guess for electrical field was set to $(E_\mathrm{R}, E_\mathrm{I}) = (10^4, -10^4)[\mathrm{Vm}^{-1}]$ in all examples. The divergent behaviour of the material gain occurred in instances where E_R changes sign, however this is purely a numerical issue and it does not affect the steady state value. The dynamical model is usually invoked when material gain at very low optical electrical field exceeds the modal loss. The initial guess for structure in Fig. 6.1c overestimated the steady state value, thus the transient lasted significantly longer, however this example illustrates that the simulation can reach the steady–state with poor initial guess that is also lower than the modal loss (this is the structure discussed in Chapter 4).

Note that the choice of initial guess plays an important role in ODE solving, mainly because this is a stiff numerical problem. In some cases, setting electrical field to very low value would prevent the method to converge. The initial guess for the density matrix elements is usually best set as the steady state solution at very low electrical field. It was also noticed that the method may diverge if states that are not relevant for key QCL transport behaviour are included in the simulation (i.e. higher continuum–like states). This is shown in Fig. 6.2.

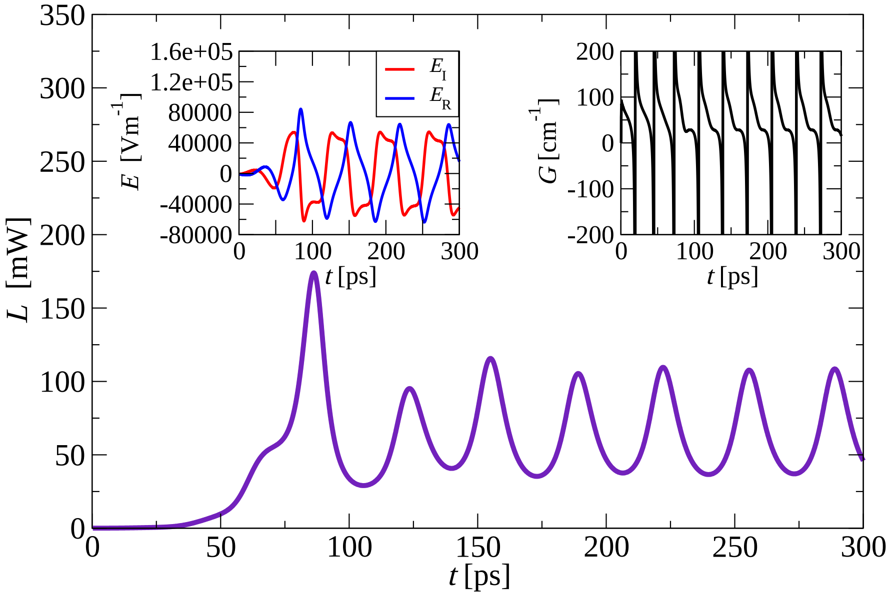

Figure 6.2: Optical power dependence on time for a 3.4 THz QCL structure [53] (record high power operation) when eleven states are included in the simulation. Insets show optical electrical field (left) and material gain dependence (right).

Simulation performed in Fig. 6.2 used eleven states for the transport consideration. In Fig. 4.14b in Chapter 4, however, it can be noticed in the inset that ULL state is the fifth state, and higher states do not affect the transport significantly, which expectedly did not cause any issues in the simulation performed in Fig. 4.14b. However, for the dynamics model, this does present complication and method diverges as shown in Fig. 6.2. Figure 6.1a) shows the simulation with six states under consideration, in which case the divergent behaviour does not occur.

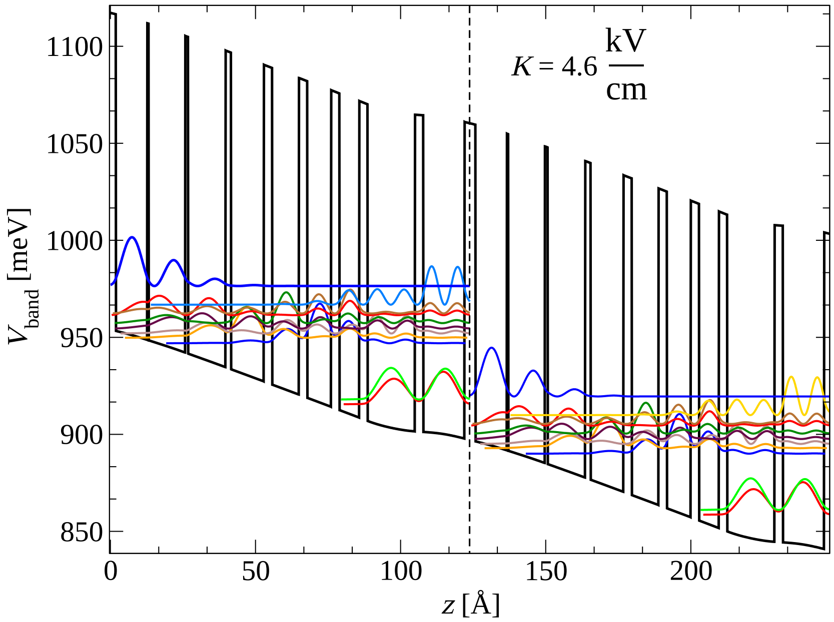

Figure 6.3: Layer thicknesses for the analysed hybrid QCL design [151], starting with the injection barrier, are **3.8**/10.8/**0.5**/12.6/**1.0**/12.9/**1.9**/11.3/**2.9**/ 9.1/**2.9**/8.2/**2.9**/6.8/**2.9**/<u>*16.3*</u>/**2.9**/14.2 nm, $Al_{0.18}Ga_{0.72}As$ barriers are shown in bold and the well doped to $3 \cdot 10^{16}$ cm^{-3} is underlined. Two periods are shown at the resonance bias $K = 4.6\ \frac{\text{kV}}{\text{cm}}$ along with the corresponding wavefunctions moduli squared.

Figure 6.3 shows the layer structure of 3.4 THz QCL laser analysed in Fig. 6.1b. This structure [151], similarly to the one analysed in Chapter 5 is based on the design in [54], however both devices were modified, and fabricated in Leeds group. This structure used barriers with $x = 0.18$ Al content and its main feature was a very wide dynamical range suitable for self-mixing interferometry application. Additionally, this structure has a Bragg grating on the top contact, which serves as a filter for lasing frequency (at 3.4 THz).

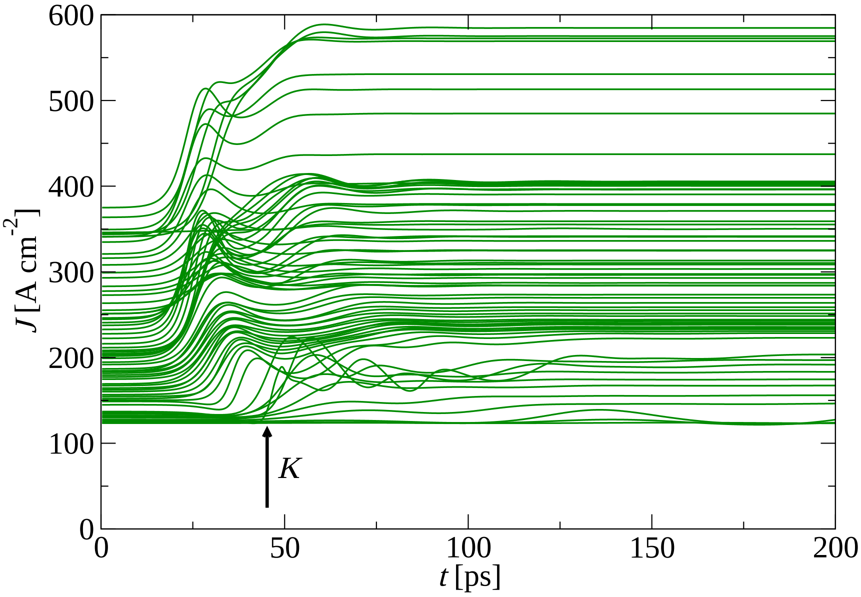

Figure 6.4: Current density dependence on time for various values of external bias, varied in range $3.8 - 5\ \frac{\mathrm{kV}}{\mathrm{cm}}$ at operating temperature of 20 K. EE scattering mechanism was included in the simulation.

Figure 6.4 shows the current density dependence on time of the Maxwell-Bloch model for various value of electric bias. It can be noticed again, that steady state is reached on a timescale that is comparable to the round trip time through the laser cavity (the laser dimensions are $1800 \times 150 \times 14.2\ \mu\mathrm{m}^3$). Note that fitting procedure discussed in Chapter 4 can also be applied by observing steady–state values of output parameters.

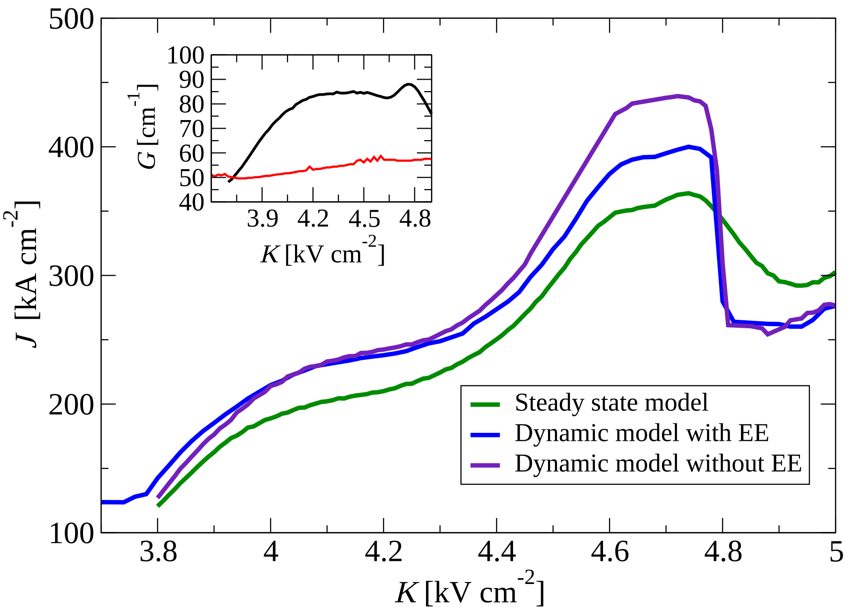

Figure 6.5: Current density dependence on time for various value of external bias, varied in range 3.8 – 5 $\frac{\text{kV}}{\text{cm}}$ at 20 K. The values of data in blue were taken as steady state solutions of the dynamics model shown in Fig. 6.4. The data in blue includes EE scattering, the data in purple does not. Data in green is obtained through steady–state model described in Chapter 4 without consideration of EE mechanism. Inset shows the material gain dependence on the applied electric field and the red line indicates the modal loss for SP waveguide, determined by the model in [87].

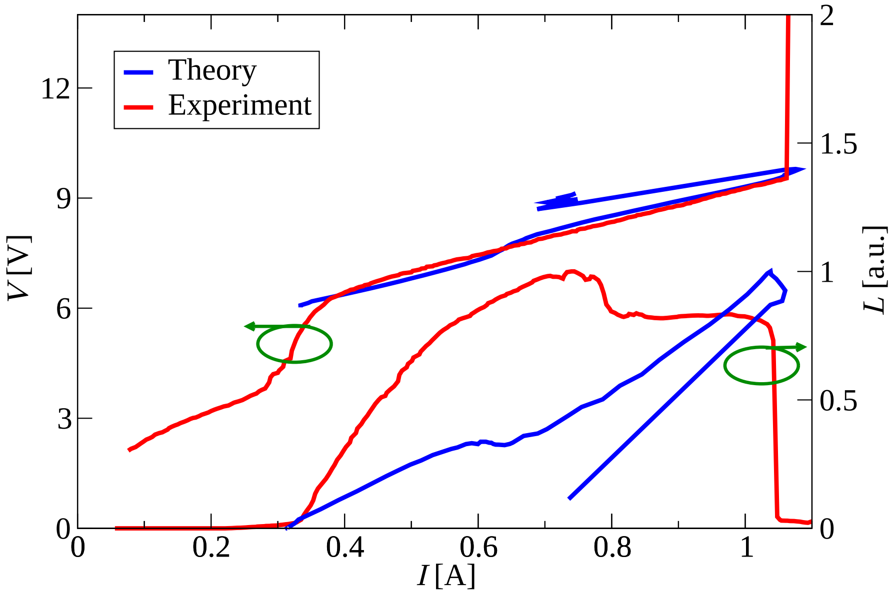

Figure 6.6: $L-I-V$ characteristic of 3.4 THz QCL structure [151] at 20 K in pulsed operation. Fitting value of contact resistance is 1.2 Ω. The optical power values are scaled for the clearer comparison of the dynamic range.

Figure 6.5 displays the current density dependence on the applied bias obtained by three methods: i) Steady–state model discussed in Chapter 4 with IFR parameters $\Delta_{\mathrm{IFR}} = 0.45$ Å, $\Lambda_{\mathrm{IFR}} = 50$ Å and without EE scattering (green), ii) Dynamic model in steady–state without EE scattering (purple) with IFR parameters $\Delta_{\mathrm{IFR}} = 0.45$ Å, $\Lambda_{\mathrm{IFR}} = 50$ Å and iii) Dynamic model in steady–state with EE scattering (blue) with IFR parameters $\Delta_{\mathrm{IFR}} = 0.25$ Å, $\Lambda_{\mathrm{IFR}} = 40$ Å. Experimentally, at 20 K, this structure has threshold current around $\sim 120\ \frac{\mathrm{A}}{\mathrm{cm}^2}$ and at the optical power peak $\sim 390\ \frac{\mathrm{A}}{\mathrm{cm}^2}$. The main fitting challenge for this structure was in matching the threshold current. The steady–state model discussed in Chapter 4 calculates optical power through minimisation algorithm by exploiting gain saturation effect, however only real part of optical electric field is considered in DM approach in order to avoid high numerical cost of dual minimisation process. For this reason, the values obtained by such model differs from dynamic model discussed in this Chapter. It was found, that for this structure, IFR parameters that match the threshold current density overestimate the current density at optical power peak if EE scattering is not included. The best fitting (with expectedly different IFR parameters) is shown by blue line in Fig. 6.5. The comparison between this result and experimental $L - I - V$ data is shown in Fig. 6.6. The NDR is displayed in both theoretical and experimental data. Similarly to [130] the model is mostly reliable to describe the rising portion of $I - L$ dependence, as the NDR effect displays itself as sudden drop of current density, rather than the increase of voltage. The shape and the slope of $I - L$ dependence is not comparable since the model performs calculation only at one cavity mode, while experimental measurement collects emitted power via detector (usually bolometer) of particular efficiency.

Chapter 7

Dynamic Model for self-mixing interferometry in Terahertz QCLs

The self-mixing interferometry occurs when a laser is exposed to external homodyne optical feedback. In most of laser applications, the reflected light is usually considered detrimental, however if a small portion of laser's own radiation is reinjected into the cavity (by use of an external mirror) the interference would act as a perturbation to laser characteristics such as threshold gain, optical power, lasing frequency and terminal voltage. Using the homodyne mixing, it is possible to study the properties of the reinjected light, by examining the perturbed response (optical power or terminal voltage). In essence this effect behaves as highly sensitive modulation technique, which may be exploited for state of the art imaging and sensing applications [91, 97, 174]. This chapter will focus on incorporating this effect into Maxwell-Bloch model discussed in the previous chapter.

7.1 Lang - Kobayashi and the three mirror model

The self - mixing effect was first observed in gas maser devices [175, 176], and since then, it was examined in a variety of laser media: semiconductor diode lasers [177, 178, 179], solid state lasers [180, 181, 182], fiber [183, 184] and fiber ring lasers [185, 186], quantum cascade lasers [187, 188, 93, 95, 97, 96, 189, 99], interband cascade lasers [190], etc. The effect has had many names in literature [91] and the widespread ones are self - mixing interferometry (SMI) and laser feedback interferometry (LFI).

From modelling point of view, the initially employed approach was for diode lasers where Maxwell-Bloch equation was considered to be affected by the semi-transparent mirror [191] which led to introduction of feedback term, however the polarisation of the medium was calculated via rate equation approach. The most widespread modelling approach, known as Lang-Kobayashi (LK) model, has been presented in [102] which in essence is a combination of rate equation model and Maxwell wave equation under slow-varying envelope approximation. Note that initial work in [191] is more general than [102], and this Chapter will focus on further generalisation, since both approaches consider two level laser systems which is not fully justifiable for highly complex structure as THz QCL.

7.1.1 Three mirror model

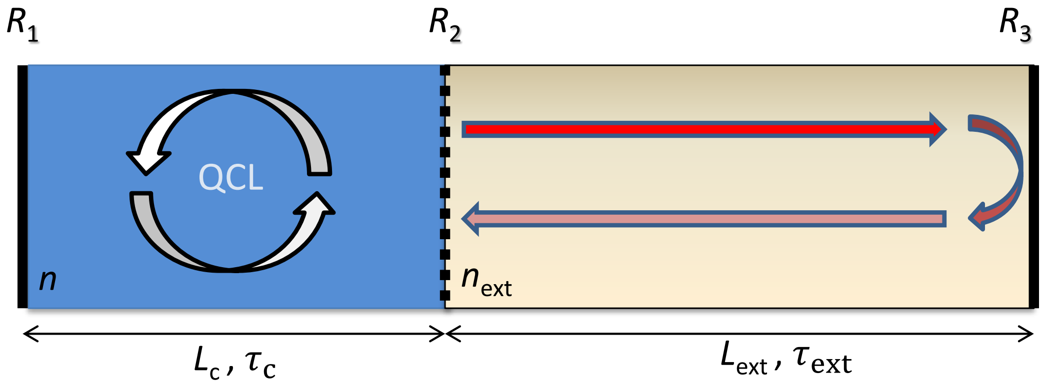

Figure 7.1: The three mirror model. QCL is characterised by its cavity round trip time $\tau_c = 2nL_c/c$. The first mirror in the laser cavity is highly reflective with reflectivity R_1. After τ_c the emitted radiation passes through semitransparent mirror (with reflectivity R_2) and propagates towards the target, represented by a third mirror with reflectivity R_3. The external cavity is characterised by its round trip time $\tau_{ext} = 2n_{ext}L_{ext}/c$, after which the light reflected off the target enters the laser cavity.

.

The simplest approach for SM effect is given by the three mirror model shown in Fig. 7.1. By simple tracing of reflections (and neglecting the higher orders) [192] it is possible to model the SM effect by creating an effective mirror that takes into account the effect of the external cavity, and substitute the effective mirror's reflectivity into the waveguide loss. In essence, the three mirror model is representing the effect of the re-injected light as a perturbation to the waveguide loss [92, 7]. This model is unable to describe the dynamics of the SM effect, however two parameters of high importance can be obtained [193, 194]:

$$\begin{aligned}\tilde{\kappa} &= \frac{\kappa}{\tau_c} = \zeta(1-R_2)\sqrt{\frac{R_3}{R_2}}\frac{1}{\tau_c} \\ C &= \tilde{\kappa}\tau_{\text{ext}}\sqrt{1+\alpha_{\text{LEF}}^2}\end{aligned} \tag{7.1}$$

where $\tilde{\kappa}$ represents the rate of reinjection of the light into the laser cavity, κ is the coupling strength, ζ is phenomenologicaly added into κ to account for additional possible loss during reinjection ($|\zeta| \leq 1$), α_{LEF} is linewidth enhancement factor. Parameter $\tilde{\kappa}$ is commonly referred to as coupling rate, and parameter C as feedback level. The feedback level is dimensionless and it is used to characterise the regimes of SM effect [91]:

- $C \leq 1$ – Weak optical feedback regime - this regime is of the greatest interest for most SM applications since the phase change due to external cavity affects the line broadening at single emitting frequency.
- $C > 1$ – Moderate optical feedback regime - this regime generates multimode frequency behaviour that splits the emission line due to mode hopping.
- $C \gg 1$ – Strong optical feedback regime - this regime re-stabilizes emission at a single frequency, however it can lead to non linearity and hysteresis in the observed signals.
- $\tilde{\kappa} \approx f_{\text{ro}}$ – Chaotic optical feedback regime - this regime occurs when coupling rate is comparable to relaxation oscillations frequency f_{ro}. The effect results in chaotic dynamics.

- $\tilde{\kappa} \gg f_{\mathrm{ro}}$ – Stable optical feedback regime - this regime is equivalent to mode locking effect where a laser is externally pumped.

The last two regimes show no (or low) dependence on external feedback phase, and the first three regimes are exploited in SM effect applications.

The three mirror model, replaces the second mirror in Fig. 7.1 with an effective mirror, given by amplitude reflection coefficient $\tilde{R}_2 = R_2 e^{j\theta_{\mathrm{f}}} = R_2 + \epsilon(1 - R_2)R_3 e^{-j\omega\tau_{\mathrm{ext}}}$ Under the assumption of weak optical feedback where $\kappa \ll 1$ and $\mathrm{Re}(R_2) \approx |R_2|$:

$$\begin{aligned} |\tilde{R}_2| &= R_2\left(1 + \kappa\cos(\omega\tau_{\mathrm{ext}})\right) \\ \theta_{\mathrm{f}} &= -\kappa\sin(\omega\tau_{\mathrm{ext}}) \end{aligned} \tag{7.2}$$

The round trip phase within the laser cavity without feedback equals an integer multiple of 2π: $-2\omega n L_{\mathrm{c}}/c + \theta_{\mathrm{f}} = -2m\pi, m = 0, \pm1, \pm2\ldots.$ At threshold where laser lases at frequency $\omega = \omega_{\mathrm{th}}$, we can take $\theta_{\mathrm{f}} = 0$. The optical feedback effectively changes the threshold gain. The mirror loss in Fabri-Perót cavity equals $\frac{1}{L_{\mathrm{c}}}\ln\left(\frac{1}{R_1 R_2}\right)$ (where r_1 and r_2 are amplitude reflections coefficients), thus the mirror loss due to the introduction of the effective mirror would only change R_2 in this expression. Under the assumption of weak feedback $\kappa \ll 1$, the change in threshold gain and the phase [192] due to optical feedback is:

$$\begin{aligned} \Delta g &= -\frac{\kappa}{L_{\mathrm{c}}}\cos(\omega_{\mathrm{th}}\tau_{\mathrm{ext}}) \\ \Delta\theta_{\mathrm{f}} &= \frac{2n_{\mathrm{g}}L_{\mathrm{c}}}{c}\left(\omega - \omega_{\mathrm{th}}\right) + \kappa\left(\sin(\omega\tau_{\mathrm{ext}}) + \alpha_{\mathrm{LEF}}\cos(\omega\tau_{\mathrm{ext}})\right) \\ &= \left(\omega - \omega_{\mathrm{th}}\right)\tau_{\mathrm{ext}} + C\,\sin\left(\omega\tau_{\mathrm{ext}} + \mathrm{tg}^{-1}(\alpha_{\mathrm{LEF}})\right) \end{aligned} \tag{7.3}$$

where n_{g} is effective group refractive index.

The last equation in Eq. (7.3) represents excess phase equation and it is often used for information extraction in SM applications as in steady state $\Delta\theta_{\mathrm{f}} = 0$ and variable parameters are the feedback level C which contains information on reflectivity of the external mirror and τ_{ext} which contains information on the refractive index of the external mirror and the external cavity length.

7.1.2 Lang – Kobayashi model

The Lang – Kobayashi (LK) model [102] represents the Maxwell equation with the optical feedback, under the slow varying envelope approximation, coupled with the rate equation in diode laser:

$$\begin{aligned} \frac{d}{dt}\left(E(t)e^{j\omega t}\right) = \left[j\omega_n + \frac{1}{2}\left(\Gamma G_{\mathrm{X}} - \frac{1}{\tau_p}\right)\right] E(t)e^{j\omega t} + \tilde{\kappa} E(t-\tau_{\mathrm{ext}})e^{j\omega(t-\tau_{\mathrm{ext}})} \\ \frac{dN_{\mathrm{c}}}{dt} = -\frac{N_{\mathrm{c}}}{\tau_{\mathrm{n}}} - G_{\mathrm{X}}(N_{\mathrm{c}})S + \frac{\eta_i I}{eV} \end{aligned} \tag{7.4}$$

where τ_{p} is the photon lifetime in the cavity, N_{c} is the carrier density, τ_{n} is the lifetime of carriers, I is the injection current, η_{i} is the injection efficiency, $S = |E|^2$ is proportional to the optical power, however it is normalised so that it is in $[\mathrm{m}^{-3}]$ units, $G_0(n)$ is the gain. Note that G_0 is not the material gain, in the original work [102] this parameter is in [1/s] units in the Maxwell wave equation, and in the population equation (Eq (7) in [102]) there seems to be some unit disparity due to the term $-G(n)|E|^2$), however this occurs due to somewhat arbitrary normalisation of E amplitude. This is a common approach with this system of equations [1] mainly designed to accommodate different functional formulas that approximate the gain profile and the injection pumping of the laser. The diode lasers have $I - V$ characteristic that is exponential after the threshold, however in many applications operation around the threshold is of highest interest, and linearisation of the gain profile is performed for convenience [7] by setting $G_{\mathrm{X}} = v_{\mathrm{g}}\alpha_{\mathrm{LEF}}(N_{\mathrm{c}} - N_{\mathrm{th}})$, where α_{LEF} is the linewidth enhancement factor, and N_{th} is the carrier density at threshold.

7.2 Reduced rate equation model for SM effect

The system given in Eq. (7.4) has been constructed for diode lasers where carrier density corresponds to electron-hole pairs that are being generated by injection process and "spent" by carrier recombination and stimulated emission which aims to clamp the gain to the loss (at operating frequency ω). The Maxwell equation in this system is often written as a set of equations that describe modulus and phase, however, since photon density S is coupled to the carrier density, it is convenient to reconstruct the system in Eq. (7.4) to target modulus of photon density $|S|$, phase of the optical field ϕ and keep carrier density equation as is. Note that due to scaling of E the obtained values would not reflect actual optical field, but rather an amplitude of its envelope.

QCL device is a unipolar device that cannot be described by a single parameter for carrier density. The simplest approach is to adopt the two–level model [189] with carrier densities N_3 and N_2 while the effect of other levels in QCL structures is taken by defining injection efficiency η_3 and η_2 at which these levels are pumped with electrons and considering lifetimes and scattering rates of two effective levels generated from parameters of a more general model. The radiative transport in QCL does occur between two levels and this model may provide an adequate treatment of LK equations. The detailed transformation of Eq. (7.4) to describe a two level QCL device given in [189, 91, 192] yields:

$$
\begin{aligned}
\frac{dN_3(t)}{dt} &= \frac{\eta_3}{e} I(t) - (N_3(t) - N_2(t)) G_0 S - \left(\frac{1}{\tau_2} + \frac{1}{\tau_{\mathrm{sp}}}\right) N_3(t) \\
\frac{dN_2(t)}{dt} &= \frac{\eta_2}{e} I(t) + (N_3(t) - N_2(t)) G_0 S + \left(\frac{1}{\tau_{32}} + \frac{1}{\tau_{\mathrm{sp}}}\right) N_3(t) - \frac{N_2(t)}{\tau_2} \\
\frac{dS(t)}{dt} &= \left(M G_0 \left(N_3(t) - N_2(t)\right) - \frac{1}{\tau_{\mathrm{p}}}\right) S(t) + M \beta_{\mathrm{sp}} \frac{N_3(t)}{\tau_{\mathrm{sp}}} + \\
&\quad + 2\tilde{\kappa} \sqrt{S(t) S(t - \tau_{\mathrm{ext}})} \cos\left(\omega_{\mathrm{th}} \tau_{\mathrm{ext}} + \phi(t) - \phi(t - \tau_{\mathrm{ext}})\right) \\
\frac{d\phi(t)}{dt} &= \frac{\alpha_{\mathrm{LEF}}}{2} \left(M G_0 \left(N_3(t) - N_2(t)\right) - \frac{1}{\tau_{\mathrm{p}}}\right) - \\
&\quad - \tilde{\kappa} \sqrt{\frac{S(t - \tau_{\mathrm{ext}})}{S(t)}} \sin\left(\omega_{\mathrm{th}} \tau_{\mathrm{ext}} + \phi(t) - \phi(t - \tau_{\mathrm{ext}})\right) \\
\frac{dT}{dt} &= \frac{1}{m c_{\mathrm{p}}} \left(I(t) V(t) - \frac{T(t) - T_0(t)}{R_{\mathrm{TH}}(T)}\right)
\end{aligned}
\tag{7.5}
$$

where M is the number of periods in QCL structure, ω_{th} is the emission frequency at threshold without the optical feedback, β_{sp} is the spontaneous emission factor, c_{p} is the specific heat capacity and G_0 is the gain factor ([1/s] unit). The last equation was added to include thermal effects. Note that all transport parameters

$(G_0, \tau_3, \tau_2, \tau_{32}, \eta_3, \eta_2)$ in this system depend on temperature and applied voltage. This information needs to be obtained through a more general model that considers more states in transport model, so actually this model represents a hybrid approach.

The system in Eq. (7.5) formulates the reduced rate equation (RRE) model and has been applied to THz QCL structure in [103, 189, 104] and it has resulted in running collaboration with the research group at University of Queensland, Brisbane, Australia. The current collaboration aim is modelling of SM effect under pulsed operation, which has been recently realised experimentally, in the collaboration group [174]. The author has visited this group as part of the project in this thesis, where he provided the temperature dependent input data by the approach presented in Chapter 4. This model can also be extended to consideration of multi–mode behavior and a publication was recently submitted by Dr. Xiaoqiong Qi in Optics Express which uses some of the data obtained in work presented in this thesis.

7.3 Self-mixing effect applications

The applications of SM effect are mainly dictated by excess phase equation in (7.3). This equation has parameters that are related to the properties of the external cavity, internal cavity and the third mirror (the target) giving several degrees of freedom for parameters variation. A detailed review of applications can be found in [91].

The phase in Eq. (7.2) provides the best sensitivity when $\omega\tau_{\text{ext}}$ equals to multiples of $\pi/2$, thus any perturbation would occur with the period that corresponds to the half of the operating wavelength. The product of ω and τ_{ext} can be manipulated and the resulting observable signal would oscillate in correspondence to half a wavelength period. For instance, if displacement of the external cavity is periodically varied (i.e. by a vibrating target) two regimes would be of interest:

- Large displacement regime where the target is periodically displaced by length that is much larger than the half of operating wavelength $\lambda/(2n_{\text{ext}})$. The observed signal will result in periodic fringes that oscillate at half of the operating wavelength, allowing measurement of n_{ext}. Note that in this setup feedback level C is constant, however in weak optical feedback regimes, all fringes occur, while the strong optical feedback would lose sensitivity and simply replicate the driving vibration signal.

- small displacement regime where $\Delta L_{\text{ext}} \ll \lambda/(2n_{\text{ext}})$. In this setup, it is required that small vibrations occur within half a wavelength for best sensitivity, and measurement is best performed with stronger feedback level to compensate for lower sensitivity in this regime.

In a very similar manner, a variation of frequency ω is possible by varying the laser's driving current. This dependence is linear for small variations of current [104], although if the laser works only in single mode, larger dynamic range is possible. The linear shift of frequency in excess phase equation would cause nearly identical behaviour as with the periodic displacement (since phase in Eq. (7.2) is sensitive to the product of ω and τ_{ext}). This measurement methodology is commonly referred to as frequency sweep and it may be exploited for measuring the properties of $\tau_{\text{ext}} = 2n_{\text{ext}}/L_{\text{ext}}$. Note that in this regime laser is tuned, thus the best sensitivity will be achieved at half of wavelength that corresponds to the tuning range (i.e. 300–800 MHz [101]).

The methodology of data extraction from the phase equation can be found in [195], while multiple examples and review of applications is available in [91, 95, 96].

7.4 Maxwell – Bloch dynamics of self-mixing effect

The LK model in section 7.1.2 has been originally constructed for diode lasers which typically have only two levels under consideration. This naturally poses an issue for modelling three or more level lasing systems such as QCL. Considerable effort was invested in the reduced rate equation (RRE) model in section 7.2, whose rate equation approach is based on work in [196]. However, the main issue with LK and RRE models is not the lack of multilevel dynamics and implementation of RE approach, but the fact that LK model has been historically calibrated to diode lasers [193]. This means that modelling approximations that are commonly made for diode lasers need to be inherited and all specifically defined parameters in diode laser models need to have the equivalents or be specifically derived for another type of laser.

For instance, LK model in Eq. 7.4 seemingly has a unit disparity since gain G_{X} has [1/s] and optical field needs to undergo specific scaling to rectify this issue. Additionally, in diode laser it is common to linearise the gain around the threshold as $G_{\mathrm{X}} = v_{\mathrm{g}} a_{\mathrm{LEF}}(N_{\mathrm{c}} - N_{\mathrm{th}})$ or use several different functional expressions for gain to describe the laser characteristics. Overall, simplifying the laser dynamics to a two level model does not necessarily offer a simpler approach since considerable effort needs to be put into determination of parameters that are equivalent to those in diode lasers.

Maxwell wave equation under the slow - varying envelope approximation, on the other hand, has a general form presented in Eq. 6.12 [169, 193] where no linearisation of the gain profile had been performed and no scaling is needed to match the units. Note that LK model in Eq. (7.4) without the feedback term ideally matches the real part of equation in Eq. 6.12 since this equation describes fundamental property of any laser. The feedback term in LK model is added as linearly proportional to the optical electric field, however it is worth investigating how does this term enter the Maxwell equations before the application of slow-varying envelope approximation. In [1], optical feedback is viewed through consideration of an equivalent electric circuit that results in adding $\left(\frac{8\gamma_{\mathrm{e}}}{\epsilon V_{\mathrm{C}}}\right)^{\frac{1}{2}} \frac{dE_n}{dt}$ to the right hand side of Maxwell wave equation obtained through Fourier method presented in Eq. (1.11) where γ_{e} are losses in the external cavity, and V_{C} is normalisation constant. By studying reflections of the electrical field wave in the compound cavity [192] it can be derived that electrical field reinjected into cavity is $\tilde{\kappa}E(t - \tau_{\mathrm{ext}})e^{-j\omega\tau_{\mathrm{ext}}}$, as LK approach suggests. For that reason, the Maxwell-Bloch system for a structure under optical feedback and under the slow-varying envelope approximation can be written as:

$$\begin{aligned}
\frac{d\rho_{\mathrm{dyn}}}{dt} &= \mathcal{L}_{\mathrm{dyn}}\rho_{\mathrm{dyn}} + B_N \\
\frac{\partial E_{\mathrm{R}}}{\partial t} &= \frac{c}{2n}\left(g - g_{\mathrm{th}}\right)E_{\mathrm{R}} + (\omega - \omega_n)E_{\mathrm{I}} + \tilde{\kappa}\,\cos(\omega\tau_{\mathrm{ext}})E_{\mathrm{R}}(t - \tau_{\mathrm{ext}}) \\
&+ \tilde{\kappa}\,\sin(\omega\tau_{\mathrm{ext}})E_{\mathrm{I}}(t - \tau_{\mathrm{ext}}) \\
\frac{\partial E_{\mathrm{I}}}{\partial t} &= -\frac{c}{2n}g_{\mathrm{th}}E_{\mathrm{I}} - (\omega - \omega_n)E_{\mathrm{R}} + \frac{eN_{\mathrm{D}}\omega}{2\epsilon_0 n^2}\,\mathrm{Re}\Big\{Tr(Z\rho_0^{+})\Big\} - \tilde{\kappa}\,\sin(\omega\tau_{\mathrm{ext}})E_{\mathrm{R}}(t - \tau_{\mathrm{ext}}) \\
&+ \tilde{\kappa}\,\cos(\omega\tau_{\mathrm{ext}})E_{\mathrm{I}}(t - \tau_{\mathrm{ext}})
\end{aligned} \tag{7.6}$$

where the feedback term is simply added to the Maxwell-Bloch dynamics equations discussed in the previous chapter. The electric field is in [V/m] units and no linearisation or alteration of the material gain is being performed. Note that these equations can be written in another form, i.e. amplitude and phase equation. For the simplicity of numerical implementation it is convenient to proceed with the system as is, since electrical field phase can be trivially extracted when Eq. (7.6) is solved.

Note that $\tilde{\kappa} = \kappa/\tau_{\mathrm{c}} = (\kappa c)(2nL_{\mathrm{c}}) = v_{\mathrm{g}}/2 \cdot \kappa/L_{\mathrm{c}}$, it is convenient to introduce a new variable $g_{\mathrm{c}} = \kappa/L_{\mathrm{c}}$ that can be physically interpreted as coupling loss. If we assume that operating frequency matches the waveguide mode ω_n, Eq. 7.6 can then be restructured as:

$$\begin{aligned}
\frac{d\rho_{\mathrm{dyn}}}{dt} &= \mathcal{L}_{\mathrm{dyn}}\rho_{\mathrm{dyn}} + B_N \\
\frac{\partial E_{\mathrm{R}}}{\partial t} &= \frac{c}{2n}\left[(g - g_{\mathrm{th}})E_{\mathrm{R}}(t) + g_{\mathrm{c}}\,\cos(\omega\tau_{\mathrm{ext}})E_{\mathrm{R}}(t - \tau_{\mathrm{ext}}) + g_{\mathrm{c}}\,\sin(\omega\tau_{\mathrm{ext}})E_{\mathrm{I}}(t - \tau_{\mathrm{ext}})\right] \\
\frac{\partial E_{\mathrm{I}}}{\partial t} &= -\frac{c}{2n}\left[g_{\mathrm{th}}E_{\mathrm{I}}(t) - g_{\mathrm{c}}\,\sin(\omega\tau_{\mathrm{ext}})E_{\mathrm{R}}(t - \tau_{\mathrm{ext}}) + g_{\mathrm{c}}\,\cos(\omega\tau_{\mathrm{ext}})E_{\mathrm{I}}(t - \tau_{\mathrm{ext}})\right] \\
&+ \frac{eN_{\mathrm{D}}\omega}{2\epsilon_0 n^2}\,\mathrm{Re}\Big\{\mathrm{Tr}(Z\rho_0^{+})\Big\}
\end{aligned} \tag{7.7}$$

Equation that corresponds to the real part of the optical electric field justifies the use of simpler models such as the three mirror approach. The optical feedback can be interpreted as an effective change of the waveguide loss in steady–state as $g_{\mathrm{th_{eff}}} = g_{\mathrm{th}} + g_{\mathrm{c}}\,\cos(\omega\tau_{\mathrm{ext}})$. This also allows using using steady state DM model by simply modulating the loss. The previous work by Leeds group [106] modelled the SM effect by altering the waveguide loss and investigating the change in QCL output characteristics. In this work, we will solve the system (7.7) and provide dynamics study of SM effect in THz QCLs.

7.4.1 Steady–state analysis

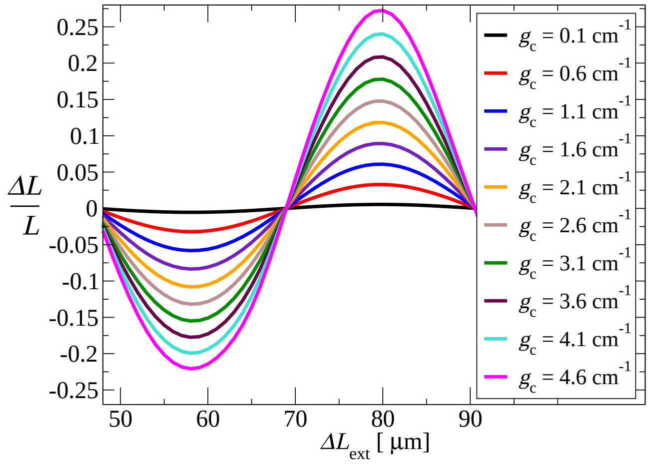

a) Relative change of optical power

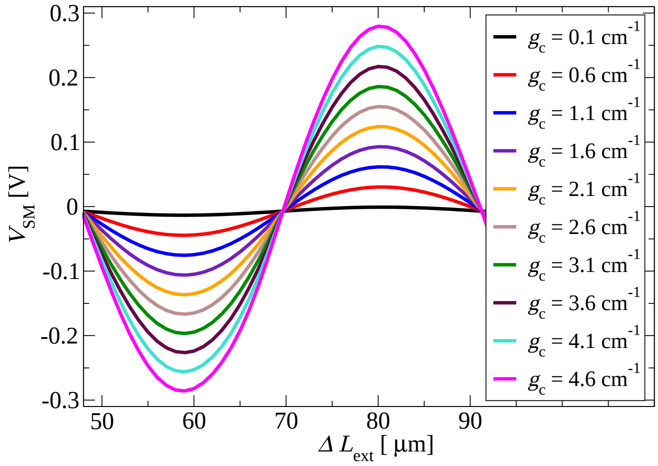

b) Voltage change

Figure 7.2: a) Relative optical power and b) self–mixing voltage dependence on external cavity length $L_{\text{ext}} = 0.7$ [m] $+ \Delta L_{\text{ext}}$ for different values of g_{c} in 3.4 THz QCL [151]. Self–mixing voltage was obtained through inverse interpolation of current density (in steady–state) using the experimental $I - V$ dependence at 20K in pulsed operation.

.

Figure 7.2 displays how the variation of external cavity length on a half wavelength scale affects the self–mixing signal in steady–state. These observations agree with steady–state excess phase model [91]. The value of coupling loss is proportional to the feedback level and these results correspond to moderate and strong feedback regimes (apart from $g_c = 0.1$ cm^{-1}). The 3.4 THz structure used in simulation [151] was fitted to the experiment in previous Chapter at 20 K under pulsed operation in Fig. 6.6. Note that the input in DM model is the external electric bias (proportional to the voltage), thus the model in Eq. 7.7 can provide optical power and current density information and the self–mixing voltage V_{SM} has been obtained through inverse interpolation, while the optical power change has been obtained directly. Note that typical SM applications exhibit voltage signals with amplitudes ≤ 10 mV [93] and operate under weak feedback regime.

With the approach presented in Fig.7.2 we can directly compare with the experiments where the external cavity length is changed on a half a wavelength scale [98] (large displacement measurement [91]). This is typically performed by sinusoidal variation of the external cavity length, therefore replicating the graphs in Fig. 7.2 over the period of the used sinusoid.

Another application of SM effect is the small displacement measurement, where the target is varied on a scale that is much smaller than the lasing wavelength. This is typically done by applying the small modulation signal on the linear portion of sinusoidal dependence displayed in Fig. 7.2.

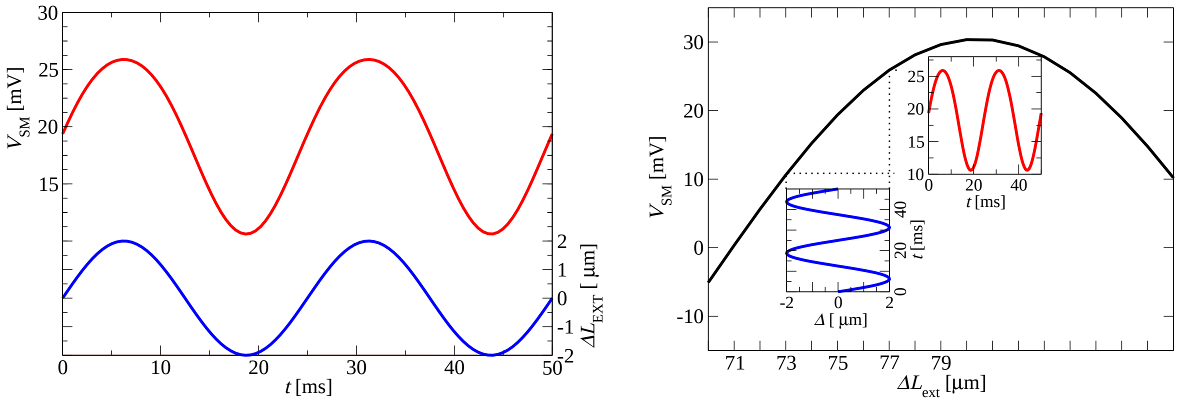

Figure 7.3: Self–mixing voltage signal (red) obtained by variation of external cavity length (blue) $L_{\mathrm{ext}} = 0.7\ [m] + 75\ [\mu\mathrm{m}] + \Delta$ for coupling loss of $g_c = 0.6$ cm^{-1}.

Figure 7.3 is generated by changing the external cavity length through sinusoidal dependence with amplitude of 2 μm, and modulating the large displacement self–mixing voltage signal at $g_c = 0.6$ cm^{-1} around $L_{\text{ext}} = 0.7\ [m] + 75\ [\mu\text{m}]$ where dependence is highly linear as presented in Fig. 7.2. Note that this result has been obtained through interpolation of the data presented in Fig.7.2, as this is a straightforward demonstration of this modulation technique.

7.4.2 Dynamics analysis

The previously displayed results have been obtained through steady–state values of dynamic results. The simulations that model displacement modulation technique (the variation of L_{ext}) have been performed at bias $K = 4.56$ kVcm that corresponds to the current density value of 357.3 $\frac{\text{A}}{\text{cm}^2}$ for 3.4 THz QCL [151] previously fitted to the experiment at 20 K cold finger temperature in Fig. 6.5 where CC scattering was included. The device dimensions used for current density and voltage scaling are $1800 \times 150 \times 14.2\ \mu\text{m}^3$, where additionally contact resistance of 1.2 Ω has been used.

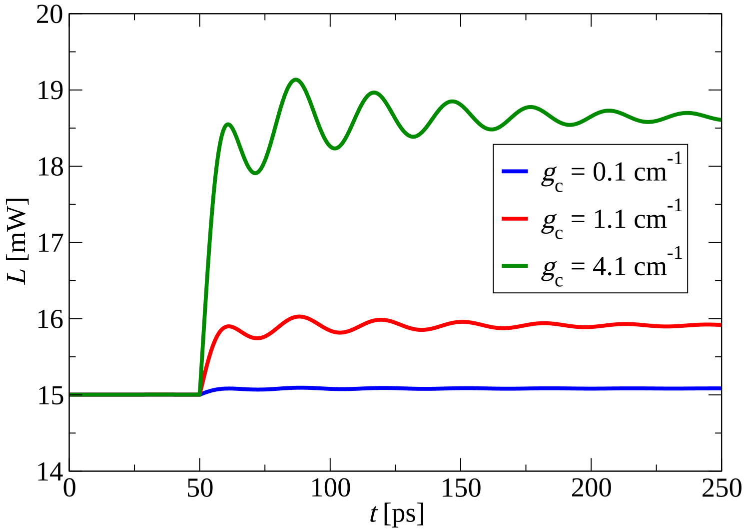

Figure 7.4: Optical power dependence on time for cavity length $L_{\text{ext}} = 0.7\ [m]{+}80\ [\mu\text{m}]$ which corresponds to the highest sensitivity, for different values of coupling loss g_c. The self–mixing feedback is applied at 50 ps at operating bias of 4.56 $\frac{\text{kV}}{\text{cm}}$.

.

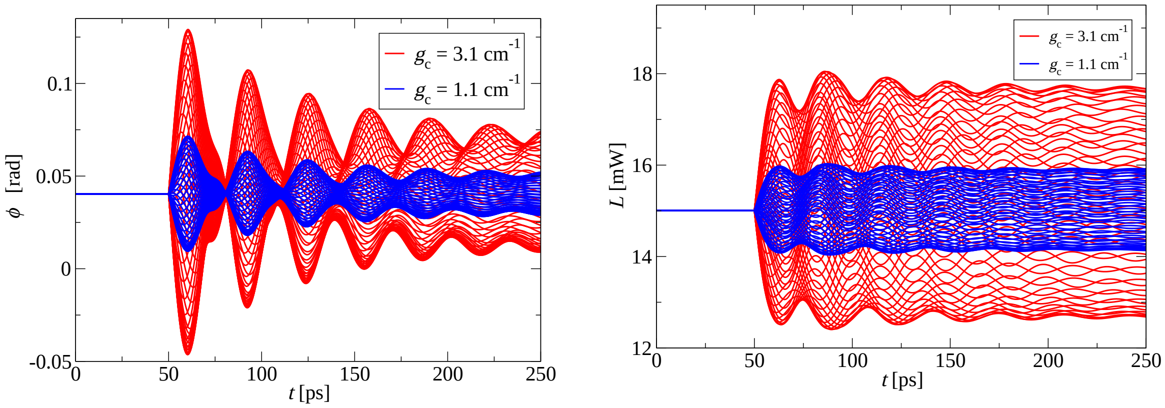

Figure 7.5: Electrical field phase and optical power dependence on time for $g_c = 1.1\ \mathrm{cm}^{-1}$, for different values of external cavity length $L_{\mathrm{ext}} = 0.7\ [m] + 75\ [\mu\mathrm{m}] + \Delta L_{\mathrm{ext}}$, where ΔL_{ext} has been varied in range 50–90 [μm].

.

Figure 7.4 shows the optical power dependence on time as the coupling loss reinjected into the cavity is increased, while external cavity length is kept constant at $L_{\mathrm{ext}} = 0.7\ [m] + 80\ [\mu\mathrm{m}]$ which corresponds to the highest sensitivity of SM effect (peak of dependencies displayed in Fig. 7.2). We can observe that reinjected light causes osculating behavior with higher feedback level. Figure 7.5 displays dynamics of electrical field phase and optical power (which is proportional to electrical field modulus squared) for various values of external cavity lengths with $g_c = 1.1\ \mathrm{cm}^{-1}$ and $g_c = 3.1\ \mathrm{cm}^{-1}$ which reflect the SM feedback strength.

The self–mixing signal is applied at 50 ps, after which the structure experiences oscillations at frequency roughly proportional to the round trip in the internal cavity (the internal cavity length is 1.8 mm, which corresponds to ~38 ps round trip time), similar to seeded laser dynamics [197]. Note that $g_c = 1.1\ \mathrm{cm}^{-1}$ value corresponds to moderate feedback regime and these pulsations reach the steady–state after several oscillation cycles, while the strong feedback $g_c = 3.1\ \mathrm{cm}^{-1}$ results in higher amplitude and longer settling time. Note that very strong feedback levels do not reach steady–state in the simulation (the time scale goes up to 250 ps), additionally the results displayed in Fig. 7.2 do not reflect the behaviour of SM effect under high feedback properly, due to drawbacks of the presented approach.

The simulations in Figs. 7.2 and 7.5 were performed around 1 A of the experimental $L - I - V$ dependence of 3.4 THz structure at 20 K [151]. The frequency in the simulations was kept constant, however the frequency shifts with the increase of current due to Stark effect. The material gain profile displayed in inset in Fig. 6.5 has been obtained from material gain dependence on frequency, at frequency value that yields the maximum material gain. The re–injection of large value of g_c would clearly cause mode hopping that is not considered by the presented approach. Additionally, THz QCLs are electrically heated, even in the pulsed regime as discussed in Chapter 4, thus any modulation of current or voltage would affect the electrical power as well.

The presented model in Eq. (7.7) is able to describe SM effect dynamics to a very high degree and the results obtained so far do agree with SM steady–state theory in three mirror model [91] for weak and moderate feedback level. However, SM effect in THz QCLs is mainly applied in CW operation (until very recent demonstration in pulsed operation [198]) where significant electrical heating occurs. The RRE model [103] couples the heat equation as well and shows that SM fringe generation significantly depends on the device temperature [103]. As the reinjected light modulates the losses in Eq. (7.7) it modulates the optical power and current density (in our model). The change of current also affects the electrical heating of the device, transport characteristics of the medium and operating frequency.

The RRE model is a hybrid approach where information on temperature dependence of model parameters are obtained through steady–state results of a more general model. A non–hybrid approach could be directly implemented in model in Eq. (7.7) by adding the heat equation in the system along with the self–self–consistent Schrödinger-Poisson algorithm. However this would create a numerical model with very high simulation time cost and its feasibility with available computational resources would be questionable. A simpler approach is to create a “look–up” table of the temperature dependence of device parameters, similarly as in RRE approach. The main advantage of the presented model over RRE approach is that it does not need device–specific calibration [189, 103, 104, 101, 174], that it includes consideration of transport in high detail and that it does not need any effective parameters present in diode laser models [7].

Chapter 8

High Temperature Performance Optimisation of THz QCLs

Quantum cascade lasers have undergone multiple stages of development since the initial proposal by Kazarinov and Suris' in 1971 [10]. The resonant tunnelling structure, based on two states in cascading setup as in Fig. 1.2 has not been realised by following that design concept exactly. Nominally, the BTC structures match the proposal paradigm if continuous cluster of states that forms LLL is considered as one effective level. The majority of other designs employ the tunnelling principle that can be effectively represented through a three-level model. The designs of THz structures are very challenging due to the low energy spacing of the radiative transition and non radiative scattering processes that strongly affect the temperature performance of the device. The current high temperature THz QCL designs rely on exploiting the LO phonon scattering process to depopulate the LLL while ULL is being pumped by the tunnelling process through a three level setup. In this chapter, we propose a novel design concept, based on a four level system that uses two LO phonon processes and two resonant tunnelling processes, to both pump and depopulate ULL and LLL, while keeping the required operation bias the same as in the resonant phonon designs. This paradigm has been proposed by the author during the late stages of this thesis project, and optimised structure has not yet been grown, fabricated and experimentally characterised. The author exploited the steady–state transport model discussed in Chapter 4 and implemented a brute-force search for the structure that matches the design criteria. The obtained results show very promising performance and will be presented in this chapter.

8.1 THz QCL designs

In section 1.3 we discussed some fundamental designs for THz QCL. The principle of operation is based on resonant tunnelling as initially proposed in [10], however realisations of QCL at terahertz frequencies have met several significant impediments on high temperature performance that limit the wide–spread industrial application of THz technology.

QCL designs realised so far, did deliver an excellent solution as sources for THz spectrum, however they still represent the pinnacle of semiconductor engineering with an operating temperature limit of ∼200 – 210 K with GaAs/AlGaAs material system [47, 36]. The hope for better performance currently lies in other material systems, however the required technology has not yet matured and only a few THz QCL have been experimentally realised with similar (or worse) performance than with GaAs [44].

In essence, the greatest challenge of any THz source is the requirement for very narrow energy spacing between the lasing levels, of 8 – 15 meV, and in difficulty of maintaining the population inversion. A multitude of factors limit the temperature performance of THz QCLs:

1. LO phonon scattering is a highly detrimental process in semiconductor materials. The resonant energy for this process in GaAs is ∼36 meV, however the process activates on a similar scale as the lasing energy separation. This process may be exploited to assist the pumping or extraction, however it may also act as a parasitic process where it affects both (or more) lasing levels.

2. The tunnelling process creates a desired leakage channel between two QCL periods, however, at high temperatures, this channel may affect both (or more) lasing levels and impede the population inversion significantly.

3. The number of layers per period in the design increases the number of quasi–bound states per period, and therefore the thermal absorption processes are more likely to take place.

4. Operating bias and the current density affect the electrical heating of the device. The current density can be reduced by reducing the doping level, however this reduces the material gain as well. The operating bias can be reduced by adding more layers into the period design, however compromise needs to be made with the previous drawback.

5. Parasitic levels are present in nearly every THz QCL design. For instance, if LO phonon process is used to depopulate the LLL, the well that creates a state that has an energy state that is $\sim$36 meV below LLL, needs to be very wide. A wide quantum well, however, will not produce just one state at low energy, but rather several higher states as well. These states are often used either as LLL or form a miniband below LLL, however in essence, they act as parasitic states that increase the probability of thermal absorption and have detrimental effect on maintenance of population inversion. Higher states also occur in continuum and there is also a danger of transport leakage. The effect of parasitic levels may be reduced by employing higher barriers within the design, however this also causes the reduction of the material gain, and the requirement of the higher doping level which increases the current density, thus another compromise needs to be made. Higher barriers also could make design more sensitive to barrier thicknesses fluctuation during the MBE growth

If we adopt a notation that a miniband of narrowly spaced states can be represented by one effective state, we can then schematically describe a vast number of THz QCL designs by an effective three level schematic model, shown in Fig. 8.1.

8.1.1 3 level schemes

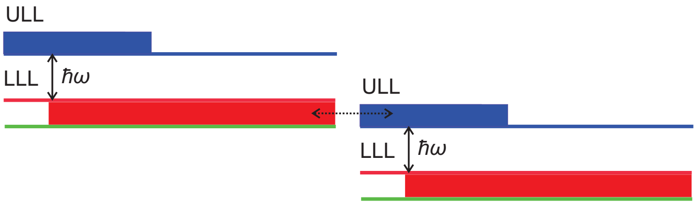

a) BTC design

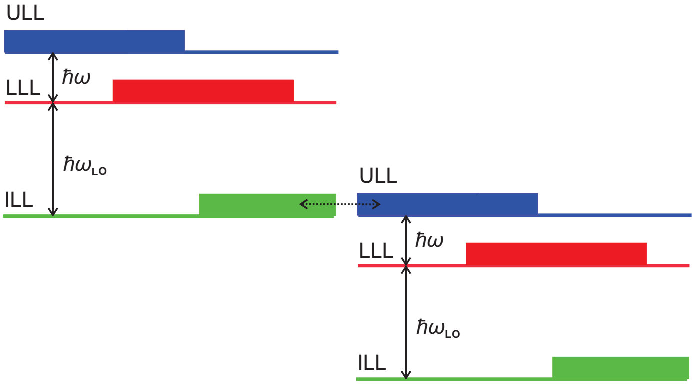

b) Resonant phonon design

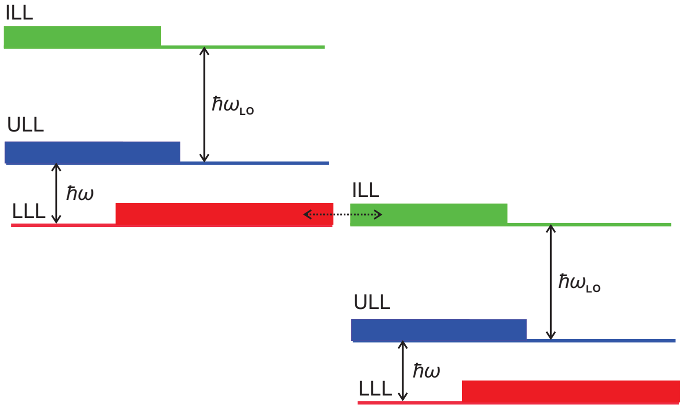

c) Scattering assisted design

Figure 8.1: Schematic diagram of effective three level schemes for THz QCL designs. The rectangles illustrate the typical wavefunction localisation (probability density) of each state within the QCL period. The dotted arrow line illustrates tunnelling process between two adjacent periods, while the solid arrow lines illustrate the transitions. Of course, other trensitions between effective "levels" also exist, however dominant mechanisms are shown.

Figure 8.1 describes the operation principle of the most common THz QCL designs. Note that any state apart from ULL in Fig. 8.1 may be a cluster (miniband) of energetically narrowly spaced states. With such schematic representation a BTC structure considered in Chapter 4 is a two–level system that most closely relates to the original proposal in [10]. However the LLL in BTC structures is in fact a very dense miniband. This results in periods of large length and many states as depicted in Fig. 4.1. Although the operating bias (and the threshold) is very low in BTC structure, the large number of states in the miniband undergoes multiple absorption processes when the temperature is increased, meaning that realising a high temperature performance with BTC design is not possible, or at least not as efficient as other design schemes.

The design in Fig. 8.1b on the other hand has delivered the record high temperature performance [36]. This design can either be implemented with just three states (reflecting the LO-phonon design) or LLL or ILL may be formed through a continuous cluster (reflecting the Hybrid design discussed in 1.3). The Hybrid designs are capable of high temperature operation and have lower operating bias than LO-phonon designs, however they suffer from similar issues as BTC structures due to formation of minibands. A closer study of these designs is needed for better insight into their operation. For instance the former high temperature record [47] that lased up to 200 K (Fig. 1.4) technically has miniband that form the LLL, but it is more frequently classified as a LO–phonon structure.

The record high temperature design [36] (inset in Fig. 4.14f) implemented the scheme in Fig. 8.1b exactly. ULL, LLL and ILL are purely bound states. This was achieved through the use of high barriers (Al content $x = 0.25$) that suppressed the parasitic level created by the widest well. This design used only two wells and parasitic levels were also designed to form a separate leakage channel. By using the model presented in Chapter 4, this structure displays material gain of 20 cm^{-1} (which is a common approximation for the waveguide loss of metal–metal waveguides) up to 250 K (Fig. 4.14f)), however due to the high barriers this design required very high doping level, that resulted in very high current density (3.25 $\frac{\mathrm{kA}}{\mathrm{cm}^2}$) and operating bias (19.5 $\frac{\mathrm{kV}}{\mathrm{cm}}$) which both cause additional electric heating (the device operated at 210 K at $\sim$ 9 A and 25 V) that reduces the operating temperature significantly, as discussed by Eq. (4.1).

A very interesting design scheme in Fig. 8.1c where LO phonon process is used to pump the ULL, rather than extract the LLL has been realised as well [199, 49]. Conceptually the pumping and extracting mechanisms have switched places, showing that tunnelling effect can be used for LLL extraction as well. This design did not show temperature performance as good as its counterpart. Note however, that not many realisations of this principle have been realised and several different proposals promise better performance [200, 201, 50]. The issues of this design lie in very high operating bias and the fact that the tunnelling is the most sensitive process in any QCL design. At first sight, extracting LLL through the tunnelling effect allows fabrication of thinner injection barriers, and ULL should not be leaking significantly since it is mainly localised in the other end of the period. However, experimental realisations delivered devices that have no significantly different performances than previous designs.

It is difficult to be conclusive which process is crucial for high temperature performance and several “exotic” proposals with asymmetric wells or barriers have been attempted and proposed [50, 202]. Both of the designs involving LO phonon transition in Fig. 8.1 have the same concept: LO phonon process is used for extraction, the tunelling process is used for injection or vice versa. It is clear that at high temperature these two processes affect the other state as well. The record high temperature design [36] actually uses 41 meV separation between LLL and ILL, mostly to suppress the depopulation of ULL at high temperature which is one solution to the issue, that also increases the operating bias of the device. The last design in 8.1 served as an inspiration to the author for the proposal that will be presented in this chapter. A simple question can be asked: “Can we add another LO phonon process to achieve both pumping and extraction by it?”.

8.1.2 4 level schemes

A summary of several realised QCLs that can be effectively shown by a 4 level scheme is presented in Fig. 8.2.

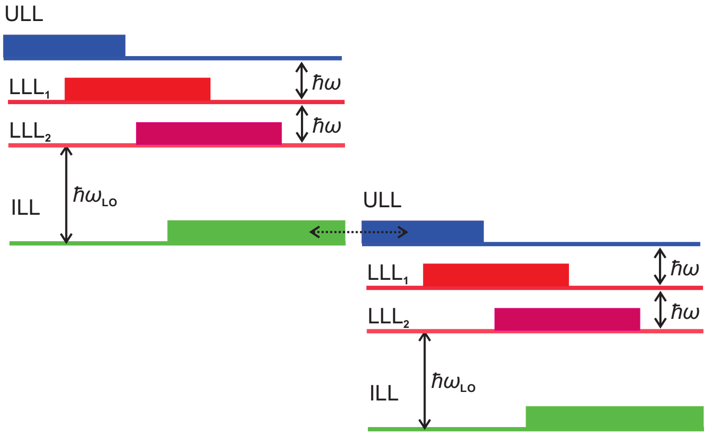

a) Dual lasing design [203]

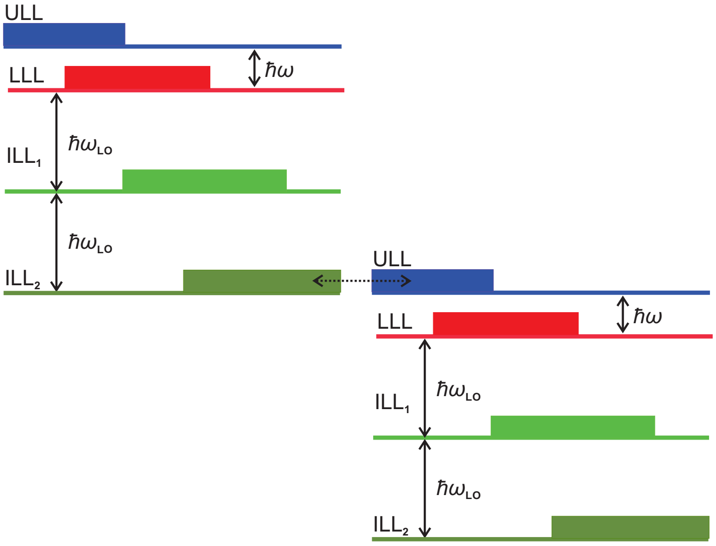

b) Double phonon design [204]

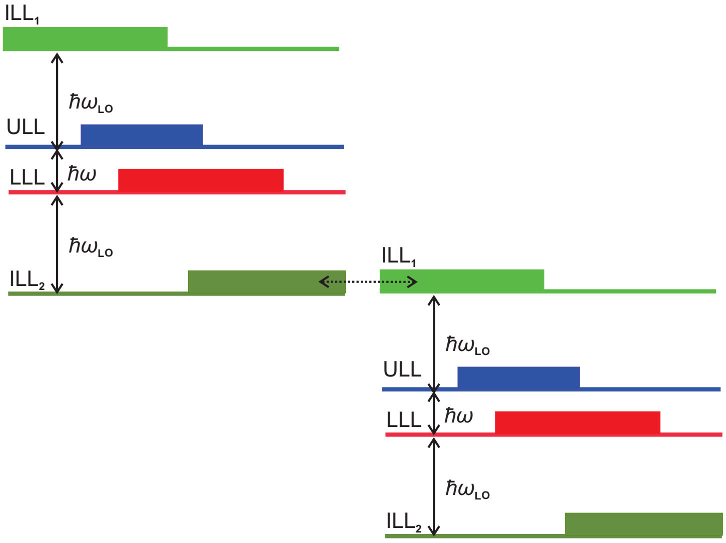

c) Phonon–Photon–Phonon design [205, 51, 48]

Figure 8.2: Schematic diagram of effective four–level schemes for THz QCL designs. The rectangles illustrate the typical wavefunction localisation (probability density) of each state within QCL period. The dotted arrow line illustrates tunnelling process between two adjacent periods, while the solid arrow lines illustrate the transitions.

Figure 8.2a shows a design where two radiative processes take place. This design is not of interest for high temperature performance, however the interesting paradigm of the operating principle has been experimentally achieved [203].

A concept in Fig. 8.2b has been investigated [204, 206] in early development of THz QCLs. The realisations showed good temperature performance (up to 138 K) which was mainly limited due to use of very high barriers ($x = 0.3$) that was required to achieve such large energy spacing. By comparing the schemes in Fig. 8.2b and Fig. 8.1b it can be concluded that this setup does not offer much improvement. The existence of two consecutive LO phonon transitions may achieve better injection of ULL, however the extraction process of LLL remains the same, along with all parasitic issues at high temperatures that occurred in the designs in Fig. 8.1.

The most interesting design is presented in Fig. 8.2c. This structure employs two LO phonon transitions to pump and extract the lasing levels, and the tunnelling process is essentially not directly employed in the maintenance of the population inversion. This design has achieved a very high temperature performance [51] of 144 K at 2.1 THz and structure in [48] lased at 1.8 THz at 155 K. Note that losses at 2.1 THz and 1.8 THz are very high [152, 207] giving hope for achieving much higher temperature performance at frequencies where losses are smaller. The device fabricated at 3.2 THz [205], however, did not provide significant improvements as it operated up to 150 K. The underlying issue of the design scheme in Fig. 8.2c can be attributed to the need of very high barriers and high operating bias.

The resonant bias of any THz QCL structure is determined by:

$$\begin{aligned}
K &= \frac{\Delta E_{\mathrm{R}}}{eL_{\mathrm{P}}} \\
\Delta E_{\mathrm{R_1a}} &= \hbar\omega + \Delta E_{\mathrm{LLL}} \\
\Delta E_{\mathrm{R_1b,c}} &= \hbar\omega + \hbar\omega_{\mathrm{LO}} + \Delta E_{\mathrm{minibands}} \\
\Delta E_{R_2a} &= 2\hbar\omega + \hbar\omega_{LO} + \Delta E_{\mathrm{minibands}} \\
\Delta E_{\mathrm{R_2b,c}} &= \hbar\omega + 2\hbar\omega_{LO} + \Delta E_{\mathrm{minibands}}
\end{aligned} \tag{8.1}$$

where ΔE_{R} is the required energy separation needed to bring the states into tunnelling resonance. $\Delta E_{\mathrm{R_{1a,b,c}}}$ corresponds to cases displayed in Fig. 8.1a,b,c while $\Delta E_{\mathrm{R_{2a,b,c}}}$ corresponds to cases displayed in Fig. 8.2a,b,c, ΔE_{LLL} is the energy spacing of miniband that forms the LLL in BTC design in Fig. 8.1a and $\Delta E_{\mathrm{minibands}}$ is added to the formula in case that some of the levels form a miniband (similarly as the case with ΔE_{LLL}).

The four level designs in Fig. 8.2 share the same issue. If two LO phonon transitions take place, the required energy separation is much larger than for the designs in Fig. 8.1 that use one LO phonon transition. This means that for similar period length, the applied voltage needs to be significantly higher as well. This can be rectified by engineering designs with longer periods, however any addition of states into the design increases the chance of thermal absorption processes that impede temperature performance. Additionally, achieving a design with such a large energy spacing is highly challenging. Note that in any quantum well system, the electrons would always tend towards the lower potential energy. Exciting the carriers to the fourth level and maintaining its population through pumping process represents a big challenge.

Overall, the design in Fig. 8.2c did not solve any problems of 3–level resonant phonon schemes, but rather doubled their issues. At high temperature, the pumping process may leak to the LLL, and on the other hand, the extraction process may also extract the ULL. In addition to this the operating bias is significantly higher leading to higher electrical heating. These issues potentially explain the non–ideal temperature performance in [205].

Note that the concepts presented in Fig. 8.2 have not been fully investigated, for instance an inverted structure similar to 8.1c can be obtained for a design in 8.2b. Any level (apart from ULL) can be formed from a miniband in the presented schemes, which would not nominally improve the temperature performance, but it might open other potential applications. A good review of THz QCL designs can be found in [208].

Interestingly, a concept similar to 8.2c that solves all discussed issues above is possible. This is an original work proposed by the author, and will be presented in the next section.

8.2 Novel proposal – Double resonance phonon–photon–phonon design

If we closely examine the phonon–photon–phonon design in Fig. 8.2b, we can notice that this is a symmetric scheme if only one period is considered. Since the ILL_1 and ULL separation is equal to the separation between LLL and ILL_2, the resonance can also be achieved by applying the old resonant phonon paradigm where ILL_2 pumps the ULL through the tunnelling process. The schematic of the design is shown in Fig. 8.3.

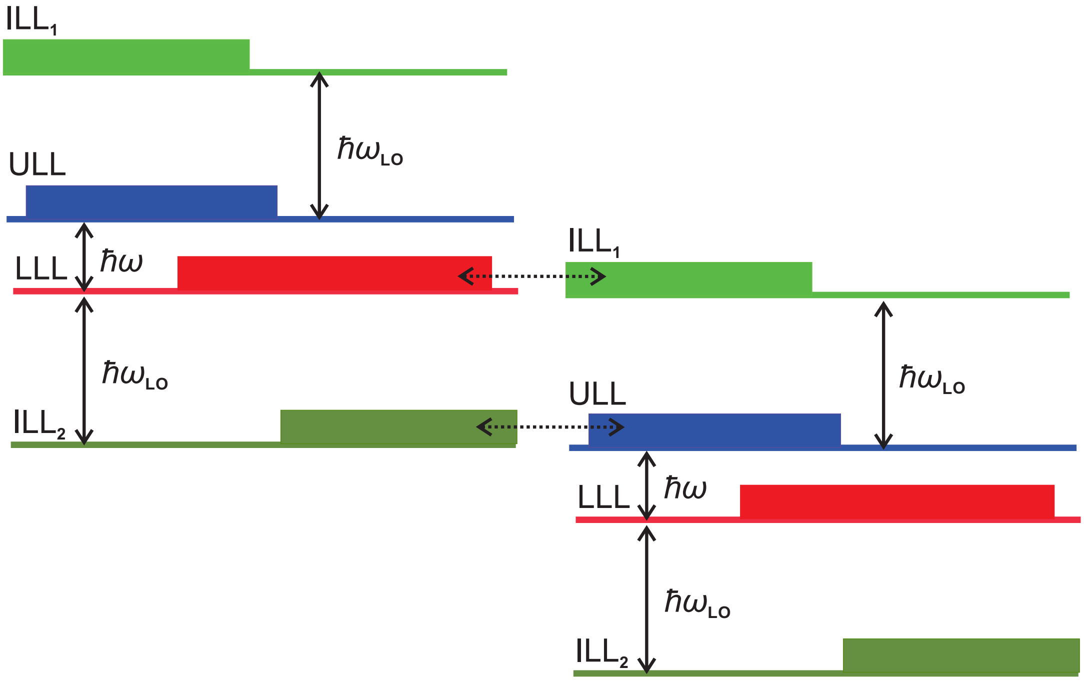

Figure 8.3: Schematic diagram of new THz QCL design proposal. The rectangles illustrate the desired wavefunction localisation of each state within the period. The dotted arrow lines illustrate the tunnelling processes between adjacent periods, while the solid arrow lines illustrate the desired transitions.

The proposal in Fig. 8.3 can be viewed as a four–level phonon-photon-phonon proposal that undergoes two tunnelling processes, or as a three level resonant phonon scheme where ILL_1 is added to act as a parasitic state that assists the extraction and pumping processes. In either case, this proposal offers the following advantages:

- The required potential drop is identical as in the three–level designs (in Eq. (8.1)): $\Delta E_{\mathrm{R}} = \hbar\omega + \hbar\omega_{\mathrm{LO}}$.
- Pumping of ULL is achieved both by the tunnelling process and the LO phonon process that extracts parasitic leakage from the previous period.
- Extraction from LLL is achieved both by the LO phonon process and through the resonant tunnelling process to the next period.

- The operating bias is lower than the one in three–level designs, since additional well (and barrier) is needed, in order to generate ILL$_1$ state, which results in larger period length.

The potential disadvantages are:

- The design may require high barriers to generate the ILL$_1$ state in order to suppress the higher parasitic states created by the widest well (that is needed to create ILL$_2$ and LLL) and to achieve operating frequency that has low loss (3.2 – 4 THz).
- The double tunnelling process may be affected by growth, as this design needs precise layer thicknesses growth to avoid parasitic depopulation of ULL.

At first sight, this design solves all parasitic processes that may be responsible for temperature degradation of three level LO phonon designs. The full symmetry of transitions in Fig. 8.3 may even treat this scheme as the authentic two level design by [10] where one needs to effectively view the resonantly coupled states as one state. At high temperature, if ILL$_1$ starts to pump the LLL as well, a part of population of LLL will be reinjected to ILL$_1$ into the next period, similarly if ILL$_2$ starts to extract the ULL as well, a part of population of ULL will be injected into ULL in the next period. Similar principle arises in case that one of the tunnelling processes starts to pump/extract the undesired state.

Although this seems to be a conceptually very good design, it is challenging to find the layer sequence to match the design criteria. The biggest challenge lies in potential parasitic states that may occur in the vicinity of ILL$_1$. Additionally, similar designs to this one do not exist in the literature (to the best of author's knowledge) thus it is not possible to alter the layers' thicknesses around already known designs. The author proposed this structure in final stage of his project, and the development of optimisation algorithm, based on the transport model presented in this thesis, was not possible. However, the author did perform a brute–force search for the design in Fig. 8.3 which will be discussed in the next section.

8.3 Brute – force optimisation of THz QCLs

The steady–state model presented in Chapter 4 displayed potential applicability for high temperature optimisation as discussed in 4.5 and presented in Fig. 4.14.

As the first step, the design in Fig. 8.3 can be achieved by adding only one (wide) well to a scattering assisted three level design, such as [49], and altering its layers. This was performed by the author, and the increase in temperature performance was instantly achieved, however the addition of another well perturbed the lasing level, and reduced the pumping transition below 36 meV which is far from optimal setup.

The numerical implementation of the DM model, performed by the author, is able to simulate a $3 - 6$ level structure at a single bias point within 10 seconds. Such a fast calculation requires disabling the calculation of optical power, reducing the number of iterations of Schrödinger-Poisson equation (which typically does converge in 8–15 iterations, although very good convergence occurs with 4 iterations in structures with a few states in the period) and neglecting EE scattering mechanism. This allows sweeping the operation bias range with 30 points within 5 minutes.

The numerical implementation also has access to a supercomputer cluster Advance Research Computing 2 (ARC2) within the University of Leeds. For that reason, the author performed a multitude of brute–force simulations.

The starting parameters and layer variation range were not taken arbitrarily. The simplest implementation of the design in Fig. 8.3 requires at least three wells. The first well needs to be very narrow (40 – 60 Å) in order to generate a state at high energy, the subsequent barrier needs to be very thin in order to achieve good coupling with the well that generates ULL, the second well needs to have the width commonly employed in two and three–well resonant phonon design (55 – 90 Å), the second barrier needs to be thick in order to generate the diagonal radiative transition which is more desirable at high temperature and the last well needs to be very wide (130–180 Å) in order to create extraction state and lower lasing level. The last layer is the injection barrier and this will not be varied, as the DM model performs the tight binding approximation and nearly every realised THz QCL has injection barrier in very narrow range 3.8–4.5 nm at x=0.15, which is typically reduced by one monolayer as x rises by 2%.

Nominally, highly doped structures would exhibit high current density and material gain would increase with doping, until the saturation [209], however this is not relevant for high temperature designs. The doping is usually applied to the widest well. Although the doping of different parts of the well is feasible during the growth, author adopted the doping value of $1.3 \cdot 10^{16}$ cm^{-3} which was used in the previous record high temperature design [47]. Note that technically, the sheet doping density per period would therefore vary as the thickness of the widest well varies, however this is a very low doping for typical THz QCLs. The reason for low doping in [47] was to reduce the current density and therefore the electrical heating. The barrier height was varied (Al content) in the range $0.15 - 0.25$, table 8.1 shows the variation range of each layer, the layer thickness step was equal to the thickness of one monolayer (2.825 Å).

Layer no.	x	Range [Å]	Number of points
1.	0	39.55 – 67.8	11
2.	0.15–0.25	5.65 – 16.95	5
3.	0	39.55 – 67.8	11
4.	0.15–0.25	19.75 – 48.025	11
5.	0	135.6 – 166.675	12
Total:	11 variations	240.1 – 367.25	79860 per one x value

Table 8.1: The layer thickness variation of a three well structure. The variation step is thickness of a single monolayer (2.825 Å), the fourth column indicates the variation resolution of each layer for one value of x. Total number of performed simulations is therefore $\approx 11 \times 79860$.

Table 8.1 shows the ranges and number of simulation points mainly for $x = 0.15$. When structures with higher barriers were simulated, it was taken into account that some layer variation ranges need to be slightly altered (i.e. barrier thicknesses can be reduced). Overall, roughly $\sim$ 900 000 QCL structures have been simulated!

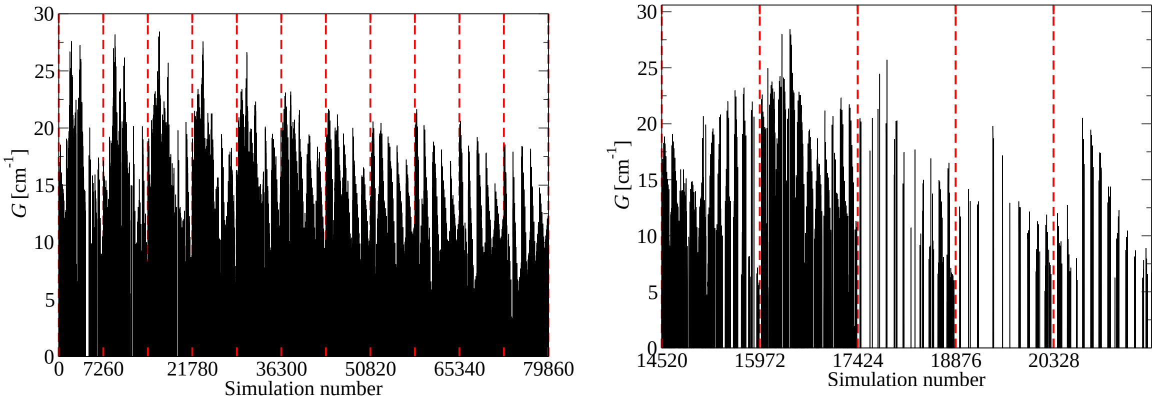

a) Layer 1 b) Layer 2

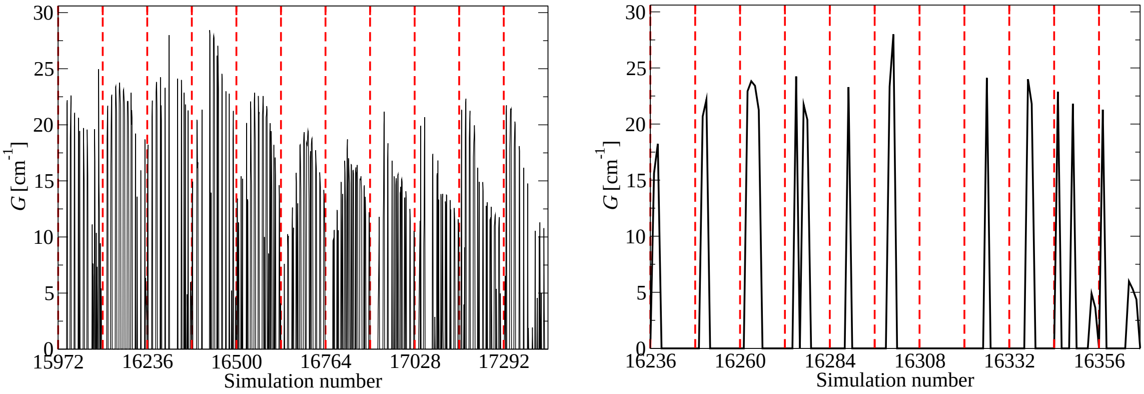

c) Layer 3 d) Layer 4

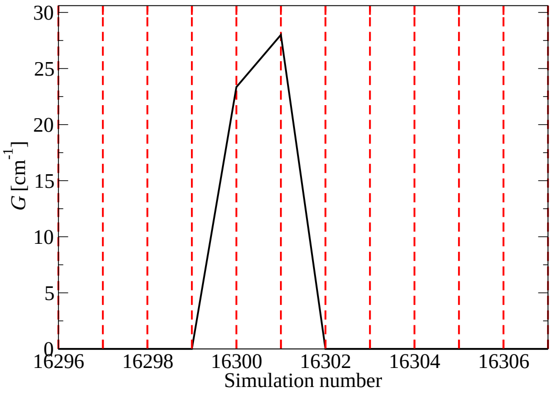

e) Layer 5

Figure 8.4: Material gain at 250 K, for structures obtained by layer thickness variation displayed in Table 8.1 where barriers had $x = 0.16$ Al fraction. The dotted vertical lines depict the number of points varied within each layer. Graph a) displays the result of all performed simulations, while b,c,d,e are zooming in towards the simulation that yielded the highest value of material gain. Note that simulations that yield material gain values below 15 cm^{-1} are set to zero for clearer presentation.

Figure 8.4a shows the material gain dependence on the number of the performed simulations. The layer thicknesses in Table 8.1 have been varied by five nested loops, thus Fig. 8.4 displays the periodicity that corresponds to the number of points varied within each layer. This figure provides visual information on whether the structure has high material gain at 250 K, and it also displays the effect of thickness variation of each layer. This information can be used during the design to depict which layer is most sensitive to growth tolerance and also to justify the layer thickness variation range used in the simulation (ideally, each enlarged graph in Fig. 8.4 should display parabolic dependence). Note that simulations that yielded material gain below 15 cm^{-1} have been suppressed.

The simulation with the highest material gain Fig. 8.4 is not necessarily optimal, and selection of the structure cannot be obtained from the graph alone. As discussed earlier, operation electric filed (corresponds to the terminal voltage) has significant effect on temperature performance. In Eq. 8.1 the resonant energy difference is nominally set to the same value as in two well resonant phonon devices ($\sim 36 + 12$ meV per period), meaning that the period length is the main factor on the resonant bias. Simulations that have smaller simulation number also have shorter periods and therefore larger resonant bias.

Figure 8.4 also does not display the lasing frequency. Several works [152, 207] show somewhat conflicting threshold gain values in metal–metal waveguides at high temperatures. The work in [152] shows that threshold gain has a minimal value of $\sim$ 20 cm^{-1} in range $3.3 - 3.8$ THz, at room temperature, while work in [207] predicts increase of threshold gain with temperature along with the frequency shift, at 300 K, minimal threshold gain $\sim$ 25 cm^{-1} would occur around 5 THz. It is beyond the scope of this thesis to provide in–depth discussion of waveguide loss models. Experimentally, the structures that lase around 3.3 THz provide the best performance, the highest operation temperature devices lase at 3.3 THz [47] and 3.8 THz[36], however due to the lack of designs at higher temperatures the value of threshold gain is debatable. For simplicity we will adopt the prediction in [152] and estimate the loss of $\sim$ 20 cm^{-1}.

The simulations in Fig. 8.4 have been performed by doping the widest well to $1.3 \cdot 10^{-16}$ cm^{-3}. This is typically a very low doping level, chosen in order to reduce the current density and electrical heating effects. Higher material gain can be obtained by higher doping. Note that similar simulation diagrams have been obtained for $x = 0.15 - 0.25$, however finding the optimal value is challenging due to the fact that higher barrier devices yield smaller material gain, which on the other hand can be counteracted with the higher doping. Additionally, the choice of doping the widest well to a preset value causes the variation of sheet doping profile since the widest well width is varied as well.

The procedure for selecting the best device first sorted the simulations results by the value of the material gain and then by the value of the resonant frequency. Designs with smaller barrier i.e. Al mole fraction in the range $x = 0.15 - 0.18$ yielded more structures with lasing frequencies below 3 THz, while higher barrier simulations provided higher frequency structures, however with the lower material gain. The layer sequences of best structures at x=0.16 and x=0.25 are presented in Fig. 8.5.

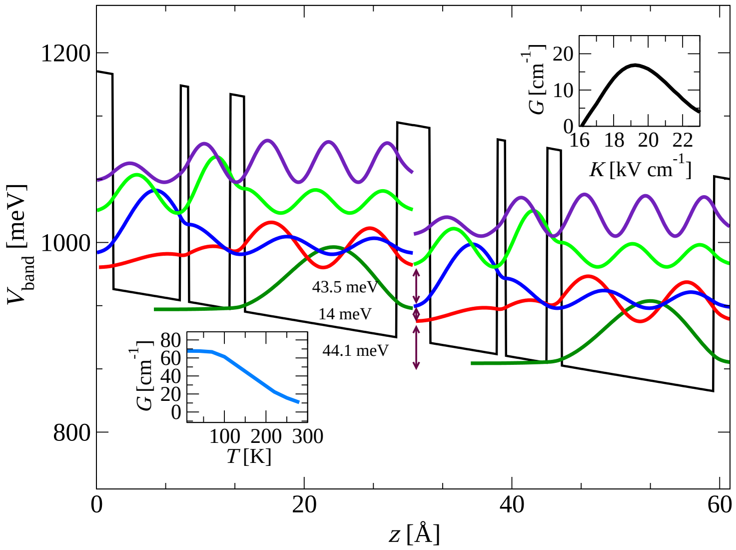

a) 3.5 THz QCL: **4.236**/4.52/**0.8475**/4.8025/**3.1075**/<u>*14.9725*</u>

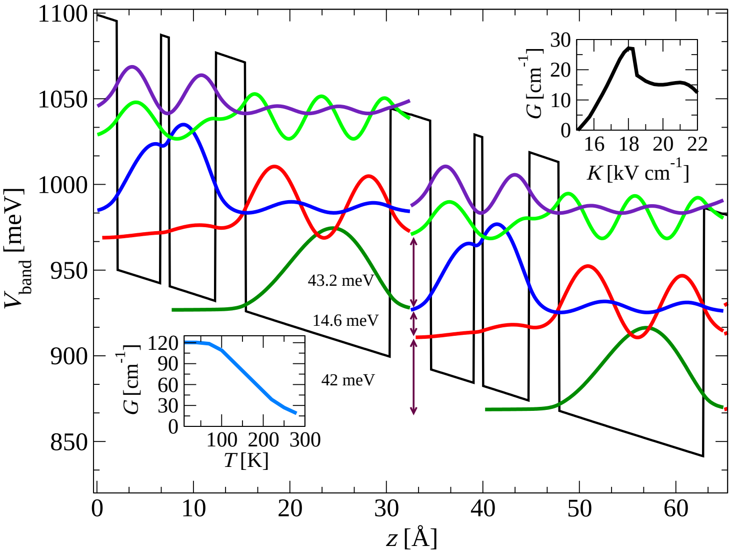

b) 3.4 THz QCL: **3.107**/6.4975/**0.8475**/3.955/**1.4125**/<u>*14.69*</u>

Figure 8.5: THz QCL design where layers in bold text use barriers a) $Al_{0.16}Ga_{0.84}As$ and b) $Al_{0.25}Ga_{0.75}As$. The well doped to $1.3 \cdot 10^{16}\text{cm}^{-3}$ is underlined. Wavefunctions are obtained at 250 K at resonant bias. Material gain dependence on bias is shown in the top inset, while its temperature dependence at resonant bias is shown in the bottom inset.

The structures in Fig. 8.5 have been selected out of multiple potential candidates that implement the design paradigm in Fig. 8.3. The injection barrier was not varied in the simulation, because DM model works within the tight binding approximation. Note that this design might accept thinner barriers because both injection and pumping process are assisted by LO phonon scattering. However, this prediction was also made for scattering assisted QCLs [200, 75] while most of experimental realisations still used the barrier thicknesses common for typical resonant phonon structures [49]. If the injection barrier thickness in the first design in Fig. 8.5 is reduced by two monolayers, to 3.672 nm, the material gain would increase by 5 cm^{-1}. Similarly, if sheet doping density is doubled in both designs, the material gain would increase by ∼7 cm^{-1}, however the current density would nearly double as well to very high value (over 3 $\frac{\mathrm{kA}}{\mathrm{cm}^2}$).

Figure. 8.5a does not implement the proposed design from Fig. 8.3 directly. The design has a parasitic state that is partially depopulating ULL. This creates a dual lasing channel, one between the ULL and LLL, and one between the parasitic state that depopulates ULL and LLL. This channel is not efficient since ULL is mostly localised at the beginning of the period and is already depopulated by the originally designed lasing transition. The high temperature operation is achieved mainly by very high material gain. Note that the bottom inset in 8.5a shows that this design displays material gain of over 120 cm^{-1} (which is the highest value that we obtained from any simulated THz QCL so far, typical values are 30-40% lower, as depicted in Fig. 4.14). On the other hand, the resonant bias is 18 kV cm^{-1} and the current density is 1.79 kA cm^{-2}. Note that the optical power was not calculated in order to increase the simulation speed, and the IFR parameters were chosen to their typical values, thus the current density estimation is approximate.

Figure. 8.5b does implement the proposed design in Fig. 8.3 although the added state is distributed throughout the entire period. The design has one higher parasitic state that may have detrimental effect on the temperature performance. The design itself does not exceed the approximated loss of 20 cm^{-1} at 250 K, however the temperature dependence of material gain, give in the bottom inset, shows an impressive improvement that exceeds the previous two record high temperature designs [47, 36]. The resonant bias is 18.75 kV cm^{-1} and the current density is 2.1 kA cm^{-2}. This would lead to lower electrical heating than the current record design [36] (19.5 kV cm^{-1} and 3.25 kA cm^{-2}), mainly credited to low doping.

The simulations conducted with barriers with $x = 0.18 - 0.22$ Al content, produced structures with very high operating frequency (4–5 THz) and structures that operate in phonon–photon–phonon scheme, shown in Fig. 8.2. Although simulations gave high material gain, the resonant bias was very high ($\geq$ 30 kV cm^{-1}). The reason why the desired design was suppressed by the simulations is the fifth parasitic state shown in Fig. 8.5. At low Al content this state creates dual lasing channel, while at high Al content it is less relevant to transport. In between, however, this state is highly parasitic and impedes the structure operation.

All simulations were performed by limiting the number of states to five, in order to increase the simulation speed. Given that it is possible for the sixth state to impede performance, it was added only in simulations for x=0.15 and x=0.23. At x=0.23 the results were very similar, however at x=0.15 the maximum material gain has dropped by 8–9 cm^{-1}, to slightly below 20 cm^{-1}. One of the best designs is presented in Fig. 8.6.

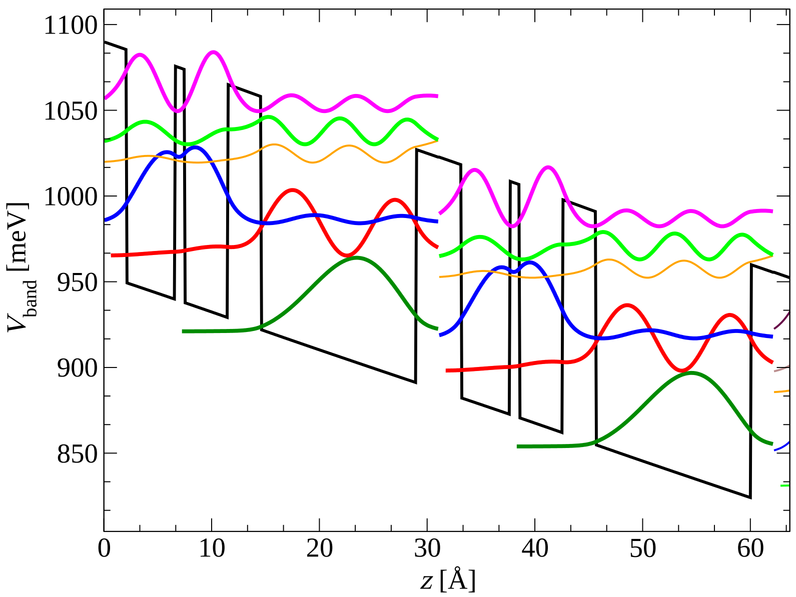

Figure 8.6: 4.43 THz QCL with layer sequence **4.236**/4.52/**0.8475**/3.955/**3.1075**/<u>*14.4075*</u>. $Al_{0.15}Ga_{0.85}As$ barriers are shown in bold and the well doped to $1.3{\cdot}10^{16}$ cm^{-3} is underlined. Two periods are shown at the resonance bias $K = 21.75\ \frac{\text{kV}}{\text{cm}}$ along with the corresponding wavefunctions moduli squared.

When the additional state is added into simulation, the operating principle in Fig. 8.6 is similar to the one in Fig. 8.5a, where the parasitic state creates dual lasing channel, however this is now the highest (sixth state) in the design, the fifth state depopulates LLL, while the forth state essentially creates a miniband with the fifth state. Due to closely separated parasitic states, the material gain at 250 K is lower. Note that addition of another state in the simulation did not have detrimental effects when very large barriers are used, mainly because high states are not relevant for transport.

Overall, the conducted simulations provide identical debate to discussion of two well THz QCL designs in resonant phonon scheme. High barriers suppress parasitic states, but increase the operating bias and threshold current, while low barriers exhibit parasitic leakage. The main difference in this debate is that typical two well THz QCL designs do not operate well at high temperatures due to high electrical heating, apart from the record temperature performance that was required high doping to counteract disadvantages of using high barriers. All designs in this chapter used very low doping, giving further motivation for device optimisation.

The new design in Fig. 8.3 has been proposed in very late stages of author's project and further work is needed in developing systematic classification of the simulated structures and implementing an optimisation algorithm instead of brute force approach. The main conclusion of this section is that parasitic states need to be considered in the design. The presented results do resemble the discussion of two well THz QCLs (as this design just adds a narrow well before it, to introduce the desired parasitic state), and the next step is simulating devices with additional well or even two wells. Addition of one well in this design, would ideally introduce another level below ULL, similar to the previous record temperature structure [47], shown in Fig. 1.4. This level would then ideally be in resonance with ILL and parasitic states, as noticed in this section, which would avoid dual lasing channel, achieve very efficient extraction of LLL and most importantly, significantly reduce the operating bias and current density.

Figure 8.7 shows a design that was obtained only by variation of well thicknesses (this was performed as a test).

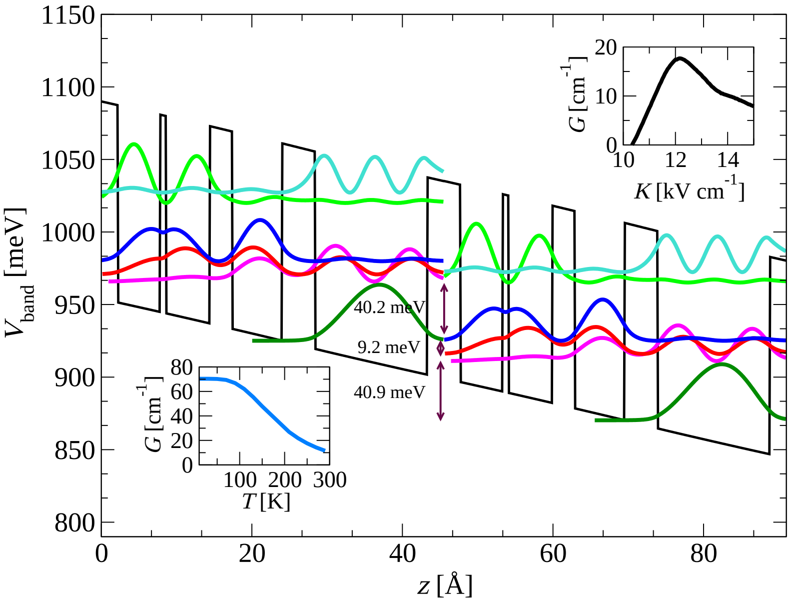

Figure 8.7: 2.6 THz QCL with layer sequence **4.4**/5.6/**0.8**/5.8/**3.0**/6.6/**4.4**/*14.9*. Al$_{0.15}$Ga$_{0.85}$As barriers are shown in bold and the well doped to $1.3 \cdot 10^{16}\mathrm{cm}^{-3}$ is underlined. Wavefunctions are obtained at 250 K at resonant bias. Material gain dependence on bias is shown in the top inset, while its temperature dependence at resonant bias is shown in the bottom inset.

The structure in Fig. 8.7 is not an optimal design, however it still displays very good temperature robustness. The parasitic states have aligned as desired, resonant bias has been significantly reduced (12.1 kV cm^{-1}) along with the current density of 1.7 kA cm^{-2}. Note that 4.4 nm barrier in the active region mainly limits the material gain value (as lasing transition is highly diagonal). Additional simulations that vary more layers are required in order to obtain the optimal design at higher frequency. This will provide a prospect of future optimisation followed by growth, fabrication and characterisation of selected set of the designs.

Note that energy spacings between levels that undergo LO–phonon transition are around 40 meV in all structures that simulations yielded as best. This also occurred in the record temperature design [36] that was optimised by NEGF model. This was expected, because the slightly higher energy than LO–phonon energy in GaAs ($\sim$ 36 meV) suppresses potential leakage that is more likely to occur at higher temperature. Note that if high material gain operation at lower temperature was of interest, the energy spacing nearer to 36 meV would most likely be more optimal.

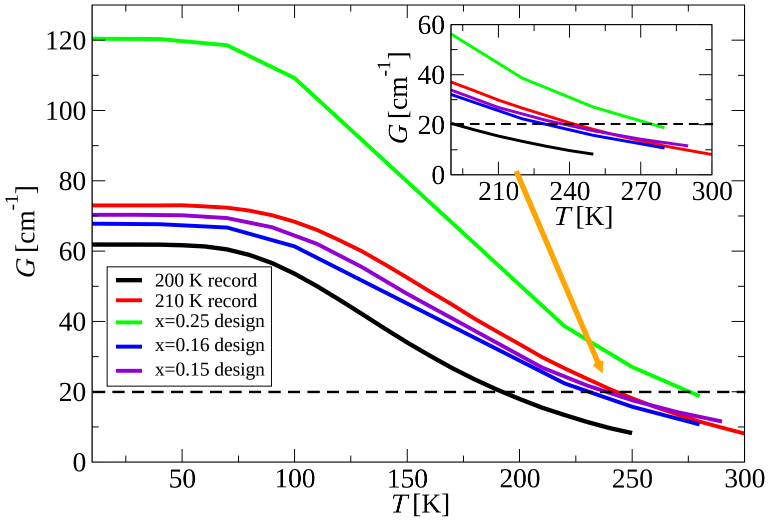

Figure 8.8: Material gain dependence on temperature at resonant bias of 200 K structure [47] (black), the record 210 K structure [36] (red), the proposed design with AlAs barrier content of x=0.25 in Fig. 8.5b (green), the proposed design with AlAs barrier content of x=0.16 in Fig. 8.5a (blue) and the proposed four well design with AlAs barrier content of x=0.15 in Fig. 8.7 (violet). The inset shows these results around the gain value of 20 cm^{-1} which is the assumed threshold gain.

Figure 8.8 displays the summary of presented designs in this Chapter and also compares with the simulations of already experimentally realised record operation temperature devices. Note that all proposals have very high gain value at 200 K and comparable behaviour with the record temperature design [36], with an important note that doping is lower (the sheet doping density per period in all proposed designs is $\sim 2 \cdot 10^{10}$ cm^{-2}, while in [36] it is $\sim 4.5 \cdot 10^{10}$ cm^{-2}) and therefore the current density is lower and resonant bias is also lower. All this suggests that these designs may provide a better performance. The four–well design has a significantly lower current density and resonant bias and is the best structure designed so far by this model, even though this is not an optimised design, and 2.6 THz frequency would exhibit higher loss.

Chapter 9

Conclusion and future work

The presented work in this thesis has provided a detailed overview of DM model for THz QCLs along with various applications. This chapter will provide overview of presented work in this thesis with discussion of model drawbacks and future work.

9.1 Transport mechanisms and self-self consistent approach

Chapter 2 discussed common transport mechanisms that are considered in THz QCL devices, modelled via Fermi–golden rule. An overview of several scattering processes is presented along with the algorithm approach for determining the electron structure.

Scattering rates obtained by Fermi–golden rule have semi-classical nature. Several works have considered more general interactions between subbands [72, 68], work [72] generalises the dissipator in DM model, while work [68] and similar NEGF models [70] implement scattering mechanisms in different manner. These works still provide very similar results as Fermi–golden rule [131, 130] justifying the use of simpler approach used in this thesis.

The most challenging component in the transport model is the description of electron-electron scattering mechanism. The approach discussed in Chapter 2 is mainly based on work in [116, 86] where the subband nonparabolicity is not considered. Additionally, inclusion of this process into kinetic balance equation represents a great challenge. This mechanism is often avoided due to its numerical complexity, however it may be of theoretical interest to examine this model, especially if QCL material choices with higher non–parabolicity need to be modelled (for example THz QCLs based on InAs/AlSb system [210, 211, 110, 60]).

The kinetic balance equation (2.33) [119, 86] provides significant simplification in solving the Schrödinger–Poission system. This neat application of energy conservation law avoided introduction of quasi–Fermi levels and electron temperatures for particular subbands [117]. The experimental pump–probe measurements suggest that this approximation is justifiable for BTC QCL designs, while designs that exploit electron–LO–phonon interaction exhibit different subband temperatures [146, 147, 148, 37, 149]. Consideration of different subband temperatures has been applied to DM model [130], and this in essence increases the numerical cost of determining the electronic structure. Due to very large number of approximations present in all THz QCL models, it is unclear whether more general consideration of subband temperature would provide better model results, however work in this thesis met significant challenges with modelling THz QCLs in CW operation and further work on subband temperatures (and heat equation effects) may provide improvement.

Chapter 2 mainly presents an overview of earlier works, however, author restructured the previous numerical implementation to significantly decrease the simulation time (from ∼2–3 hours to ∼ 5–10 minutes at single bias point) and exploited the Leeds group's access to supercomputer cluster ARC2 to parallelise simulations. This allowed the author to consider optical effects, dynamics effects and apply the overall model for design optimisation.

Note that author did not fully exploit the large number of zero elements (sparse matrices) in DM model. The latest profiling of the numerical code indicates that the main simulation bottleneck is the Schrödinger equation solver and transport-mechanism solver, and there is a space for additional numerical improvements along with the development of "user–friendly" simulator for THz QCLs.

9.2 Density Matrix Model

Chapters 3 and 6 presented the theoretical outline of DM model. The underlying mathematical formulation has been explained in detail, leading to algebraic simplification given by Eq. (3.22) and (6.9). This is an original contribution of the author, published in [74, 83]. The mathematics of DM model is unavoidably cumbersome when compared to RE approach in 1.6.1, however the conducted algebraic formulation of DM superoperator allows relatively simple numerical implementation.

This model is technically the generalisation of [82] and continuation of work in [73, 61], where the main aim was to generalise the approach to be independent on the number of states considered. Note that [82] has also been applied for optimisation of the former record temperature design [47]. The main drawback of the model is mainly within the determination of period interaction Hamiltonian in Eq. 3.3. This expression essentially measures the wavefunction overlap in the injection barrier and it is based on work in [133] that considered only a two–well quantum system. A minor drawback is also the use of semi–classical scattering rates and a dissipator that is essentially identical to RE approach (Eq. 3.10). The work in [72] avoids both drawbacks by constructing the Hamiltonian in different manner and generalising the dissipator, so that it slightly resembles NEGF approaches.

The model in this thesis represents a generalisation of RE approach where coherent transport is added through inter–period interaction Hamiltonian. Note that nearly all equations within RE approach are also present in DM system as well. The difference between the implemented DM approach and RE approach is the use of single period wavefunction basis under tight–binding approximation and different inter–period interaction. Overall, the model has medium mathematical and computational complexity among various QCL models [76]. Some future development may be conducted similarly to [72]. In comparison to the NEGF models, DM approach offers very low numerical cost which is the essential property in optimisation schemes, note that in Chapter 8 over a million QCL structures were simulated within roughly a week of time (this was mainly achieved by the use of supercomputer cluster ARC2 at University of Leeds, single QCL structure simulation time was ~ 5 minutes).

9.3 Steady–state density matrix modelling

Chapter 4 discussed the fitting procedure to the experimental results in detail. The fabrication and growth processes have tolerances that may generate structures that have different properties, even when based on the same design. This was taken into account through interface roughness scattering mechanism which introduces Gaussian distribution–like perturbation Hamiltonian (Eq. 2.18) and two fitting parameters. The IFR correlation length Λ_{IFR} displays has a smaller influence than IFR r.m.s height Δ_{IFR}, and both have mostly linear effect on output characteristics as shown in Fig.4.2.

The main issue that was encountered Chapter 4 was in fitting the temperature dependence of experimental QCL characteristics, both in pulsed and CW operation. It is clear that the conducted fitting approach did not consider that multiple pairs of IFR parameters may provide the desired match with the experiment, and development of more systematic approach may be required. However, the analysis presented in Chapter 4 has shown that issue also lies in temperature degradation of material gain and current density which may be attributed to the lack of different subband temperatures in kinetic balance equation or even in a missing transport mechanism.

Some improvement may be obtained by consideration of heat equation in Eq. (1.8). The commonly used linear approximation is known to have different linear slope with different cold finger temperature [189, 86] which may be exploited, however this would result in construction of parametric model with too many fitting parameters.

CW operation experiences very high electrical heating and applying the heat equation is debatable, mostly because the temperature profile over the QCL ridge is not uniform [45, 86] as shown in Fig. 1.9, and this breaks the periodicity of QCL structure and makes the application of periodic approach for transport questionable. Overall, the pulsed operation may be reliably fitted at any cold finger temperature for a variety of designs, while some caution is needed in CW simulations.

9.4 Acoustic–phonon modulation

Chapter 5 has discussed a new THz QCL modulation technique, recently accepted for publication in [107]. Acoustic phonon effect generates a strain signal that travels through semiconductor medium and may be used for perturbing the active part of the medium. Voltage modulation properties of this effect have been demonstrated in resonant tunnelling diode [164, 165] and weekly coupled superlattice structures [161] and the joint research between University of Leeds and University of Nottingham has demonstrated and theoretically explained this effect for the first time in THz QCL structures [107].

Chapter 5 was focused on theoretical approach, developed by the author of this thesis, that was used to explain the experimental observations in joint publication [107].

The presented theory applies time dependent perturbation approach discussed in Chapter 2.3 (Eq. (2.6)) in order to investigate the effect of strain induced by the acoustic phonon perturbation on resonant tunnelling process. The calculations were able to explain the experimental observations qualitatively, namely that the propagating strain would always cause the increase of voltage, while the optical power difference would change its sign, depending on whether the effect is applied on the rising or falling edge of $I - L$ characteristic of QCL.

The TDP approach is a rough approximation of this effect. The acoustic signal propagates through QCL structure on timescale similar to the lifetimes and the propagating nature of this perturbation indicates the generation of electric field domains (as signal is affecting the QCL period by period, and not all periods at once). Modelling of this effect in detail is very challenging. A slight improvement may be conducted by Landau-Zener–like model [166, 167]. It also may be of interest to implement this effect as a new scattering mechanism in order to investigate its effect on transport, however due to a small amplitude of the perturbation (~ 1 meV), this effect would not have as significant contribution to the transport as other scattering mechanisms.

9.5 Self–mixing effect modelling

Chapter 6 presented Maxwell-Bloch model by coupling the density matrix model to Maxwell wave equation under slow–varying envelope approximation.

The MB models are usually implemented in systems with several states [79, 76] although general formulation exists in the literature [169, 193], where the main challenge is constructing the DM superoperator for the particular problem of interest. The work presented in Chapter 6 is an original contribution that resulted in publication [83]. The potential future improvements of the model are in implementing the travelling wave approximation for Maxwell wave equation (Appendix A), which would allow better insight into spatial properties of optical wave within the cavity and allow modelling of coupled cavity effects such as frequency comb generation. Travelling wave method, on the other hand, has both spatial and temporal dependence, which would also extend to the density matrix elements as in [88, 197], thus the time complexity of the model would greatly increase. Another potential improvement of the model is examining multimode operation of THz QCLs. This typically requires additional differential equations for different optical electric field modes and it may be performed without affecting the density matrix equations (i.e. only adding equations for electric field modes, with specially added model for mode suppression by the material gain of the medium [212]).

Chapter 7 extended the MB model to external homodyne reinjection of light, enabling modelling of SM effect. The model solves 10 N^2 differential equations and includes detailed transport information through DM approach. To the best of the author's knowledge, this is the first general formulation of SM effect model. The existing Lang–Kobayashi [102] model in the literature is originally constructed for diode lasers, and subsequent applications of this model to different laser systems required determining parameters equivalent to those in diode laser [7]. In terms of THz QCL structure, a hybrid model [189, 103, 104, 174] that models QCL as a two level system with parameters derived from a model with N–level system has been widely applied. Recently, a great interest is drawn by using SM effect in pulsed operation [174], where hybrid approach may experience difficulties.

The formulation in Chapter 7 is able to provide a non–hybrid approach and is an original work by the author of this thesis. However, SM effect applications are usually conducted under CW operation where the laser gets significantly heated. As discussed in Chapter 4, electrical heating is also present under pulsed operation. This raises the necessity of coupling the thermal equation to the system, similarly as in [189]. This is a demanding future work in the numerical sense, as the addition of thermal equation would require the self–self–consistent Schrödinger–Poission algorithm to be invoked at each time step within the differential equation solver. The system in Chapter 7 has $10N^2$ size and currently for $N = 11$, ∼10-40 minutes is needed for self–self–consistent Schrödinger–Poission algorithm (40 minutes is needed if electron-electron scattering is included) and ∼4 hours for ODE solver in 2000 time points at single electric bias value. Coupling these approaches together would create a very general model, however this is not feasible within reasonable simulation time. The simpler approach would be to determine transport properties separately in order to obtain their temperature dependence, and then use these data through a look up table (as was done in [189]) or reducing the transport model to an effective model with fewer states.

9.6 Design optimisation

Chapter 8 discussed the THz QCL designs and proposed a novel design that is a good candidate for high temperature performance.

The current record high temperature design [36] has been obtained through optimisation technique that uses NEGF transport model. This structure lases up to 210 K, however due to high barriers, high doping and short period (two quantum wells) this operation is achieved at very high threshold current (9 A) and operation bias, which cause very high electrical heating. Modelling this structure by DM approach presented in this thesis, without specific IFR fitting, shows that this design has material gain over 20 cm^{-1} up to 250 K, however when the electrical heating is taken into account, the operating temperature prediction agrees with the experimentally achieved results.

The operation temperature prediction has also been discussed in Chapter 4. Due to very efficient numerical implementation of the transport model, developed by the author, the search for newly proposed design in Fig. 8.3 may be conducted through brute force approach.

Note that this proposal was constructed in very late stages of author's project, thus Chapter 8 only presents the results obtained very recently. Three–well QCL designs have been investigated through brute force simulations. The first quantum well in the design is added to introduce a parasitic state that would extract LLL from previous period and pump the ULL in its own period, therefore achieving double resonant phonon-photon-phonon operation. Such three–well QCL design therefore resembles the two–well design for typical resonant–phonon QCLs structure. The overall conclusion of this Chapter has resulted in similar arguments and discussion that were made for advantages and disadvantages of two–well resonant–phonon devices, however, the main difference is that all proposed designs in Chapter 8 have material gain over 20 cm^{-1} up to 240 - 250 K, have lower doping profile and lower threshold current than the record high temperature design [36], giving hope for better performance. Additional consideration of four-well and five-well designs is needed in order to propose a structure that best matches the author's proposal in Fig. 8.3.

The conducted simulations have shown a great potential of the model developed in the thesis for systematic design optimisations e.g. by genetic algorithm [61] and a need for a "user–friendly" THz QCL simulator (the current implementation does not have graphic user interface, and uses Bash scripts on terminal within Linux operating system).

This thesis only modelled GaAs/AlGaAs THz QCL structures as this is currently dominant material setup in practice. However, great interest is drown by material systems that have lower effective mass or higher LO–phonon energies. Changing the material system in the model may seem straightforward as only material parameters need to be updated [5], however the Schrödinger–Poisson equation that is discussed in Chapter 2 uses 2 − band Kane model for subband nonparabolicity. In author's publication [112] prior to this thesis project, a 14 band nonparabolicity parameters were used where various THz QCL structures were modelled in different material systems, showing significant effects of nonparabolicity model. Additionally, the materials with low effective mass may also exhibit undesired transport from other valleys [110, 60], note that the entire model formulation in Chapter 2 is focusing at the bottom Gamma valley of the conduction band profile. The future work needs to consider these effects and update the Schrödinger–Poisson equation solvers accordingly.

9.7 Future and ongoing collaborative work

9.7.1 Reduced and parametric dynamics models

The steady–state model solves $9N^2$ equations (where N is the number of states per QCL period), making any analytic study impossible. A variety of laser models [1] use the effective two, three or four level schemes which provide very convenient and intuitive physical interpretations of the model. Historically, the majority of the dynamic Maxwell - Bloch models have been implemented in such schemes. Chapter 6 presents a general Maxwell - Bloch dynamics approach in neat mathematical formulation, however effective and reduced dynamics models are also capable of high quality study of various effects.

The model developed in this thesis has been employed in several collaborative works that exploit the general scope of the model and provide effective parameters for the reduced models.

The long running collaboration with a group in University of Queensland, Brisbane, Australia has generated an effective two level dynamic model for the self mixing effect [189, 91]. This model uses a large data set of various temperature dependent parameters as material gain, lasing states' lifetimes, current density, voltage, etc., generated by the approach in this chapter. Recently, a state-of-the-art application of SM effect under pulsed operation of the QCL device has been performed in Queensland group [198], and modelling efforts on both sides are being conducted towards improvement of the effect with the prospect of new joint publications.

Similar methodology can also be applied for the study of multimode operation of THz QCLs where a set of dynamic equations is being coupled to the effective two level model. A publication has been submitted by Tina Xiaoqiong Qi in Optics Express [213] where the author of this thesis has provided the steady state data obtained by the model in this thesis.

Another ongoing collaboration with Quantum Electronics group at University of Belgrade, Serbia uses the model to provide effective parameters for a three level laser structure for the dynamical Maxwell-Bloch study of self-pulsation effect. This effect has been observed in mid-infrared QCL [214, 215] and the and a collaboration effort is agreed in investigating this effect in THz QCLs.

9.7.2 Wavefunction basis exploitation

The steady–state model aslo provides detailed transport information and various theoretical concepts can be studied by analysing the wavefunctions of interest. Note that the model predicts the lasing frequency with very high precision and in some cases it may be of interest to observe the lasing principle of the device and discuss the diagonality of transitions, dipole matrix elements, oscillation strength, etc.

Chapter 5 discuss in detail a modulation technique that requires time-dependent perturbation theory approach where wavefunctions that model provides are essential elements of the approach.

Appendix A

Maxwell equation simplification

Maxwell's wave equation for a homogeneous, isotropic medium, without the external magnetic field is [1]:

$$\nabla^2 \mathbf{E} - \frac{1}{v_{\mathrm{g}}^2}\frac{\partial^2 \mathbf{E}}{\partial t^2} - \frac{\sigma}{\epsilon_0 c^2}\frac{\partial \mathbf{E}}{\partial t} = \frac{1}{\epsilon_0 c^2}\frac{\partial^2 \mathbf{P}}{\partial t^2} \tag{A.1}$$

where $\mathbf{E}(\mathbf{r}, t)$ is the optical electric field, $\mathbf{P}(\mathbf{r}, t)$ is the medium polarisation, $v_{\mathrm{g}} = cn^{-1}$ is the group velocity, σ is the conductivity that accounts for the ohmic losses in the cavity [1].

A.0.1 Travelling wave method derivation

Let us assume that the electrical field has no spatial variation in plane $\frac{\partial E_x}{\partial x} = \frac{\partial E_y}{\partial y} = 0$ and that the propagation in the z direction is given as a linear combination of the forward f^+ and the backward f^- propagating plane waves in the form $E(z,t) = \frac{1}{2}\, f^+(z,t)e^{i(kz+\omega t)} + \frac{1}{2}f^-(z,t)e^{-i(kz+\omega t)} + c.c$, where k and ω are the corresponding wave number and the frequency, respectively, and $\omega = kv_g$. Additionally, we assume that the polarisation will follow the electric field in the similar form: $P(z,t) = P^+(z,t)e^{i(kz-\omega t)} + P^-(z,t)e^{-i(kz+\omega t)} + c.c$ The partial derivatives are:

$$\begin{aligned}
\frac{\partial E}{\partial t} &= \frac{1}{2}\left[\left(\frac{\partial f^+}{\partial t} - i\omega f^+\right) e^{i(kz-\omega t)} + \left(\frac{\partial f^-}{\partial t} - i\omega f^-\right) e^{-i(kz+\omega t)}\right] + c.c \\
\frac{\partial^2 E}{\partial t^2} &= \frac{1}{2}\left[\left(\frac{\partial^2 f^+}{\partial t^2} - 2i\omega\frac{\partial f^+}{\partial t} - \omega^2 f^+\right) e^{i(kz-\omega t)}\right. \\
&\quad \left. + \left(\frac{\partial^2 f^-}{\partial t^2} - 2i\omega\frac{\partial f^-}{\partial t} - \omega^2 f^-\right) e^{-i(kz+\omega t)}\right] + c.c \\
\frac{\partial^2 E}{\partial z^2} &= \frac{1}{2}\left[\left(\frac{\partial^2 f^+}{\partial z^2} + 2ik\frac{\partial f^+}{\partial z} - k^2 f^+\right) e^{i(kz-\omega t)}\right. \\
&\quad \left. + \left(\frac{\partial^2 f^-}{\partial z^2} - 2ik\frac{\partial f^-}{\partial z} - k^2 f^-\right) e^{-i(kz+\omega t)}\right] + c.c \\
\frac{\partial^2 P}{\partial t^2} &= \left(\frac{\partial^2 P^+}{\partial t^2} - 2i\omega\frac{\partial P^+}{\partial t} - \omega^2 P^+\right) e^{i(kz-\omega t)} \\
&\quad + \left(\frac{\partial^2 P^-}{\partial t^2} - 2i\omega\frac{\partial P^-}{\partial t} - \omega^2 P^-\right) e^{-i(kz+\omega t)} + c.c
\end{aligned} \tag{A.2}$$

The slow-varying envelope approximation assumes that

$$\begin{gathered}
\frac{\partial^2}{\partial t^2} << \omega\frac{\partial}{\partial t}, \qquad \frac{\partial^2}{\partial z^2} << k\frac{\partial}{\partial z} \\
\frac{\partial}{\partial t} << \omega
\end{gathered} \tag{A.3}$$

First we apply the first approximation from Eq. (A.3) and substitute Eq. (A.2) without the second derivatives into Eq. (A.1) and group the terms with the same exponentials:

$$\begin{aligned}
&\frac{1}{2}\left(2ik\frac{\partial f^+}{\partial z} - \frac{\sigma}{\epsilon_0 c^2}\left(\frac{\partial f^+}{\partial t} - i\omega f^+\right) - k^2 f^+ - \frac{1}{v_{\mathrm{g}}^2}\left(-2i\omega\frac{\partial f^+}{\partial t} - \omega^2 f^+\right)\right) e^{i(kz-\omega t)} + \\
&\frac{1}{2}\left[\frac{\partial^2 f^-}{\partial z^2} - 2ik\frac{\partial f^-}{\partial z} - k^2 f^- - \frac{\sigma}{\epsilon_0 c^2}\left(\frac{\partial f^-}{\partial t} - i\omega f^-\right)\right. \\
&\left. - \frac{1}{v_{\mathrm{g}}^2}\left(-2i\omega\frac{\partial f^-}{\partial t} - \omega^2 f^-\right)\right] e^{-i(kz+\omega t)} + c.c \\
&= \frac{1}{\epsilon_0 c^2}\left(-2i\omega\frac{\partial P^+}{\partial t} - \omega^2 P^+\right) e^{i(kz-\omega t)} + \frac{1}{\epsilon_0 c^2}\left(-2i\omega\frac{\partial P^-}{\partial t} - \omega^2 P^-\right) e^{-i(kz+\omega t)} + c.c
\end{aligned} \tag{A.4}$$

Next we use the identity $v_{\mathrm{g}} = cn^{-1} = \omega k^{-1}$, we can also split Eq. (A.4) into two independent equations that correspond to the different exponential terms, and ignore $c.c$:

$$\begin{aligned}
&\frac{1}{2}\left(2ik\frac{\partial f^+}{\partial z}+2i\omega\frac{\partial f^+}{\partial t}-k^2f^++\frac{k^2}{\omega^2}\omega^2f^+-\frac{\sigma}{\epsilon_0c^2}\left(\frac{\partial f^+}{\partial t}-i\omega f^+\right)\right)\\
&=\frac{1}{\epsilon_0c^2}\left(-2i\omega\frac{\partial P^+}{\partial t}-\omega^2P^+\right)\\
&\frac{1}{2}\left(-2ik\frac{\partial f^-}{\partial z}+2i\omega\frac{\partial f^-}{\partial t}-k^2f^-+\frac{k^2}{\omega^2}\omega^2f^--\frac{\sigma}{\epsilon_0c^2}\left(\frac{\partial f^-}{\partial t}-i\omega f^-\right)\right)\\
&=\frac{1}{\epsilon_0c^2}\left(-2i\omega\frac{\partial P^-}{\partial t}-\omega^2P^-\right)
\end{aligned} \tag{A.5}$$

It is clear that k^2 terms will cancel out, and next we apply the second approximation in Eq. (A.3) and divide both equations by $i\omega$:

$$\begin{aligned}
\frac{k}{\omega}\frac{\partial f^+}{\partial z}+\frac{\partial f^+}{\partial t}+\frac{\sigma}{\epsilon_0c^2}f^+&=\frac{i\omega P^+}{\epsilon_0c^2}\\
-\frac{k}{\omega}\frac{\partial f^-}{\partial z}+\frac{\partial f^-}{\partial t}+\frac{\sigma}{\epsilon_0c^2}f^-&=\frac{i\omega P^-}{\epsilon_0c^2}
\end{aligned} \tag{A.6}$$

if we now use $v_g = k\omega^{-1} = cn^{-1}$ and rearrange Eq. (A.6) by dividing by v_g, we get two equations that correspond to Eq. (1.10) from travelling wave section in chapter 1.6.3.

A.0.2 Fourier method derivation

Let us assume that electric field can be expanded as $\mathbf{E}(\mathbf{r},t) = \sum_n \mathbf{u_n}(\mathbf{r})E_n(t)$ where $\mathbf{u_n}(\mathbf{r})$ are the orthogonal cavity modes that satisfy the Laplace equation $(\nabla^2 + k_n^2)\mathbf{u_n}(\mathbf{r}) = 0$, where $k_n = \omega_n nc^{-1}$ is the wave number that corresponds to the eigenmodes at frequency ω_n. Let us also assume that the polarisation will follow the electric field symmetry as $\mathbf{P}(\mathbf{r},t) = \sum_n \mathbf{u_n}(\mathbf{r})P_n(t)$. By substituting $\mathbf{E}(\mathbf{r},t)$ and $\mathbf{P}(\mathbf{r},t)$ into Eq. (A.1) we get:

$$\sum_n\left[\nabla^2\mathbf{u_n}E_n(t)-\frac{1}{v_g^2}\mathbf{u_n}\frac{\partial^2E_n}{\partial t^2}-\frac{\sigma}{\epsilon_0c^2}\mathbf{u_n}\frac{\partial E_n}{\partial t}\right]=\sum_n\frac{1}{\epsilon_0c^2}\mathbf{u_n}\frac{\partial^2P_n}{\partial t^2} \tag{A.7}$$

If we add and subtract a term $\pm k_n^2\mathbf{u_n}E_n(t)$ under the sum on the left hand side of Eq. (A.7), the Laplacian term would cancel with $-k_n^2$ term. We can then multiply the entire equation by $-v_g^2$ and apply $v_g = \omega k_n^{-1} = cn^{-1}$, we then obtain:

$$\sum_n \left[\mathbf{u_n}\frac{\partial^2 E_n}{\partial t^2} + \frac{\sigma}{\epsilon_0 n^2}\mathbf{u_n}\frac{\partial E_n}{\partial t} + w_n^2 \mathbf{u_n} E_n(t)\right] = -\sum_n \frac{1}{\epsilon_0 n^2}\mathbf{u_n}\frac{\partial^2 P_n}{\partial t^2} \tag{A.8}$$

Finally, to obtain the individual equation for mode $\mathbf{n}$ we can multiply Eq. (A.8) by $\mathbf{u_m}$, integrate, and use the orthogonality property of the expansion basis. The resulting equation is:

$$\frac{\partial^2 E_n}{\partial t^2} + \frac{\sigma}{\epsilon_0 n^2}\frac{\partial E_n}{\partial t} + \omega_n^2 E_n = -\frac{1}{\epsilon_0 n^2}\frac{\partial^2 P_n}{\partial t^2} \tag{A.9}$$

which is identical to Eq. (1.11) from the 1.6.3 section.

This equation can be further simplified under the slow-varying envelope approximation. We assume that electric field has a cosine form at carrier frequency ω, modulated by an envelope $E(t)$ as $E_n(t) = E(t)(e^{i\omega t} + e^{-i\omega t})$. We assume that the polarisation would also follow this form $P_n(t) = P(t)(e^{i\omega t} + e^{-i\omega t})$. The partial derivatives are:

$$\begin{aligned}
\frac{\partial E_n}{\partial t} &= \left(\frac{\partial E}{\partial t} + i\omega E\right)e^{i\omega t} + \left(\frac{\partial E}{\partial t} - i\omega E\right)e^{-i\omega t} \\
\frac{\partial^2 E_n}{\partial t^2} &= \left(\frac{\partial^2 E}{\partial t^2} + 2i\omega\frac{\partial E}{\partial t} - \omega^2 E\right)e^{i\omega t} + \left(\frac{\partial^2 E}{\partial t^2} - 2i\omega\frac{\partial E}{\partial t} - \omega^2 E\right)e^{-i\omega t} \\
\frac{\partial^2 P_n}{\partial t^2} &= \left(\frac{\partial^2 P}{\partial t^2} + 2i\omega\frac{\partial P}{\partial t} - \omega^2 P\right)e^{i\omega t} + \left(\frac{\partial^2 P}{\partial t^2} - 2i\omega\frac{\partial P}{\partial t} - \omega^2 P\right)e^{-i\omega t}
\end{aligned} \tag{A.10}$$

It is clear that if we substitute Eq. (A.10) into Eq. (A.9), terms around the same exponential would result into two complex conjugate equations. For that reason, we can focus only on terms with $e^{i\omega t}$. Similarly, as for slow-varying envelope approximation for the travelling wave method in Eq. (A.3), we can neglect the second order time derivatives:

$$2i\omega\frac{\partial E}{\partial t} - \omega^2 E + \frac{\sigma}{\epsilon_0 n^2}\left(\frac{\partial E}{\partial t} + i\omega E\right) + \omega_n^2 E = -\frac{1}{\epsilon_0 n^2}\left(2i\omega\frac{\partial P}{\partial t} - \omega^2 P\right) \tag{A.11}$$

Next we apply $\frac{\partial}{\partial t} << \omega$ and assume that the carrier frequency is nearly at resonance with the cavity mode frequency $\omega \approx \omega_n$ which makes term $\omega_n^2 - \omega \approx 2\omega(\omega_n - \omega)$, and if we divide Eq. (A.11) by $2i\omega$:

$$\frac{\partial E}{\partial t} - i(\omega_n - \omega)E + \frac{\sigma}{2\epsilon_0 n^2}E = -\frac{i\omega P}{2\epsilon_0 n^2} \tag{A.12}$$

When the terms in Eq. (A.12) are rearranged so that the derivative is on one side, this equation is identical to Eq. (1.12) from Fourier method section in chapter 1.6.3.

Appendix B

Slow envelope approximation

If the conduction band potential is set to zero, general solution of the Schrödinger equation for the atomic potential is presented through the orthogonal set of the Bloch functions $u_{n,\mathbf{k}}(\mathbf{r}) = \frac{1}{\sqrt{V_c}} e^{i\mathbf{kr}} U_{n,\mathbf{k}}$, where $\mathbf{k}$ is Bloch wavevector, $U_{n,\mathbf{k}}$ is the periodic part of the Bloch function which follows the periodicity of the atomic potential and V_c is the volume of the crystal.

The conduction band potential represents a perturbation over the atomic potential, and we can formulate that the solution of the Schrödinger equation with the conduction band potential can be expanded through basis of Bloch's functions as $\psi_{n,\mathbf{k}} = \sum_{n,\mathbf{k}} a_{n,\mathbf{k}} u_{n,\mathbf{k}}$. When this is substituted into the Schrödinger equation, we obtain a set of equations in the usual sum form. In order to extract an equation for particular expansion term n, we may exploit orthogonality of the Bloch functions basis, multiply the set by $\psi^*_{n,\mathbf{k'}}$ and integrate over the volume, this yields:

$$\frac{1}{V_\mathrm{c}} \sum_{n,\mathbf{k}} a_{n,\mathbf{k}} \int_{V_c} e^{i\mathbf{kr}} U_{n,\mathbf{k}}(\mathbf{r}) U(\mathbf{r}) e^{-i\mathbf{k'r}} U^*_{n,\mathbf{k'}}(\mathbf{r}) d\mathbf{r} = a_{n,\mathbf{k}}(E - E_{n,\mathbf{k}}) \tag{B.1}$$

where $E_{n,\mathbf{k}}$ are the solution eigenvalues of the Schrödinger equation that correspond to the system unperturbed by the conduction band potential (the atomic potential only) and has Bloch function basis as eigenfunctions.

If we assume that the conduction band potential $U(\mathbf{r})$ is slow-varying, we can use its Fourier transform $U(\mathbf{r}) = \sum_q u(\mathbf{q}) e^{i\mathbf{qr}}$ where $\mathbf{q}$ is small, this simplifies Eq. (B.1):

$$\sum_{n,\mathbf{k},\mathbf{q}} a_{n,\mathbf{k}} \frac{u(\mathbf{q})}{V_c} \int_{V_c} e^{i(\mathbf{k}\text{-}\mathbf{k'}+\mathbf{q})\mathbf{r}} U_{n,\mathbf{k}}(\mathbf{r}) U^*_{n,\mathbf{k'}}(\mathbf{r}) d\mathbf{r} = a_{n,\mathbf{k}}(E - E_{n,\mathbf{k}}) \tag{B.2}$$

The Bloch functions are periodic due to the crystal lattice and this property can be exploited to further simplify Eq. (B.2) and perform the integration only over the primitive cell, rather than the entire crystal. The coordinate $\mathbf{r} = \mathbf{r} + \mathbf{R_i}$ can be expressed through the relative position $\mathbf{r'}$ and the position of the i-th cell $\mathbf{R_i}$. This simplifies the integration, the derivation can be found in [108], simplified form is:

$$\sum_{n,\mathbf{k},\mathbf{q}} a_{n,\mathbf{k}} \frac{u(\mathbf{q})}{V_{cell}} \Delta_{\mathbf{k}\text{-}\mathbf{k'}+\mathbf{q}} \int_{V_{cell}} U_{n,\mathbf{k}+\mathbf{q}}(\mathbf{r'}) U^*_{n,\mathbf{k'}}(\mathbf{r'}) d\mathbf{r'} = a_{n,\mathbf{k'}}(E - E_{n,\mathbf{k'}}) \tag{B.3}$$

The slow-varying approximation for the conduction band potential allows the integral in Eq. (B.3) to be expanded into Taylor series (because $\mathbf{q}$ is small), where the first would be dominant. The integral would then satisfy the normalisation condition and be equal to V_{cell}, therefore simplifying the Schrödinger equation to:

$$\sum_{\mathbf{q}} a_{n,\mathbf{k'}+\mathbf{q}} u(\mathbf{q}) = a_{n,\mathbf{k'}}(E - E_{n,\mathbf{k'}}) \tag{B.4}$$

The envelope function can be introduced as $\Psi_{3\mathrm{D}} = \sum_{\mathbf{k'}} a_{n,\mathbf{k'}} e^{i\mathbf{k'}\mathbf{r}}$ and Eq. (B.4) can be restructured to read:

$$\begin{aligned} \sum_{\mathbf{q}} u(\mathbf{q}) e^{-i\mathbf{q}\mathbf{r}} \sum_{\mathbf{k}} a_{n,\mathbf{k}} e^{i\mathbf{k}\mathbf{r}} &= E \sum_{\mathbf{k'}} a_{n,\mathbf{k'}} e^{i\mathbf{k'}\mathbf{r}} - \sum_{\mathbf{k'}} E_{n,\mathbf{k'}} a_{n,\mathbf{k'}} e^{i\mathbf{k'}\mathbf{r}} \\ U(\mathbf{r})\Psi_{3\mathrm{D}}(\mathbf{r}) &= E\Psi_{3\mathrm{D}}(\mathbf{r}) - \frac{1}{8\pi^3} \int_{\mathbf{k'}} a_{n,\mathbf{k'}} E_{n,\mathbf{k'}} e^{i\mathbf{k'}\mathbf{r}} \end{aligned} \tag{B.5}$$

The second equation in Eq. (B.5) is derived by the identification of all the previous substitutions and transformation of the sum over $\mathbf{k'}$ into an integral. The very important step towards the slow-varying envelope approximation, is in handling the integral in Eq. (B.5). We are mainly interested in laser modelling with direct semiconductor such as GaAs and isotropic effective mass. This allows us to focus only at the Brillouin zone centre (Γ_c point) where $\mathbf{k'}$ tends to zero, which allows us to write the dispersion relation in parabolic form as $E_{n,\mathbf{k}'} = E_{n,0} + \frac{\hbar^2 k'^2}{2m}$, where $E_{n,0}$ is the energy around the Γ_{c} point of the n-th band. We can then perform the inverse Fourier transform of (B.5) which yields Eq. (2.1) from the section 2.1:

$$-\frac{\hbar^2}{2m}\left(\nabla_{\mathbf{r}}^2 + U(\mathbf{r})\right)\Psi_{\mathrm{3D}}(\mathbf{r}) = (E - E_{n,0})\Psi_{\mathrm{3D}}(\mathbf{r}) \tag{B.6}$$

In this derivation, we have introduced several approximation that transform the Schrödinger equation in order to omit the general form that includes the atomic potential. In essence, the derivation is formulating the Schrödinger equation that depends only on perturbation of the system (the conduction band potential), while the effects of the unperturbed system are taken into account by knowing the material properties. Equation Eq. (B.6) is a general form of the Schrödinger equation that can be restructured differently, depending on the form of the spatial confinement determined by the conduction band potential.

Appendix C

Finite difference method for the Schrödinger-Poisson equation

The finite difference method is a standard technique for solving differential equations. In one dimension the dependent variable (z) is discretized in n_z equidistant points with separation h_z and the first and the second derivative of the function $f(z)$ are given as:

$$\begin{aligned} \frac{df_i}{dz} &= \frac{f_i - f_{i-1}}{h_z} \\ \frac{d^2 f_i}{dz^2} &= \frac{f_{i+1} - 2f_i + f_{i-1}}{h_z^2} \end{aligned} \tag{C.1}$$

The first derivative in Eq. (C.1) is given nearly by the definition (where $h_z \to 0$) through the forward Euler rule, while the second derivative may be defined in several forms (depending on the desired precision). In Eq. (C.1), the second derivative is given through central difference rule where three points are needed. This determines how many diagonals would the matrix form of the discretized differential equation have.

Schrödinger equation

The Schrödinger equation is of the second order, and when Eq. (C.1) is applied, it follows the following rule:

$$
\begin{aligned}
&a_i\psi_{i-1} + b_i\psi_i + c_i\psi_{i+1} = E\psi_i \\
&b_i = \frac{\hbar^2}{h_z^2}\left(\frac{1}{m^*_{i+\frac{1}{2}}} + \frac{1}{m^*_{i-\frac{1}{2}}}\right) + V_i \\
&a_{i+1} = c_i = -\frac{\hbar^2}{2m^*_{i+\frac{1}{2}}h_z^2}
\end{aligned}
\tag{C.2}
$$

where $i+\frac{1}{2}$ represents linear interpolation of the effective around point z_i.

When difference equation rule in Eq. (C.2) is applied for every point of the $z - axis$, the resulting matrix problem is:

$$
\begin{pmatrix}
b_0 & c_0 & 0 & \cdots & 0 \\
a_1 & b_1 & c_1 & \cdots & 0 \\
0 & \ddots & \ddots & \ddots & 0 \\
0 & \cdots & a_{n_z-2} & b_{n_z-2} & c_{n_z-2} \\
0 & \cdots & 0 & a_{n_z} & b_{n_z-1}
\end{pmatrix}
\begin{pmatrix}
\psi_0 \\ \psi_1 \\ \vdots \\ \psi_{n_z-2} \\ \psi_{n_z-1}
\end{pmatrix}
= E
\begin{pmatrix}
\psi_0 \\ \psi_1 \\ \vdots \\ \psi_{n_z-2} \\ \psi_{n_z-1}
\end{pmatrix}
\tag{C.3}
$$

This is a tridiagonal eigenvalue problem which could be solved by numerous approaches available in numerical packages, such as LAPACK in C++. However, the effective mass is energy dependent due to the nonparabolicity $m^* = m_\mathrm{d}(1 + \alpha_k E)$ which transforms Eq. (C.3) into a nonlinear eigenvalue problem in the form $H(E)\psi = E\psi$. The methodology for solving such a problem is to search for zero eigenvalue solutions of $(H(E) - EI)\,\psi = \lambda_0\psi$ where I is an identity matrix and the solution of Eq. (C.3) is a set of energies that yield $\lambda_0 = 0$.

Poisson equation

The Poisson equation is of the second order as well, however its form is significantly simpler than the Schrödinger equation and does not yield an eigenvalue problem. Its finite-difference form is $\phi_{i-1} - 2\phi_i + \phi_{i+1} = -\frac{h_z^2}{\epsilon_0 n^2}c_i$ where $c_i = e(N^+_{\mathrm{d}_i} - \rho_{\mathrm{c}_i})$ represents the charge density in accordance with expressions for $N_\mathrm{d}(z)$ and ρ_c from the section 2.2.

The matrix form of the discretized Poisson equation is:

$$\begin{pmatrix} -2 & 1 & 0 & \cdots & 0 \\ 1 & -2 & 1 & \cdots & 0 \\ 0 & \ddots & \ddots & \ddots & 0 \\ 0 & \cdots & 1 & -2 & 1 \\ 0 & \cdots & 0 & 1 & -2 \end{pmatrix} \begin{pmatrix} \phi_1 \\ \phi_2 \\ \vdots \\ \phi_{n_z-1} \\ \phi_{n_z} \end{pmatrix} = -\frac{h_z^2}{\epsilon_0 n^2} \begin{pmatrix} c_1 \\ c_2 \\ \vdots \\ c_{n_z-1} \\ c_{n_z} \end{pmatrix} \tag{C.4}$$

This is a linear diagonal dominant matrix equation and instead of the inversion of the coefficient matrix, the Thomas algorithm solution is given by [114]:

$$\begin{aligned} \phi_{n_z} &= \frac{h_z^2}{\epsilon_0 n^2} \frac{c_{n_z}}{2} \\ \phi_i &= \frac{\frac{h_z^2}{\epsilon_0 n^2} c_i + \phi_{i+1}}{2}, \qquad i \neq n_z \end{aligned} \tag{C.5}$$

Note that the Thomas algorithm in Eq. (C.5) requires only alteration of the charge density function and avoids the direct inversion of the tridiagonal $n_z - 1 \times n_z - 1$ coefficient matrix in Eq. (C.4).

The resulting potential from the Eq. (C.5) needs to be added to the potential in the Schrödinger equation $V = V_{\mathrm{CB}} - eKz + \phi$ which consists of the conduction band potential V_{CB} and the potential drop due to the applied external bias K.

Appendix D

Algebraic properties of matrix systems

D.1 Kronecker product

The Kronecker product $\otimes$ between two matrices $A_{m\times n}$ and $B_{p\times q}$ is defined as:

$$A \otimes B \begin{pmatrix} a_{11}B & \cdots & a_{1n}B \\ \vdots & \ddots & \vdots \\ a_{m1}B & \cdots & a_{mn}B \end{pmatrix}_{mp\times nq} \tag{D.1}$$

The resulting matrix has $mp \times nq$ size. We will focus on cases when both A and B are square matrices of $N \times N$ size. The most relevant application for the density matrix model is ability of Kronecker product to linearise matrix equations in form $AXB = C$ where X is an unknown matrix, and C is a matrix of the same size as A, X and B.

Consider a 2×2 cases $AX = C$ and $XB = D$ where:

$$\begin{gathered} \begin{pmatrix} a_{11} & a_{12} \\ a_{21} & a_{22} \end{pmatrix} \begin{pmatrix} x_{11} & x_{12} \\ x_{21} & x_{22} \end{pmatrix} = \begin{pmatrix} c_{11} & c_{12} \\ c_{21} & c_{22} \end{pmatrix} \\ \begin{pmatrix} x_{11} & x_{12} \\ x_{21} & x_{22} \end{pmatrix} \begin{pmatrix} b_{11} & b_{12} \\ b_{21} & b_{22} \end{pmatrix} = \begin{pmatrix} d_{11} & d_{12} \\ d_{21} & d_{22} \end{pmatrix} \end{gathered} \tag{D.2}$$

The products in Eq. (D.2) are:

$$\begin{aligned} \begin{pmatrix} a_{11}x_{11}+a_{12}x_{21} & a_{11}x_{12}+a_{12}x_{22} \\ a_{21}x_{11}+a_{22}x_{21} & a_{21}x_{12}+a_{22}x_{22} \end{pmatrix} &= \begin{pmatrix} c_{11} & c_{12} \\ c_{21} & c_{22} \end{pmatrix} \\ \begin{pmatrix} x_{11}b_{11}+x_{12}b_{21} & x_{11}b_{12}+x_{12}b_{22} \\ x_{21}b_{11}+x_{22}b_{21} & x_{21}b_{12}+x_{22}b_{22} \end{pmatrix} &= \begin{pmatrix} d_{11} & d_{12} \\ d_{21} & d_{22} \end{pmatrix} \end{aligned} \tag{D.3}$$

Each element of the left hand matrices in Eq. (D.3) is a separate equation, and if we write them following row-wise separation, we obtain four linear equations from each product. We can then formulate a vector x' that represents row-wise vectorisation of matrix X and write the equations in Eq. (D.3) as:

$$\begin{aligned} \begin{pmatrix} a_{11} & 0 & a_{12} & 0 \\ 0 & a_{11} & 0 & a_{12} \\ a_{21} & 0 & a_{22} & 0 \\ 0 & a_{21} & 0 & a_{22} \end{pmatrix} \begin{pmatrix} x_{11} \\ x_{12} \\ x_{21} \\ x_{22} \end{pmatrix} &= \begin{pmatrix} c_{11} \\ c_{12} \\ c_{21} \\ c_{22} \end{pmatrix} \\ \begin{pmatrix} b_{11} & b_{21} & 0 & 0 \\ b_{12} & b_{22} & 0 & 0 \\ 0 & 0 & b_{11} & b_{21} \\ 0 & 0 & b_{12} & b_{22} \end{pmatrix} \begin{pmatrix} x_{11} \\ x_{12} \\ x_{21} \\ x_{22} \end{pmatrix} &= \begin{pmatrix} d_{11} \\ d_{12} \\ d_{21} \\ d_{22} \end{pmatrix} \end{aligned} \tag{D.4}$$

Equations in Eq. (D.4) can be written as $(A \otimes I)x' = c'$ and $(I \otimes B^T)x' = d'$ where I is 2×2 identity matrix and c' and d' are column vectors obtained by row-wise vectorisation of C and D matrix, respectively:

$$\begin{aligned} \begin{pmatrix} a_{11}I & a_{12}I \\ a_{21}I & a_{22}I \end{pmatrix} \begin{pmatrix} x_{11} \\ x_{12} \\ x_{21} \\ x_{22} \end{pmatrix} = \begin{pmatrix} c_{11} \\ c_{12} \\ c_{21} \\ c_{22} \end{pmatrix} &= (A \otimes I)x' = c' \\ \begin{pmatrix} B^T & 0_{2\times2} \\ 0_{2\times2} & B^T \end{pmatrix} \begin{pmatrix} x_{11} \\ x_{12} \\ x_{21} \\ x_{22} \end{pmatrix} = \begin{pmatrix} d_{11} \\ d_{12} \\ d_{21} \\ d_{22} \end{pmatrix} &= (I \otimes B^T)x' = d' \end{aligned} \tag{D.5}$$

This derivation generalises further to show that any system in form $AXB = C$ can be linearised as $(A \otimes B^T)x' = c'$. For the density matrix model, linearisation of the commutator $[H, \rho]$ is $(H \otimes I - I \otimes H^T)\rho'$. Kronecker tensor product can also be used for description of various banded partitioned matrices. For instance, generating a block diagonal matrix of $k \times k$ block size, with blocks B on the main diagonal is obtained by $I_k \times B$ where I_k is identity matrix of $k \times k$ size.

D.2 Khatri–Rao product

Khatri–Rao product $\boxtimes$ is an algebraic operation defined for partitioned matrices [137, 138, 139, 141]. If A and B are partitioned matrices, with equal numbers of partitions in rows and columns (with $K \times J$ partition size), Khatri–Rao product is defined as:

$$A \boxtimes B = \begin{pmatrix} A_{11} \otimes B_{11} & \cdots & A_{1J} \otimes B_{1J} \\ \vdots & \ddots & \vdots \\ A_{K1} \otimes B_{K1} & \cdots & A_{KJ} \otimes B_{KJ} \end{pmatrix} \tag{D.6}$$

The formal definition in Eq. (D.6) allows partitions to be rectangular matrices of different sizes as long as the definition of Kronecker product in Eq. (D.1) is satisfied. Khatri–Rao product may be interpreted as dot product of partitioned matrices A and B where “dot” represents the Kronecker product.

Khatri–Rao product may be used for algebraic description of various banded matrices. The main property of interest, is ability to describe linear systems consisting of equations involving Kronecker product.

Consider a system of three equations:

$$\begin{aligned} A_1 \otimes B_1^T x'_1 &= c'_1 \\ A_2 \otimes B_3^T x'_2 &= c'_2 \\ A_3 \otimes B_3^T x'_3 &= c'_3 \end{aligned} \tag{D.7}$$

where $A_{1,2,3}$, $B_{1,2,3}$ and $c'_{1,2,3}$ are linearised forms of equations $A_k X_k B_k = C_k$. For simplicity, assume that A_k, B_k and C_k are square $N \times N$ matrices. The system in Eq. (D.7) can be written as:

$$\begin{aligned} \begin{pmatrix} A_1 \otimes B_1^T & 0 & 0 \\ 0 & A_2 \otimes B_2^T & 0 \\ 0 & 0 & A_3 \otimes B_3^T \end{pmatrix} \begin{pmatrix} x'_1 \\ x'_2 \\ x'_3 \end{pmatrix} &= \begin{pmatrix} c'_1 \\ c'_2 \\ c'_3 \end{pmatrix} \\ \left(\begin{pmatrix} A_1 & 0 & 0 \\ 0 & A_2 & 0 \\ 0 & 0 & A_3 \end{pmatrix} \boxtimes \begin{pmatrix} B_1^T & 0 & 0 \\ 0 & B_2^T & 0 \\ 0 & 0 & B_3^T \end{pmatrix} \right) \begin{pmatrix} x'_1 \\ x'_2 \\ x'_3 \end{pmatrix} &= \begin{pmatrix} c'_1 \\ c'_2 \\ c'_3 \end{pmatrix} \end{aligned} \tag{D.8}$$

This is clearly a new linear system and it is clear that this approach extends to coupled systems as shown in Chapter 4.

D.3 Linearisation of AX^TB

Kronecker product can be used to linearise equation $AXB = C$ as $(A \otimes B^T)x' = c'$ where x' and c' are row-wise vectorised forms of X and C respectively. If vectorisation was done column-wise, the linearisation would read $(B^T \otimes A)x_\mathrm{c} = c_\mathrm{c}$. However, if we have an equation involving both X and X^T, linearisation of AX^TB cannot be performed through Kronecker product, mainly because of vectorisation of X and order of equations involved in AX^TB.

Consider a 2×2 case of $AX^T = E$ and $X^TB = F$ where:

$$\begin{aligned} \begin{pmatrix} a_{11} & a_{12} \\ a_{21} & a_{22} \end{pmatrix} \begin{pmatrix} x_{11} & x_{21} \\ x_{12} & x_{22} \end{pmatrix} &= \begin{pmatrix} e_{11} & e_{12} \\ e_{21} & e_{22} \end{pmatrix} \\ \begin{pmatrix} x_{11} & x_{21} \\ x_{12} & x_{22} \end{pmatrix} \begin{pmatrix} b_{11} & b_{12} \\ b_{21} & b_{22} \end{pmatrix} &= \begin{pmatrix} f_{11} & f_{12} \\ f_{21} & f_{22} \end{pmatrix} \end{aligned} \tag{D.9}$$

The products in Eq. (D.9) are:

$$\begin{aligned} \begin{pmatrix} a_{11}x_{11} + a_{12}x_{12} & a_{11}x_{21} + a_{12}x_{22} \\ a_{21}x_{11} + a_{22}x_{12} & a_{21}x_{21} + a_{22}x_{22} \end{pmatrix} &= \begin{pmatrix} e_{11} & e_{12} \\ e_{21} & e_{22} \end{pmatrix} \\ \begin{pmatrix} x_{11}b_{11} + x_{21}b_{21} & x_{11}b_{12} + x_{21}b_{22} \\ x_{12}b_{11} + x_{22}b_{21} & x_{12}b_{12} + x_{22}b_{22} \end{pmatrix} &= \begin{pmatrix} f_{11} & f_{12} \\ f_{21} & f_{22} \end{pmatrix} \end{aligned} \tag{D.10}$$

If we formulate x' through row-wise vectorisation similarly as in Eq. (D.4) and write equations in Eq. (D.10) in row-wise order, the resulting system is:

$$\begin{gathered}
\begin{pmatrix} a_{11} & a_{12} & 0 & 0 \\ 0 & 0 & a_{11} & a_{12} \\ a_{21} & a_{22} & 0 & 0 \\ 0 & 0 & a_{21} & a_{22} \end{pmatrix} \begin{pmatrix} x_{11} \\ x_{12} \\ x_{21} \\ x_{22} \end{pmatrix} = \begin{pmatrix} e_{11} \\ e_{12} \\ e_{21} \\ e_{22} \end{pmatrix} \\
\begin{pmatrix} b_{11} & 0 & b_{21} & 0 \\ b_{12} & 0 & b_{22} & 0 \\ 0 & b_{11} & 0 & b_{21} \\ 0 & b_{12} & 0 & b_{22} \end{pmatrix} \begin{pmatrix} x_{11} \\ x_{12} \\ x_{21} \\ x_{22} \end{pmatrix} = \begin{pmatrix} d_{11} \\ d_{12} \\ d_{21} \\ d_{22} \end{pmatrix}
\end{gathered} \tag{D.11}$$

The 4×4 matrices in Eq. (D.11) do not have directly associated type of algebraic product as in Eq. Eq. (D.5). Visually, linearisation of AX^T diagonally displaces rows of A, while X^TB displaces columns of B. These operations may be performed by Khatri–Rao product as:

$$\begin{gathered}
\begin{pmatrix} I_{2\times2} \\ I_{2\times2} \end{pmatrix} \boxtimes \begin{pmatrix} A_{\mathrm{R}_1} \\ A_{\mathrm{R}_2} \end{pmatrix} \begin{pmatrix} x_{11} \\ x_{12} \\ x_{21} \\ x_{22} \end{pmatrix} = \begin{pmatrix} e_{11} \\ e_{12} \\ e_{21} \\ e_{22} \end{pmatrix} = (I_{\mathrm{R}} \boxtimes A_{\mathrm{R}})x' = e' \\
\begin{pmatrix} I_{2\times2} & I_{2\times2} \end{pmatrix} \boxtimes \begin{pmatrix} B_{\mathrm{C}_1} & B_{\mathrm{C}_2} \end{pmatrix} \begin{pmatrix} x_{11} \\ x_{12} \\ x_{21} \\ x_{22} \end{pmatrix} = \begin{pmatrix} f_{11} \\ f_{12} \\ f_{21} \\ f_{22} \end{pmatrix} = (I_{\mathrm{C}} \otimes B_{\mathrm{C}})x' = f'
\end{gathered} \tag{D.12}$$

This also gives:

$$(I_{\mathrm{C}} \boxtimes B_{\mathrm{C}}) = (I_{\mathrm{R}} \boxtimes B_{\mathrm{R}})^T \tag{D.13}$$

where A_{R} is partitioned matrix where each partition is a row of the original matrix. I_{R} is partitioned matrix where each row is identity matrix. Similarly B_{C} is partitioned matrix, where each partition is a column of the original matrix and I_{C} has identity matrices as its column partitions. Note that identity in Eq. (D.13) follows directly from Eq. (D.11) if we equalise a and b elements and transpose the 4×4 matrices.

This formulation generalises for matrices A and B as $AX^TB \rightarrow A_\mathrm{R} \boxtimes (B^T)_\mathrm{C}$ where $(B^T)_\mathrm{C}$ represents partitioning of matrix B^T into columns:

$$AX^TB \rightarrow \begin{pmatrix} A_{\mathrm{R}_1} \\ A_{\mathrm{R}_2} \\ \vdots \\ A_{\mathrm{R}_N} \end{pmatrix} \boxtimes \begin{pmatrix} B^T_{\mathrm{C}_1} & B^T_{\mathrm{C}_2} & \cdots & B^T_{\mathrm{C}_N} \end{pmatrix} x' = \begin{pmatrix} A_{\mathrm{R}_1} \otimes B^T_{\mathrm{C}_1} \\ A_{\mathrm{R}_2} \otimes B^T_{\mathrm{C}_2} \\ \vdots \\ A_{\mathrm{R}_N} \otimes B^T_{\mathrm{C}_N} \end{pmatrix} x' \tag{D.14}$$

note that the requirement is that the number of columns in B^T matches the number of rows in A.

For the density matrix model, Eq. (D.12) will be relevant when linearisation of terms in form $[A,\rho] + [B,\rho^T]$ is required:

$$\begin{gathered} [A,\rho] + [B,\rho^T] = C \\ \rightarrow (A \otimes I - I \otimes A^T)\rho' + (I_\mathrm{R} \boxtimes B_\mathrm{R} - (I_\mathrm{R} \boxtimes B_\mathrm{R})^T)\rho' = c' \end{gathered} \tag{D.15}$$

D.4 Normalisation of DM superoperator

Normalisation condition in density matrix formalism states that sum of diagonal elements of the density matrix has unity value. This corresponds to the probability conservation within the chosen basis. This condition can be set in several ways. The easiest approach is to delete one equation that corresponds to one of the diagonal elements of the density matrix and replaced it with the normalisation condition, this would add a constant term to the superoperator of the system as in Eq. (3.23) and allow straightforward solution in steady state. This approach is not compatible with the dynamic model, as most solvers require a specific vector of equations, which places the derivatives on one side.

Another approach is to reformulate the normalisation condition by reordering terms and setting one diagonal element of the density matrix to equal one minus all other diagonal elements:

$$\rho_{jj} = 1 - \sum_{i \neq j} \rho^{\mathrm{DC}}_{0_{ii}} \tag{D.16}$$

This equation needs to be substituted across the entire system where the selected ρ_{jj} occurs and the system will "shrink" by the row and the column that correspond to ρ_{jj} element. To illustrate this, consider a linear system of differential equations $LX = \frac{dX}{dt}$:

$$\begin{pmatrix} a_{11} & a_{12} & a_{13} \\ a_{21} & a_{22} & a_{23} \\ a_{31} & a_{32} & a_{33} \end{pmatrix} \begin{pmatrix} x_1 \\ x_2 \\ x_3 \end{pmatrix} = \frac{d}{dt} \begin{pmatrix} x_1 \\ x_2 \\ x_3 \end{pmatrix} \tag{D.17}$$

If we implement $x_3 = Y - x_2 - x_1$ ($Y = 1$, however we will keep the general notion) and delete the third equation, the system in Eq. (D.17) becomes:

$$\begin{pmatrix} a_{11} - a_{13} & a_{12} - a_{13} \\ a_{21} - a_{23} & a_{22} - a_{23} \end{pmatrix} \begin{pmatrix} x_1 \\ x_2 \end{pmatrix} + Y \begin{pmatrix} a_{13} \\ a_{23} \end{pmatrix} = \frac{d}{dt} \begin{pmatrix} x_1 \\ x_2 \end{pmatrix} \tag{D.18}$$

Two effects can be noticed in Eq. (D.18):

- The column that corresponds to x_3 in the initial system in Eq. (D.18) excluding the a_{33} element, remained as a free term in Eq. (D.18) times the constant Y.
- The same column is subtracted from columns that correspond to x_1 and x_2 variable.

If we partition the system in Eq. (D.17) in column from as $(A_1\ A_2\ A_3)X = \frac{dX}{dt}$, the condition $x_3 = 1 - x_2 - x_1$ modifies the system as:

$$(A_{1\mathrm{R}} - A_{3\mathrm{R}} \quad A_{2\mathrm{R}} - A_{3\mathrm{R}}) \odot X_{\mathrm{R}} + Y A_{3\mathrm{R}} = \frac{dX_{\mathrm{R}}}{dt} \tag{D.19}$$

where R notation refers to the fact that the last equation in Eq. (D.17) is removed and original columns are “shrank” by the last element, $\odot$ only refers that this is a dot type product when partitioned form is used.

The normalisation condition for the DM model used in this thesis follows the outline in Eqs. (D.18,D.19), however there is a slight complication in which columns and which rows need to be altered. The system in Eq. 6.9 has $10N^2 \times 10N^2$ size, however normalisation condition only affects the diagonal elements of ρ_0^{DC} that are located in $N^2 \times N^2$ partition in the the 10th (real part) and 9th (imaginary part) row of the overall system. The selected diagonal element was the one that corresponds to the last state in the basis, whose equation is written in $10N^2$-th row (real part) and $9N^2$-th row (imaginary part). The normalisation condition $\rho_{0_{NN}}^{\mathrm{DC}} = \sum_{i \neq N} 1 - \rho_{0_{ii}}^{DC}$ affects the system created in Eq. 6.9 as follows:

- Rows $10N^2$ and $9N^2$ are deleted from the system
- Columns $10N^2$ and $9N^2$ (after the previous shedding) are also deleted from the system, and stored in column vectors C_{R} and C_{I}, respectively.
- Each column that targets real part of diagonal elements $\rho_{0_{ii}}^{\mathrm{DC}}, i \neq N$ is subtracted by column C_{R}
- Each column that targets imaginary part of diagonal elements $\rho_{0_{ii}}^{\mathrm{DC}}, i \neq N$ is subtracted by column C_{I}
- Column C_{R} is added as free term to the system (note that C_{I} is not added, since in that case $Y = 0$ in Eq. (D.19))

The system can then be written as in Eq. (6.10). Note that overall Maxwell-Bloch system is coupled, and the optical electric field equations can be added at the bottom of the DM system, or at the position of the deleted equations due to the normalisation condition. In either case, the overall system will have $10N^2$ differential equations, which can be solved by various packages within C++ GSL library.

References

[1] A. Siegman, *Lasers.* University Science Books, 1986.

[2] D. A. Deacon, L. Elias, J. M. Madey, G. Ramian, H. Schwettman, and T. I. Smith, “First operation of a free-electron laser,” *Physical Review Letters*, vol. 38, no. 16, p. 892, 1977.

[3] M. J. Weber, *Handbook of Laser Wavelengths.* CRC press, 1998.

[4] R. N. Hall, G. E. Fenner, J. Kingsley, T. Soltys, and R. Carlson, “Coherent light emission from GaAs junctions,” *Physical Review Letters*, vol. 9, no. 9, p. 366, 1962.

[5] I. Vurgaftman, J. Meyer, and L. Ram-Mohan, “Band parameters for iii–v compound semiconductors and their alloys,” *Journal of Applied Physics*, vol. 89, no. 11, pp. 5815–5875, 2001.

[6] G. P. Agrawal and N. K. Dutta, *Semiconductor Lasers.* Springer Science & Business Media, 2013.

[7] L. A. Coldren, S. W. Corzine, and M. L. Mashanović, *Diode Lasers and Photonic Integrated Circuits.* John Wiley & Sons, 2012.

[8] L. Esaki and R. Tsu, “Superlattice and negative differential conductivity in semiconductors,” *IBM Journal of Research and Development*, vol. 14, no. 1, pp. 61–65, 1970.

[9] R. Tsu and L. Esaki, “Tunneling in a finite superlattice,” *Applied Physics Letters*, vol. 22, no. 11, pp. 562–564, 1973.

[10] R. Kazarinov, “Possibility of amplification of electromagnetic waves in a semiconductor with superlattice,” *Sov. Phys.-Semicond.*, vol. 5, no. 4, pp. 707–709, 1971.

[11] J. Faist, F. Capasso, D. L. Sivco, C. Sirtori, A. L. Hutchinson, and A. Y. Cho, “Quantum Cascade Laser,” *Science*, vol. 264, no. 5158, pp. 553–556, 1994.

[12] C. Gmachl, F. Capasso, D. L. Sivco, and A. Y. Cho, “Recent progress in quantum cascade lasers and applications,” *Rep. Prog. Phys.*, vol. 64, no. 11, p. 1533, 2001.

[13] F. Capasso, “High-performance midinfrared quantum cascade lasers,” *Optical Engineering*, vol. 49, no. 11, pp. 111102–111102–9, 2010.

[14] H. Page, C. Becker, A. Robertson, G. Glastre, V. Ortiz, and C. Sirtori, “300 k operation of a GaAs-based quantum-cascade laser at $\lambda \approx 9$ μm,” *Applied Physics Letters*, vol. 78, no. 22, pp. 3529–3531, 2001.

[15] C. Pflügl, W. Schrenk, S. Anders, G. Strasser, C. Becker, C. Sirtori, Y. Bonetti, and A. Muller, “High-temperature performance of GaAs-based bound-to-continuum quantum-cascade lasers,” *Applied physics letters*, vol. 83, no. 23, pp. 4698–4700, 2003.

[16] Y. Bai, N. Bandyopadhyay, S. Tsao, S. Slivken, and M. Razeghi, “Room temperature quantum cascade lasers with 27% wall plug efficiency,” *Applied Physics Letters*, vol. 98, no. 18, p. 181102, 2011.

[17] M. Razeghi, W. Zhou, S. Slivken, Q.-Y. Lu, D. Wu, and R. McClintock, “Recent progress of quantum cascade laser research from 3 to 12 μm at the center for quantum devices,” *Applied optics*, vol. 56, no. 31, pp. H30–H44, 2017.

[18] J. Devenson, R. Teissier, O. Cathabard, and A. Baranov, “InAs / AlSb quantum cascade lasers emitting below 3 μm,” *Applied physics letters*, vol. 90, no. 11, p. 111118, 2007.

[19] M. Rochat, D. Hofstetter, M. Beck, and J. Faist, "Long-wavelength ($\lambda \approx$ 16 μm), room-temperature, single-frequency quantum-cascade lasers based on a bound-to-continuum transition," *Applied Physics Letters*, vol. 79, no. 26, pp. 4271–4273, 2001.

[20] G. Wysocki, R. Lewicki, R. F. Curl, F. K. Tittel, L. Diehl, F. Capasso, M. Troccoli, G. Hofler, D. Bour, S. Corzine, R. Maulini, M. Giovannini, and J. Faist, "Widely tunable mode-hop free external cavity quantum cascade lasers for high resolution spectroscopy and chemical sensing," *Appl. Phys. B*, vol. 92, no. 3, pp. 305–311, 2008.

[21] R. F. Curl, F. Capasso, C. Gmachl, A. A. Kosterev, B. McManus, R. Lewicki, M. Pusharsky, G. Wysocki, and F. K. Tittel, "Quantum cascade lasers in chemical physics," *Chemical Physics Letters*, vol. 487, no. 1-3, pp. 1–18, 2010.

[22] R. Martini and E. Whittaker, "Quantum cascade laser-based free space optical communications," in *Free-Space Laser Communications*, pp. 393–406, Springer, 2005.

[23] M. Hannemann, A. Antufjew, K. Borgmann, F. Hempel, T. Ittermann, S. Welzel, K. Weltmann, H. Völzke, and J. Röpcke, "Influence of age and sex in exhaled breath samples investigated by means of infrared laser absorption spectroscopy," *Journal of breath research*, vol. 5, no. 2, p. 027101, 2011.

[24] F. Hempel, V. Artyushenko, F. Weichbrodt, and J. Röpcke, "Application of quantum cascade lasers and infrared-fibres for the monitoring and control of industrial plasma processes," in *Journal of Physics: Conference Series*, vol. 157, p. 012003, IOP Publishing, 2009.

[25] J. Röpcke, P. Davies, N. Lang, A. Rousseau, and S. Welzel, "Applications of quantum cascade lasers in plasma diagnostics: a review," *Journal of Physics D: Applied Physics*, vol. 45, no. 42, p. 423001, 2012.

[26] J. B. McManus, J. H. Shorter, D. D. Nelson, M. S. Zahniser, D. E. Glenn, and R. M. McGovern, “Pulsed quantum cascade laser instrument with compact design for rapid, high sensitivity measurements of trace gases in air,” *Appl. Phys. B*, vol. 92, no. 3, p. 387, 2008.

[27] E. Bründermann, D. R. Chamberlin, and E. E. Haller, “High duty cycle and continuous terahertz emission from germanium,” *Applied Physics Letters*, vol. 76, no. 21, pp. 2991–2993, 2000.

[28] K. Kawase, J.-i. Shikata, H. Minamide, K. Imai, and H. Ito, “Arrayed silicon prism coupler for a terahertz-wave parametric oscillator,” *Applied optics*, vol. 40, no. 9, pp. 1423–1426, 2001.

[29] B. Knyazev, G. Kulipanov, and N. Vinokurov, “Novosibirsk terahertz free electron laser: instrumentation development and experimental achievements,” *Measurement Science and Technology*, vol. 21, no. 5, p. 054017, 2010.

[30] R. Köhler, A. Tredicucci, F. Beltram, H. E. Beere, E. H. Linfield, A. G. Davies, D. A. Ritchie, R. C. Iotti, and F. Rossi, “Terahertz semiconductor-heterostructure laser,” *Nature*, vol. 417, no. 6885, pp. 156–159, 2002.

[31] B. S. Williams, “Terahertz quantum-cascade lasers,” *Nature photonics*, vol. 1, no. 9, p. 517, 2007.

[32] M. Tonouchi, “Cutting-edge terahertz technology,” *Nature photonics*, vol. 1, no. 2, p. 97, 2007.

[33] C. Walther, M. Fischer, G. Scalari, R. Terazzi, N. Hoyler, and J. Faist, “Quantum cascade lasers operating from 1.2 to 1.6 thz,” *Applied Physics Letters*, vol. 91, no. 13, p. 131122, 2007.

[34] G. Scalari, C. Walther, M. Fischer, R. Terazzi, H. Beere, D. Ritchie, and J. Faist, “THz and sub-THz quantum cascade lasers,” *Laser & Photon. Rev.*, vol. 3, no. 1-2, pp. 45–66, 2009.

[35] M. Wienold, B. Röben, X. Lü, G. Rozas, L. Schrottke, K. Biermann, and H. T. Grahn, “Frequency dependence of the maximum operating temperature for quantum-cascade lasers up to 5.4 thz,” *Applied Physics Letters*, vol. 107, no. 20, p. 202101, 2015.

[36] L. Bosco, M. Franckié, G. Scalari, M. Beck, A. Wacker, and J. Faist, “Thermoelectrically cooled thz quantum cascade laser operating up to 210 k,” *Applied Physics Letters*, vol. 115, no. 1, p. 010601, 2019.

[37] M. S. Vitiello, G. Scalari, B. Williams, and P. De Natale, “Quantum cascade lasers: 20 years of challenges,” *Optics express*, vol. 23, no. 4, pp. 5167–5182, 2015.

[38] S. F. Shayesteh, T. Dumelow, T. Parker, G. Mirjalili, L. Vorobjev, D. Donetsky, and A. Kastalsky, “Far-infrared spectra of reflectivity, transmission and hot-hole emission in p-doped multiple quantum wells,” *Semiconductor Science and Technology*, vol. 11, no. 3, p. 323, 1996.

[39] M. Dyksik, M. Motyka, W. Rudno-Rudziński, G. Sek, J. Misiewicz, D. Pucicki, K. Kosiel, I. Sankowska, J. Kubacka-Traczyk, and M. Bugajski, “Optical properties of active regions in terahertz quantum cascade lasers,” *Journal of Infrared, Millimeter, and Terahertz Waves*, vol. 37, no. 7, pp. 710–719, 2016.

[40] A. Wade, G. Fedorov, D. Smirnov, S. Kumar, B. Williams, Q. Hu, and J. Reno, “Magnetic-field-assisted terahertz quantum cascade laser operating up to 225 k,” *Nature Photonics*, vol. 3, no. 1, p. 41, 2009.

[41] K. Fujita, S. Jung, Y. Jiang, J. H. Kim, A. Nakanishi, A. Ito, M. Hitaka, T. Edamura, and M. A. Belkin, “Recent progress in terahertz difference-frequency quantum cascade laser sources,” *Nanophotonics*, vol. 7, no. 11, pp. 1795–1817, 2018.

[42] M. Razeghi, Q. Lu, N. Bandyopadhyay, W. Zhou, D. Heydari, Y. Bai, and S. Slivken, “Quantum cascade lasers: from tool to product,” *Optics express*, vol. 23, no. 7, pp. 8462–8475, 2015.

[43] D. Indjin, P. Harrison, R. W. Kelsall, and Z. Ikonić, "Mechanisms of temperature performance degradation in quantum-cascade lasers," *Appl. Phys. Lett.*, vol. 82, no. 9, pp. 1347–1349, 2003.

[44] S. Kumar, "Recent progress in terahertz quantum cascade lasers," *IEEE Journal of Selected Topics in Quantum Electronics*, vol. 17, no. 1, pp. 38–47, 2011.

[45] C. A. Evans, *The optical and thermal properties of quantum cascade lasers.* PhD thesis, University of Leeds, 2008, `http://etheses.whiterose.ac.uk/5079/`.

[46] B. S. Williams, H. Callebaut, S. Kumar, Q. Hu, and J. L. Reno, "3.4-thz quantum cascade laser based on longitudinal-optical-phonon scattering for depopulation," *Applied Physics Letters*, vol. 82, no. 7, pp. 1015–1017, 2003.

[47] S. Fathololoumi, E. Dupont, C. W. I. Chan, Z. R. Wasilewski, S. R. Laframboise, D. Ban, A. Mátyás, C. Jirauschek, Q. Hu, and H. C. Liu, "Terahertz quantum cascade lasers operating up to $\sim$ 200 K with optimized oscillator strength and improved injection tunneling," *Opt. Express*, vol. 20, no. 4, pp. 3866–3876, 2012.

[48] S. Kumar, C. W. I. Chan, Q. Hu, and J. L. Reno, "A 1.8-thz quantum cascade laser operating significantly above the temperature of $\hbar\ \omega$/k b," *Nature Physics*, vol. 7, no. 2, p. 166, 2011.

[49] Y. Han, L. Li, A. Grier, L. Chen, A. Valavanis, J. Zhu, J. Freeman, N. Isac, R. Colombelli, P. Dean, *et al.*, "Extraction-controlled terahertz frequency quantum cascade lasers with a diagonal lo-phonon extraction and injection stage," *Optics express*, vol. 24, no. 25, pp. 28583–28593, 2016.

[50] L. Wang, T.-T. Lin, K. Wang, T. Grange, S. Birner, and H. Hirayama, "Short-period scattering-assisted terahertz quantum cascade lasers operating at high temperatures," *Scientific reports*, vol. 9, no. 1, p. 9446, 2019.

[51] S. Khanal, J. L. Reno, and S. Kumar, “2.1 thz quantum-cascade laser operating up to 144 k based on a scattering-assisted injection design,” *Optics express*, vol. 23, no. 15, pp. 19689–19697, 2015.

[52] G. Scalari, N. Hoyler, M. Giovannini, and J. Faist, “Terahertz bound-to-continuum quantum-cascade lasers based on optical-phonon scattering extraction,” *Applied Physics Letters*, vol. 86, no. 18, p. 181101, 2005.

[53] L. Li, L. Chen, J. Zhu, J. Freeman, P. Dean, A. Valavanis, A. Davies, and E. Linfield, “Terahertz quantum cascade lasers with >1 W output powers,” *Electronics letters*, vol. 50, no. 4, pp. 309–311, 2014.

[54] M. Wienold, B. Röben, L. Schrottke, R. Sharma, A. Tahraoui, K. Biermann, and H. T. Grahn, “High-temperature, continuous-wave operation of terahertz quantum-cascade lasers with metal-metal waveguides and third-order distributed feedback,” *Opt. Express*, vol. 22, pp. 3334–3348, Feb 2014.

[55] G. Binnig, H. Rohrer, C. Gerber, and E. Weibel, “Surface studies by scanning tunneling microscopy,” *Physical review letters*, vol. 49, no. 1, p. 57, 1982.

[56] A. Y. Cho and J. Arthur, “Molecular beam epitaxy,” *Progress in solid state chemistry*, vol. 10, pp. 157–191, 1975.

[57] M. Henini, *Molecular Beam Epitaxy: From Research to Mass Production.* Newnes, 2012.

[58] L. Li, J. Zhu, L. Chen, A. Davies, and E. Linfield, “The MBE growth and optimization of high performance terahertz frequency quantum cascade lasers,” *Optics express*, vol. 23, no. 3, pp. 2720–2729, 2015.

[59] J. Zhu, *MBE growth, fabrication, and electrical characterisation of terahertz frequency quantum cascade lasers.* PhD thesis, University of Leeds, 2015, `http://etheses.whiterose.ac.uk/11459/`.

[60] H. Detz, A. M. Andrews, M. A. Kainz, S. Schönhuber, T. Zederbauer, D. MacFarland, M. Krall, C. Deutsch, M. Brandstetter, P. Klang, *et al.*, "Evaluation of material systems for thz quantum cascade laser active regions," *physica status solidi (a)*, vol. 216, no. 1, p. 1800504, 2019.

[61] A. Grier, *Modelling the optical and electronic transport properties of AlGaAs and AlGaN intersubband devices and optimisation of quantum cascade laser active regions*. Phd, University of Leeds, 2015, `http://etheses.whiterose.ac.uk/11221/`.

[62] A. Grier, A. Valavanis, C. Edmunds, J. Shao, J. D. Cooper, G. Gardner, M. J. Manfra, O. Malis, D. Indjin, Z. Ikonić, and P. Harrison, "Coherent vertical electron transport and interface roughness effects in AlGaN/GaN intersubband devices," *J. Appl. Phys.*, vol. 118, no. 22, p. 224308, 2015.

[63] O. Demichel, L. Mahler, T. Losco, C. Mauro, R. Green, J. Xu, A. Tredicucci, F. Beltram, H. E. Beere, D. A. Ritchie, *et al.*, "Surface plasmon photonic structures in terahertz quantum cascade lasers," *Optics express*, vol. 14, no. 12, pp. 5335–5345, 2006.

[64] M. Chamberlain, M. Cardona, and B. Ridley, "Optical modes in GaAs/AlAs superlattices," *Physical Review B*, vol. 48, no. 19, p. 14356, 1993.

[65] C. A. Evans, D. Indjin, Z. Ikonić, and P. Harrison, "The role of temperature in quantum-cascade laser waveguides," *Journal of Computational Electronics*, vol. 11, no. 1, pp. 137–143, 2012.

[66] P. Hohenberg and W. Kohn, "Inhomogeneous electron gas," *Physical review*, vol. 136, no. 3B, p. B864, 1964.

[67] J. Callaway and N. March, "Density functional methods: theory and applications," in *Solid State Physics*, vol. 38, pp. 135–221, Elsevier, 1984.

[68] A. Wacker, "Semiconductor superlattices: a model system for nonlinear transport," *Physics Reports*, vol. 357, no. 1, pp. 1–111, 2002.

[69] A. Wacker, M. Lindskog, and D. O. Winge, "Nonequilibrium Green's Function Model for simulation of quantum cascade laser devices under operating conditions," *IEEE Journal of Selected Topics in Quantum Electronics*, vol. 19, no. 5, 2013.

[70] D. O. Winge, M. Lindskog, and A. Wacker, "Nonlinear response of quantum cascade structures," *Appl. Phys. Lett.*, vol. 101, no. 21, p. 211113, 2012.

[71] M. Paulsson, "Non equilibrium green's functions for dummies: Introduction to the one particle negf equations," *arXiv preprint cond-mat/0210519*, 2002.

[72] A. Pan, B. A. Burnett, C. O. Chui, and B. S. Williams, "Density matrix modeling of quantum cascade lasers without an artificially localized basis: A generalized scattering approach," *Physical Review B*, vol. 96, no. 8, p. 085308, 2017.

[73] T. V. Dinh, A. Valavanis, L. J. M. Lever, Z. Ikonić, and R. W. Kelsall, "Extended density-matrix model applied to silicon-based terahertz quantum cascade lasers," *Phys. Rev. B*, vol. 85, no. 23, p. 235427, 2012.

[74] A. Demić, A. Grier, Z. Ikonić, A. Valavanis, C. A. Evans, R. Mohandas, L. Li, E. H. Linfield, A. G. Davies, and D. Indjin, "Infinite-period density-matrix model for terahertz-frequency quantum cascade lasers," *IEEE Transactions on Terahertz Science and Technology*, vol. 7, pp. 368–377, July 2017.

[75] H. Yasuda, T. Kubis, P. Vogl, N. Sekine, I. Hosako, and K. Hirakawa, "Nonequilibrium Green's function calculation for four-level scheme terahertz quantum cascade lasers," *Appl. Phys. Lett.*, vol. 94, no. 15, p. 151109, 2009.

[76] C. Jirauschek and T. Kubis, "Modeling techniques for quantum cascade lasers," *Appl. Phys. Rev.*, vol. 1, no. 1, p. 011307, 2014.

[77] K. Blum, *Density Matrix Theory and Applications*, vol. 64. Springer Science & Business Media, 2012.

[78] R. Terazzi and J. Faist, “A density matrix model of transport and radiation in quantum cascade lasers,” *New J. Phys.*, vol. 12, no. 3, p. 033045, 2010.

[79] R. W. Boyd, *Nonlinear Optics.* Academic Press, 2008.

[80] S. Kumar and Q. Hu, “Coherence of resonant-tunneling transport in terahertz quantum-cascade lasers,” *Phys. Rev. B*, vol. 80, no. 24, p. 245316, 2009.

[81] H. Callebaut and Q. Hu, “Importance of coherence for electron transport in terahertz quantum cascade lasers,” *J. Appl. Phys.*, vol. 98, no. 10, p. 104505, 2005.

[82] E. Dupont, S. Fathololoumi, and H. C. Liu, “Simplified density-matrix model applied to three-well terahertz quantum cascade lasers,” *Phys. Rev. B*, vol. 81, no. 20, p. 205311, 2010.

[83] A. Demić, Z. Ikonić, R. W. Kelsall, and D. Indjin, “Density matrix superoperator for periodic quantum systems and its application to quantum cascade laser structures,” *AIP Advances*, vol. 9, no. 9, p. 095019, 2019.

[84] E. Schöll, *Theory of Transport Properties of Semiconductor Nanostructures*, vol. 4. Springer Science & Business Media, 2013.

[85] T. Almqvist, D. O. Winge, E. Dupont, and A. Wacker, “Domain formation and self-sustained oscillations in quantum cascade lasers,” *The European Physical Journal B*, vol. 92, no. 4, p. 72, 2019.

[86] P. Harrison and A. Valavanis, *Quantum Wells, Wires and Dots: Theoretical and Computational Physics of Semiconductor Nanostructures.* 4th edition, John Wiley & Sons, 2016.

[87] C. A. Evans, D. Indjin, Z. Ikonic, P. Harrison, M. S. Vitiello, V. Spagnolo, and G. Scamarcio, “Thermal modeling of terahertz quantum-cascade lasers: comparison of optical waveguides,” *IEEE Journal of Quantum Electronics*, vol. 44, no. 7, pp. 680–685, 2008.

[88] P. Tzenov, D. Burghoff, Q. Hu, and C. Jirauschek, “Time domain modeling of terahertz quantum cascade lasers for frequency comb generation,” *Opt. Express*, vol. 24, no. 20, pp. 23232–23247, 2016.

[89] D. Mittleman, “Terahertz imaging,” in *Sensing with terahertz radiation*, pp. 117–153, Springer, 2003.

[90] D. L. Woolard, W. R. Loerop, and M. Shur, *Terahertz Sensing Technology: Emerging Scientific Applications & Novel Device Concepts*, vol. 2. World scientific, 2003.

[91] T. Taimre, M. Nikolić, K. Bertling, Y. L. Lim, T. Bosch, and A. D. Rakić, “Laser feedback interferometry: a tutorial on the self-mixing effect for coherent sensing,” *Adv. Opt. Photon., AOP*, vol. 7, no. 3, pp. 570–631, 2015.

[92] D. M. Kane and K. A. Shore, *Unlocking Dynamical Diversity: Optical Feedback Effects on Semiconductor Lasers*. John Wiley & Sons, 2005.

[93] P. Dean, Y. L. Lim, A. Valavanis, R. Kliese, M. Nikolić, S. P. Khanna, M. Lachab, D. Indjin, Z. Ikonić, P. Harrison, *et al.*, “Terahertz imaging through self-mixing in a quantum cascade laser,” *Optics letters*, vol. 36, no. 13, pp. 2587–2589, 2011.

[94] A. Valavanis, P. Dean, Y. L. Lim, R. Alhathlool, M. Nikolic, R. Kliese, S. P. Khanna, D. Indjin, S. J. Wilson, A. D. Rakic, *et al.*, “Self-mixing interferometry with terahertz quantum cascade lasers,” *IEEE Sensors Journal*, vol. 13, no. 1, pp. 37–43, 2012.

[95] P. Dean, A. Valavanis, J. Keeley, K. Bertling, Y. Leng Lim, R. Alhathlool, S. Chowdhury, T. Taimre, L. H. Li, D. Indjin, *et al.*, “Coherent three-dimensional terahertz imaging through self-mixing in a quantum cascade laser,” *Applied Physics Letters*, vol. 103, no. 18, p. 181112, 2013.

[96] P. Dean, O. Mitrofanov, J. Keeley, I. Kundu, L. Li, E. H. Linfield, and A. Giles Davies, “Apertureless near-field terahertz imaging using the self-mixing effect in a quantum cascade laser,” *Applied Physics Letters*, vol. 108, no. 9, p. 091113, 2016.

[97] P. Dean, A. Valavanis, J. Keeley, K. Bertling, Y. Lim, R. Alhathlool, A. Burnett, L. Li, S. Khanna, D. Indjin, *et al.*, “Terahertz imaging using quantum cascade lasers—a review of systems and applications,” *Journal of Physics D: Applied Physics*, vol. 47, no. 37, p. 374008, 2014.

[98] Y. Leng Lim, P. Dean, M. Nikolić, R. Kliese, S. P. Khanna, M. Lachab, A. Valavanis, D. Indjin, Z. Ikonić, P. Harrison, *et al.*, “Demonstration of a self-mixing displacement sensor based on terahertz quantum cascade lasers,” *Applied Physics Letters*, vol. 99, no. 8, p. 081108, 2011.

[99] T. Taimre, K. Bertling, Y. L. Lim, P. Dean, D. Indjin, and A. D. Rakić, “Methodology for materials analysis using swept-frequency feedback interferometry with terahertz frequency quantum cascade lasers,” *Optics express*, vol. 22, no. 15, pp. 18633–18647, 2014.

[100] Y. L. Lim, T. Taimre, K. Bertling, P. Dean, D. Indjin, A. Valavanis, S. P. Khanna, M. Lachab, H. Schaider, T. W. Prow, *et al.*, “High-contrast coherent terahertz imaging of porcine tissue via swept-frequency feedback interferometry,” *Biomedical optics express*, vol. 5, no. 11, pp. 3981–3989, 2014.

[101] A. D. Rakić, T. Taimre, K. Bertling, Y. L. Lim, P. Dean, D. Indjin, Z. Ikonić, P. Harrison, A. Valavanis, S. P. Khanna, M. Lachab, S. J. Wilson, E. H. Linfield, and A. G. Davies, “Swept-frequency feedback interferometry using terahertz frequency QCLs: a method for imaging and materials analysis,” *Opt. Express*, vol. 21, no. 19, pp. 22194–22205, 2013.

[102] R. Lang and K. Kobayashi, “External optical feedback effects on semiconductor injection laser properties,” *IEEE Journal of Quantum Electronics*, vol. 16, no. 3, pp. 347–355, 1980.

[103] G. Agnew, A. Grier, T. Taimre, Y. L. Lim, M. Nikolić, A. Valavanis, J. Cooper, P. Dean, S. P. Khanna, M. Lachab, E. H. Linfield, A. G. Davies, P. Harrison, Z. Ikonić, D. Indjin, and A. D. Rakić, “Efficient prediction of terahertz quantum cascade laser dynamics from steady-state simulations,” *Appl. Phys. Lett.*, vol. 106, no. 16, p. 161105, 2015.

[104] G. Agnew, A. Grier, T. Taimre, Y. L. Lim, K. Bertling, Z. Ikonić, A. Valavanis, P. Dean, J. Cooper, S. P. Khanna, M. Lachab, E. H. Linfield, A. G. Davies, P. Harrison, D. Indjin, and A. D. Rakić, “Model for a pulsed terahertz quantum cascade laser under optical feedback,” *Opt. Express*, vol. 24, no. 18, pp. 20554–20570, 2016.

[105] T. Kanada and K. Nawata, “Injection laser characteristics due to reflected optical power,” *IEEE Journal of Quantum Electronics*, vol. 15, no. 7, pp. 559–565, 1979.

[106] A. Grier, P. Dean, A. Valavanis, J. Keeley, I. Kundu, J. D. Cooper, G. Agnew, T. Taimre, Y. L. Lim, K. Bertling, A. D. Rakić, L. H. Li, P. Harrison, E. H. Linfield, Z. Ikonić, A. G. Davies, and D. Indjin, “Origin of terminal voltage variations due to self-mixing in terahertz frequency quantum cascade lasers,” *Opt. Express*, vol. 24, no. 19, pp. 21948–21956, 2016.

[107] A. Dunn, C. Poyser, P. Dean, A. Demić, A. Valavanis, D. Indjin, M. Salih, I. Kundu, L. Li, A. Akimov, A. G. Davies, E. Linfield, J. Cunningham, and A. Kent, “High-speed modulation of a terahertz quantum cascade laser by coherent acoustic phonon pulses,” *Nature communications*, 2020 (accepted for publication).

[108] V. Jovanović, *Theory and design of GaAs and GaN-based quantum cascade lasers and quantum well infrared photodetectors.* PhD thesis, University of Leeds, 2005.

[109] O. Madelung, *Introduction to Solid-state Theory*, vol. 2. Springer Science & Business Media, 2012.

[110] H. Yasuda, “Intervalley scattering in terahertz quantum cascade lasers with GaSb and InGaSb wells,” *AIP advances*, vol. 8, no. 2, p. 025125, 2018.

[111] A. Valavanis, *n-type silicon-germanium based terahertz quantum cascade lasers.* Phd, University of Leeds, 2009, `http://etheses.whiterose.ac.uk/1262/`.

[112] A. Demić, J. Radovanović, and V. Milanović, "Analysis of the influence of external magnetic field on transition matrix elements in quantum well and quantum cascade laser structures," *Superlattices and Microstructures*, vol. 96, pp. 134–149, 2016.

[113] J. D. Cooper, A. Valavanis, Z. Ikonić, P. Harrison, and J. E. Cunningham, "Finite difference method for solving the Schrödinger equation with band nonparabolicity in mid-infrared quantum cascade lasers," *J. Appl. Phys.*, vol. 108, no. 11, p. 113109, 2010.

[114] B. N. Datta, *Numerical Linear Algebra and Applications*, vol. 116. Siam, 2010.

[115] G. Bastard, *Wave Mechanics Applied to Semiconductor Heterostructures.* New York, NY (USA); John Wiley and Sons Inc., 1990.

[116] J. H. Smet, C. G. Fonstad, and Q. Hu, "Intrawell and interwell intersubband transitions in multiple quantum wells for far-infrared sources," *Journal of Applied Physics*, vol. 79, no. 12, pp. 9305–9320, 1996.

[117] P. Harrison, D. Indjin, and R. Kelsall, "Electron temperature and mechanisms of hot carrier generation in quantum cascade lasers," *Journal of Applied Physics*, vol. 92, no. 11, pp. 6921–6923, 2002.

[118] V. Jovanović, S. Höfling, D. Indjin, N. Vukmirović, Z. Ikonić, P. Harrison, J. Reithmaier, and A. Forchel, "Influence of doping density on electron dynamics in GaAs/AlGaAs quantum cascade lasers," *Journal of Applied Physics*, vol. 99, no. 10, p. 103106, 2006.

[119] D. Indjin, P. Harrison, R. W. Kelsall, and Z. Ikonic, "Self-consistent scattering model of carrier dynamics in GaAs-AlGaAs terahertz quantum-cascade lasers," *IEEE Photonics Technology Letters*, vol. 15, no. 1, pp. 15–17, 2003.

[120] K. E. Atkinson, *An Introduction to Numerical Analysis.* John Wiley & Sons, 2008.

[121] R. McWeeny, “Some recent advances in density matrix theory,” *Reviews of Modern Physics*, vol. 32, no. 2, p. 335, 1960.

[122] U. Fano, “Description of states in quantum mechanics by density matrix and operator techniques,” *Reviews of Modern Physics*, vol. 29, no. 1, p. 74, 1957.

[123] G. Lindblad, “On the generators of quantum dynamical semigroups,” *Communications in Mathematical Physics*, vol. 48, no. 2, pp. 119–130, 1976.

[124] A. Kossakowski, “On quantum statistical mechanics of non-hamiltonian systems,” *Reports on Mathematical Physics*, vol. 3, no. 4, pp. 247 – 274, 1972.

[125] V. Gorini, A. Kossakowski, and E. C. G. Sudarshan, “Completely positive dynamical semigroups of n-level systems,” *Journal of Mathematical Physics*, vol. 17, no. 5, pp. 821–825, 1976.

[126] T. Banks, L. Susskind, and M. E. Peskin, “Difficulties for the evolution of pure states into mixed states,” *Nuclear Physics B*, vol. 244, no. 1, pp. 125 – 134, 1984.

[127] I. Savić, N. Vukmirović, Z. Ikonić, D. Indjin, R. W. Kelsall, P. Harrison, and V. Milanović, “Density matrix theory of transport and gain in quantum cascade lasers in a magnetic field,” *Phys. Rev. B*, vol. 76, no. 16, p. 165310, 2007.

[128] B. A. Burnett and B. S. Williams, “Density matrix model for polarons in a terahertz quantum dot cascade laser,” *Phys. Rev. B*, vol. 90, no. 15, p. 155309, 2014.

[129] B. A. Burnett and B. S. Williams, “Origins of terahertz difference frequency susceptibility in midinfrared quantum cascade lasers,” *Phys. Rev. Applied*, vol. 5, no. 3, p. 034013, 2016.

[130] O. Jonasson, *Quantum transport in semiconductor heterostructures using density-matrix and Wigner-function formalisms.* PhD thesis, The University of Wisconsin-Madison, 2016.

[131] O. Jonasson, F. Karimi, and I. Knezevic, "Partially coherent electron transport in terahertz quantum cascade lasers based on a Markovian master equation for the density matrix," *J Comput Electron*, vol. 15, no. 4, pp. 1192–1205, 2016.

[132] O. Jonasson, S. Mei, F. Karimi, J. Kirch, D. Botez, L. Mawst, and I. Knezevic, "Quantum transport simulation of high-power 4.6-μm quantum cascade lasers," in *Photonics*, vol. 3, p. 38, Multidisciplinary Digital Publishing Institute, 2016.

[133] A. Yariv, C. Lindsey, and U. Sivan, "Approximate analytic solution for electronic wave functions and energies in coupled quantum wells," *J. Appl. Phys.*, vol. 58, no. 9, pp. 3669–3672, 1985.

[134] L. Molinari, "Transfer matrices and tridiagonal-block hamiltonians with periodic and scattering boundary conditions," *Journal of Physics A: Mathematical and General*, vol. 30, no. 3, p. 983, 1997.

[135] D. S. Watkins, *Fundamentals of Matrix Computations*, vol. 64. John Wiley & Sons, 2004.

[136] A. Graham, *Kronecker Products and Matrix Calculus: With Applications.* John Wiley & Sons, 1982.

[137] C. G. Khatri and C. R. Rao, "Solutions to some functional equations and their applications to characterization of probability distributions," *Sankhyā: The Indian Journal of Statistics, Series A (1961-2002)*, vol. 30, no. 2, pp. 167–180, 1968.

[138] C. R. Rao, "Estimation of heteroscedastic variances in linear models," *Journal of the American Statistical Association*, vol. 65, no. 329, pp. 161–172, 1970.

[139] C. R. Rao and M. B. Rao, *Matrix Algebra and its Applications to Statistics and Econometrics.* World Scientific, 1998.

[140] H. L. Van Trees, *Detection, Estimation, and Modulation Theory.* John Wiley & Sons, 2004.

[141] S. Liu and G. Trenkler, "Hadamard, khatri-rao, kronecker and other matrix products," *Int. J. Inf. Syst. Sci*, vol. 4, no. 1, pp. 160–177, 2008.

[142] S. Liu, "Several inequalities involving khatri–rao products of positive semidefinite matrices," *Linear Algebra and its Applications*, vol. 354, no. 1-3, pp. 175–186, 2002.

[143] F. Karimi, A. H. Davoody, and I. Knezevic, "Dielectric function and plasmons in graphene: A self-consistent-field calculation within a markovian master equation formalism," *Phys. Rev. B*, vol. 93, p. 205421, May 2016.

[144] J. R. Freeman, O. Marshall, H. E. Beere, and D. A. Ritchie, "Improved wall plug efficiency of a 1.9 thz quantum cascade laser by an automated design approach," *Applied Physics Letters*, vol. 93, no. 19, p. 191119, 2008.

[145] M. Wienold, L. Schrottke, M. Giehler, R. Hey, W. Anders, and H. Grahn, "Low-voltage terahertz quantum-cascade lasers based on lo-phonon-assisted interminiband transitions," *Electronics letters*, vol. 45, no. 20, pp. 1030–1031, 2009.

[146] M. S. Vitiello, G. Scamarcio, V. Spagnolo, B. S. Williams, S. Kumar, Q. Hu, and J. L. Reno, "Measurement of subband electronic temperatures and population inversion in thz quantum-cascade lasers," *Applied Physics Letters*, vol. 86, no. 11, p. 111115, 2005.

[147] M. S. Vitiello, G. Scamarcio, and V. Spagnolo, "Non equilibrium electrons in thz quantum cascade lasers," in *Novel In-Plane Semiconductor Lasers V*, vol. 6133, p. 61330K, International Society for Optics and Photonics, 2006.

[148] M. S. Vitiello, G. Scamarcio, V. Spagnolo, C. Worrall, H. E. Beere, D. A. Ritchie, C. Sirtori, J. Alton, and S. Barbieri, "Subband electronic temperatures and electron-lattice energy relaxation in terahertz quantum cascade lasers with different conduction band offsets," *Applied Physics Letters*, vol. 89, no. 13, p. 131114, 2006.

[149] G. Scamarcio, M. S. Vitiello, and V. Spagnolo, "Hot electrons in THz quantum cascade lasers," *Journal of Infrared, Millimeter, and Terahertz Waves*, vol. 34, no. 5-6, pp. 357–373, 2013.

[150] H. Li, J. Cao, Y. Han, Z. Tan, and X. Guo, "Temperature profile modelling and experimental investigation of thermal resistance of terahertz quantum-cascade lasers," *Journal of Physics D: Applied Physics*, vol. 42, no. 20, p. 205102, 2009.

[151] P. Rubino, *Near-field Imaging Using Self Mixing in Terahertz frequency Quantum Cascade Lasers*. PhD thesis, University of Leeds, 2019, `http://etheses.whiterose.ac.uk/25163/`.

[152] Y. Han, L. Li, J. Zhu, A. Valavanis, J. Freeman, L. Chen, M. Rosamond, P. Dean, A. Davies, and E. Linfield, "Silver-based surface plasmon waveguide for terahertz quantum cascade lasers," *Optics express*, vol. 26, no. 4, pp. 3814–3827, 2018.

[153] A. Yamamoto, T. Mishina, Y. Masumoto, and M. Nakayama, "Coherent oscillation of zone-folded phonon modes in GaAs-AlAs superlattices," *Physical review letters*, vol. 73, no. 5, p. 740, 1994.

[154] A. Huynh, B. Perrin, and A. Lemaître, "Semiconductor superlattices: A tool for terahertz acoustics," *Ultrasonics*, vol. 56, pp. 66–79, 2015.

[155] M. Pascual-Winter, A. Fainstein, B. Jusserand, B. Perrin, and A. Lemaître, "Spectral responses of phonon optical generation and detection in superlattices," *Physical Review B*, vol. 85, no. 23, p. 235443, 2012.

[156] P. Ruello and V. E. Gusev, “Physical mechanisms of coherent acoustic phonons generation by ultrafast laser action,” *Ultrasonics*, vol. 56, pp. 21–35, 2015.

[157] G. Tas and H. J. Maris, “Electron diffusion in metals studied by picosecond ultrasonics,” *Physical Review B*, vol. 49, no. 21, p. 15046, 1994.

[158] T. Saito, O. Matsuda, and O. Wright, “Picosecond acoustic phonon pulse generation in nickel and chromium,” *Physical Review B*, vol. 67, no. 20, p. 205421, 2003.

[159] H. T. Grahn, H. J. Maris, and J. Tauc, “Picosecond ultrasonics,” *IEEE Journal of Quantum Electronics*, vol. 25, no. 12, pp. 2562–2569, 1989.

[160] C. Thomsen, H. T. Grahn, H. J. Maris, and J. Tauc, “Surface generation and detection of phonons by picosecond light pulses,” *Physical Review B*, vol. 34, no. 6, p. 4129, 1986.

[161] C. L. Poyser, *The interaction of coherent acoustic phonons with electrons in semiconductor superlattices.* PhD thesis, University of Nottingham, 2015, http://eprints.nottingham.ac.uk/30591/.

[162] A. Akimov, A. Scherbakov, D. Yakovlev, C. Foxon, and M. Bayer, “Ultrafast band-gap shift induced by a strain pulse in semiconductor heterostructures,” *Physical review letters*, vol. 97, no. 3, p. 037401, 2006.

[163] J. Tucker, “Quantum limited detection in tunnel junction mixers,” *IEEE Journal of Quantum Electronics*, vol. 15, no. 11, pp. 1234–1258, 1979.

[164] D. Moss, A. Akimov, O. Makarovsky, R. Campion, C. Foxon, L. Eaves, A. Kent, and B. Glavin, “Ultrafast acoustical gating of the photocurrent in a p- i- n tunneling diode incorporating a quantum well,” *Physical Review B*, vol. 80, no. 11, p. 113306, 2009.

[165] E. Young, A. Akimov, M. Henini, L. Eaves, and A. Kent, “Subterahertz acoustical pumping of electronic charge in a resonant tunneling device,” *Physical review letters*, vol. 108, no. 22, p. 226601, 2012.

[166] G.-F. Wang, D.-F. Ye, L.-B. Fu, X.-Z. Chen, and J. Liu, "Landau-Zener tunneling in a nonlinear three-level system," *Physical Review A*, vol. 74, no. 3, p. 033414, 2006.

[167] R. K. Malla and M. Raikh, "Landau-Zener transition in a two-level system coupled to a single highly excited oscillator," *Physical Review B*, vol. 97, no. 3, p. 035428, 2018.

[168] M. Galassi, J. Davies, J. Theiler, B. Gough, G. Jungman, P. Alken, M. Booth, and F. Rossi, "Gnu scientific library," *No. Release*, vol. 2, 1996.

[169] Y. Castin, K. Mo, *et al.*, "Maxwell-Bloch equations: A unified view of nonlinear optics and nonlinear atom optics," *Physical Review A*, vol. 51, no. 5, p. R3426, 1995.

[170] S. Barbieri, W. Maineult, S. S. Dhillon, C. Sirtori, J. Alton, N. Breuil, H. E. Beere, and D. A. Ritchie, "13 ghz direct modulation of terahertz quantum cascade lasers," *Applied Physics Letters*, vol. 91, no. 14, p. 143510, 2007.

[171] R. P. Green, A. Tredicucci, N. Q. Vinh, B. Murdin, C. Pidgeon, H. E. Beere, and D. A. Ritchie, "Gain recovery dynamics of a terahertz quantum cascade laser," *Physical Review B*, vol. 80, no. 7, p. 075303, 2009.

[172] D. R. Bacon, J. R. Freeman, R. A. Mohandas, L. Li, E. H. Linfield, A. G. Davies, and P. Dean, "Gain recovery time in a terahertz quantum cascade laser," *Applied Physics Letters*, vol. 108, no. 8, p. 081104, 2016.

[173] C. G. Derntl, G. Scalari, D. Bachmann, M. Beck, J. Faist, K. Unterrainer, and J. Darmo, "Gain dynamics in a heterogeneous terahertz quantum cascade laser," *Applied Physics Letters*, vol. 113, no. 18, p. 181102, 2018.

[174] A. Rakić, T. Taimre, K. Bertling, Y. Lim, P. Dean, A. Valavanis, and D. Indjin, "Sensing and imaging using laser feedback interferometry with quantum cascade lasers," *Applied Physics Reviews*, vol. 6, no. 2, p. 021320, 2019.

[175] P. King and G. Steward, “Metrology with an optical maser,” *New Sci*, vol. 17, no. 180, p. 14, 1963.

[176] D. E. T. Ashby and D. Jephcott, “Measurement of plasma density using a gas laser as an infrared interferometer,” *Applied Physics Letters*, vol. 3, no. 1, pp. 13–16, 1963.

[177] J. Crowe and R. Craig Jr, “GaAs laser linewidth measurements by heterodyne detection,” *Applied Physics Letters*, vol. 5, no. 4, pp. 72–74, 1964.

[178] A. Seko, Y. Mitsuhashi, T. Morikawa, J. Shimada, and K. Sakurai, “Self-quenching in semiconductor lasers and its applications in optical memory readout,” *Applied Physics Letters*, vol. 27, no. 3, pp. 140–141, 1975.

[179] Y. Mitsuhashi, T. Morikawa, K. Sakurai, A. Seko, and J. Shimada, “Self-coupled optical pickup,” *Optics Communications*, vol. 17, no. 1, pp. 95–97, 1976.

[180] K. Otsuka, “Highly sensitive measurement of doppler-shift with a microchip solid-state laser,” *Jpn. J. Appl. Phys*, vol. 31, no. 11, pp. L1546–L1548, 1992.

[181] S. Okamoto, H. Takeda, and F. Kannari, “Ultrahighly sensitive laser-doppler velocity meter with a diode-pumped Nd: YVO4 microchip laser,” *Review of scientific instruments*, vol. 66, no. 5, pp. 3116–3120, 1995.

[182] P. Nerin, P. Puget, P. Besesty, and G. Chartier, “Self-mixing using a dual-polarisation Nd: YAG microchip laser,” *Electronics Letters*, vol. 33, no. 6, pp. 491–492, 1997.

[183] S. Blaize, B. Bérenguier, I. Stéfanon, A. Bruyant, G. Lérondel, P. Royer, O. Hugon, O. Jacquin, and E. Lacot, “Phase sensitive optical near-field mapping using frequency-shifted laser optical feedback interferometry,” *Optics Express*, vol. 16, no. 16, pp. 11718–11726, 2008.

[184] H. Hao, D. Guo, M. Wang, W. Xia, and X. Ni, “Micro-displace sensor based on self-mixing interference of the fiber laser with phase modulation,” *Photonic sensors*, vol. 4, no. 4, pp. 379–384, 2014.

[185] D. Han, M. Wang, and J. Zhou, “Self-mixing speckle in an erbium-doped fiber ring laser and its application to velocity sensing,” *IEEE Photonics Technology Letters*, vol. 19, no. 18, pp. 1398–1400, 2007.

[186] M. Wang, W. Xia, X. Dai, and Y. Zhao, “Self-mixing interference in fiber ring laser and its multiplexing,” in *21st International Conference on Optical Fiber Sensors*, vol. 7753, p. 77531Z, International Society for Optics and Photonics, 2011.

[187] J. Von Staden, T. Gensty, W. Elsäßer, G. Giuliani, and C. Mann, “Measurements of the α factor of a distributed-feedback quantum cascade laser by an optical feedback self-mixing technique,” *Optics letters*, vol. 31, no. 17, pp. 2574–2576, 2006.

[188] R. P. Green, J.-H. Xu, L. Mahler, A. Tredicucci, F. Beltram, G. Giuliani, H. E. Beere, and D. A. Ritchie, “Linewidth enhancement factor of terahertz quantum cascade lasers,” *Applied Physics Letters*, vol. 92, no. 7, p. 071106, 2008.

[189] G. Agnew, *Efficient device-specific dynamic modelling of terahertz quantum cascade lasers*. PhD thesis, School of Information Technology and Electrical Engineering, University of Queensland, Australia, 2019, `https://espace.library.uq.edu.au/view/UQ:c6eeb83`.

[190] K. Bertling, Y. Lim, T. Taimre, D. Indjin, P. Dean, R. Weih, S. Höfling, M. Kamp, M. Von Edlinger, J. Koeth, *et al.*, “Demonstration of the self-mixing effect in interband cascade lasers,” *Applied Physics Letters*, vol. 103, no. 23, p. 231107, 2013.

[191] M. B. Spencer and W. E. Lamb Jr, “Laser with a transmitting window,” *Physical Review A*, vol. 5, no. 2, p. 884, 1972.

[192] J. R. Tucker, *A self-mixing imaging system based on an array of vertical-cavity surface-emitting lasers (VCSELs).* PhD thesis, University of Queensland, Australia, 2007, `https://espace.library.uq.edu.au/view/UQ:158638`.

[193] G. Van Tartwijk and D. Lenstra, "Semiconductor lasers with optical injection and feedback," *Quantum and Semiclassical Optics: Journal of the European Optical Society Part B*, vol. 7, no. 2, p. 87, 1995.

[194] G. Acket, D. Lenstra, A. Den Boef, and B. Verbeek, "The influence of feedback intensity on longitudinal mode properties and optical noise in index-guided semiconductor lasers," *IEEE Journal of Quantum Electronics*, vol. 20, no. 10, pp. 1163–1169, 1984.

[195] R. Kliese, T. Taimre, A. A. A. Bakar, Y. L. Lim, K. Bertling, M. Nikolić, J. Perchoux, T. Bosch, and A. D. Rakić, "Solving self-mixing equations for arbitrary feedback levels: a concise algorithm," *Applied optics*, vol. 53, no. 17, pp. 3723–3736, 2014.

[196] Y. Petitjean, F. Destic, J.-C. Mollier, and C. Sirtori, "Dynamic modeling of terahertz quantum cascade lasers," *IEEE Journal of Selected Topics in Quantum Electronics*, vol. 17, no. 1, pp. 22–29, 2010.

[197] J. R. Freeman, J. Maysonnave, S. Khanna, E. H. Linfield, A. G. Davies, S. S. Dhillon, and J. Tignon, "Laser-seeding dynamics with few-cycle pulses: Maxwell-Bloch finite-difference time-domain simulations of terahertz quantum cascade lasers," *Physical Review A*, vol. 87, no. 6, p. 063817, 2013.

[198] Y. L. Lim, K. Bertling, T. Taimre, T. Gillespie, C. Glenn, A. Robinson, D. Indjin, Y. Han, L. Li, E. H. Linfield, *et al.*, "Coherent imaging using laser feedback interferometry with pulsed-mode terahertz quantum cascade lasers," *Optics express*, vol. 27, no. 7, pp. 10221–10233, 2019.

[199] D. Burghoff, C. Wang Ivan Chan, Q. Hu, and J. L. Reno, “Gain measurements of scattering-assisted terahertz quantum cascade lasers,” *Applied Physics Letters*, vol. 100, no. 26, p. 261111, 2012.

[200] T. Liu, T. Kubis, Q. Jie Wang, and G. Klimeck, “Design of three-well indirect pumping terahertz quantum cascade lasers for high optical gain based on nonequilibrium Green’s function analysis,” *Applied Physics Letters*, vol. 100, no. 12, p. 122110, 2012.

[201] A. Wacker, “Extraction-controlled quantum cascade lasers,” *Applied Physics Letters*, vol. 97, no. 8, p. 081105, 2010.

[202] A. Albo, Y. V. Flores, Q. Hu, and J. L. Reno, “Split-well direct-phonon terahertz quantum cascade lasers,” *Applied Physics Letters*, vol. 114, no. 19, p. 191102, 2019.

[203] B. Wen, C. Xu, S. Wang, K. Wang, M. C. Tam, Z. Wasilewski, and D. Ban, “Dual-lasing channel quantum cascade laser based on scattering-assisted injection design,” *Optics express*, vol. 26, no. 7, pp. 9194–9204, 2018.

[204] B. S. Williams, S. Kumar, Q. Qin, Q. Hu, and J. L. Reno, “Terahertz quantum cascade lasers with double-resonant-phonon depopulation,” *Applied physics letters*, vol. 88, no. 26, p. 261101, 2006.

[205] E. Dupont, S. Fathololoumi, Z. Wasilewski, G. Aers, S. Laframboise, M. Lindskog, S. Razavipour, A. Wacker, D. Ban, and H. Liu, “A phonon scattering assisted injection and extraction based terahertz quantum cascade laser,” *Journal of Applied Physics*, vol. 111, no. 7, p. 073111, 2012.

[206] C. Jirauschek and P. Lugli, “MC simulation of double-resonant-phonon depopulation THz qcls for high operating temperatures,” *Journal of Computational Electronics*, vol. 7, no. 3, pp. 436–439, 2008.

[207] R. Khabibullin, N. Shchavruk, D. Ponomarev, D. Ushakov, A. Afonenko, O. Y. Volkov, V. Pavlovskiy, and A. Dubinov, “Terahertz quantum cascade lasers with silver-and gold-based waveguides,” in *EPJ Web of Conferences*, vol. 195, p. 04002, EDP Sciences, 2018.

[208] S. Kumar *et al.*, *Development of terahertz quantum-cascade lasers.* PhD thesis, Massachusetts Institute of Technology, 2007.

[209] V. D. Jovanović, D. Indjin, N. Vukmirović, Z. Ikonić, P. Harrison, E. H. Linfield, H. Page, X. Marcadet, C. Sirtori, C. Worrall, H. E. Beere, and D. A. Ritchie, "Mechanisms of dynamic range limitations in GaAs/AlGaAs quantum-cascade lasers: Influence of injector doping," *Appl. Phys. Lett.*, vol. 86, no. 21, p. 211117, 2005.

[210] F. Barho, H. Philip, Z. Loghmari, M. Bahriz, A. Baranov, and R. Teissier, "Long wavelength (λ= 10-18 μm) mid-ir quantum cascade lasers operating in a continuous wave at room temperature," in *2019 44th International Conference on Infrared, Millimeter, and Terahertz Waves (IRMMW-THz)*, pp. 1–1, IEEE, 2019.

[211] H. Nguyen Van, Z. Loghmari, H. Philip, M. Bahriz, A. N. Baranov, and R. Teissier, "Long wavelength (λ¿ 17 μm) distributed feedback quantum cascade lasers operating in a continuous wave at room temperature," in *Photonics*, vol. 6, p. 31, Multidisciplinary Digital Publishing Institute, 2019.

[212] I. Kundu, F. Wang, X. Qi, H. Nong, P. Dean, J. R. Freeman, A. Valavanis, G. Agnew, A. T. Grier, T. Taimre, *et al.*, "Ultrafast switch-on dynamics of frequency-tuneable semiconductor lasers," *Nature communications*, vol. 9, no. 1, p. 3076, 2018.

[213] X. Qi, G. Agnew, T. Taimre, Y. L. Lim, K. Bertling, A. Demić, P. Dean, D. Indjin, and A. D. Rakić, "Laser feedback interferometry in multi-mode terahertz quantum cascade lasers," *Optics Express*, 2020 (under review).

[214] N. Vuković, J. Radovanovic, V. Milanovic, and D. L. Boiko, "Analytical expression for Risken-Nummedal-Graham-Haken instability threshold in quantum cascade lasers," *Optics express*, vol. 24, no. 23, pp. 26911–26929, 2016.

[215] N. Vuković, J. Radovanović, V. Milanović, and D. L. Boiko, "Low-threshold RNGH instabilities in quantum cascade lasers," *IEEE Journal of Selected Topics in Quantum Electronics*, vol. 23, no. 6, pp. 1–16, 2017.